Titre: Title:	Innovative Multiport Interferometric Receiver Architectures for Multichannel and Multifunction Millimeter-Wave and Terahertz Systems and Application
Auteur: Author:	Jie Deng
Date:	2025
Type:	Mémoire ou thèse / Dissertation or Thesis
Référence: Citation:	Deng, J. (2025). Innovative Multiport Interferometric Receiver Architectures for Multichannel and Multifunction Millimeter-Wave and Terahertz Systems and Application [Thèse de doctorat, Polytechnique Montréal]. PolyPublie. https://publications.polymtl.ca/70595/

POLYTECHNIQUE MONTRÉAL

affiliée à l'Université de Montréal

Innovative Multiport Interferometric Receiver Architectures for Multichannel and Multifunction Millimeter-Wave and Terahertz Systems and Applications

JIE DENG

Département de génie électrique

Thèse présentée en vue de l'obtention du diplôme de *Philosophiæ Doctor*

Génie électrique

Novembre 2025

POLYTECHNIQUE MONTRÉAL

affiliée à l'Université de Montréal

Cette thèse intitulée :

Innovative Multiport Interferometric Receiver Architectures for Multichannel and Multifunction Millimeter-Wave and Terahertz Systems and Applications

présentée par **Jie DENG**

en vue de l'obtention du diplôme de *Philosophiæ Doctor*

a été dûment acceptée par le jury d'examen constitué de:

Gunes KARABULUT KURT, présidente
Ke WU, membre et directeur de recherche
Jean-Jacques LAURIN, membre
Ammar B. KOUKI, membre externe

DEDICATION

To my parents

ACKNOWLEDGEMENTS

I am deeply grateful to my supervisor, Prof. Ke Wu, for his inspiring guidance, unwavering support, and the immense confidence he placed in me, especially during challenging times when my work faced obstacles. I sincerely thank him for giving me the opportunity to pursue my Ph.D. within his research group at the Poly-Grames Research Center.

I would also like to express my heartfelt thanks to Dr. Pascal Burasa for his unwavering support and assistance, not only throughout my Ph.D. studies but also in my daily life. In particular, he has taught me how to maintain a positive mindset in the face of challenges. I am deeply grateful for all his help.

I would like to extend my sincere gratitude to the technical and administrative teams at the Poly-Grames Research Center. In particular, I am deeply thankful to Louis-Philippe Carignan, Traian Antonescu, and Steve Dube for their outstanding work on circuit fabrication, as well as to David Dousset and Maxime Thibault for their invaluable support with the measurements.

I would also like to take this opportunity to thank my friends and colleagues for their valuable academic discussions and suggestions: Chunmei Liu, Qingtao Chen, Ben You, Kang Zhou, Jianye Mai, Seyed Ali Keivann, Yasser Bigdeli, Thomas Micallef, Dongzhe Zheng, Desong Wang, Xiaoqiang Gu, Muhib Ur Rahman, and Chandan Roy, for contributing to a pleasant and vibrant research environment.

Lastly, I am profoundly grateful to my parents for their unwavering support, boundless understanding, and unconditional love. Their constant encouragement has been the foundation of my perseverance throughout this journey. I am truly blessed to have them by my side, offering strength and comfort in every step of my academic and personal growth.

RÉSUMÉ

Avec le développement rapide de diverses applications, telles que les appareils intelligents, l'intelligence artificielle, l'Internet des objets, la cartographie environnementale en 3D, les médias 3D et les véhicules autonomes, le besoin de débits de données ultra-élevés et de communications de haute qualité non compressées est devenu essentiel. Ces applications nécessitent une faible latence, une haute fiabilité et une synchronisation précise, ce qui motive le besoin de solutions de communication avancées. Pour répondre à ces exigences évolutives, une réévaluation fondamentale des principes traditionnels de communication sans fil est nécessaire, entraînant une nouvelle recherche et une innovation technologique. En réponse, les technologies sans fil de prochaine génération évoluent vers des architectures hautement intégrées, multifonctionnelles, multimodes et multicanaux. Une solution prometteuse pour relever ces défis est l'adoption des architectures interférométriques multiport, qui ont gagné en reconnaissance en tant que technique compétitive et efficace pour le développement des front-ends. Ces architectures offrent des avantages significatifs par rapport aux systèmes traditionnels basés sur des mélangeurs, tels que les architectures hétérodyne et homodyne, en raison de leur simplicité, de leurs capacités à large bande, de leur rentabilité, de leur adéquation aux fréquences millimétriques (mmW) et térahertz (THz), et de leur faible consommation d'énergie. Dans ce contexte, cette thèse vise à développer des récepteurs interférométriques multiport innovants pour les systèmes de communication sans fil mmW et THz.

Ce travail commence par une investigation approfondie du développement des récepteurs interférométriques, retraçant leur évolution et les avancées technologiques qui ont façonné leur conception. Une comparaison détaillée des performances entre les front-ends traditionnels basés sur des mélangeurs et les front-ends interférométriques multiport est fournie, offrant une compréhension complète des mécanismes opérationnels sous-jacents, ainsi que des compromis en termes de performance, de complexité et de coût. De plus, diverses architectures interférométriques sont examinées, mettant en évidence leurs principales caractéristiques, considérations de conception et avantages distincts, tels qu'une plage dynamique améliorée, une consommation d'énergie réduite et une sensibilité accrue. Les applications pratiques de ces architectures sont ensuite présentées et discutées, en se concentrant sur leurs applications dans des domaines tels que les communications sans fil, les systèmes radar et les technologies de détection. Ces discussions

inspirent le développement d'architectures interférométriques innovantes, visant à repousser les limites des capacités actuelles et à répondre aux exigences croissantes des systèmes futurs.

Une nouvelle architecture de récepteur à double entrée autonome, basée sur la technique interférométrique, est proposée et démontrée dans ce travail pour les systèmes sans fil multicanaux parallèles. Le récepteur proposé utilise des chemins de canal radiofréquence (RF) à double entrée et une unité matérielle unique pour la traduction de fréquence, c'est-à-dire la conversion des signaux vers la bande de fréquence intermédiaire (IF). Cette conception permet d'extraire les signaux IF démodulés à partir de deux ports de sortie, contrairement aux quatre généralement requis dans les systèmes multiports traditionnels. En réduisant le nombre de ports de sortie, l'architecture proposée réduit considérablement la complexité des circuits, la taille, le coût et la consommation d'énergie. Dans les systèmes conventionnels, les chemins RF doubles sont souvent implémentés à l'aide de deux plateformes réceptrices à six ports séparées. Par conséquent, pour les systèmes MIMO (Multiple Input Multiple Output) à chemins de fréquence diversifiés N, le nombre de plateformes récepteur proposées est réduit à N/2, ce qui entraîne une réduction significative de la taille du système par rapport aux récepteurs MIMO traditionnels.

La technique de diversité de polarisation est largement utilisée dans les récepteurs RF de pointe, améliorant leurs performances en prenant en charge des flux de données simultanés et indépendants sur un même canal de fréquence. Cette approche double efficacement la capacité du canal et optimise l'utilisation du spectre par rapport aux récepteurs à polarisation unique. Dans ce travail, une solution de récepteur interférométriques tout-en-un pour des systèmes sans fil à polarisation duale multicanaux est proposée et démontrée. Le récepteur bénéficie de l'utilisation d'un schéma de guide d'ondes carré, permettant d'intégrer des caractéristiques de polarisation duale. Cette conception permet l'excitation simultanée de deux polarités orthogonales, à savoir horizontale et verticale, au sein d'un seul récepteur matériel modulaire, tout en garantissant des performances fiables. Pour valider le concept, un prototype expérimental a été développé, fabriqué et testé. Le démultiplexage expérimental réussie des signaux modulés en polarisation duale valide davantage l'efficacité de la conception proposée.

De plus, dans les systèmes l'Internet des objets (IoT), où une variété de nœuds capteurs sans fil, réseaux et étiquettes d'identification mmW sont largement déployés dans l'environnement, il existe un besoin croissant de solutions de communication et d'énergie efficaces. Dans ce contexte, nous

proposons un réseau de récepteurs interférométriques conçu pour des systèmes de communication, détection et transfert d'énergie combinés. Le réseau de récepteurs vise à minimiser la consommation d'énergie tout en permettant le fonctionnement autonome d'un réseau soutenant la récolte d'énergie sans fil, la réception de données, le stockage, le traitement et la communication. Il utilise un réseau de transducteurs orthomodaux (OMT) pour réaliser la diversité de polarisation, doublant ainsi la capacité du canal. En outre, le réseau de récepteurs intègre un redresseur différentiel, fabriqué à l'aide de la technologie CMOS de 65 nm, pour permettre le transfert d'énergie sans fil. Cette intégration permet au système de soutenir simultanément la communication sans fil et la récolte d'énergie.

L'intégration des technologies micro-ondes (MW) et THz offre une solution prometteuse pour soutenir les futurs systèmes sans fil multifonctionnels et multistandard, tels que les plates-formes combinées de détection et de communication. Cependant, la coexistence des opérations MW et THz dans un seul récepteur présente des défis importants. Ceux-ci incluent l'adaptation à un système à double bande avec un grand rapport de fréquence tout en répondant à des exigences de performance strictes. Pour surmonter ces défis, un récepteur interférométrique à double bande conjoint conçu pour des opérations simultanées MW et THz est proposé dans ce travail. Le récepteur interférométrique proposé conserve les avantages des architectures interférométriques conventionnelles, telles qu'une configuration simple et une faible consommation d'énergie. Il permet la réception simultanée des signaux MW et THz sur deux canaux de fréquence sur une seule plate-forme matérielle, avec les deux signaux étant ensuite traduits ou convertis vers des bandes IF différentes. Il s'agit du premier récepteur interférométrique capable de fonctionner simultanément sur les fréquences MW et THz.

ABSTRACT

With the rapid development of diverse applications, including smart devices, artificial intelligence, the Internet of Things, three dimensional (3D) environmental mapping, 3D media, and autonomous vehicles, the need for ultra-high data rates and uncompressed, high-quality communications has become essential. These applications require low latency, high reliability, and precise synchronization, driving the need for advanced communication solutions. To meet these evolving requirements, a fundamental reassessment of traditional wireless communication principles is necessary, prompting renewed research and technological innovation. In response, next-generation wireless technologies are advancing toward highly integrated, multifunctional, multimode, and multichannel architectures. One promising solution to address these challenges is the adoption of multiport interferometric architectures, which have gained recognition as a competitive and efficient technique for front-end development. These architectures offer significant advantages over traditional mixer-based systems such as heterodyne and homodyne architectures, due to their simplicity, broadband capabilities, cost-effectiveness, suitability for millimeter-wave (mmW) and terahertz (THz) frequencies, and low power consumption. Against this backdrop, this thesis aims to develop innovative multiport interferometric receivers for emerging and future mmW and THz wireless communication systems.

This thesis begins with an in-depth investigation of the development of interferometric receivers, tracing their evolution and the technological advances that have shaped their design. A detailed performance comparison between traditional mixer-based front-ends and multiport interferometric front-ends is provided, offering a comprehensive understanding of the underlying operational mechanisms, as well as the trade-offs in terms of performance, complexity, and cost. Furthermore, various interferometric architectures are reviewed, emphasizing their key features, design considerations, and distinct advantages, such as improved dynamic range, reduced power consumption, and enhanced sensitivity. The practical applications of these architectures are then presented and discussed, focusing on their applications in areas like wireless communications, radar systems, and sensing technologies. These discussions inspire the development of innovative interferometric architectures, aiming to push the boundaries of current capabilities and meet the growing demands of future systems.

In this thesis, a novel self-contained dual-input receiver architecture based on the interferometric technique is proposed and demonstrated for parallel-multichannel wireless systems. The proposed

receiver utilizes dual-input radio frequency (RF) channel paths and a single hardware unit for frequency translation, i.e., converting signals to the intermediate frequency (IF) band. This design enables demodulated IF signals to be extracted from two output ports, in contrast to the four typically required in traditional multiport systems. By reducing the number of output ports, the proposed architecture significantly lowers circuit complexity, size, cost, and power consumption. In conventional systems, dual RF input paths are often implemented using two separate six-port receiver platforms. Therefore, for N-path frequency-diversified multiple-input multiple-output (MIMO) systems, the number of proposed receiver platforms is reduced to N/2, leading to a significant reduction in system size compared to legacy MIMO receivers.

The polarization diversity technique has been widely used in the state-of-the-art RF receivers, enhancing their performance by supporting simultaneous, independent data streams over the same frequency channel. This approach effectively doubles channel capacity and optimizes spectrum utilization compared to single-polarization receivers. In this thesis, an all-in-one interferometric receiver solution for dual-polarization multichannel wireless systems is proposed and demonstrated. The receiver benefits from the use of a square waveguide scheme, enabling dual-polarization features. This design allows for the simultaneous excitation of two orthogonal polarizations, namely, horizontal and vertical, within a single modular hardware receiver, while ensuring reliable performance. To validate the concept, we developed, fabricated, and tested an experimental prototype. The successful experimental demodulation of dual-polarization modulated signals further validates the effectiveness of the proposed design.

In addition, Internet of Things (IoT)-based systems, where a variety of wireless sensor nodes, networks, and mmW identification tags are extensively deployed in the environment, there is a growing need for efficient communication and energy solutions. In this context, we propose an interferometric receiver array designed for joint communication, sensing, and power transfer systems. The receiver array aims to minimize power consumption while enabling the autonomous operation of a network that supports wireless energy harvesting, data reception, storage, processing, and communication. It uses the orthomode transducers (OMTs) array to achieve polarization diversity, effectively doubling channel capacity. Additionally, the receiver array integrates a differential rectifier, fabricated using 65-nm bulk complementary metal-oxide-semiconductor (CMOS) technology, to enable wireless power transfer. This integration allows the system to simultaneously support wireless communication and energy harvesting.

Integrating microwave (MW) and THz technologies offers a promising solution for supporting future multifunctional and multistandard wireless systems, such as joint sensing and communication platforms. However, the coexistence of MW and THz operations within a single receiver presents significant challenges. These include accommodating a dual-band system with a large frequency ratio while meeting stringent performance requirements. To overcome these challenges, a joint dual-band interferometric receiver designed for simultaneous MW and THz operations is proposed in this thesis. The proposed interferometric receiver retains the advantages of conventional interferometric architectures, such as a simple configuration and low power consumption. It enables concurrent reception of MW and THz signals across two frequency channels on a single hardware platform, with both signals then being translated or converted to different IF bands. This is the first interferometric receiver capable of simultaneously operating across both MW and THz frequencies.

TABLE OF CONTENTS

LIST OF TABLES

LIST OF FIGURES

LISTE OF SYMBOLS AND ABBREVIATIONS

2D	Two-dimentional
3D	Three-dimensional
5G	Fifth generation
6G	Sixth generation
AOA	Angle-of-arrival
AWG	Arbitrary waveform generator
ADS	Advanced designed system
AI	Artificial intelligence
ADCs	Analog-to-digital converters
BW	Bandwidth
BiCMOS	Bipolar complementary metal-oxide-semiconductor
CMOS	Complementary metal-oxide-semiconductor
CSRR	Complementary split-ring resonator
CPW	Coplanar waveguide
CNC	Computer numerical control
CST	Computer simulation technology
DR	Dynamic range
DC	Direct current
EM	Electromagnetic
EVMs	Error vector magnitudes
E	Electric
GSG	Ground-signal-ground
H-P.	Horizontal polarized

H	Horizontal
HB	Harmonic balance
IoT	Internet of Things
ISAC	Integrated sensing and communication
IF	Intermediate frequency
I	In-phase
ICs	Integrated circuits
JRC	Joint radar and communication
LO	Local oscillator
LOS	Line-of-sight
LNA	Low-noise amplifier
MDS	Minimum detectable signal
MW	Microwave
mmW	Millimeter-wave
MIMO	Multiple-input multiple-output
MHMIC	Miniature hybrid microwave integrated circuits
MMIC	Monolithic microwave integrated circuit
M-QAM	M-quadrature-amplitude modulation
NLOS	Non-line-of-sight
NF	Noise figure
N	Number
OMTs	Orthomode transducers
PCB	Printed circuit board
PCE	Power conversion efficiency

Q	Quadrature
QAM	Quadrature-amplitude modulation
QPSK	Quadrature phase shift keying
RX	Receiver
RF	Radio frequency
RL	Output load
SiGe	Silicon-Germanium
SIW	Substrate-integrated waveguide
SNR	Signal-to-noise ratio
TR	Transmission line
THz	Terahertz
V-P.	Vertical polarized
V	Vertical
VNAs	Vector network analyzers

LIST OF APPENDICES

CHAPTER 1 INTRODUCTION

1.1 Research background

The rapid proliferation of emerging systems and applications—such as smart devices, artificial intelligence (AI), multimedia services, virtual reality, the Internet of Things (IoT), fifth generation (5G)/sixth generation (6G), three dimensional (3D) environmental sensing and mapping, and autonomous mobility—is placing increasingly complex and stringent performance demands on future wireless systems [1], [2], [3], [4], [5], [6], [7], [8], [9], [10], [11], [12]. These evolving requirements necessitate a fundamental re-examination of traditional wireless communication principles, thereby driving renewed research efforts and technological innovation. Meeting the demands of emerging systems and applications calls for breakthroughs in several critical areas, including power efficiency, data transmission speed, system reliability, latency reduction, channel capacity, network adaptability, cost-effectiveness, and seamless connectivity [13], [14], [15], [16], [17]. As these demands continue to grow, future wireless systems must go beyond supporting real-time data processing and intelligent decision-making. They must also facilitate dynamic resource allocation while maintaining high levels of efficiency, scalability, and performance consistency across diverse operating environments.

To address these multifaceted challenges, next-generation wireless technologies are advancing toward highly integrated, multifunctional, multimode, and multichannel architectures [18], [19], [20], [21]. This evolution significantly enhances system flexibility, interoperability, and performance across a wide range of applications, effectively bridging the gap between communication, sensing, imaging, and computational intelligence. A central focus of this transformation is the development of joint radar and communication (JRC), also recently known as integrated sensing and communication (ISAC)—a paradigm that fuses wireless data transmission with real-time environmental awareness [22], [23], [24], [25], [26], [27], [28], [29], [30].

ISAC enables the simultaneous execution of high-speed communication, precise localization, and situational awareness, making it particularly suitable for emerging intelligent wireless systems such as autonomous vehicles, smart cities, and next-generation industrial automation. In parallel, other disruptive technologies are also gaining momentum, including reconfigurable intelligent surfaces for dynamic signal control, unified architectures for joint data communication, radar sensing, and

power transfer, as well as ultra-wideband imaging for high-resolution environmental mapping. Together, these cutting-edge advancements are laying the foundation for intelligent, adaptive, and highly connected wireless networks, capable of supporting the next era of pervasive, hyper-connected environments.

Undoubtedly, an environmentally friendly front-end with operational agility and flexibility is essential for enabling disruptive wireless technologies and fostering innovative ecosystems. To meet the stringent demands of emerging systems, such front-ends must satisfy several critical performance criteria, including wide operational frequency range, high sensitivity, low power consumption, high dynamic range, and linearity. They must also be capable of withstanding strong blockers and interference, all while maintaining a compact physical footprint. In particular, minimizing power consumption is crucial for enhancing overall energy efficiency.

Traditionally, the front-ends of transmitters, receivers, and transceivers rely on highly nonlinear mixer-based architectures—such as heterodyne, homodyne, and low intermediate frequency (IF) configurations—for frequency conversion (i.e., up-conversion or down-conversion) [31], [32], [33], [34], [35], [36], [37]. Numerous architectural variations have been implemented in practical systems [38]. A comprehensive classification of frequency conversion techniques is provided in [18], broadly categorizing them into two schemes from a frequency-domain perspective: linear and nonlinear interferometric techniques.

In nonlinear interferometric systems, each mixer-based channel typically comprises at least one mixer and one local oscillator (LO). The LO provides a reference signal that mixes with the input RF signal to produce an output at the desired frequency—either up-shifted for transmission or down-shifted to the IF for further processing. However, the core mixer operates in a highly nonlinear regime, necessitating high LO driving power. As a result, driving multiple mixers becomes increasingly challenging, presenting significant barriers to the scalability and widespread adoption of such architectures in 5G, 6G, and future wireless platforms—particularly in mobile and energy-constrained applications. This challenge is further exacerbated at millimeter-wave (mmW) [39], [40], [41], [42], [43], [44], [45], [46], [47], [48] and terahertz (THz) [49], [50], [51], [52], [53], [54], [55], [56], [57], [58], [59], [60], [61], [62] frequencies, where the generation of sufficiently high LO power is either difficult or practically infeasible due to the limited availability of efficient high-power sources.

To address the design challenges associated with high power consumption in front-end systems, a promising solution lies in the development of multiport interferometric architectures. This approach offers significant potential across a wide range of platforms—including microwave, mmW, THz, electronic-photonic, and optical systems—with a particular emphasis on key functionalities for communication, sensing, and imaging applications [63], [64], [65], [66], [67], [68], [69], [70], [71], [72], [73], [74], [75], [76], [77], [78], [79], [80].

1.2 Research objectives

The primary objectives of this Ph.D. research are to propose, investigate, and design innovative interferometric architectures and technologies for mmW and THz wireless systems. The study is carried out through both theoretical analysis and experimental validation, with a particular emphasis on key factors such as bandwidth performance, circuit complexity, cost, power consumption, dynamic range, and sensitivity. Specifically, this research focuses on the following aspects:

(1) Various multiport interferometric architectures are investigated, providing a thorough understanding of their underlying operational mechanisms. The key technological features of these architectures are summarized, followed by a discussion of their practical applications. This comprehensive overview offers valuable insights into the development and potential of multiport interferometric technology.

(2) The concept of concurrent multi-band operation is explored to boost system throughput and introduce diversity to combat channel fading. In particular, multi-band operation within multiport interferometric architectures offers a highly desirable feature for next-generation frequency-diversified multiple-input multiple-output (MIMO) systems.

(3) The orthogonal polarization modes, namely H-polarized (H-P.) and V-polarized (V-P.) modes, are explored in multiport interferometric architectures. These modes enable the simultaneous transmission of independent data streams, effectively doubling the system's channel capacity and accelerating practical applications in high-throughput data transmission systems.

(4) THz band offers a vast spectral resource, with an absolute bandwidth significantly larger than that of its lower-frequency counterparts. This compelling feature drives the development of wireless systems in the THz frequency range. This research explores and develops THz front-ends,

with a focus on addressing the challenges associated with THz hardware circuits. To minimize transmission loss, metallic waveguide technology is adopted in the design of THz interferometric front-ends.

1.3 Thesis outline

This Ph.D. thesis presents original research on multiport interferometric technology for mmW and THz wireless systems. Several multifunctional front-end receivers based on the multiport interferometric architecture are proposed and designed. For each case, the theoretical foundations, physical realizations, and experimental prototypes are comprehensively investigated and detailed. The thesis is organized as follows:

Chapter 1 introduces the research background and objectives of this Ph.D. thesis, focusing on multiport interferometric architectures and technologies for mmW and THz applications. Additionally, the outline of the thesis is presented.

Chapter 2 reviews the development of multiport interferometric architectures, from the four-port to the nine-port architecture, and discusses their characteristics and application scenarios, aiming to provide an overview of the state-of-the-art in this field.

Chapter 3 presents a dual-input multiport interferometric receiver designed for mmW parallel-multichannel wireless systems. The main advantage of the proposed receiver topology is its self-contained parallel channels, in contrast to conventional interferometric receivers, which helps reduce circuit complexity, size, cost, and power consumption. Furthermore, the proposed receiver utilizes only two output ports, compared to the traditional four. An experimental prototype was designed and fabricated to validate the receiver's performance in simultaneous operation across the 24- and 28-GHz mmW frequency bands.

Chapter 4 introduces a dual-polarization waveguide interferometric receiver that enables simultaneous independent data streams on the same frequency channel, effectively doubling the channel capacity and enhancing spectrum efficiency compared to single-polarized counterparts. Square waveguide technology is employed to support orthogonal polarization. The receiver comprises a multiport circuit and four pairs of power detectors. The core multiport circuit integrates dual-polarization components, including cruciform couplers, orthomode transducers (OMTs), and phase shifters. The receiver's operating mechanism is analyzed and explained through a

mathematical model. An experimental prototype was designed, fabricated, and tested, with successful demodulation of various digitally modulated signals at different data rates. The experimental results demonstrate the excellent performance of the receiver, confirming its potential for use in multifunction and dual-polarized wireless systems.

Chapter 5 focuses on the integration of wireless communication and energy harvesting at mmW bands. To achieve this, a receiver array architecture based on interferometric technology is proposed. The receiver array supports dual-polarization operation without increasing circuit complexity. Each unit-cell of the array can be dynamically allocated to synthesize channels for data reception, sensing, and energy harvesting. For wireless power transfer, a CMOS differential rectifier is integrated into each receiver unit. The recovered data and generated direct current (DC) power from the various receiver units are processed concurrently, resulting in high capacity and efficient power and data management. An experimental prototype was fabricated to validate the proposed concept. Various modulations and energy harvesting functions were successfully measured and demonstrated. The experimental results confirm that the proposed receiver is highly suitable for versatile, unified communications and IoT sensor applications in future radio environments, including 5G, 6G, and beyond.

Chapter 6 explores integrating microwave (MW) and THz technologies into a single hardware platform, addressing limitations in packaging and assembly while enabling seamless wireless sensing and communication with efficient information fusion for groundbreaking applications. Based on this background, a joint MW/THz interferometric receiver is proposed, studied, and demonstrated, aimed at future multifunctional wireless sensing and communication systems. The chapter provides a detailed analysis and discussion of the proposed receiver architecture. An experimental prototype was designed and fabricated using a Miniature Hybrid Microwave Integrated Circuits (MHMIC) process. To validate the proposed architecture, the prototype was tested, and various M-quadrature-amplitude modulation (QAM) signals were successfully demodulated in both the MW band (5.8 GHz) and THz band (150 GHz), confirming the receiver's performance.

Chapter 7 concludes the research presented in this thesis by providing a summary of the contributions made through the development of multiport interferometric architectures tailored for mmW and THz applications. It highlights the innovative features of these architectures and

underscores their potential to shape the future of wireless systems. Additionally, the chapter addresses key challenges encountered throughout the research and offers insights into emerging trends and technologies. These recommendations emphasize areas where further investigation could substantially propel the field forward, such as the integration of artificial intelligence and the exploration of novel applications in the evolving landscape of 6G and beyond.

CHAPTER 2 LITERATURE REVIEW

2.1 Research background

Since Edwin Howard Armstrong invented the superheterodyne architecture around 1918 [38], various alternative architectures—such as homodyne (zero-IF), low-IF, and image rejection—have been implemented in transmitters and receivers. The superheterodyne architecture remains widely used in receiver design, where it downconverts the modulated carrier to IF signal. The IF signal is then demodulated into baseband signals via complex mixing. This architecture generally achieves a wide dynamic range, though this advantage comes at the cost of increased complexity. In contrast, the homodyne architecture offers a simpler configuration. In this approach, the LO signal has the same frequency as the radio frequency (RF) signal, and zero-IF conversion is accomplished through complex mixing rather than real mixing. As a result, there is no need for an additional image-rejection bandpass filter before the mixer. However, this design is prone to issues such as mismatches, LO leakage, and intermodulation products.

Obviously, each of these architectures has its own set of advantages and disadvantages. For different application scenarios, the relevant parameters of each architecture must be carefully considered. It is also worth noting that these classical architectures are built on mixer-based technology, which requires a high-power LO signal to drive nonlinear and multitoned mixing between the RF and reference signals. While high-power LO signals can be easily generated at lower frequencies, generating them at mmW and THz frequencies poses significant challenges due to the lack of appropriate sources in these bands. To overcome these challenges, a novel technology—multiport interferometric architecture—has been proposed. Unlike conventional designs, this technology eliminates the need for high-power LO signals, significantly reducing LO power consumption. As a result, it emerges as a promising solution for mmW and THz applications.

2.2 Brief introduction to multiport interferometric technology

The multiport interferometric concept, originally introduced in the early 1970s by G. Engen and C. Hoer, has become widely used for simple and accurate power measurement setups. They later expanded its application to measure complex reflection coefficients in microwave network analysis, providing a cost-effective alternative to conventional solutions [81], [82], [83], [84]. This technology remains essential, particularly in high-frequency bands where equipment is costly, and

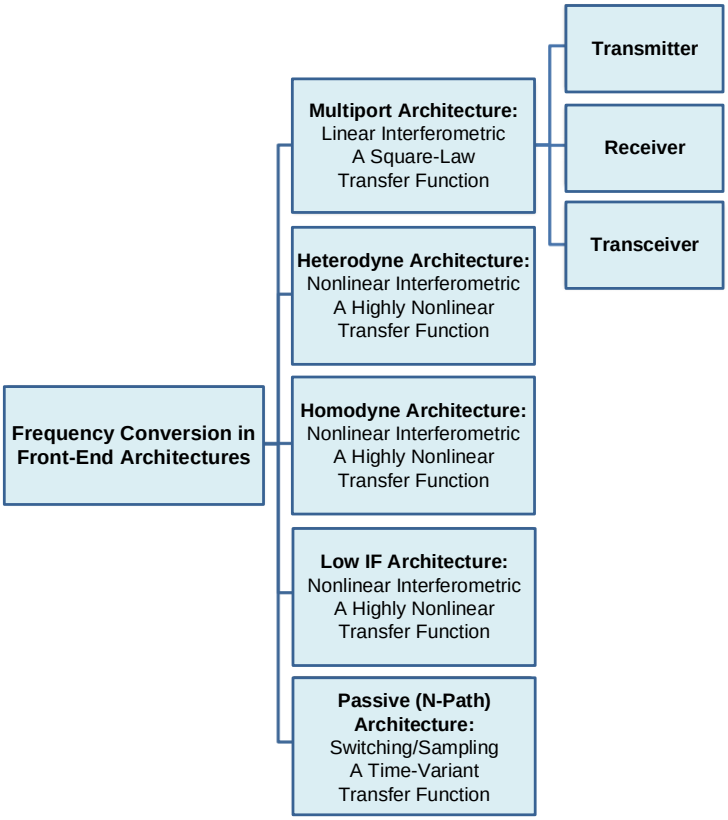

Figure 2.1 Block diagram illustrating the frequency conversion mechanisms in various front-end architectures, highlighting the multiport configuration employed in the transmitter, receiver, and transceiver designs

for specialized applications that require affordable testing devices. In 1994, multiport technology was initially redesigned for wireless communication receivers [85], [86], and since then, it has evolved into a versatile architecture applicable to wireless transmitters, receiver, transceiver, automotive radar systems, imaging systems, and various advanced applications [87], [88], [89], [90], [91], [92], [93], [94], [95], [96], [97], [98], [99], [100], [101], [102], [103], [104], [105], [106], [107], [108], [109], [110], [111], [112], [113], [114], [115], [116], [117], [118], [119], [120], [121], [122], [123], [124], [125], [126], [127], [128], [129], [130], [131], [132].

In contrast to traditional mixer-based nonlinear interferometric architectures that depend on high-power LO signals and nonlinear mixing components, the multiport interferometric architecture based on a linear interference principle as shown in Figure 2.1. It should be mentioned that this architecture linearly combines LO and RF signals with precisely defined amplitude and phase

Table 2.1 Feature comparison of heterodyne, homodyne, low-IF, and multiport architectures

Performance Attribute	Multiport Architecture	Heterodyne Architecture	Homodyne Architecture	Low IF Architecture
LO Power Consumption	Low	High	High	High
Sensitivity	Good	Excellent	Good	Good
Dynamic Range	Average	Excellent	Good	Good
Noise Figure	Average	Excellent	Average	Good
Linearity	Average	Excellent	Good	Good
Filter Requirement	Average	High	Average	Average
Port-to-Port Isolation	Easy-to-achieve	Difficult-to-achieve	Average	Average
Harmonic Control	Easy	Difficult	Average	Average
Wideband Performance	Excellent	Average	Average	Average
mmW and THz Applications	Excellent	Good	Good	Good
Structure Complexity	Average	High	Low	Average
Circuit Size	Average	Large	Small	Average

relationships, operating at lower power levels within the square-law region of the detectors. This results in notable improvements in energy efficiency and system simplicity.

Power detection in these systems can be realized using a variety of device technologies, such as transistors [133], [134], [135] and diodes [136], [137], [138], [139], [140], thus offering flexibility in design and integration across a range of frequency bands and platforms. To offer a clearer comparison of various front-end architectures, Table 2.1 presents a comparison of key

characteristics between nonlinear interference-based techniques (such as heterodyne, homodyne, and low-IF architectures) and their multiport archiecture counterparts, using the receivers as representative case studies [87]. The multiport interferometric architecture stands out due to its significant advantages—particularly in its low LO power requirements, wideband operation, and strong applicability for high-frequency band such as mmW and THz applications. As a result of these benefits, multiport interferometric technology has gained considerable research interest in recent years.

2.3 Multiport Interferometric Receiver Architectures

Since the introduction of the multiport interferometric architecture, a variety of variants have been developed to address the changing system requirements and performance goals across different technological domains. These architectures are typically categorized into four-port to nine-port configurations based on their geometric structure in front-end systems. Each category plays a crucial role in improving system performance for communication, sensing, and imaging applications. To facilitate the upcoming discussions, a comprehensive summary of these architectural variants is provided, outlining their key features, design considerations, and distinct advantages. Additionally, the practical contributions of each variant to specific application scenarios are examined, offering insights into their relevance and impact at the system level.

Variety of multiport interferometric receiver architectures have been propsoed over the past several decades. As shown in Figure 2.2(c) [141], a typical example is the six-port receiver. This architecture consists of a passive six-port network, four power detectors connected to its output ports. The modulated RF signal is captured via the antenna and the RF signal is filtered and then amplified by a low-noise amplifier (LNA) before entering port 1 of the six-port network. Port 2 is driven by a LO signal. Inside the six-port network, the LO and RF signals combine to generate output signals with specific amplitude and phase relationships. These outputs are measured by output diode detectors, which operate in their square-law region, where the detected voltage is approximately proportional to the input power. The output signals are then filtered to eliminate unwanted noise and amplified to enhance the signal levels. Subsequently, the signals are next digitized using analog-to-digital converters (ADCs) for further digital processing. From this digitized data, the in-phase (I) and quadrature (Q) components are extracted, enabling precise reconstruction of the original modulated signal. To address challenges related to circuit complexity,

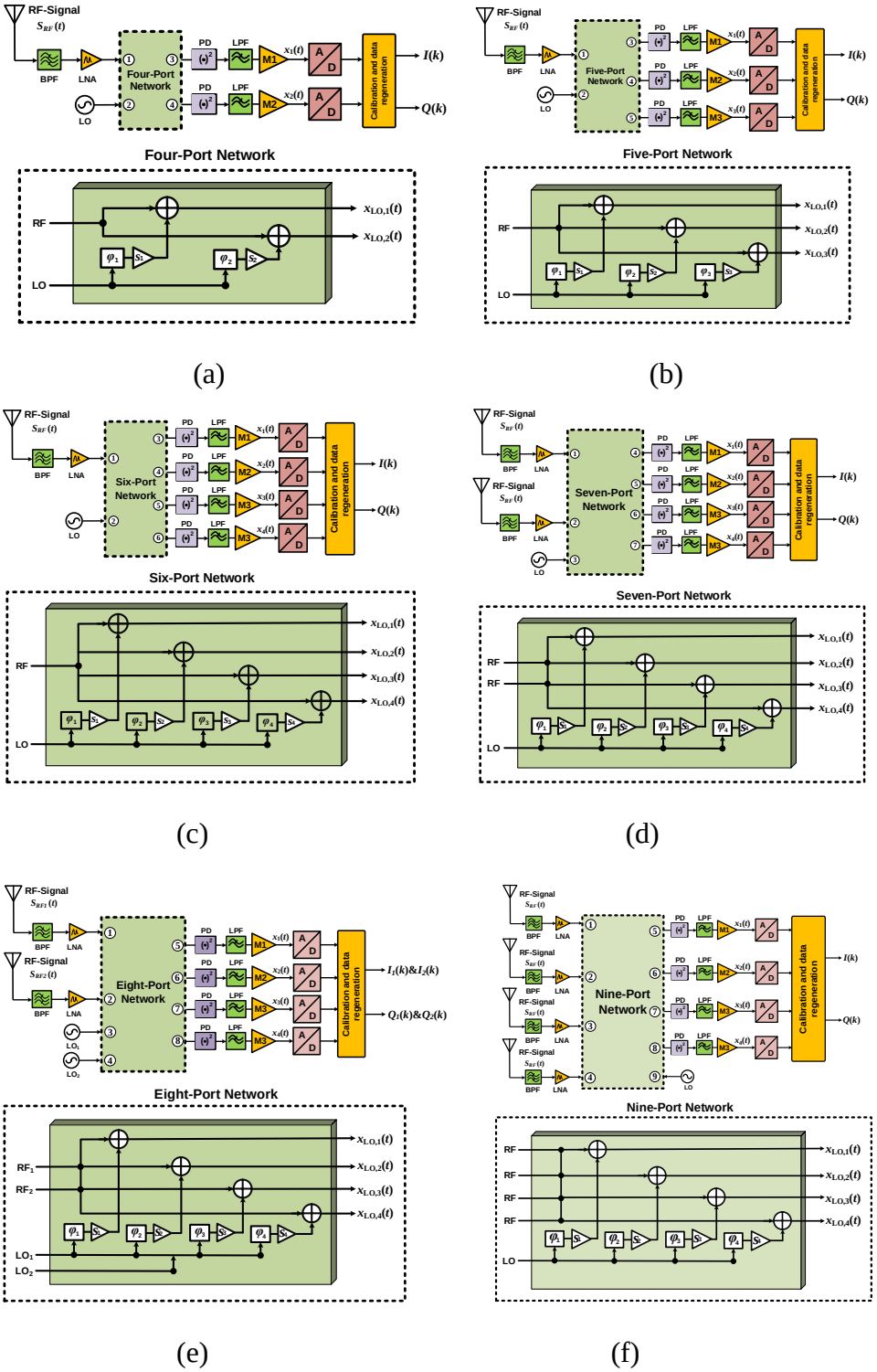

Figure 2.2 (a) Four-port architecture [142], (b) Five-port architecture [143], (c) Six-port architecture [141], (d) Seven-port architecture [144], (e) Eight-port architecture [145], (f) Nine-port architecture [146]

Table 2.2 Summary of the state-of-the-art multiport interferometric receivers

Multiport Interferometric Receiver			
Reference	**Frequency**	**Applications Scenarios**	**Technology**
[107]	2.4 GHz	Sensing (Angular displacement)	PCB
[124]	3.38 GHz/3.82 GHz	Wireless communication (Concurrent dual-band transmission)	PCB
[119]	23.75 GHz	Sensing (localization and targets discrimination)	PCB
[146]	5.0 GHz	Wireless communication (Single-band transmission)	PCB
[126]	2.44 GHz	Imaging (Near-Field microwave microscopy)	PCB
[120]	20 GHz	Sensing (phase discriminator for monopulse tracker)	MMIC
[167]	35 GHz	Imaging (Non-destructive evaluation)	PCB
[151]	28 GHz	Wireless communication (Concurrent dual-band transmission)	PCB
[162]	60 GHz	Sensing (2D-AOA detection)	PCB
[160]	2.448 GHz	Sensing (Localization and identification)	PCB
[122]	60 GHz	Sensing (Industrial radar or AOA detection)	MHMIC
[125]	28 GHz	Wireless communication (Single-band transmission)	CNC
[153]	60 GHz	Wireless communication (Single-band transmission)	CNC
[79]	28 GHz	Wireless communication (Single-band transmission)	PCB
[123]	180 GHz	Wireless communication (Single-band transmission)	SiGe BiCMOS

[163]	61 GHz	Sensing (Sheet thickness monitoring)	PCB
[145]	28 GHz	Wireless communication (Dual-polarization transmission)	CNC
[121]	120 GHz	Sensing (Industrial radar and biomedical application)	SiGe BiCMOS
[152]	5.88 GHz/150 GHz	Wireless communication (Concurrent dual-band transmission)	PCB
[276]	60 GHz	Imaging (Near-field millimeter wave microscope)	PCB

size, cost, and power consumption, in [142] and [143], four-port and five-port interferometric receivers were introduced, respectively, as illustrated in Figure 2.2(a) and (b). In contrast to the six-port receiver archiecture, which has four output ports, these archiectures have fewer output ports, which reduces the number of power detectors and ADCs. This reduction simplifies the complexity of the system architecture, lowers power consumption and cost, while still maintaining performance through efficient signal processing.

In contrast, a seven-port interferometric receiver architecture [144] was proposed with increasing the number of ports. As shown in Figure 2.2(d), this architecture can enable dual-polarization operation and improving signal processing capabilities compared to single-input RF port configurations. In [145], an eight-port interferometric receiver was proposed, as illustrated in Figure 2.2(e). In this architecture, ports 1 and 2 are connected to two separate antennas to receive the modulated signals, while ports 3 and 4 are connected by two distinct LO sources. This design supports parallel multi-channel operation, further enhancing system flexibility and performance. Similarly, a nine-port interferometric receiver architecture, shown in Figure 2.2(f), utilizes four spatially distributed antenna elements, replacing the traditional six-port junction made of hybrid couplers or other circuit-based topologies [146]. It should be mentioned that Figure 2.2 from [87]. This design, incorporating multiple antenna elements, is particularly well-suited for backhaul and point-to-point communication applications. The multiport interferometric receivers, as low-power solutions, have attracted considerable attention. Table 2.2 [87] presents a comprehensive comparison and survey of these receiver architectures.

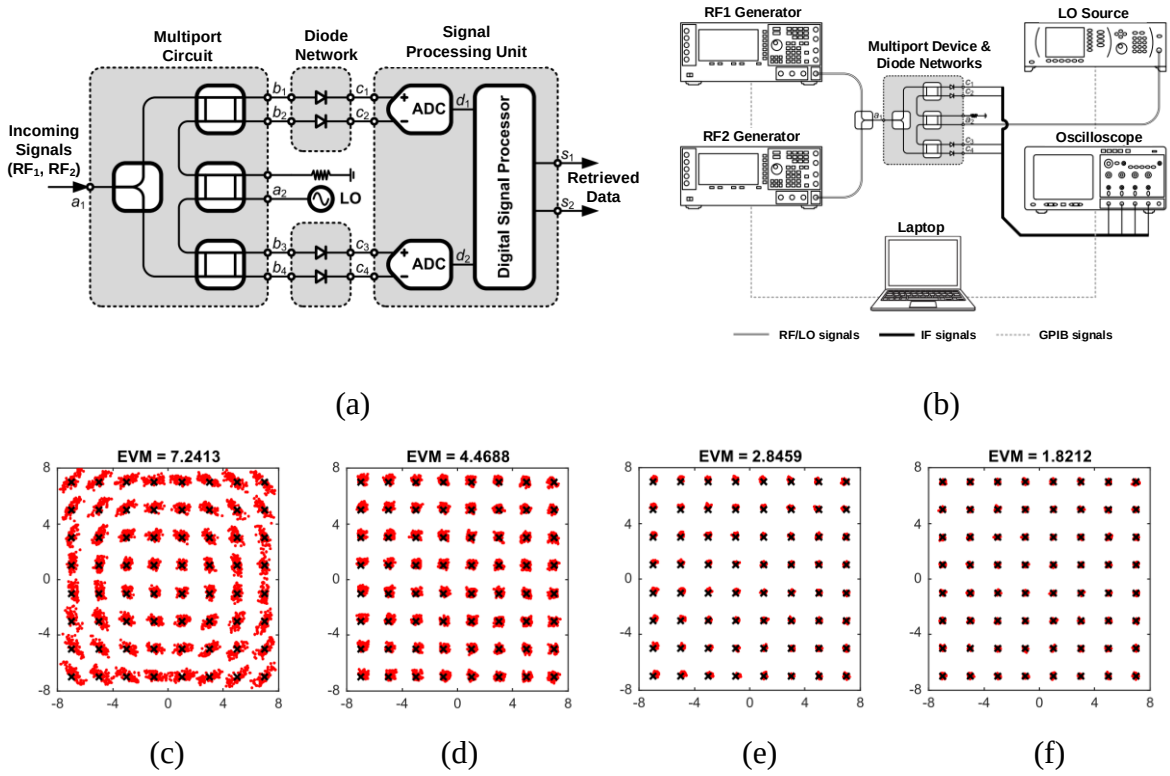

Figure 2.3 (a) Simplified block diagrams of the proposed concurrent multiport interferometric receiver, (b) Experimental setup, (c) Measured constellation diagrams without calibration, (d) Measured constellation diagrams without frequency drift adjustment only, (e) Measured constellation diagrams with channel imbalance calibration, (f) Measured constellation diagrams with IQ imbalance calibration [124]

2.4 Multifacted Applications

2.4.1 Communication

To meet the growing demands of emerging applications in next-generation communication systems, a variety of advanced front-end architectures built upon multiport interferometric technology have been proposed and successfully implemented. These front-ends are designed to support key capabilities such as multiband operation, multifunctionality, multi-polarization, and full-duplex communication [147], [148], [149], [150], [151], [152]. The combination of these features within a single circuit platform provides significant advantages for high-performance wireless communication. Recent developments in front-ends, demonstrating novel techniques and improved

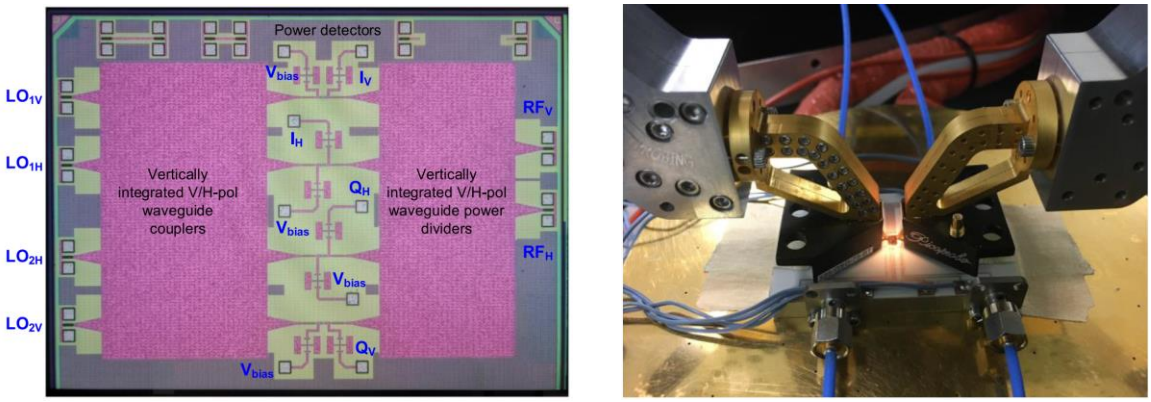

(a) (b)

Figure 2.4 (a) Microphotograph of the fabricated prototype chip, (b) Experimental setup of the chip [155]

performance, have made multiport interferometric architectures especially attractive for applications requiring very low LO power levels. [153].

By enabling greater diversity, alleviating channel fading, and accommodating multiple services simultaneously, multiband operation delivers notable performance improvements. In [154], a compact multiport receiver architecture capable of concurrent dual-band transmission is proposed. This design, illustrated in Figure 2.3, is based on the classical multiport interferometric structure but employs only one LO source. Unlike conventional dual-band architectures that rely on two LO signals, this receiver achieves frequency translation to the IF band with a single LO. The two RF channels from the multiport network are downconverted to a same IF band. A linear matrix transformation is applied to reconstruct the original data streams, thereby reducing interchannel interference and enhancing signal fidelity. As shown in Figures 2.3(c)–(f), the measurement results demonstrate the excellent performance of the concurrent dual-band receiver.

By enabling two orthogonal polarization channels, polarization diversity can nearly double the available channel capacity and substantially improve spectrum usage compared to single-polarization receivers. The work in [155] presents a dual-polarized multiport receiver fabricated in a standard CMOS technology. Using substrate-integrated waveguide (SIW) structures, the receiver supports both V- and H-polarization modes. With its self-packaged nature, the design is highly compatible with 3D on-chip integration, benefiting from the multilayer stack-up provided by

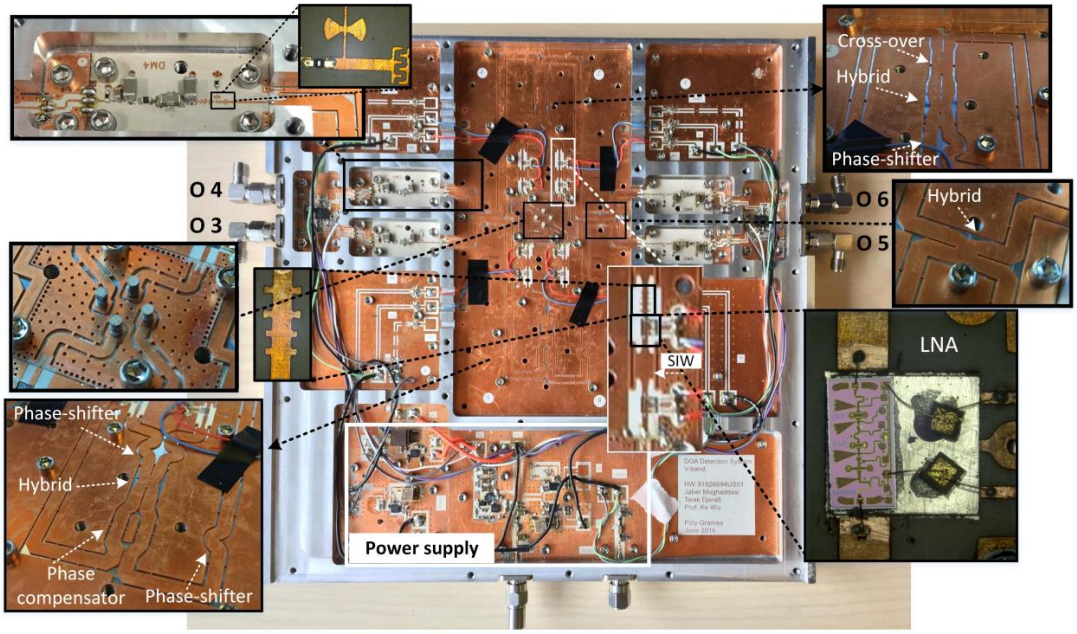

Figure 2.5 Photograph of the fabricated multiport interferometer-enabled 2D angle-of-arrival (AOA) estimation system [162]

advanced CMOS manufacturing. This approach supports high-density receiver arrays while simultaneously reducing topological complexity, structural losses, and power consumption. A proof-of-concept prototype was fabricated using a standard 65-nm CMOS process to validate the proposed technique, as shown in Figure 2.4(a), with the corresponding on-wafer characterization setup shown in Figure 2.4(b). Experimental results confirm that the receiver can reliably demodulate multiple polarized M-QAM waveforms, achieving measured EVM values better than –20 dB at a 300-GHz carrier. This approach is poised to significantly advance THz IC technologies aimed at high-density wireless communication systems.

2.4.2 Sensing

Wireless sensors serve as key enablers in applications spanning IoT networks, biomedical instrumentation, automotive systems, robotics, and industrial manufacturing. With advantages such as scalability, flexibility, and remote operability, they are particularly effective in large-scale or resource-constrained environments where real-time monitoring is crucial. By providing continuous data from locations that are otherwise inaccessible or costly to monitor, these sensors significantly enhance operational efficiency and system reliability. Due to its inherently low power consumption,

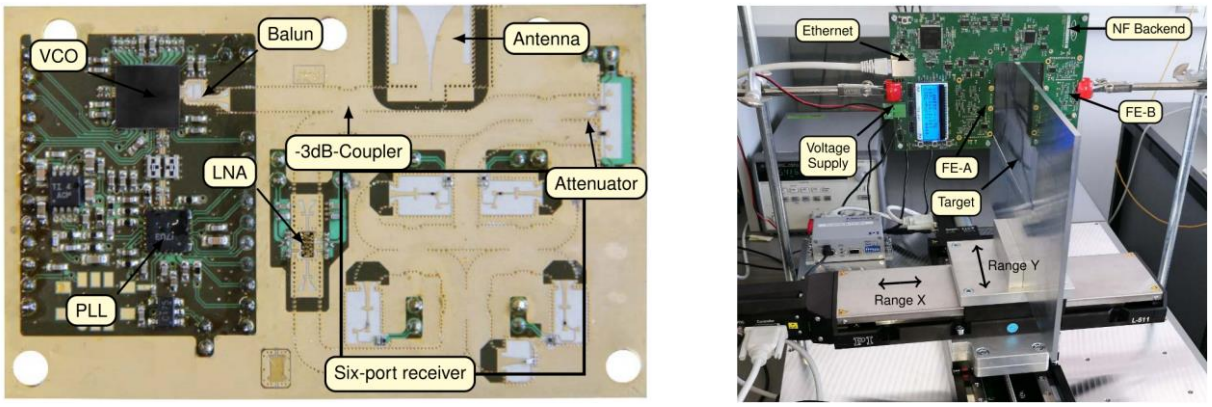

(a) (b)

Figure 2.6 (a) Photograph of the interferometric radar for sheet thickness monitoring, (b) Photograph of the measurement setup [163]

multiport interferometric technology is widely used in portable sensors designed for long battery life [156]. This energy-efficient approach is ideal for long-term deployments with minimal maintenance or battery replacement needs. A variety of sensor types based on multiport interferometric technology have been proposed for angular displacement detection, indoor localization and identification, and dielectric properties measurement [157], [158], [159], [160], [161]. For instance, angle-of-arrival (AOA) estimation is vital for tasks like industrial machinery localization, object positioning, and accurate antenna-to-antenna alignment. High-precision AOA information supports accurate tracking and positioning, boosting operational efficiency in industrial environments and enhancing communication system performance through real-time antenna reorientation. To estimate the direction of arrival of an incoming plane wave in both horizontal and vertical planes, a multiport 2-D AOA detection system is proposed in [162]. The detection system is implemented using an eight-port network consisting of four input ports and four output ports. The input ports are connected to four antennas, while the output ports are connected to four power detectors. The signals captured by the antennas—each carrying directional information about the incoming beam—are processed using a simple signal-processing algorithm to accurately estimate both angular components. A prototype 2-D AOA detection system was developed for mmW applications, and a photograph of the prototype is shown in Figure 2.5. Extensive system-level measurements were performed to assess its performance. At 58 GHz, the

measured results closely match the ideal values, confirming the excellent accuracy of the proposed 2-D AOA detection system.

In [163], a high-precision sheet thickness measurement system was developed using an interferometric radar approach. The system operates at 61 GHz and is built with two cooperating six-port radars based on SIW technology, which offers strong resistance to external interference due to its self-packaging nature. The radar front end includes a signal source, coupler, antenna, variable attenuator, LNA, and six-port receiver. A prototype of the system is shown in Figure 2.6(a). Performance validation was carried out through measurements on the prototype, as illustrated in Figure 2.6(b). The results confirm that the system meets the target specifications and demonstrate the potential of millimeter-wave interferometric techniques as effective alternatives to conventional measurement solutions.

2.4.3 Imaging

Imaging systems play a vital role in applications such as security screening, non-destructive evaluation, environmental sensing, and medical diagnostics. To meet these requirements, various imaging techniques have been developed across microwave, mmW, and THz frequency ranges. While mmW and THz waves suffer greater attenuation compared to microwaves, they provide superior spatial resolution and are therefore ideal for short-range, high-precision imaging. As the need for more efficient and economical imaging grows, new methods continue to emerge. Among them, multiport interferometric technology offers a simple, low-cost, and highly promising solution for future imaging platforms [164], [165], [166]. Non-destructive testing and evaluation technologies are indispensable for detecting corrosion, structural defects, and material inconsistencies in metals, providing high-resolution capabilities for numerous applications. With the semiconductor industry’s growing requirement for precise imaging tools capable of resolving fine defects and mapping thickness variations in thin conductive layers, there is an increasing push toward solutions suitable for use outside controlled laboratory settings. In response, [167] proposes a compact and economical near-field microscopy platform that incorporates a six-port reflectometer and a low-cost microstrip probe. Figure 2.7 shows the experimental setup of the proposed near-field scanning microscope platform, which includes a six-port reflectometer, an oscillator, a tunable matching network, and an evanescent millimeter-wave probe. The system also integrates a signal conditioning block, analog-to-digital converters, and a digital processing unit to

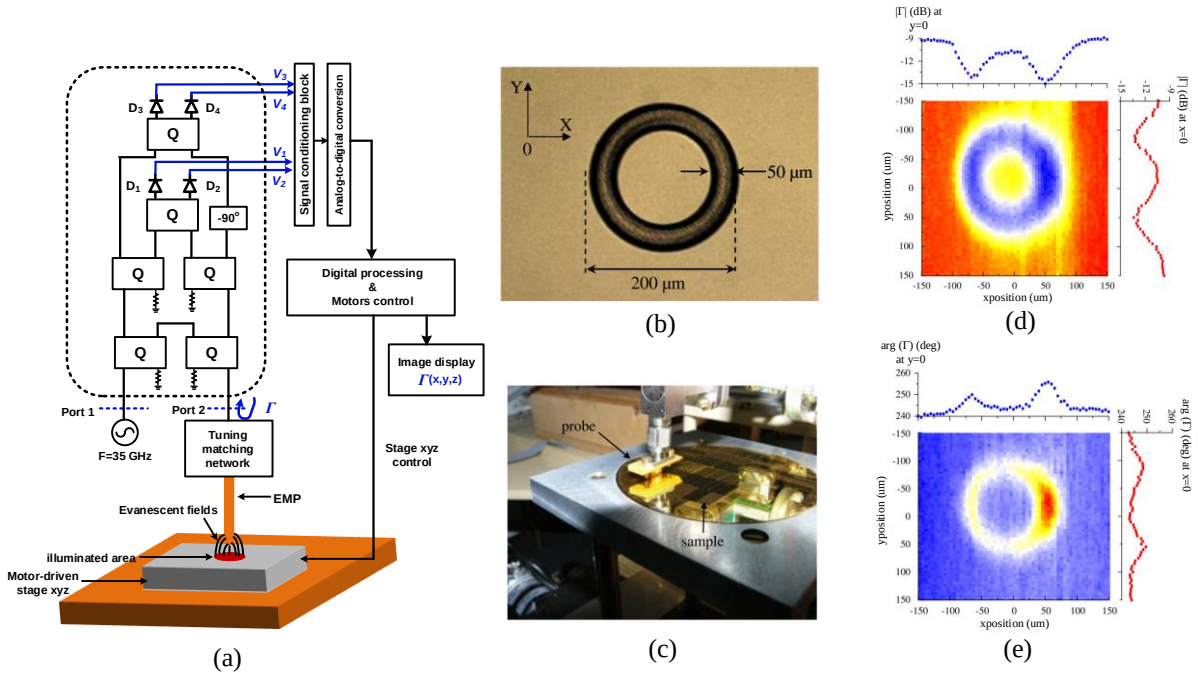

Figure 2.7 (a) Setup of the six-port near-field scanning microscope, (b) Optical microphotograph of the test sample, (c) Measurement configuration, (d) Magnitude image of the reflection coefficient, (e) Phase-shift image of the reflection coefficient [167]

enable accurate measurement and data analysis. The performance of the platform was verified using a test sample featuring a gold pattern deposited on a silicon substrate. Figures 2.7(b)–(c) show the layer stack, measurement setup, and optical micrograph of the sample. The corresponding millimeter-wave scans in Figures 2.7(d)–(e) accurately capture the patterned structure with exceptional clarity. The system attains high spatial resolution and strong image contrast even without the use of additional signal processing or normalization techniques.

This technique is highly cost-effective, as it avoids the need for expensive microwave instruments such as traditional vector network analyzers (VNAs). Additionally, its low power consumption and compact size make it well suited for practical deployment. These advantages highlight its strong potential for near-field mapping of thin metallic layers, achieving spatial resolutions on the order of only a few microns.

CHAPTER 3 ARTICLE 1: SELF-CONTAINED DUAL-INPUT INTERFEROMETRIC RECEIVER FOR PARALLELED-MULTICHANNEL WIRELESS SYSTEMS

Jie Deng, Pascal Burasa, and Ke Wu

Published in: IEEE Transactions on Circuits and Systems I: Regular Papers

Publication date: December 07, 2023

Abstract: In this paper, a self-contained dual-input receiver architecture based on the interferometric technique is proposed and demonstrated for the first time for paralleled-multichannel wireless systems. Different from conventional counterparts, the proposed receiver consists of dual-input RF channel paths, and only one sole hardware is used to realize frequency translation, i.e., the conversion to intermediate frequency (IF) band. Demodulated IF signals can be extracted from two output ports instead of four ports in legacy multiport systems, thereby further reducing circuit complexity, size, cost, and power consumption. A mathematical model of the receiver architecture is formulated and applied to examine its modes of operation. For the proof of concept, a dual-band and dual-polarized prototype RX frontend is designed and fabricated to validate the proposed architecture. The transmission and demodulation of multiple digital modulation signals including QPSK, 16-QAM, 32-QAM, and 64-QAM are successfully demonstrated experimentally. Those measured results confirm that the proposed receiver architecture achieves good and desired performances. Based on the proposed self-contained dual-input receiver architecture, a multiband and multifunction polarization-diversified wireless system featuring compact size, low-cost, and low-power consumption suitable for 5G, 6G, and beyond can be realized.

Index Terms: Dual polarization, direct conversion receiver, fifth generation (5G), interferometric, interferometer millimeterwave (mmW), multi-input receiver, multiband, multifunction, sixth generation (6G), six-port.

3.1 Introduction

Recently, due to the continued proliferation and exponential expansion of various emerging applications and wireless systems such as smart devices, artificial intelligence (AI), the Internet of

Things (IoT), 3D environmental sensing and mapping, autonomous driving and mobility, etc., radiofrequency (RF) and millimeter-wave (mmW) wireless multifunction communication and sensing technologies have gained much attention and they have been studied worldwide [12], [147] [168], [169], [170], [171], [172], [173], [174], [175]. This has driven a rapid and robust development of a multitude of high data-rate, low latency, reliable communication links and sensing systems. As an effective solution, the frequency-diversified MIMO scheme [176], [177], [178] has been considered and deployed. To further increase data-rate for communication, polarization diversity has also been introduced in the wireless systems, based on orthogonal polarization modes, i.e., the H-polarized (H-pol.) and V-polarized (V-pol.) modes, which supports simultaneous independent data streams, thereby doubling the effective channel capacity of system. However, increased power consumption, system cost, and structure size for realizing such high-data transmission throughputs based on both frequency- and polarization-diversified MIMO frontends, present questionable hurdles and critical issues for a wide-spread adoption and a massive deployment within 5G, 6G, and future wireless communication and sensing technology platforms.

Generally, the development of conventional receivers (RX) is mainly based on the fundamental mixer architecture for frequency translation [31], [32], [179] where at least one mixer and one local oscillator (LO) source are used in each channel. The mixer operates in a highly nonlinear regime and generally requires a relatively higher LO driving power. Figure 3.1(a) describes a typical RX frontend using the popular homodyne architecture. Multiple mixers are required along different receiving channels, therefore, inherently increasing the overall receiver complexity and required power consumption. Driving all of those mixers is challenging and daunting, in particular, for high-mmW and terahertz (THz) bands, where it is difficult or even impractical to generate high LO power due to the lack of effective high-power sources.

To relieve the design requirements of the receiver channel from such a high-power consumption, a promising multiport interferometric receiver architecture was proposed and developed [18], [70], [76], [79], [101], [104], [124], [146], [148], [148], [162], [180], [181], [182], [183], [184], [185], [186]. As illustrated in Figure 3.1(b), the six-port interferometric receiver exploits a linear interference concept, as opposed to its mixer-based receiver architecture counterpart which operates based on a nonlinear interference principle, thus greatly reducing power consumption. In

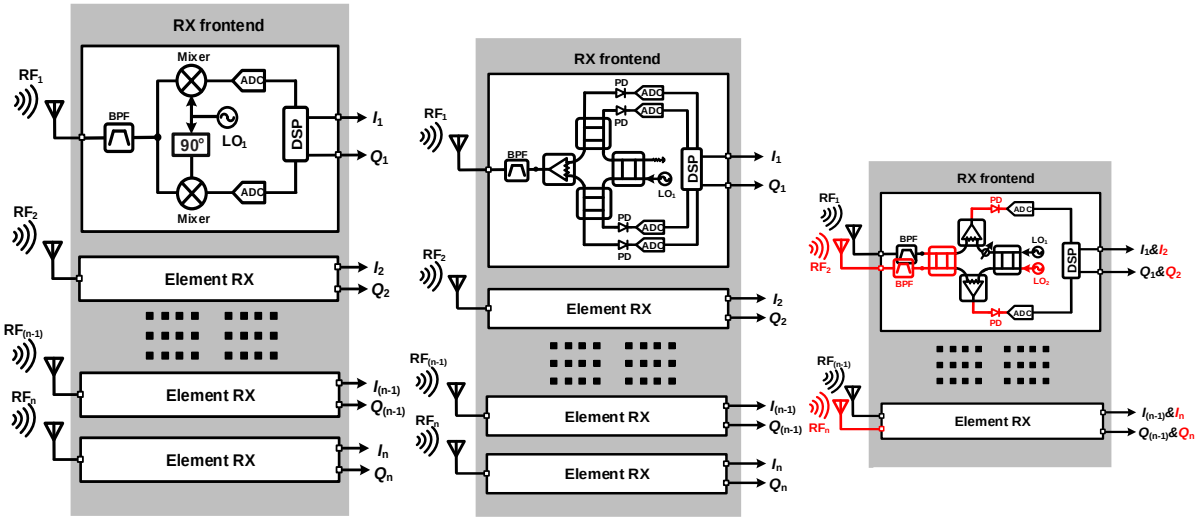

(a) (b) (c)

Figure 3.1 (a) Conventional mixer-based RX architecture. (b) Conventional six-port RX architecture. (c) Proposed self-contained dual-input multiport RX architecture

addition, compared to the conventional mixer-based receiver architectures, the multiport interferometric architecture offers several attractive advantages in terms of wideband performance, multiband flexibility, and system robustness with respect to power level variations, which make it a good candidate for multiband and multifunction wireless systems. In [182], for example, an RX frontend based on the multiport interferometric architecture was reported for MIMO systems.

Different multiport interferometric receiver techniques have been proposed to relax both system complexity and power consumption issues. For example, typical five-port and four-port interferometric receivers were presented in [74], [91], [142], [187], [188], [189], [190], [191], [192], [193]. Unlike the four output ports of the six-port receivers, those types of receivers reduce the number of output ports. In this case, the receiver development is set to minimize the number of power detectors and Analog-to-Digital (ADC) converters. A comparison study has shown that ADCs account for most of the power consumption of receivers [194]. Therefore, it is beneficial to reduce the number of ADCs for realizing low-complexity and low-power operations. Such significant advancements have expanded the application scenarios of multiport interferometric receivers. In [74], [76], [146], [191] among others, concurrent dual-band interferometric receivers were proposed to enable multifunctionalities. Nevertheless, such receivers still require a relatively

broader-bandwidth platform, since the dual-band or multiband signal is received in a serial manner (received through one input). Besides, as illustrated in Figures 3.1(a) and (b), the frequency-diversified RX frontend based on the six-port interferometric architecture has the same number of RX blocks as the mixer-based RX frontend topology. Therefore, the number reduction of receiver blocks becomes meaningful for not only a minimized manufacturing cost but also circuit-level simplification with low loss, low noise, etc. This is even more important for integrated receivers (e.g., CMOS or integrated circuits-ICs solutions) where the cost is proportional to the die size. Indeed, there is still a crucial need for the development of interferometric-based compact, low-power, low-complexity, and high-data-rate mmW MIMO receiver for future wireless multifunction communication and sensing systems.

To solve such an issue, a multiport interferometric receiver architecture is proposed, studied, and demonstrated in this work. The proposed receiver consists of dual RF channel paths. Paralleled multi-channel operation is enabled by two distinct RF paths. Usually, those two RF paths are implemented with two separate six-port receiver platforms. Therefore, for N-paths frequency-diversified MIMO systems in this work, the number of the proposed receiver platform would decrease to N/2, as shown in Figure 3.1(c) for the proposed receiver, thereby greatly reducing the cost, size, complexity, and power consumption as opposed to the legacy MIMO receivers. Thanks to the dual-input RF paths, polarization diversity can also be flexibly arranged by using different polarization antennas. For the proof of concept, a dual-band dual-polarized interferometric RX frontend is designed, fabricated, and measured. The receiver's detailed analysis together with experiments are presented. To the best of our knowledge, this is the first multiport interferometric RX frontend to achieve paralleled dual-band dual-polarized operations. Although the RX prototype is implemented with a PCB technology, it can be extended to ICs development such as CMOS process. The performance of the RX prototype is assessed by demodulating various digital modulation signals. The results validate the proposed scheme. The simplicity, low cost, compact size, and flexibility make the proposed receiver architecture a good candidate for frequency- and polarization-diversified MIMO frontends in next-generation multifunction wireless platforms (5G, 6G and beyond) featuring simultaneous data communication and parametric sensing.

The paper is organized as follows. Section 3.2 presents the system architecture of the proposed multiport receiver. Besides, a detailed analysis and operating principle of the proposed receiver are elucidated and discussed. Section 3.3 describes the design and implementation of each basic circuit

building block. Section 3.4 describes the dual-polarized antenna array. Various demodulation measurements and performance comparisons for the proposed dual-band dual-polarized multiport receiver are shown in Section 3.5. Finally, the conclusion is drawn in Section 3.6.

3.2 Receiver architecture

RF/mmW systems are widely used in wireless communications to achieve high data transmission throughput. The cost of these systems is high judging from various aspects. Figure 3.1 shows the block diagram of a frequency- and polarization-diversified RX frontend architecture. By simply increasing the number of receiver blocks, MIMO communication can be realized. However, the whole system's physical size and complexity will be increased, especially for dual-polarized MIMO systems. Therefore, it is necessary to reduce the size of the entire system. This is not only to minimize the manufacturing cost, but also to simplify the circuit complexity and reduce the power consumption. To this end, a self-contained dual-input multiport receiver architecture for frequency diversity RX frontend is proposed as shown in Figure 3.1(c). Compared to the conventional single-path receiver [Figure 3.1(b)], the proposed receiver will reduce the receiver block by half for realizing the same RX frontend. The receiver consists of hybrid couplers, power combiners, and a 90° phase shifter to accommodate the intended dual RF paths. Thus, the receiver simultaneously supports two parallel independent modulated signals. The modulated RF signals can be expressed as:

$$\begin{cases} a_{\mathrm{RF1}} = \mid a_{\mathrm{RF1}} \mid\mid I_1(t) + jQ_1(t) \mid e^{j(w_{\mathrm{RF1}}(t)+\theta_{\mathrm{RF1}})} & (3.1) \\ a_{\mathrm{RF2}} = \mid a_{\mathrm{RF2}} \mid\mid I_2(t) + jQ_2(t) \mid e^{j(w_{\mathrm{RF2}}(t)+\theta_{\mathrm{RF2}})} & (3.2) \end{cases}$$

The LO signals can be formulated by:

$$\begin{cases} a_{\mathrm{LO1}} = \mid a_{\mathrm{LO1}} \mid e^{j(w_{\mathrm{LO1}}(t)+\Phi_{\mathrm{LO1}})} & (3.3) \\ a_{\mathrm{LO2}} = \mid a_{\mathrm{LO2}} \mid e^{j(w_{\mathrm{LO2}}(t)+\Phi_{\mathrm{LO2}})} & (3.4) \end{cases}$$

where I and Q represent the in-phase and quadrature components, respectively. After the multiport circuit, the mixed modulated RF signals and LO signals are derived by the following equations:

$$\begin{aligned}\mathrm{RF}_{\mathrm{mix}} &= |a_{\mathrm{RF1}}||I_1(t)+jQ_1(t)|e^{j(w_{\mathrm{RF1}}(t)+\theta_{\mathrm{RF1}})}+|a_{\mathrm{RF2}}||I_2(t)+jQ_2(t)|e^{j(w_{\mathrm{RF2}}(t)+\theta_{\mathrm{RF2}})} \\ &= |a_{\mathrm{RF1}}|[I_1(t)\cos(w_{\mathrm{RF1}}t+\theta_{\mathrm{RF1}})-Q_1(t)\sin(w_{\mathrm{RF1}}t+\theta_{\mathrm{RF1}})] \\ &+ |a_{\mathrm{RF2}}|[I_2(t)\cos(w_{\mathrm{RF2}}t+\theta_{\mathrm{RF2}})-Q_2(t)\sin(w_{\mathrm{RF2}}t+\theta_{\mathrm{RF2}})] \\ &+ |a_{\mathrm{RF1}}|[I_1(t)\sin(w_{\mathrm{RF1}}t+\theta_{\mathrm{RF1}})+Q_1(t)\cos(w_{\mathrm{RF1}}t+\theta_{\mathrm{RF1}})]j \\ &+ |a_{\mathrm{RF2}}|[I_2(t)\sin(w_{\mathrm{RF2}}t+\theta_{\mathrm{RF2}})+Q_2(t)\cos(w_{\mathrm{RF2}}t+\theta_{\mathrm{RF2}})]j\end{aligned} \tag{3.5}$$

and

$$\begin{aligned}\mathrm{LO}_{\mathrm{mix}} &= |a_{\mathrm{LO1}}|e^{j(w_{\mathrm{LO1}}(t)+\Phi_{\mathrm{LO1}})}+|a_{\mathrm{LO2}}|e^{j(w_{\mathrm{LO2}}(t)+\Phi_{\mathrm{LO2}})} \\ &= |a_{\mathrm{LO1}}|\cos(w_{\mathrm{RF1}}t+\Phi_{\mathrm{LO1}})+|a_{\mathrm{LO2}}|\cos(w_{\mathrm{RF2}}t+\Phi_{\mathrm{LO2}}) \\ &+ [|a_{\mathrm{LO1}}|\sin(w_{\mathrm{RF1}}t+\Phi_{\mathrm{LO1}})+|a_{\mathrm{LO2}}|\sin(w_{\mathrm{RF2}}t+\Phi_{\mathrm{LO2}})]j\end{aligned} \tag{3.6}$$

where a_{RF1}, a_{RF2}, a_{LO1}, and a_{LO2} are the signal amplitudes, and θ_{RF1}, θ_{RF2}, Φ_{LO1}, and Φ_{LO2} the signal phases. To avoid the interference between the down-converted two frequencies and the second-order distortion components, the assignment of the LO signals and RF signals should comply with the following conditions:

$$f_{\mathrm{IF1}} = f_{\mathrm{RF1}} - f_{\mathrm{LO1}} \tag{3.7}$$

$$f_{\mathrm{IF2}} = f_{\mathrm{RF2}} - f_{\mathrm{LO2}} \tag{3.8}$$

$$|f_{\mathrm{IF2}} - f_{\mathrm{IF1}}| > \frac{1}{2}(\mathrm{BW}_{\mathrm{RF1}} + \mathrm{BW}_{\mathrm{RF2}}) \tag{3.9}$$

$$|f_{\mathrm{LO1}} - f_{\mathrm{RF1}}| > \frac{3}{2}\mathrm{BW}_{\_\mathrm{RF1}} \tag{3.10}$$

where f_{RF1} is the frequency of the modulated RF_1 signal, f_{LO1} the LO_1 signal, $\mathrm{BW}_{\mathrm{RF1}}$ the bandwidth of RF_1 signal, f_{RF2} the frequency of the modulated RF_2 signal, f_{LO2} the LO_2 signal, and $\mathrm{BW}_{\mathrm{RF2}}$ the

bandwidth of RF_2 signal. Then, the modulated RF_1 and RF_2 signals and LO_1 and LO_2 signals are superposed through a linear interference by the multiport circuit under different relative phase conditions. The superposed RF and LO signals are subject to power detectors for down-conversion. The down-converted signals can be expressed as follows:

$$\begin{aligned}
P_{\text{out_}i} &= \frac{\Re}{2}[|a_{\text{LO1}}|^2 + |a_{\text{LO2}}|^2 + (I_1^2 + Q_1^2)|a_{\text{RF1}}|^2 \\
&+ (I_2^2 + Q_2^2)|a_{\text{RF2}}|^2] + \Re|a_{\text{RF1}}||a_{\text{RF2}}|\cos(w_{\text{RF2}}t - w_{\text{RF1}}t + \theta_{\text{RF2},i} \\
&- \theta_{\text{RF1},i})(I_1^2 + Q_1^2)^{1/2}(I_2^2 + Q_2^2)^{1/2} + \Re|a_{\text{LO1}}||a_{\text{LO2}}|\cos(w_{\text{LO2}}t \\
&- w_{\text{LO1}}t + \Phi_{\text{LO2},i} - \Phi_{\text{LO1},i}) + \Re k_{\text{RF2}}k_{\text{LO2}}[\sin(w_{\text{RF2}}t - w_{\text{LO2}}t + \theta_{\text{RF2},i} \\
&- \Phi_{\text{LO2},i})]Q_2 + \Re k_{\text{RF2}}k_{\text{LO1}}[\sin(w_{\text{RF2}}t - w_{\text{LO1}}t + \theta_{\text{RF2},i} - \Phi_{\text{LO1},i})]Q_2 \\
&+ \Re k_{\text{RF2}}k_{\text{LO2}}[\cos(w_{\text{RF2}}t - w_{\text{LO2}}t + \theta_{\text{RF2},i} - \Phi_{\text{LO2},i})]I_2 \\
&+ \Re k_{\text{RF2}}k_{\text{LO1}}[\cos(w_{\text{RF2}}t - w_{\text{LO1}}t + \theta_{\text{RF2},i} - \Phi_{\text{LO1},i})]I_2 \\
&+ \Re k_{\text{RF1}}k_{\text{LO1}}[\sin(w_{\text{RF1}}t - w_{\text{LO1}}t + \theta_{\text{RF1},i} - \Phi_{\text{LO1},i})]Q_1 \\
&+ \Re k_{\text{LO2}}k_{\text{RF1}}[\sin(w_{\text{LO2}}t - w_{\text{RF1}}t + \Phi_{\text{LO2},i} - \theta_{\text{RF1},i})]Q_1 \\
&+ \Re k_{\text{RF1}}k_{\text{LO1}}[\cos(w_{\text{RF1}}t - w_{\text{LO1}}t + \theta_{\text{RF2},i} - \Phi_{\text{LO1},i})]I_1 \\
&+ \Re k_{\text{LO2}}k_{\text{RF1}}[\cos(w_{\text{LO2}}t - w_{\text{RF1}}t + \Phi_{\text{LO2},i} - \theta_{\text{RF1},i})I_1
\end{aligned} \tag{3.11}$$

Where $\Re$ is the voltage responsivity of the power detector and k_{RF2} and k_{LO2} are the power ratios of the RF and LO signals, respectively. The desired down-converted signals are:

$$\begin{aligned}
P_{\text{out1_IF1}} &= \Re\kappa[\sin(w_{\text{RF2}}t - w_{\text{LO2}}t + \theta_{\text{RF2,1}} - \Phi_{\text{LO2,1}})Q_1 \\
&\quad - \cos(w_{\text{RF2}}t - w_{\text{LO2}}t + \theta_{\text{RF2,1}} - \Phi_{\text{LO2,1}})I_1] \\
P_{\text{out1_IF1}} &= \Re\kappa[\sin(w_{\text{RF2}}t - w_{\text{LO2}}t + \theta_{\text{RF2,2}} - \Phi_{\text{LO2,2}})Q_1 \\
&\quad + \cos(w_{\text{RF2}}t - w_{\text{LO2}}t + \theta_{\text{RF2,2}} - \Phi_{\text{LO2,2}})I_1] \\
P_{\text{out2_IF2}} &= \Re\kappa[\sin(w_{\text{RF2}}t - w_{\text{LO2}}t + \theta_{\text{RF2,1}} - \Phi_{\text{LO2,1}})Q_2 \\
&\quad - \cos(w_{\text{RF2}}t - w_{\text{LO2}}t + \theta_{\text{RF2,1}} - \Phi_{\text{LO2,1}})I_2] \\
P_{\text{out2_IF2}} &= \Re\kappa[\sin(w_{\text{RF2}}t - w_{\text{LO2}}t + \theta_{\text{RF2,2}} - \Phi_{\text{LO2,2}})Q_2 \\
&\quad + \cos(w_{\text{RF2}}t - w_{\text{LO2}}t + \theta_{\text{RF2,2}} - \Phi_{\text{LO2,2}})I_2]
\end{aligned} \tag{3.12}$$

These signals are sent to subsequent digital signal processing (DSP), then I and Q information can be recovered.

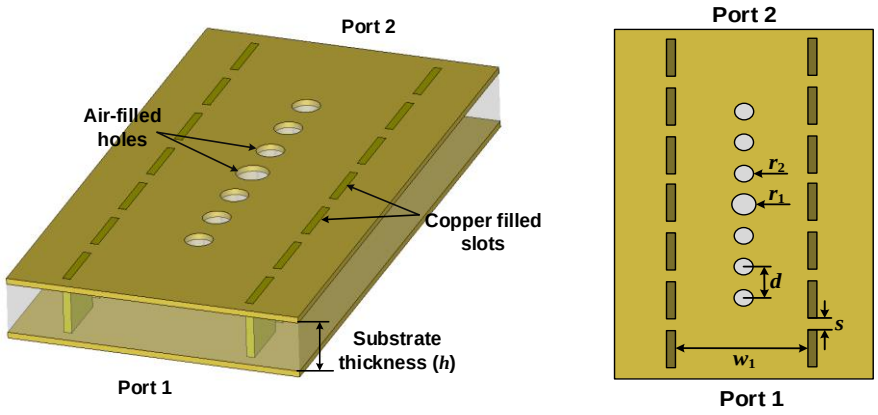

(a) (b)

Figure 3.2 Structure of the proposed 90° phase shifter. (a) Isometric view. (b) Vertical view

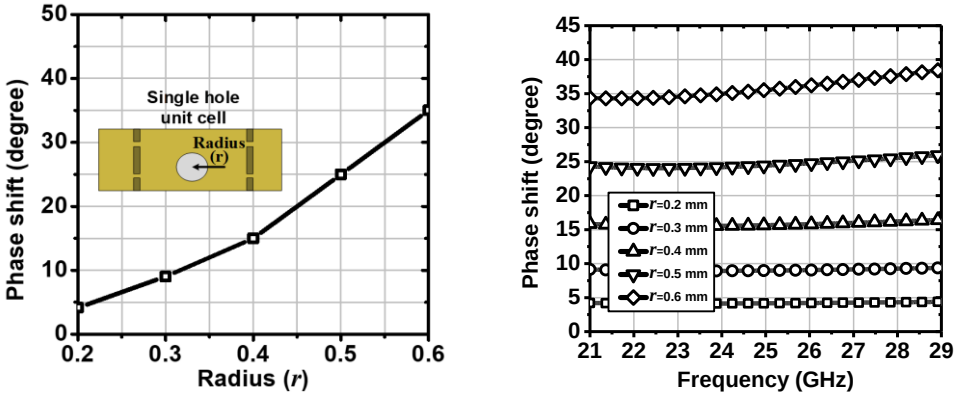

(a) (b)

Figure 3.3 (a) Phase shift relationship for different hole radius. (b) Phase shift versus operating frequency under different hole radius.

3.3 Circuit-level implementation

3.3.1 Phase shifter

The phase shifter is a critical and challenging block for design in the multiport receiver since it directly affects demodulated performances. A classic and simple delay line technique [195] has widely been used in the design of phase shifters. However, these types of phase shifters suffer from narrow bandwidth. To expand the bandwidth, a 90° self-compensating phase shifter based on a delay line and equal-length unequal-width structure was proposed in [196]. However, this type of phase shifter has different physical lengths between the main line and reference line, which breaks

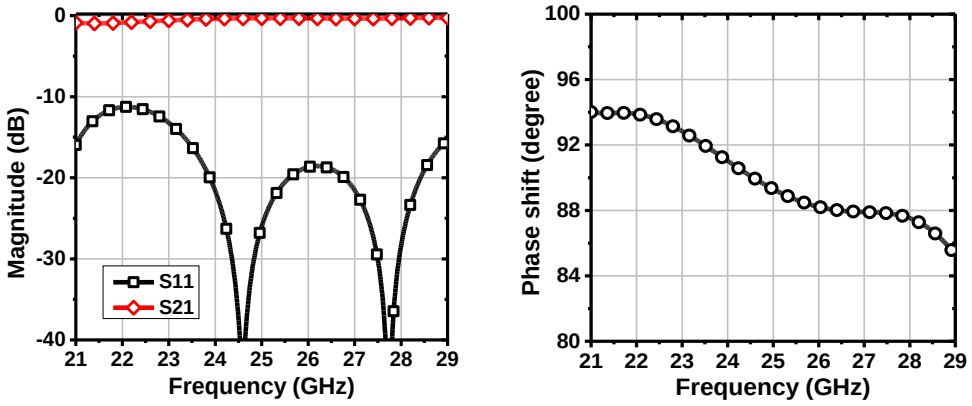

(a) (b)

Figure 3.4 Phase shifter performance. (a) Return loss and insertion loss. (b) Phase shift response.

down the symmetry of the circuit and makes it difficult for system integration. Conversely, the equal-length phase shifter is preferable. To achieve an equal-length broadband phase shifter, an effective solution was derived in [197]. By varying the dielectric permittivity through the air-filled holes, a flat phase shift can be achieved over a broad bandwidth.

Figure 3.2 shows the configuration of the proposed phase shifter. The phase shift can be changed by adjusting the size of the air-filled holes. The commercial electromagnetic software CST Microwave Studio is used to simulate the proposed phase shifter. From Figure 3.3, it can be seen that the phase shift increases as the hole radius increases. Meanwhile, the phase shift remains relatively flat over the operating frequency range from 21 to 29 GHz. The simulated results of the proposed 90° phase shifter are presented in Figure 3.4. The return loss is better than 10 dB and the insertion loss is around 0.5 dB. The phase shift is around 88°±4°. The final dimension parameters are as follows: d=1.28 mm, r_1=0.41 mm, r_2=0.35 mm, w_1=2.51 mm, and s=0.45 mm.

3.3.2 Hybrid coupler

The structure of the proposed hybrid coupler is shown in Figure 3.5. It is based on a modified Riblet-type metallic waveguide coupler, which presents a more compact size than the branch-line or multi-slot couplers [198]. The coupler consists of two input waveguide sections, a coupling cavity, and two output waveguide sections. According to the odd-even mode analysis [199], when

Table 3.1 Dimension parameters of the hybrid coupler

Parameter	Value (mm)	Parameter	Value (mm)
w_1	2.51	w_{gap}	0.46
l_{c1}	0.62	w_{c1}	4.62
l_{c2}	0.75	w_{c2}	4.92
l_{c3}	0.81	w_{c3}	5.72

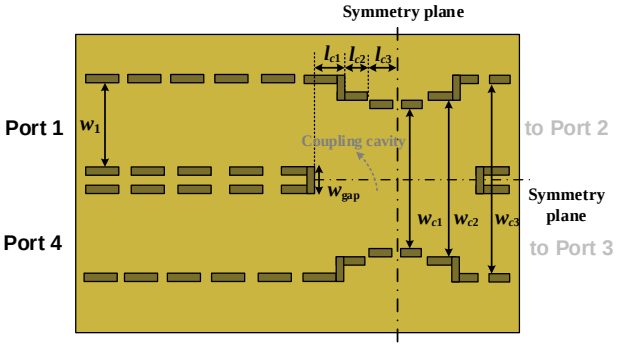

Figure 3.5 Structure of the proposed hybrid coupler.

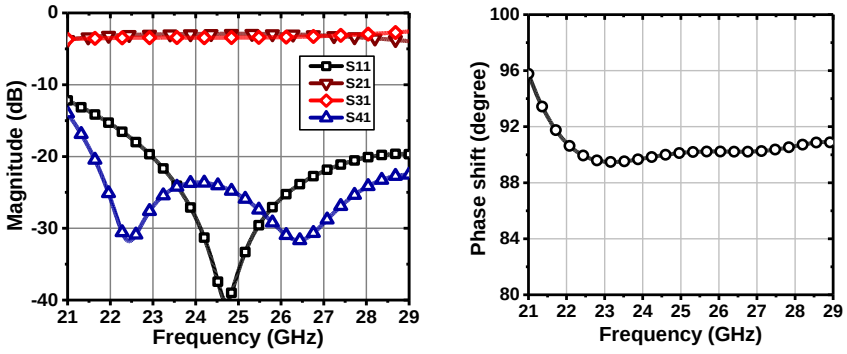

(a) (b)

Figure 3.6 (a) S-parameters of the proposed hybrid coupler. (b) Phase shift response of the proposed hybrid coupler.

port 1 excites the TE_{10} mode, both even-TE_{10} and odd-TE_{20} modes will be excited in the coupling cavity. By adjusting the dimension of the coupling cavity, high-order modes such as TE_{30} mode can be suppressed. The excited TE_{10} mode and TE_{20} modes will cancel each other at the isolating

port, i.e., port 4, and will superimpose at ports 2 and 3. The output signals on ports 2 and 3 are equal in amplitude but 90° out of phase. To expand the bandwidth performance, the impedance matching steps are implemented in the coupling cavity as shown in Figure 3.5. The metallic lateral walls are realized with the metalized slots to prevent the undesired radiation.

Figure 3.6 shows the simulated results of the proposed coupler. The optimal dimension parameters are listed in Table 3.1. It can be seen that over the frequency range of interest from 21 to 29 GHz, the simulated reflection coefficient at the input port (S_{11}) is less than -10 dB and the isolation (S_{41}) is better than 10 dB. The transmissions (S_{21} and S_{31}) steadily fluctuate around 3 ± 0.5 dB. The phase imbalance between the two output ports is less than 4°.

3.3.3 Power combiner

The received RF signal and LO signal should be combined together before being fed into the power detector. Wilkinson power combiners are widely adopted since they provide a high degree of isolation between the two input ports. In this work, a power combiner based on Wilkinson architecture [200], [201], [202], [203], [204], is proposed as shown in Figures 3.7(a) and (b). The power combiner consists of two input ports, i.e., ports 2 and 3, an output port i.e., ports 1, and a central ring. A metal post is inserted into the central ring to adjust the power division ratio and the impedance matching between the input and output ports. In order to improve the isolation, resistors are inserted into two slots created over the top and bottom surfaces of the central ring. These two slots must be in the symmetrical center of the circuit to prevent radiation [205].

The equivalent circuit model of the power combiner is shown in Figures 3.7(c) and (d). From an odd- and even-mode analysis, the following conditions should be satisfied to achieve broadband matching:

$$\frac{\tan\theta_1 \tan\theta_2}{\tan\theta_1 + \tan\theta_2} = 2j \tag{3.13}$$

$$\frac{2 + jr\tan\theta_2}{1 + j\cot\theta_1} = r + 2j\tan\theta_2 \tag{3.14}$$

$$\frac{1}{\tan^2\theta_1} = 1 - \frac{r}{2} \tag{3.15}$$

Table 3.2 Dimension parameters of the power combiner

Parameter	Value (mm)
w_1	2.51
w_{slot}	0.33
l_{slot}	2.86
r_{out}	3.41
r_{in}	0.44
Φ_1	91.5
Φ_2	88.5

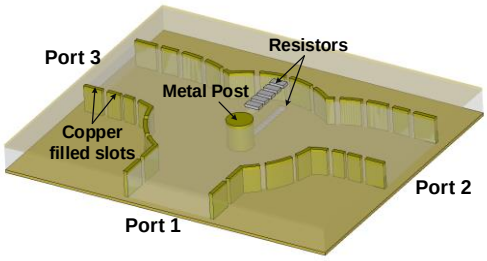

(a)

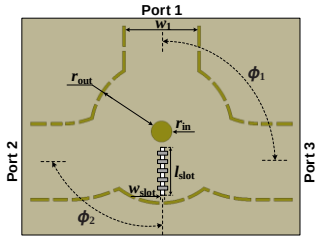

(b)

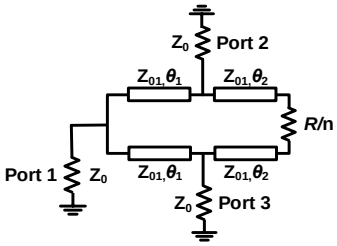

(c)

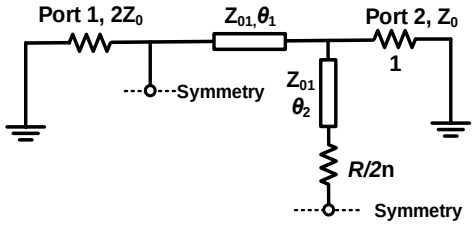

(d)

Figure 3.7 (a) 3D view of the proposed power combiner. (b) Vertical view. (c) Circuit model of the power combiner. (d) Symmetrical circuit model of the power combiner

$$\frac{1}{\tan\theta_1} = -\tan\theta_2 \tag{3.16}$$

where θ_1 and θ_2 are the lengths of transmission line sections, and r is the resistance. The power combiner is simulated with the CST Microwave Studio. The dimensional parameters are summarized in Table 3.2. The simulated results together with E-field distribution are shown in Figures 3.8. Both input and output ports are well matched over the band of interest from 22 to 28

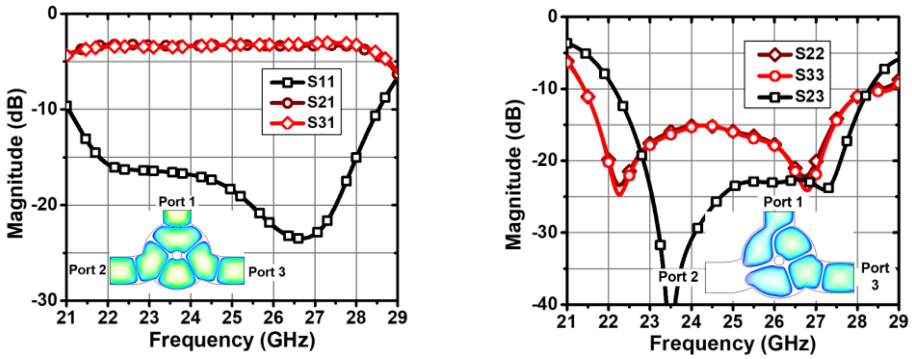

(a) (b)

Figure 3.8 The performance of the proposed power combiner. (a) Simulated reflection coefficient (S_{11}) and transmissions (S_{21} and S_{31}) (b) Simulated isolation (S_{23}) and reflection coefficient (S_{22} and S_{33}). Insets are the simulated electric field distributions for port 1 excitation (left side) and port 2 excitation (right side), respectively

GHz. The return losses and the isolation are better than 10 dB, and the insertion losses are around 0.5 dB.

3.3.4 Power detector

Figure 3.9 shows the circuit topology of the implemented power detector, which consists of a λ/4 stub, a matching network, a zero bias Schottky diode SMS7630-40, and a low pass filter. The λ/4 stub provides the DC return path for the diode. The matching network is used to transform the impedance of the diode to 50 Ohm so that more RF power enters the diode. The low pass filter is added after the diode to extract low-frequency signal and remove high-order harmonic components.

To accurately predict the behavior of the power detector, the diode model is given in Figure 3.9. The model includes series resistor R_s, junction capacitor C_j, and nonlinear junction resistor R_j. Since the diode package parasitics affect the power detector performance, especially in the mmW band, the parasitic inductor L_p and capacitor C_p are modeled. The packaging parameters and SPICE model [206] of the diode are listed in Table 3.3.

Keysight Advanced Designed System (ADS) harmonic balance (HB) simulator and S-parameter simulation controller are used to simulate the proposed power detector. Table 3.4 summarizes the

Table 3.3 Spice and packaging parameters of SMS7630-40 diode

C_{j0}(pF)	I_s(A)	R_s(Ω)	n	M	V_{bi}(V)	C_p(pF)	L_p(nH)
0.14	5e-6	20	1.05	0.4	0.34	0.16	0.7

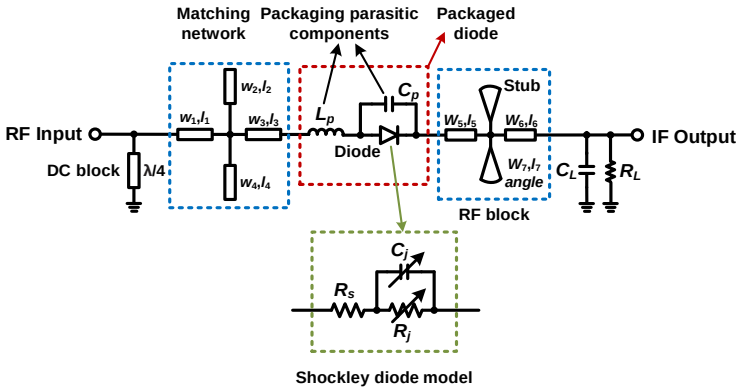

Figure 3.9 Circuit topology of the proposed power detector

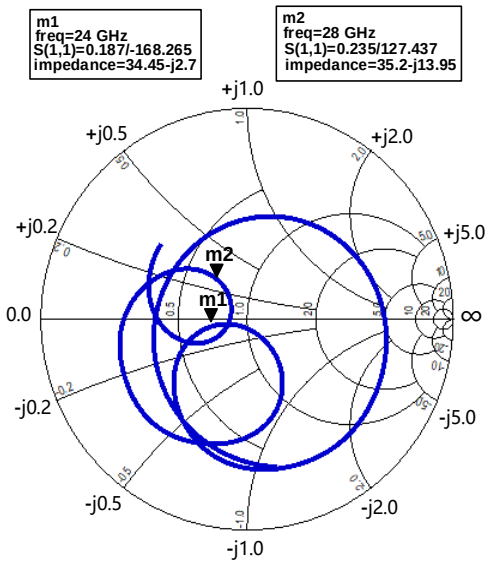

Figure 3.10 Simulated impedance matching performance of the proposed power detector in the frequency range from 20 to 30 GHz.

dimension parameters. Figure 3.10 shows the simulated impedance-matching performance at the frequency range from 20 to 30 GHz. The impedance of 34.45-j2.7 Ohm and 35.2-j13.95 Ohm are

Table 3.4 Parameters of designed power detector

Parameter	Value (mm)	Parameter	Value (mm)
w_1	3.22	w_5	1.12
l_1	0.41	l_5	1.47
w_2	0.66	w_6	1.12
l_2	1.74	l_6	1.47
w_3	2.92	w_7	0.82
l_3	0.31	l_7	1.32
w_4	1.22	θ	80
l_4	1.52	--	--

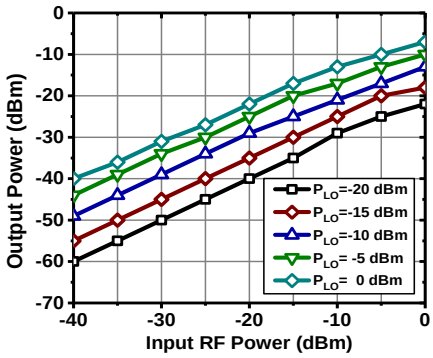

Figure 3.11 Simulated output power with different LO source powers for 24 GHz RF input signal

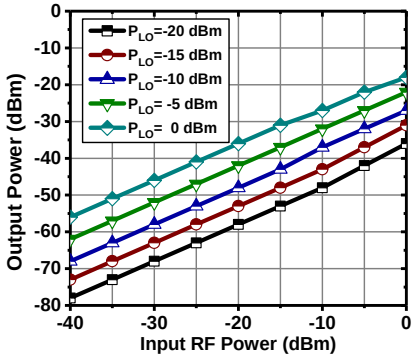

Figure 3.12 Simulated output power with different LO source power for 28 GHz RF input signal

obtained at 24 GHz and 28 GHz, respectively. Conversion characteristics of the power detector are presented in Figures 3.11 and 12. It can be seen that with the increase of the LO or RF power, the

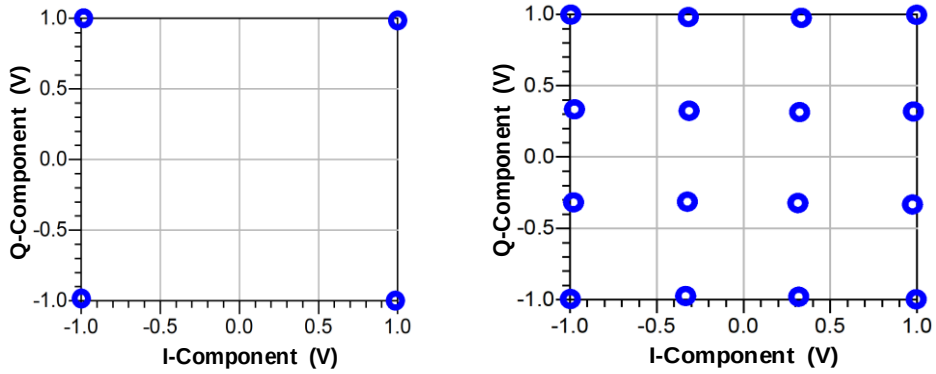

(a) (b)

Figure 3.13 Simulated constellation diagrams of the demodulated RF signals. (a) QPSK signal at RF_1 channel. (b) 16-QAM signal at RF_2 channel

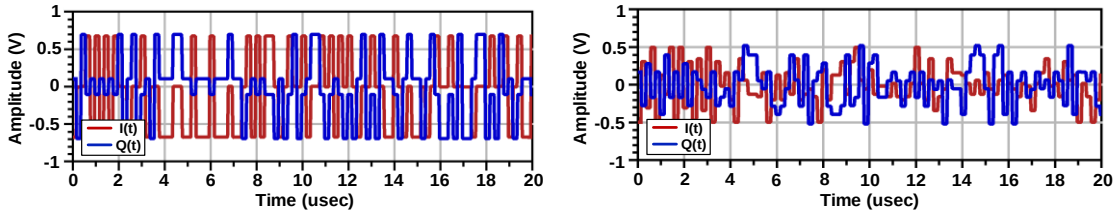

(a) (b)

Figure 3.14 Simulated results for recovered in-phase and quadrature components at different modulation schemes. (a) QPSK signal at RF_1 channel. (b) 16-QAM signal at RF_2 channel

output power increases. Figure 3.11 shows that when the LO and RF powers are 0 dBm, the output power peaks at about -8 dBm. On the other hand, Figure 3.12 shows that the output power is around -20 dBm when both the LO and RF power are set to be 0 dBm. It can be observed that the square-law behavior of the power detector is below -5 dBm of input power.

3.3.5 System simulation

A system-level simulation based on the proposed architecture in Figure 3.1(c) is implemented in ADS. All sub-circuit blocks, i.e. the phase shifter, the coupler, the power combiner, and the power detectors are co-simulated. As an example, two RF channels, namely f_{RF1} and f_{RF2}, are chosen to be 24.1 and 28.3 GHz, respectively. The LO frequencies (f_{LO1} and f_{LO2}) are 24 and 28 GHz. Under this condition, the intermediate frequencies (f_{IF1} and f_{IF2}) become 100 MHz and 300 MHz,

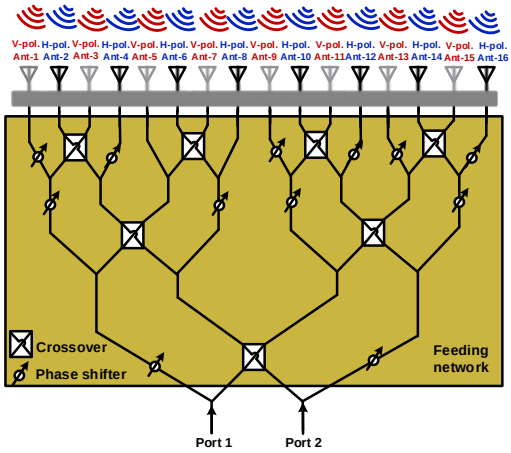

(a)

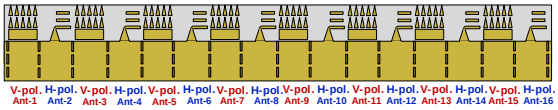

(b)

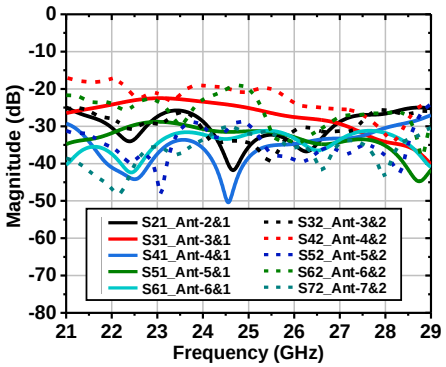

(c)

Figure 3.15 (a) Block diagram of the dual-polarized antenna array. (b) Implementation of the antenna array. (c) Simulated two-element mutual coupling of the antenna array form 1 to 6 and 2 to 7 as a case study

respectively. The transmitted data streams are modulated with digital modulations in QPSK and 16-QAM. The demodulated constellation diagrams with a symbol rate of 5 MS/s are depicted in Figure 3.13, with the corresponding recovered in-phase and quadrature components in Figure 3.14. The simulated EVMs are -36.4 dB and -34.1 dB for QPSK and 16-QAM, respectively. I-Q mismatch may be attributed to the circuit imperfections and intermodulations. The calibration

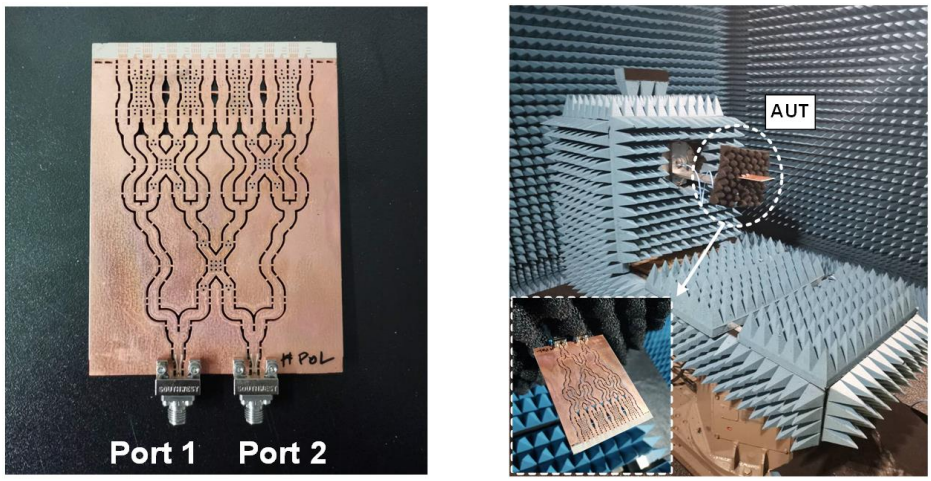

(a) (b)

Figure 3.16 (a) Photograph of the fabricated single-layer dual-polarized antenna array. (b) Measurement setup in compact range anechoic chamber for far field radiation pattern measurement

algorithm as in [124] and [191] can be adopted to further improve the performances. While the above example presents the demodulated results for QPSK and 16-QAM, the proposed receiver is also applicable to other higher-order digital modulations, analog modulations, and other advanced modulation schemes.

3.4 Dual-polarized antenna array

A dual-polarized antenna should be integrated with the receiver to enable the reception of orthogonally polarized signals. In this work, a dual-polarized antenna array [207] is implemented, which is shown in Figure 3.15(a). The antenna is a single-layer end-fire structure, which is easy to be directly integrated with the proposed receiver blocks.

The quasi-Yagi antenna [208] and the open-end antenna [209] are used for H- and V-polarizations, respectively. As shown in Figure 3.15(b), the radiators are interlaced and periodically arranged to achieve the orthogonal polarization with a compact structure. In this manner, a high inter-port isolation can be obtained. Figure 3.15(c) shows the simulated two-element mutual coupling of the antenna array, where the results analyze the coupling between antennas from 1 to 6 and 2 to 7 for a case study. The maximum mutual coupling is about -20 dB. Some mutual coupling reduction

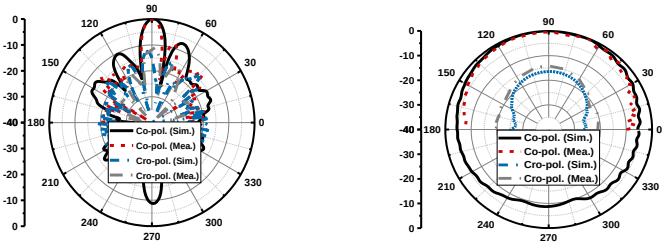

(a)

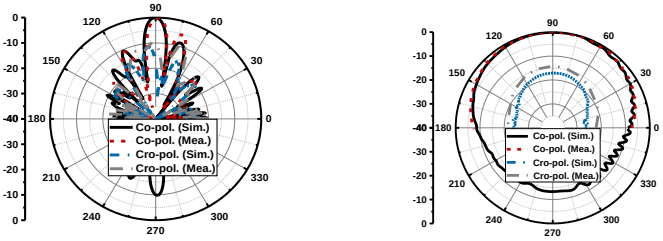

(b)

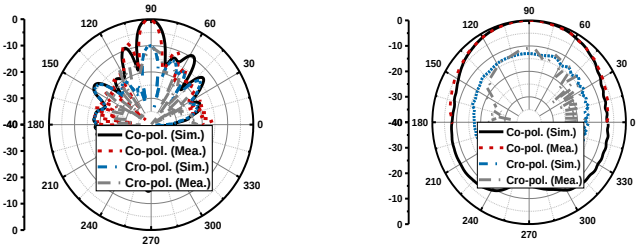

(c)

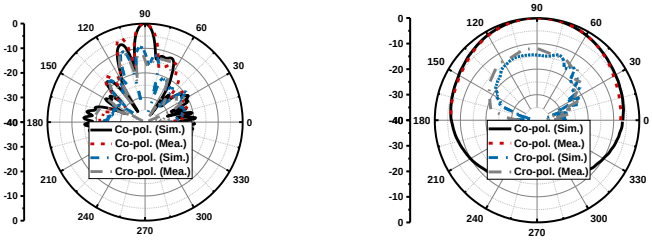

(d)

Figure 3.17 Simulated and measured radiation patterns of the proposed dual-polarized antenna array. (a) H-polarized operation at 24 GHz. (b) H-polarized operation at 28 GHz. (c) V-polarized operation at 24 GHz. (d) V-polarized operation at 28 GHz

techniques can be used to further improve the isolation. Two polarization channels are achieved in

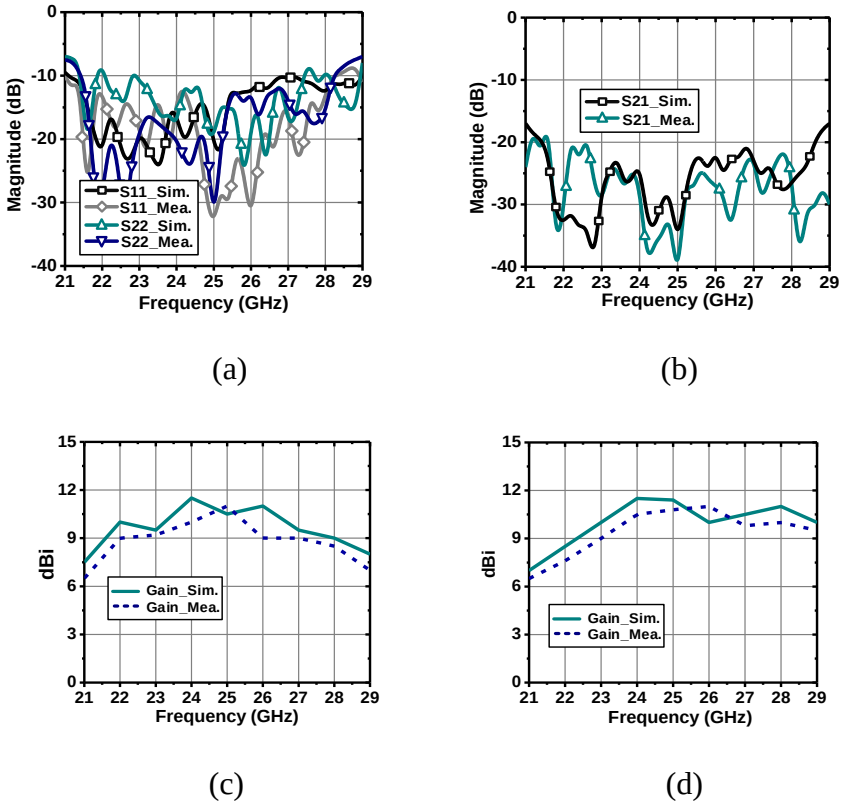

Figure 3.18 Simulated and measured results of the proposed dual-polarized antenna array. (a) Reflection coefficients of ports 1 and 2. (b) Isolation between ports 1 and 2. (c) Gain of the H-polarized operation. (d) Gain of the V-polarized operation

a single-layer substrate, owing to the feeding network with crossovers and phase shifters. Any phase shifting difference between different paths are compensated by the phase shifters.

Figure 3.16 shows the photograph of the fabricated antenna array together with the measurement setup. Port 1 is used to feed the open-end antennas and enable V-polarized radiation whereas port 2 is used to feed the quasi-Yagi antenna and enable H-polarized radiation. Simulated and measured radiation patterns for both polarizations are depicted in Figure 3.17, which validate the radiation performance in a wide frequency range. The measured and simulated radiation patterns present a good agreement.

Figure 3.18 shows the simulated and measured S-parameters and gains of the fabricated antenna array. The measured reflection coefficient is less than -10 dB for both H- and V-polarizations from 22 to 28 GHz frequency range. The measured isolation between ports 1 and 2 is better than 20 dB

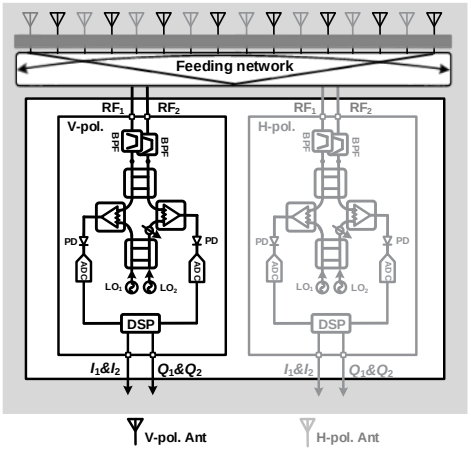

(a)

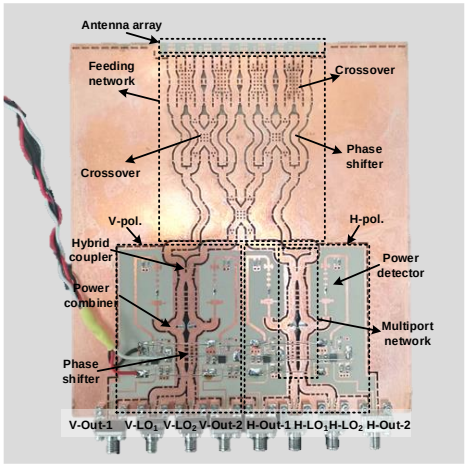

(b)

Figure 3.19 The proposed dual-input dual-polarized dual-band RX. (a) Simplified block diagram. (b) Photograph of the fabricated prototype.

over the entire band. Optimal gains for both H- and V-polarizations are from 24 to 28 GHz. The average gain is around 11 dBi. The peak gains are 11.7 dBi and 11.9 dBi for H- and V-polarizations, respectively.

3.5 Fabrication and measurement results

As illustrated in Figure 3.19(a), the modulated signals, i.e., RF_1 and RF_2, after the antenna array, enter the multi-port circuit in parallel. Therefore, paralleled multi-channel operation is enabled by two distinct RF paths as opposed to the conventional single RF path receiver architecture. For the proof of concept, a dual-input dual-polarized multiport receiver prototype was fabricated as shown in Figure 3.19(b). The experimental test bench is set up to evaluate the performance of the RX as

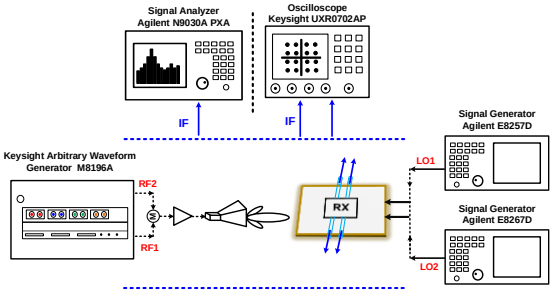

(a)

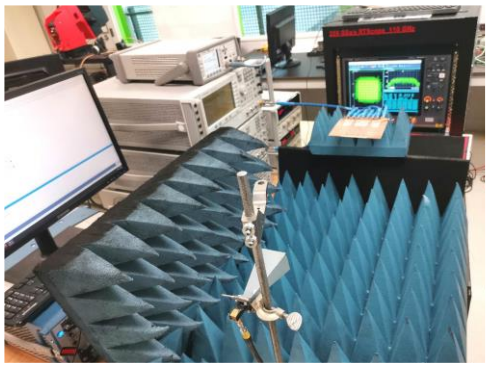

(b)

Figure 3.20 Measurement setup for the dual-polarized dual-band RX. (a) Block diagram. (b) Photograph of the test setup

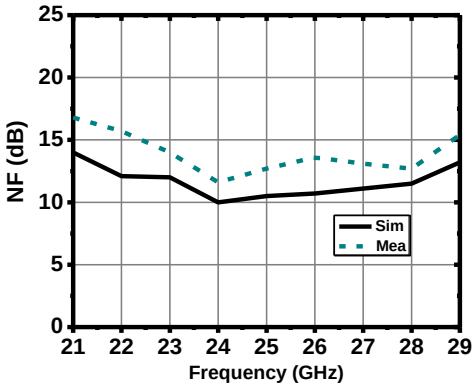

Figure 3.21 Simulated and measured noise figure (NF) of the proposed Rx

shown in Figure 3.20. Agilent M8196A Arbitrary Waveform Generator (AWG) is used to generate the intended M-QAM signals at the RF_1 and RF_2 channels, where the operating frequencies (f_{RF1} and f_{RF2}) are 24.1 and 28.3 GHz, respectively. Two signal generators, Agilent E8257D PSG Analog

Table 3.5 Summary of retrieved constellation diagrams with different orders of modulations (M-QAM) and different operating status

Modes {RF_1, RF_2}	RF_1 channel		RF_2 channel	
Modulation	4-QAM	16-QAM	4-QAM	16-QAM
V-pol. Constellation	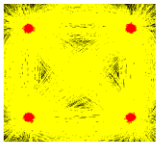	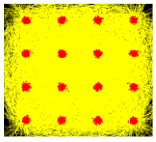	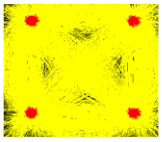	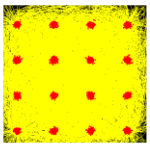
V-pol. EVM	-29.72 dB	-30.65 dB	-28.27 dB	-30.75 dB
Modulation	32-QAM	64-QAM	32-QAM	64-QAM
V-pol. Constellation	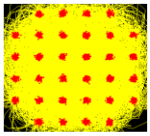	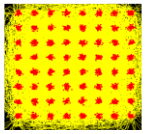	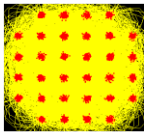	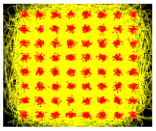
V-pol. EVM	-30.36 dB	-29.83 dB	-31.05 dB	-29.37 dB
Modulation	4-QAM	16-QAM	4-QAM	16-QAM
H-pol. Constellation	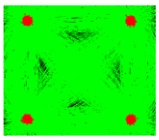	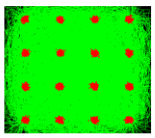	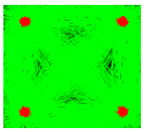	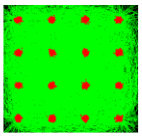
H-pol. EVM	-29.52 dB	-30.47 dB	-28.87 dB	-30.84 dB
Modulation	32-QAM	64-QAM	32-QAM	64-QAM
H-pol. Constellation	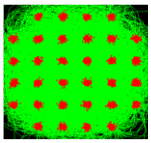	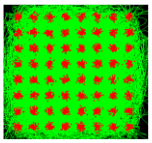	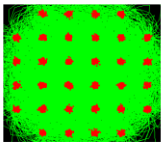	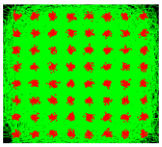
H-pol. EVM	-30.12 dB	-28.81 dB	-30.31 dB	-30.24 dB

Signal Generator and Agilent E8267D PSG Vector Signal Generator, are used as the required LO sources. The LO frequencies (f_{LO1} and f_{LO2}) are set to be 24 and 28 GHz.

A 10 MHz synchronization signal is used for the signal generators synchronization. Keysight UXR0702AP Real-Time Oscilloscope is used to capture the output signals from the prototyped RX. Keysight Technologies' 89600 VSA software visualizes the received constellation and calculates the EVM of the received bit sequence. Various modulation schemes (QPSK, 16-QAM, 32-QAM and 64-QAM) at different symbol rates have been experimentally demonstrated.

For 1 meter communication range and 12 dBm transmitted power, the received power is about -20 dBm and -24 dBm at 24 GHz and 28 GHz, respectively, under an antenna gain of 20-dBi and 10-dBi for the Tx and the Rx, respectively. It is worth mentioning that, the Tx and the Rx are in line-of-sight alignment. The noise figure (NF) is defined by the loss of the passive multiport circuit and the noise figure of the power detector. Figure 3.21 shows the simulated and measured NF of the whole Rx array. It can be seen that the simulated NF are about 10 and 11.5 dB at 24 and 28 GHz, respectively. Measured NF are about 11.6 and 12.7 dB at 24 and 28 GHz, respectively. The simulated Rx gain is about -9.2 and -10.6 dB at 24 and 28 GHz, respectively, and -11.8 and -12.5 dB measured results. It should be mentioned that the low noise amplifier can be used in the design to greatly improve the noise and gain performance of the receiver. The minimum detectable signal (MDS) for 64-QAM signal is about -52 dBm, and the dynamic range (DR) is about 43 dB, under LO power of 3 dBm. It is worthwhile noting that the interferometric receiver, as a passive Rx, is a good candidate for low-power direct conversion to baseband or IF receivers.

Table 3.5 summarizes the retrieved constellation diagrams of different orders of digital modulations (QPSK, QAM-16, QAM-32, and QAM-64) in both received signal channels and polarizations. It also presents the measured EVM for the different modulation signals with 5 MS/s symbol rate and a root-raised cosine pulse filter (a=0.35). From Table V, we can observe that the modulated signals are successfully demodulated with different points in the complex plane. The maximum EVM of the constellation diagram does not exceed -28.27 dB for both polarizations, free from any postprocessing linearization and calibration. Therefore, the proposed RX achieves a good performance. The EVM and SNR gradually deteriorate as the symbol rate increases. This is mainly due to the speed of the power detector used in this work [210], which is related to its rise time. Therefore, the demodulated performance of the proposed RX can be further improved with high-

Table 3.6 Performance summary and comparison with the state-of-the-art receivers based on interferometric technology

Ref.	Modulation signal	Freq. (GHz)	Symbol rate	EVM (dB)	After AC	Pol. type	Paralleled-Multichannel
[76]	16-QAM /64-QAM	2.5/3.0	2 Msps	-34.89/ -34.42	Yes	Single -pol.	No
	LTE /WCDMA	2.5/3.0	3 Msps /3.84 Msps	-33.97/ -34.42	Yes	Single -pol.	No
[189]	16-QAM /64-QAM	2.3/2.6	2 Msps	-34.89/- 37.72	Yes	Single -pol.	No
	WCDMA/LTE	2.3/2.6	3.84 Msps /3 Msps	-34.70/- 35.08	Yes	Single -pol.	No
[124]	M-QAM {4, 16 ,64, 256}	3.38/ 3.82	5 Msps	<-33.97	Yes	Single -pol.	No
[181]	4-QAM	28	500 Ksps	/	No	Single -pol	No
[184]	QPSK	2.45	200 Ksps	<-24.58	Yes	Single -pol.	No
[146]	4-QAM	5	2 Msps	-26.93	No	Single -pol.	No
	16-QAM	5	4 Msps	-22.49	No	Single -pol.	No
	32-QAM	5	5 Msps	-19.9	No	Single -pol.	No
[79]	4-QAM	28	1 Msps	-24.22	No	Single -pol.	No
	16-QAM	28	1 Msps	-24.83	No	Single -pol.	No
	32-QAM	28	1 Msps	-26.19	No	Single -pol.	No
[148]	BPSK	60	40 Msps	<-27.95	No	Single -pol.	No
	16-QAM		5 Msps				
[183]	16-QAM	2.4	10 Msps	/	No	Single -pol.	No
[184]	4-QAM	2.2	10 Msps	/	No	Single -pol.	No

[185]	4-QAM	1.8	1.4 Msps	<-17.9	No	Single -pol.	No
	16-QAM		1.4 Msps	<-18.3			
[186]	4-QAM	15	1.25 Gsps	/	No	Single -pol.	No
TW	**4-QAM**	**24/28**	**5 Msps**	**-29.72v/ -28.26v** **-29.52h/ -28.85h**	**No**	**Dual-pol.**	**Yes**
	16-QAM	**24/28**	**5 Msps**	**-30.65v/ -30.73v** **-30.47h/ -30.84h**	**No**	**Dual-pol.**	**Yes**
	32-QAM	**24/28**	**5 Msps**	**-30.36v/ -31.05v** **-30.12h/ -30.31h**	**No**	**Dual-pol.**	**Yes**
	64-QAM	**24/28**	**5 Msps**	**-29.83v/ -29.37v** **-28.81h/ -30.24h**	**No**	**Dual-pol.**	**Yes**

TW: This Work; AC: Algorithm Calibration

speed power detectors. Table 3.6 compares this work with several state-of-the-art studies on the subject. This work based on the proposed dual-input multiport architecture achieves paralleled dual-band dual-polarized operation for the first time. It shows a good performance in terms of EVM and can be further enhanced with efficient calibration algorithms as in [76], [124], [191] and [194]. The measured results validate the usefulness and effectiveness of the proposed RX architecture for frequency- and polarization-diversified MIMO applications.

3.6 Conclusion

In this work, a self-contained dual-input receiver architecture based on the interferometric technique has been proposed, studied and experimentally demonstrated. The most significant advantage of the proposed receiver topology is its self-contained paralleled RF channels as opposed to conventional RXs. In addition, the proposed RX has only two output ports instead of the

traditional four ports. This makes the proposed RX suitable for low power, low cost, compact, and low complex multifunctional frequency- and polarization-diversified MIMO wireless systems. An experimental prototype was designed and fabricated to validate the proposed RX architecture. Various modulations, including QPSK, 16-QAM, 32-QAM, and 64-QAM, have been measured and demonstrated. Experimental results confirm that the proposed receiver scheme achieves good performances without any calibration procedure. Therefore, high-data-rate communications could be supported.

CHAPTER 4 ARTICLE 2: ALL-IN-ONE DUAL-POLARIZATION WAVEGUIDE RECEIVER FOR MULTICHANNEL WIRELESS SYSTEMS

Jie Deng, Pascal Burasa, and Ke Wu

Published in: IEEE Transactions on Microwave Theory and Techniques

Publication date: January 29, 2024

Abstract: In this work, a monoblock hardware receiver solution for dual-polarization multichannel wireless systems is proposed and demonstrated for the first time. The receiver benefits from the use of a square waveguide scheme enabling dual-polarization features. Two orthogonalized polarizations, namely, horizontally and vertically polarized waves, can simultaneously be excited in a single-modular hardware receiver while maintaining reliable performances. Compared to conventional dual polarization receiver architectures with two separate hardware platforms, the proposed receiver is set to greatly reduce the circuit complexity, size, cost, and power consumption. Besides, due to the self-contained dual-input radio frequency (RF) channels, paralleled-multiband operation can also be realized. The core multiport circuit consists of integrated dual polarization components, namely, cruciform couplers, orthomode transducers (OMTs), and phase shifters. The operating mechanism of the receiver is studied and explained with a mathematical model. To validate the concept, an experimental prototype is developed, fabricated, and measured. Paralleled-multichannel transmission of various M-quadratic-amplitude modulation (QAM) signals is successfully demodulated experimentally. It is found that the proposed waveguide receiver presents a viable candidate for future multistandard wireless systems.

Index Terms: Direct conversion receiver, dual polarization, multichannel, multifunction, multiport interferometric receiver, square metallic waveguide, wireless systems.

4.1 Introduction

Wireless systems have recently experienced a huge and rapid development due to the ever-increasing demands of emerging high-resolution and immersive applications such as multimedia services, 3D environment mapping, virtual and augmented reality, etc. [18], [170], [173], [176],

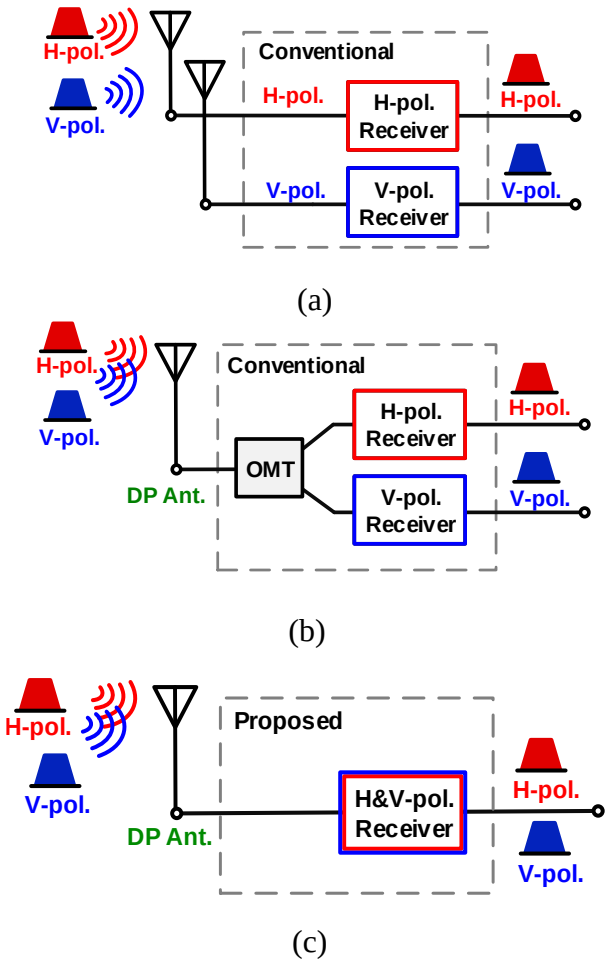

Figure 4.1 Concept diagram of dual-polarized receiver system. (a) Conventional dual receiver modules with separated H-Pol. and V-Pol. antennas. (b) Conventional dual receiver modules sharing dual-polarized antenna. (c) Proposed solution with only one receiver module

[211], [212], [213], [214], [215], [216]. These developments require high data rate, low latency, reliable links, large channel capacity, and smart connectivity to maintain the plurality of services. To meet such demands, efficient solutions and technologies should be introduced. For example, the polarization diversity technique has been widely used in state-of-the-art RF receivers to improve its capability and support simultaneous independent data streams on the same frequency channel, thereby doubling the effective channel capacity and improving spectrum usage compared with single-polarized counterparts [217], [218], [219], [220].

As illustrated in Figure 4.1(a), most conventional dual-polarized receivers need two separate circuit modules to deal with dual- polarization signals, which would increase the size, cost, complexity,

and power consumption of the whole system. It is desirable to realize a more compact and efficient receiver with dual polarization. Many studies have been conducted to relax the number of circuit modules needed for dual-polarization operations. As shown in Figure 4.1(b), there has been a significant advancement of receiver [221], [222] by using a dual-polarized antenna. Although the receiver requires only one antenna, this architecture still needs two independent receiver channel modules. To tackle the abovementioned underlying technical challenges, innovative solutions should be explored and developed where both horizontal and vertical polarizations are integrated into a single circuit platform. Such a solution becomes meaningful for not only a minimized manufacturing cost, but also an enhanced receiver performance such as lower loss, noise, power consumption, etc.

Multiport interferometric receiver has been known to feature reduced circuit complexity and low power consumption [70], [74], [76], [77], [79], [80], [94], [95], [96], [100], [101], [102], [104], [105], [114], [124], [125], [127], [142], [146], [150], [181], [182], [187], [188], [191], [223], [224], [225], [226]. A multiport interferometric receiver, typically called a “six-port” receiver, consists of two inputs and four outputs for a single-band channel operation. Two inputs are set to receive the LO and RF signals, respectively. Four power detectors are connected to the outputs to retrieve the unknown RF signal through a linear interference with the known LO signal, thanks to the linear square-law power detections. To improve the channel utilization as well as the system throughput, significant advancements in concurrent dual-band operation of multiport interferometric receivers have been made and demonstrated in [74], [76], [96], [124], [191]. However, these receiver architectures require wider bandwidth performance since a dual-band or multiband signal is serially received through one input. To further improve the effective channel capacity, additional receiving paths, i.e., multiple circuit modules, are required to enable the orthogonal polarizations [127]. Different sets of sub-circuits for the input signals would increase the component count. As a result, the circuit footprint, cost, and complexity will be increased.

In this work, an all-in-one dual-polarized receiver based on the interferometric technique, as illustrated in Figure 4.1(c), is proposed to solve the aforementioned issues. Both horizontal and vertical polarizations are encapsulated into a single-modular hardware receiver. Therefore, it enhances not only the compactness, cost, and complexity, but also the receiver performance, especially in the case an array. To this end, the proposed receiver benefits from the use of a square

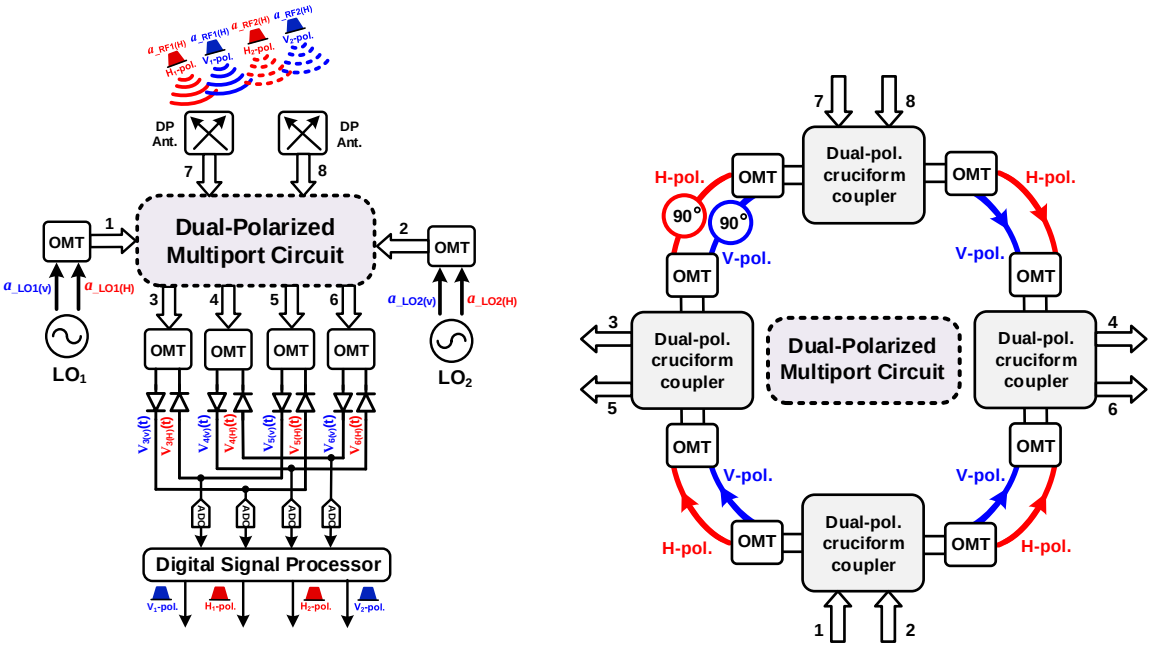

(a) (b)

Figure 4.2 Proposed metallic interferometric waveguide receiver systems. (a) Multiport interferometric architecture. (b) Configuration of internal multiport circuit

waveguide enabling dual-polarization features. In addition, different from conventional six-port topologies, the proposed receiver adopts a novel eight-port architecture, where a novel dually polarized cruciform waveguide coupler and a dually polarized phase shifting solution are proposed. Therefore, dual-polarization multichannel transmission is enabled using a mono-block hardware receiver solution. To the authors' best knowledge, such an all-in-one dual-polarized multichannel receiver has never been reported yet.

Section 4.2 introduces the architecture of the proposed multiport interferometric receiver and highlights its advantages compared to traditional receivers. Besides, the operating principle of the receiver is presented and discussed in detail. Section 4.3 details the key circuit blocks including the dual-polarized cruciform coupler, orthomode transducers (OMT), dual-polarized phase shifter, dual-polarized antenna, and waveguide transition. In Section 4.4, the integration of those circuit blocks is described. The final implementation and measurements of the prototype are presented in Section 4.5. Finally, conclusions are drawn in Section 4.6.

4.2 Receiver architecture

The configuration of the proposed metallic interferometric waveguide receiver is shown in Figure 4.2, which is based on the square waveguide technology to enable the orthogonal polarization. If both pols operate at the same carrier frequency, the effective channel capacity can be doubled. Different from the traditional "six-port" configuration, the proposed architecture exhibits "eight-port" because of its eight input and output ports, enabling for a parallel dual-band dual-polarized operation. The receiver mainly consists of a dual-polarized multiport circuit designed with four cruciform couplers and a 90° phase shifter and four-pair power detectors at ports 3 through 6. The power detectors use the balanced detection scheme to simply the design [139]. Ports 7 and 8 are two input ports connected to two dual-polarized antennas. The modulated dual-band dual-polarized signals sent by transmitters are captured by the receiving antennas. These vertical and horizontal polarized signals can be expressed as:

$$\begin{cases} a_{\_RF_i(\mathrm{V})} = \left| a_{\_RF_i(\mathrm{V})} \right| \cdot \left| \mathrm{I}_{V_i}(\mathrm{t}) + \mathrm{jQ}_{V_i}(\mathrm{t}) \right| e^{\mathrm{j}w_{RF_i(\mathrm{V})}(\mathrm{t})} & (4.1) \\ a_{\_RF_j(\mathrm{H})} = \left| a_{\_RF_j(\mathrm{H})} \right| \cdot \left| \mathrm{I}_{H_j}(\mathrm{t}) + \mathrm{jQ}_{H_j}(\mathrm{t}) \right| e^{\mathrm{j}w_{RF_j(\mathrm{H})}(\mathrm{t})} & (4.2) \end{cases}$$

where I_{Vi} and Q_{Vi}, i=1, 2, represent the in-phase and quadrature components of the vertical-polarized signal, respectively. I_{Hj} and Q_{Hj}, j=1, 2, represent the in-phase and quadrature components of the horizontal-polarized signal, respectively. $|a_{\_RFi(\mathrm{V})}|$ and $|a_{\_RFj(\mathrm{H})}|$ are the amplitude of the signals. Then, the captured signals directly enter the dual-polarized multiport circuit, where it is superposed with two local oscillator (LO) signals through linear interference. Ports 1 and 2 are two local oscillator (LO) input ports. The two LO signals are fed to ports 1 and 2 by OMTs. The input LO signals can be expressed as:

$$\begin{cases} a_{\_LO_i(\mathrm{V})} = \left| a_{\_LO_i(\mathrm{V})} \right| e^{\mathrm{j}(w_{LO_i(\mathrm{V})}(\mathrm{t}) + \Phi_{LOi(\mathrm{V})})} & (4.3) \\ a_{\_LO_j(\mathrm{H})} = \left| a_{\_LO_j(\mathrm{H})} \right| e^{\mathrm{j}(w_{LO_j(\mathrm{H})}(\mathrm{t}) + \Phi_{LO_j(\mathrm{H})})} & (4.4) \end{cases}$$

where $a_{\_LOi(\mathrm{V})}$ and $a_{\_LOj(\mathrm{H})}$, i, j=1, 2, are the amplitude of LO signals. $\Phi_{\_LOi(\mathrm{V})}$ and $\Phi_{\_LOj(\mathrm{H})}$ the phases of LO signals. The output ports of the multiport circuit are ports 3-6, each of which contains dually polarized RF and LO signals. To separate the orthogonally polarized signal, each output port connects an OMT. It should be noted that, to avoid the interference of the down-converted frequencies, the RF signals and LO signals are selected with the following conditions [76]:

$$\left| f_{LO_1(\mathrm{H})} - f_{RF_1(\mathrm{H})} \right| > \frac{3}{2}\mathrm{BW}_{\mathrm{RF}_1(\mathrm{H})}, \qquad f_{IF_1(\mathrm{H})} = f_{RF_1(\mathrm{H})} - f_{LO_1(\mathrm{H})} \tag{4.5}$$

$$\left| f_{IF_2(\mathrm{H})} - f_{IF_1(\mathrm{H})} \right| > \frac{(\mathrm{BW}_{\mathrm{RF}_1(\mathrm{H})} + \mathrm{BW}_{\mathrm{RF}_2(\mathrm{H})})}{2}, \qquad f_{IF_2(\mathrm{H})} = f_{RF_2(\mathrm{H})} - f_{LO_2(\mathrm{H})} \tag{4.6}$$

$$\left| f_{LO_1(\mathrm{V})} - f_{RF_1(\mathrm{V})} \right| > \frac{3}{2}\mathrm{BW}_{\mathrm{RF}_1(\mathrm{V})}, \qquad f_{IF_1(\mathrm{V})} = f_{RF_1(\mathrm{V})} - f_{LO_1(\mathrm{V})} \tag{4.7}$$

$$\left| f_{IF_2(\mathrm{V})} - f_{IF_1(\mathrm{V})} \right| > \frac{(\mathrm{BW}_{\mathrm{RF}_1(\mathrm{V})} + \mathrm{BW}_{\mathrm{RF}_2(\mathrm{V})})}{2}, \qquad f_{IF_2(\mathrm{V})} = f_{RF_2(\mathrm{V})} - f_{LO_2(\mathrm{V})} \tag{4.8}$$

where $\mathrm{BW}_{RF1(\mathrm{H})}$ and $\mathrm{BW}_{RF2(\mathrm{H})}$ are bandwidth of $f_{RF1(\mathrm{H})}$ and $f_{RF2(\mathrm{H})}$, denoted as two horizontally polarized carrier signals, respectively, and $\mathrm{BW}_{RF1(\mathrm{V})}$ and $\mathrm{BW}_{RF2(\mathrm{V})}$ are bandwidth of $f_{RF1(\mathrm{V})}$ and $f_{RF2(\mathrm{V})}$ standing for two vertically polarized carrier signals, respectively. Then, the separated signals are fed to the power detectors. The output voltage of those detectors is proportional to the square magnitude of their input signals [76].

$$\begin{aligned} V_{k(V)}(t) &= \eta \left| S_{\mathrm{i}1}(a_{\_LO_1(\mathrm{V})} + a_{\_LO_2(\mathrm{V})}) + S_{\mathrm{i}2}(a_{\_RF_1(\mathrm{V})} + a_{\_RF_2(\mathrm{V})}) \right|^2 \\ V_{k(H)}(t) &= \eta \left| S_{\mathrm{i}1}(a_{\_LO_1(\mathrm{H})} + a_{\_LO_2(\mathrm{H})}) + S_{\mathrm{i}2}(a_{\_RF_1(\mathrm{H})} + a_{\_RF_2(\mathrm{H})}) \right|^2 \\ &\qquad \text{for } k = 3, 4, ...6 \end{aligned} \tag{4.9}$$

in which η is a constant related to the characteristics of power detectors. Due to the nonlinearity of diodes, the output includes rectified waves, difference signals, and harmonic signals [188]. From the voltage differences between two output ports of the detectors, the desired down-converted signals can be extracted as follows:

$$\begin{aligned} V_{3(V)}(t) - V_{5(V)}(t) = cG[&\sin(2\pi f_{IF_1(\mathrm{V})}t) I_{V_1} - \cos(2\pi f_{IF_1(\mathrm{V})}t) Q_{V_1}] \\ &+ \sin(2\pi f_{IF_2(\mathrm{V})}t) I_{V_2} - \cos(2\pi f_{IF_2(\mathrm{V})}t) Q_{V_2}] \end{aligned} \tag{4.10}$$

$$\begin{aligned} V_{4(V)}(t) - V_{6(V)}(t) = cG[&\sin(2\pi f_{IF_1(\mathrm{V})}t) I_{V_1} + \cos(2\pi f_{IF_1(\mathrm{V})}t) Q_{V_1}] \\ &+ \sin(2\pi f_{IF_2(\mathrm{V})}t) I_{V_2} + \cos(2\pi f_{IF_2(\mathrm{V})}t) Q_{V_2}] \end{aligned} \tag{4.11}$$

$$\begin{aligned} V_{3(H)}(t) - V_{5(H)}(t) = cG[&\sin(2\pi f_{IF_1(\mathrm{H})}t) I_{H_1} - \cos(2\pi f_{IF_1(\mathrm{H})}t) Q_{H_1}] \\ &+ \sin(2\pi f_{IF_2(\mathrm{H})}t) I_{H_2} - \cos(2\pi f_{IF_2(\mathrm{H})}t) Q_{H_2}] \end{aligned} \tag{4.12}$$

$$V_{4(H)}(t) - V_{6(H)}(t) = cG[\sin(2\pi f_{IF_1(\mathrm{H})}t)I_{H_1} + \cos(2\pi f_{IF_1(\mathrm{H})}t)Q_{H_1}] \\ \sin(2\pi f_{IF_2(\mathrm{H})}t)I_{H_2} + \cos(2\pi f_{IF_2(\mathrm{H})}t)Q_{H_2}] \tag{4.13}$$

Equations (4.10) and (4.11) represent the vertically polarized component, which can be expressed as matrix form (4.14):

$$\begin{bmatrix} \Delta V_{3\text{–}5(V)} \\ \Delta V_{4\text{–}6(V)} \end{bmatrix} \\ = cG \begin{bmatrix} \sin(2\pi f_{IF_1(\mathrm{V})}t) & -\cos(2\pi f_{IF_1(\mathrm{V})}t) & \sin(2\pi f_{IF_2(\mathrm{V})}t) & -\cos(2\pi f_{IF_2(\mathrm{V})}t) \\ \sin(2\pi f_{IF_1(\mathrm{V})}t) & \cos(2\pi f_{IF_1(\mathrm{V})}t) & \sin(2\pi f_{IF_2(\mathrm{V})}t) & \cos(2\pi f_{IF_2(\mathrm{V})}t) \end{bmatrix} \begin{bmatrix} I_{V1} \\ Q_{V1} \\ I_{V2} \\ Q_{V2} \end{bmatrix} \tag{4.14}$$

Equations (4.12) and (4.13) represent the horizontally polarized component, which can be expressed as matrix form (4.15):

$$\begin{bmatrix} \Delta V_{3\text{–}5(H)} \\ \Delta V_{4\text{–}6(H)} \end{bmatrix} \\ = cG \begin{bmatrix} \sin(2\pi f_{IF_1(\mathrm{H})}t) & -\cos(2\pi f_{IF_1(\mathrm{H})}t) & \sin(2\pi f_{IF_2(\mathrm{H})}t) & -\cos(2\pi f_{IF_2(\mathrm{H})}t) \\ \sin(2\pi f_{IF_1(\mathrm{H})}t) & \cos(2\pi f_{IF_1(\mathrm{H})}t) & \sin(2\pi f_{IF_2(\mathrm{H})}t) & \cos(2\pi f_{IF_2(\mathrm{H})}t) \end{bmatrix} \begin{bmatrix} I_{H1} \\ Q_{H1} \\ I_{H2} \\ Q_{H2} \end{bmatrix} \tag{4.15}$$

Subsequently, their signals are first filtered, amplified, and then converted to the digital domain to be further processed and used in synthesizing the complex I/Q components.

4.3 Circuit implementations

In this section, each component of the multiport circuit is separately designed according to pre-defined performances or specifications for the proposed receiver. As a demonstrative example, the

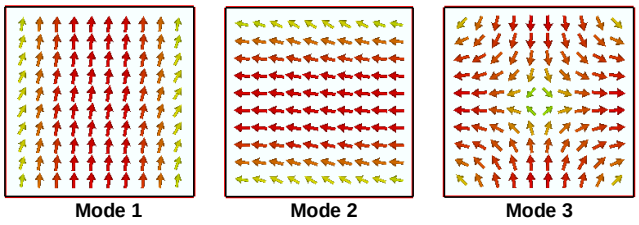

(a) (b) (c)

Figure 4.3 E-field mode of square waveguide. (a) TE_{10} mode. (b) TE_{01} mode. (c) TE_{11} mode

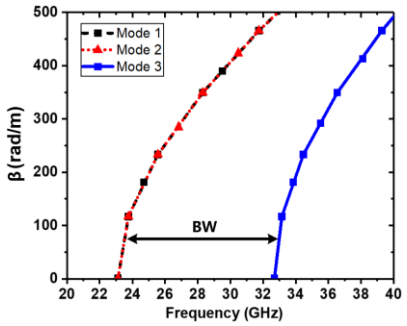

Figure 4.4 Dispersion curves of the first three modes in a square waveguide

receiver is considered to operate in the frequency range of 26-30 GHz for millimeter-wave applications. To handle two orthogonal polarizations, square waveguide technology is adopted in the circuit development. Figure 4.3 shows the square waveguide (a=b=6.35 mm) used in each component design, from which it can be seen that two orthogonal polarization modes, i.e., TE_{10} mode and TE_{01} modes, can be excited. Figure 4.4 illustrates a single-mode bandwidth of 23-32.4 GHz for the square waveguide while satisfying the target band of 26-30 GHz for demonstration.

4.3.1 Dually-polarized cruciform waveguide coupler

A key component of the proposed dually polarized multiport circuit is a dually polarized waveguide coupler, which provides the required amplitudes and phases. Those parameters would affect the performance of the receiver system. Although various kinds of directional couplers were widely studied and developed in the past, those couplers based on the conventional rectangular waveguide technology can only support single-polarization operations. The study of dually polarized couplers

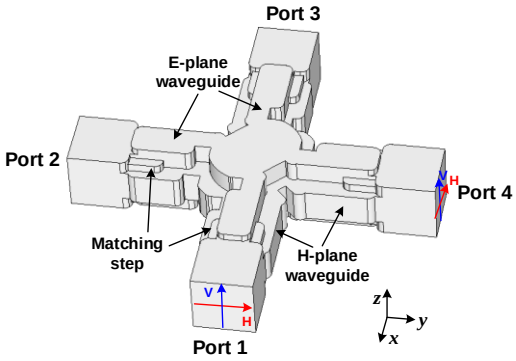

(a)

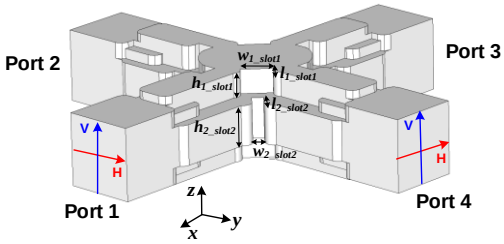

(b)

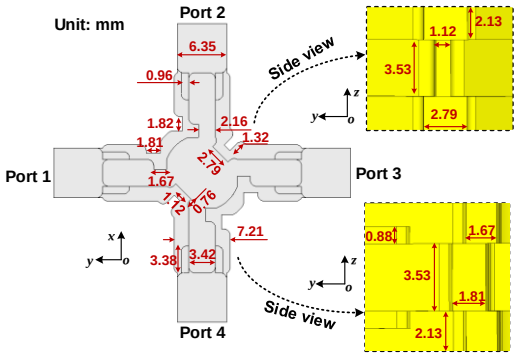

(c)

Figure 4.5 Structure of the proposed dually polarized cruciform coupler. (a) Three-dimensional view. (b) Side view. (c) Vertical view

in the square waveguide technology has received very limited interests in the literature. Several dually polarized waveguide couplers have been proposed in [227], [228], [229]. Those using aperture coupling on the broad wall of two paralleled square waveguides enable dually polarized operation. However, they suffer from a large size and have a limited bandwidth. Therefore, proposed in this work is an innovative dually polarized cruciform waveguide coupler having a

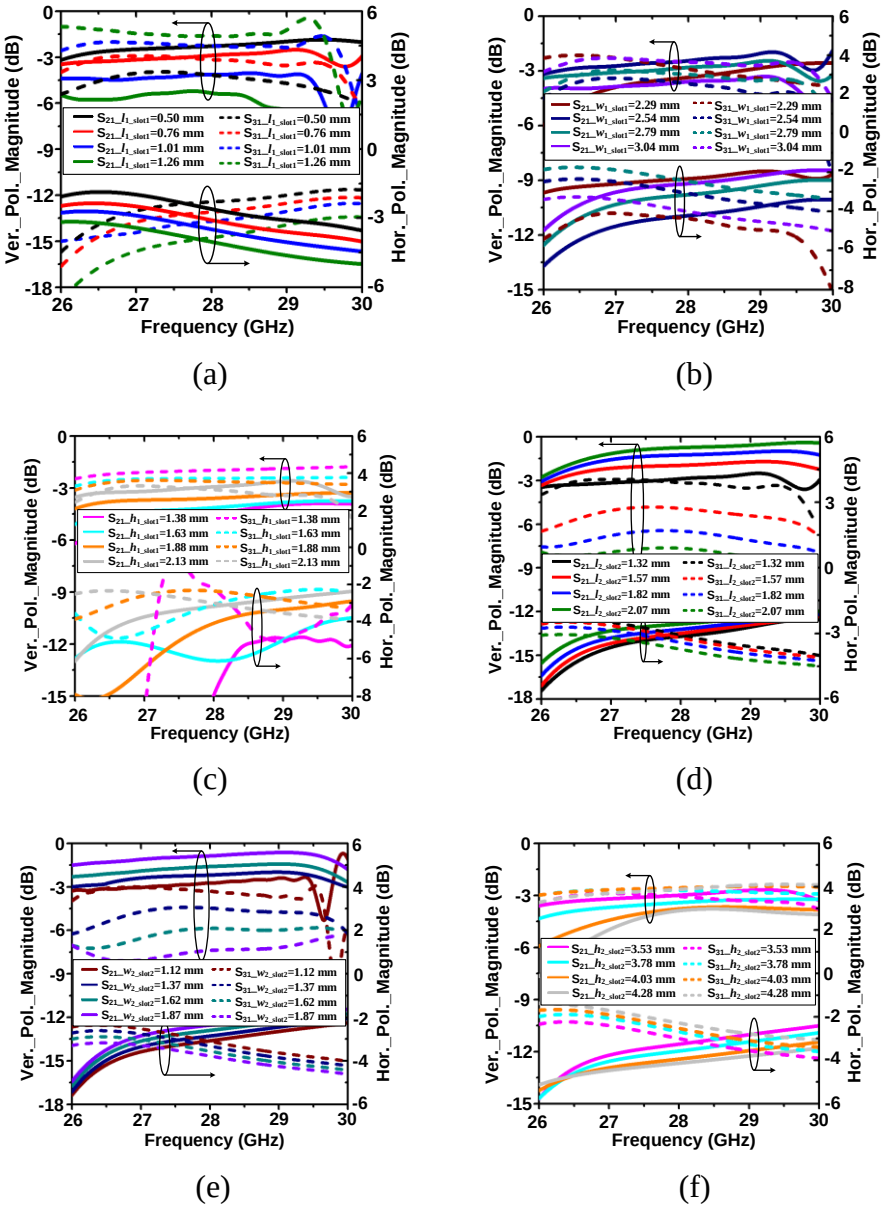

Figure 4.6 Parametric study showing the effect of changing the dimensions of the two paired slots in the central coupling region. (a) l_{1_slot1}. (b) w_{1_slot1}. (c) h_{1_slot1}. (d) l_{2_slot2}. (e) w_{2_slot2}. (f) h_{2_slot2}

compact size and a wide bandwidth, which was inspired by a holistic integration of both E-plane cruciform waveguide coupler [230] and H-plane cruciform waveguide coupler [231].

Figure 4.5 shows the configuration of the proposed cruciform waveguide coupler. It consists of four square waveguide ports, four waveguide arms, and a center coupling cavity. The coupling

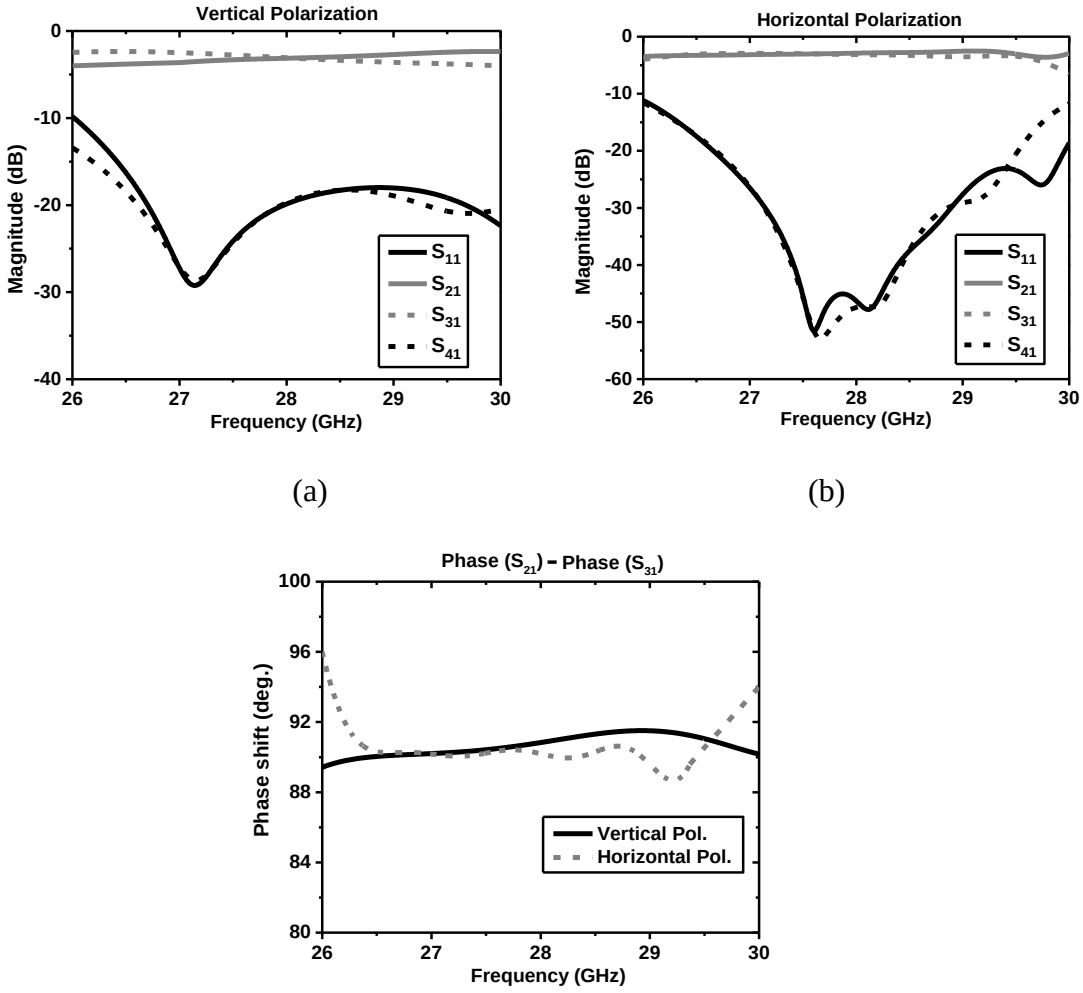

Figure 4.7 Cruciform coupler performance. (a) Magnitude of scattering parameters for vertically polarized mode. (b) Magnitude of scattering parameters for horizontally polarized mode. (c) Phase shift for both vertically and horizontally polarized modes

cavity connects the input and output ports through orthogonally placed waveguide arms. Therefore, the geometry of the coupler forms so-called a "cruciform" shape. Two paired slots are placed at the diagonal plane of the cruciform waveguide coupler to control the ratio of signal coupling. To achieve a 3-dB coupling, a parameter study is carried out to further understand the coupler behavior. The effects of the changing the width, height, and length of the two paired slots are studied and investigated. As shown in Figure 4.6, it can be observed that the $slot_1$ mainly affects the coupling of the horizontal-polarized mode performance, while the $slot_2$ affects the coupling of the vertical-

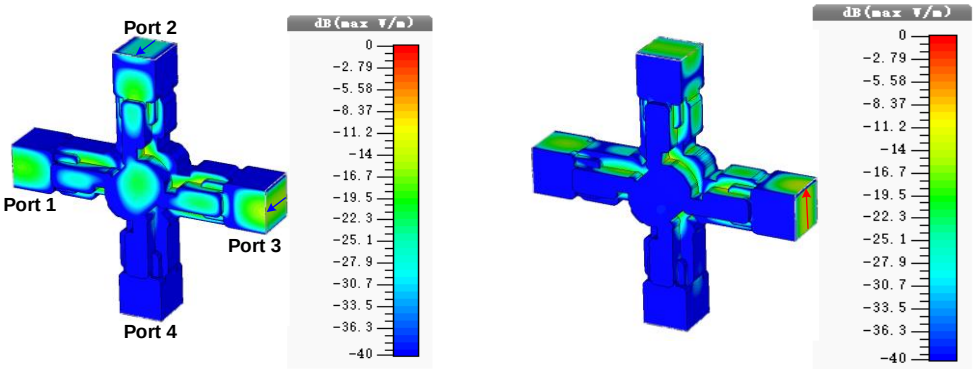

(a) (b)

Figure 4.8 (a) E-field distribution of the vertically polarized mode. (b) E-field distribution of the horizontally polarized mode

polarized mode performance. Therefore, for horizontal-polarized mode, the coupling decreases by increasing l_{1_slot1}. Similarly, with the increase of w_{1_slot1}, the coupling will decrease, but the coupling increases with increasing h_{1_slot1}. For vertical-polarized mode, when the l_{2_slot2} increases, the coupling increases. However, the coupling decreases by increasing w_{2_slot2}. With the reduction of h_{2_slot2}, the coupling will increase. Therefore, by properly adjusting the dimensions of slots, i.e., l_{1_slot1}=0.76 mm, w_{1_slot1}=2.79 mm, h_{1_slot1}=2.13 mm, l_{2_slot2}=1.32 mm, w_{2_slot2}=1.12 mm, and h_{2_slot2}=3.53 mm, a 3-dB coupling between output ports, i.e., ports 2 and 3, will be acheived. The port 1 is the input port. Ports 2 and 3 are coupling and through ports, receptively, and port 4 is the isolated port. Therefore, when port 1 excites two orthogonal polarized signals, both orthogonal signals will be equally divided to ports 2 and 3 while port 4 is isolated. To achieve a better impedance matching, several matching steps are added in the four waveguide arms. Figure 4.7 shows the simulated results of the cruciform waveguide coupler for both orthogonal polarization modes. For the vertically-polarized mode, i.e., TE_{10} mode, it can be observed that the input reflection coefficient (S_{11}) is below -15 dB from 26.5 to 30 GHz. Meanwhile, the isolation (S_{41}) between output ports is better than 15 dB. The output amplitudes (S_{21} and S_{31}) are around -3.3 ± 0.6 dB and the phase imbalances between these two output ports are ranged from 89° to 92°. Similarly, for the horizontally polarized mode, i.e., TE_{01} mode, it can be seen that over the frequency range from 26.5 to 30 GHz, the input reflection coefficient (S_{11}) is below -15 dB. The isolation (S_{41}) between output ports is better than 20 dB. The output amplitudes (S_{21} and S_{31}) are

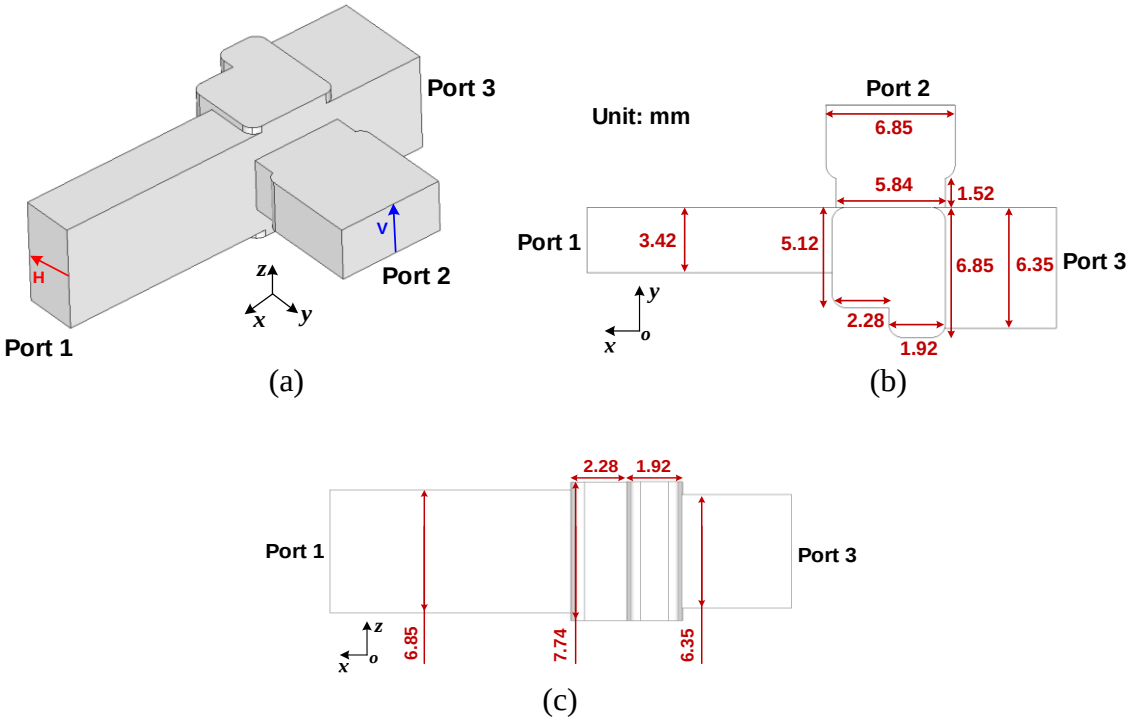

Figure 4.9 Structure of the proposed OMT. (a) Three-dimensional view. (b) Side view. (c) Vertical view.

around -3.2 ± 0.3 dB and the phase differences between these two output ports are from 88° to 94°. Figure 4.8 shows the simulated E-field distributions of the proposed cruciform coupler for two orthogonal polarization modes. It can be observed that when port 1 is used to excite the vertically polarized signal, the signal is equally divided into ports 2 and 3 through the center coupling cavity. There is no signal flowing into the isolated port, i.e., port 4. Similarly, when port 1 is set to excite the horizontally polarized signal, the signal is equally divided into ports 2 and 3. There is no signal flowing into the isolated port. The behavior of E-field distribution demonstrates the dually-polarized characteristics of the proposed cruciform waveguide coupler.

4.3.2 Orthomode transducer

The proposed receiver makes use of an OMT to separate the orthogonal polarizations. The asymmetric OMT geometry [232], [233] as shown in Figure 4.9, is adopted in this work because it does not require posts or septum and it is relatively easy to design and fabricate. The OMT consists of a common square waveguide arm and two rectangular waveguide arms. One rectangular waveguide arm is directly connected horizontally to the square waveguide arm. The other arm is

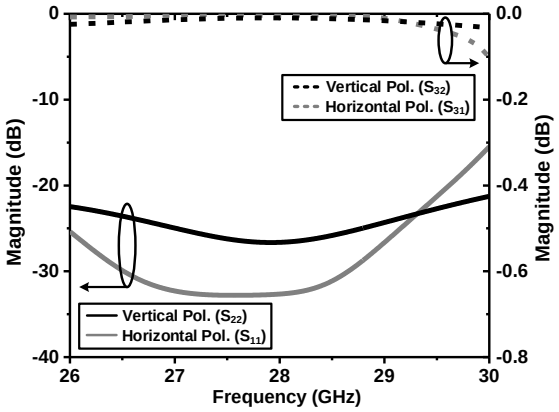

(a)

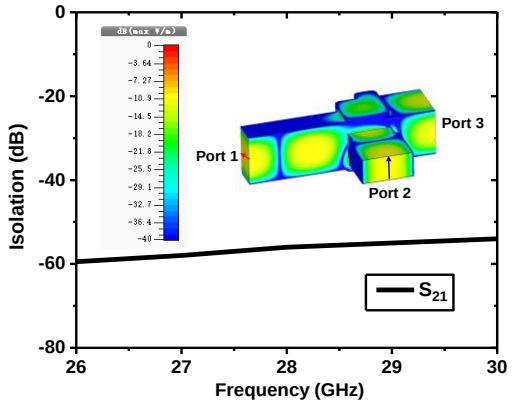

(b)

Figure 4.10 Simulated results of the proposed OMT. (a) Return losses and insertion losses. (b) Isolation

orthogonal to the common arm. The horizontally-connected waveguide arm is an E-plane waveguide supporting the TE_{01} mode and the orthogonally-connected waveguide arm is an H-plane waveguide supporting the TE_{10} mode. The whole structure of the OMT forms a branching T-junction. The central T-junction region separates or combines the TE_{10} mode and TE_{01} mode, and meets the needed polarization isolation and impedance matching performance, simultaneously. Due to the geometrical variations and discontinuities in the central junction region, the design of the multistage waveguide steps [234] are introduced to improve the matching performance while limiting the coupling of cross-polarized mode components.

Figure 4.10 shows the simulated results of the proposed OMT. It can be seen that over the frequency range from 26 to 30 GHz, the reflection coefficient for vertical polarization is lower than -21 dB and the reflection coefficient for horizontal polarization is lower than -15 dB. The insertion losses

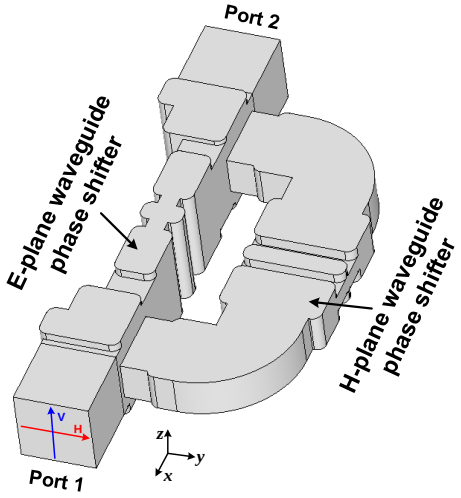

Figure 4.11 Structure of the proposed dual-polarized waveguide phase shifter

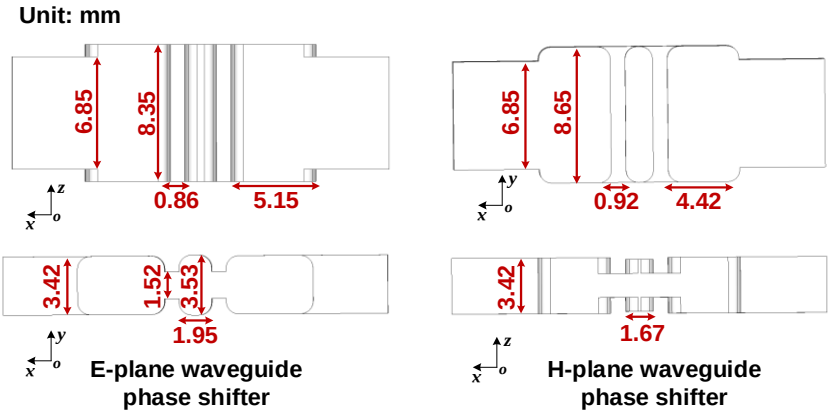

(a) (b)

Figure 4.12 Detailed structure views. (a) E-plane waveguide phase shifter. (b) H-plane waveguide phase shifter

for both polarizations are better than 0.2 dB. A high isolation of more than 55 dB is achieved. The simulated E-field distributions of the proposed OMT are presented in Figure 4.10(b). It can be observed that when port 3 excites both orthogonally polarized signals, the horizontally polarized signal is directed to port 2, while the vertically polarized signal is guided to port 1.

4.3.3 Dually polarized waveguide phase shifter

The phase shifter is a crucial component in the construction of a multiport circuit to provide the required phase shifting performance. It is hard to consider multiple metrics such as phase error,

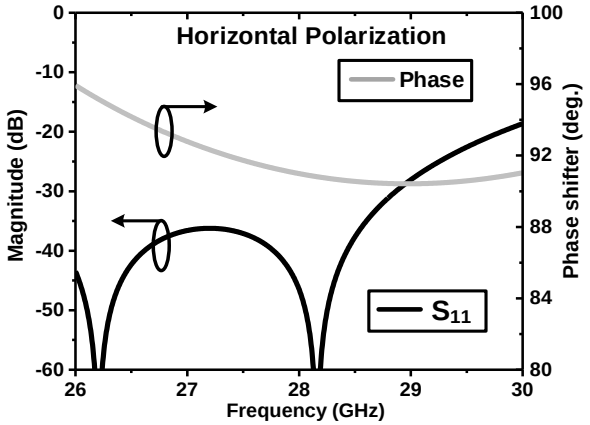

(a)

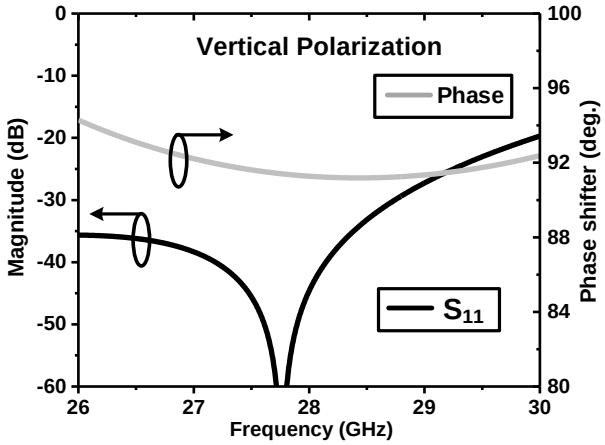

(b)

Figure 4.13 Simulated performance of the proposed dually polarized phase shifter. (a) Horizontal polarization. (b) Vertical polarization

bandwidth, insertion loss, compact size, and large phase shift range at the same time, especially for dually polarized phase shifter. The classical delay-line technique has been used in a dually polarized phase shifter [227] achieving a simple structure. However, this phase shifter has a limited bandwidth performance. A tapered waveguide [228] structure was implemented to achieve a dually polarized phase shifter. Nevertheless, such a phase shifter suffers from a large size, which limits its applications.

In this work, a dually polarized phase shifter as shown in Figure 4.11 is proposed to solve the abovementioned problems. The phase shifter integrates two compact waveguide phase shifters

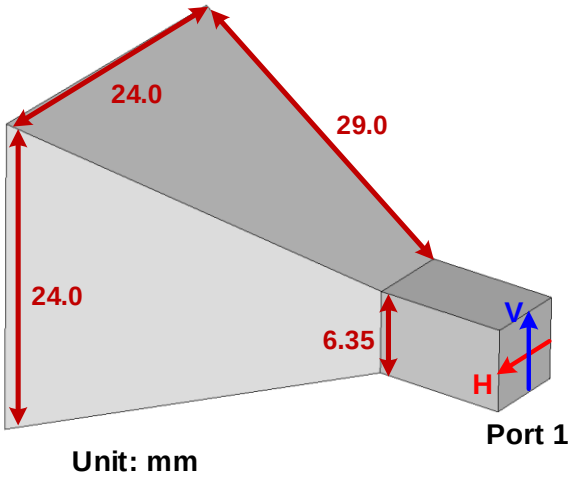

Figure 4.14 The structure of dual-polarized square waveguide horn antenna

involving H-plane and E-plane, respectively [52], [53] through two OMTs, allowing the vertical and horizontal polarizations to be controlled independently. In this way, a wide bandwidth performance can easily be obtained by adjusting the H-plane and the E-plane waveguide phase shifters.

Figure 4.12 shows the detailed joint structure of the H-plane and E-plane waveguide phase shifters. It can be seen that both E-plane and H-plane waveguide phase shifters are composed of multi-stepped waveguides. Due to the change of the guide wavelength and discontinuities, the multi-stepped waveguide generates a β_1 phase constant compared with a typical rectangular waveguide corresponding to β_2 phase constant. Therefore, different combinations of β_1 and β_2 sections allow to achieve the desired phase shifting. The simulated results of the phase shifter for both orthogonal polarizations are shown in Figure 4.13. It can be observed that for the horizontal polarization, the reflection coefficient is lower than -20 dB and the phase shift is around 93°±3° over the frequency range from 26 to 30 GHz. Similarly, for the vertical polarization, the reflection coefficient is lower than -20 dB and the phase shift is around 92°±2°.

4.3.4 Dually polarized waveguide antenna

In order to achieve enough antenna gain over the entire band of interest, a dually polarized square waveguide horn antenna is used in this work. In general, the dually polarized antenna arrays can be adopted to satisfy a high-gain requirement. However, such a design will result in high

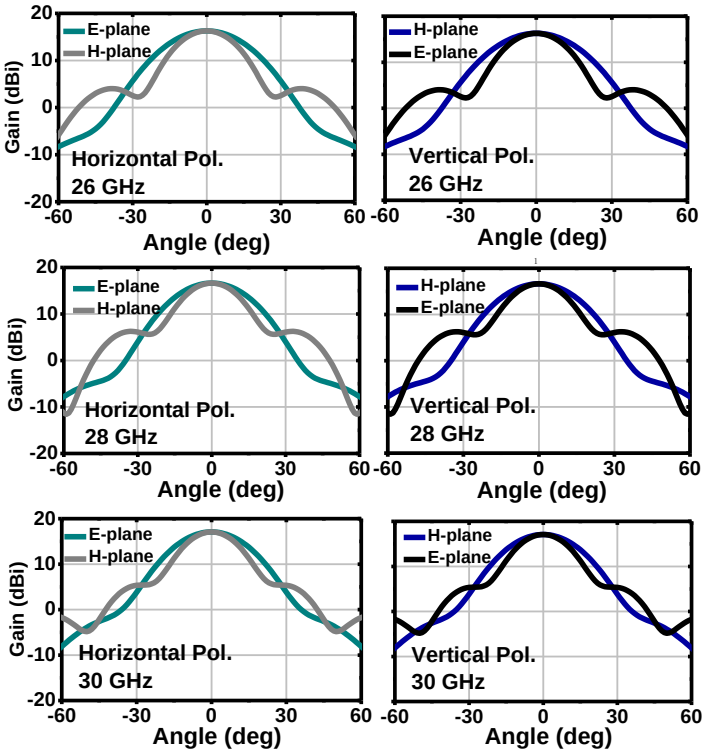

(a)

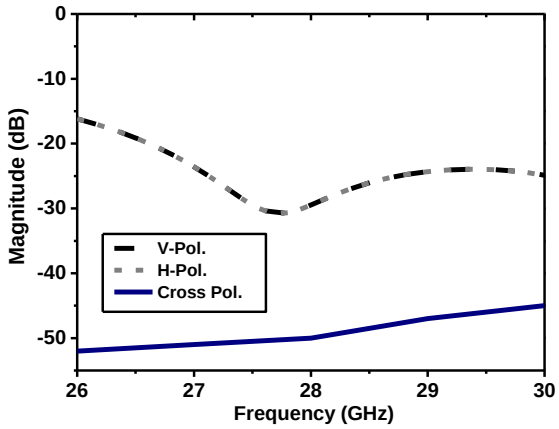

(b)

Figure 4.15 Simulated performance of the proposed square waveguide horn antenna. (a) Radiation pattern. (b) Refection coefficient and cross polarization

manufacturing costs and increase the complexity of integration. Thus, a square waveguide horn antenna is chosen as a compromise for our preliminary verification due to its low cost and easy fabrication and integration. Figure 4.14 shows the structure of the proposed square waveguide horn

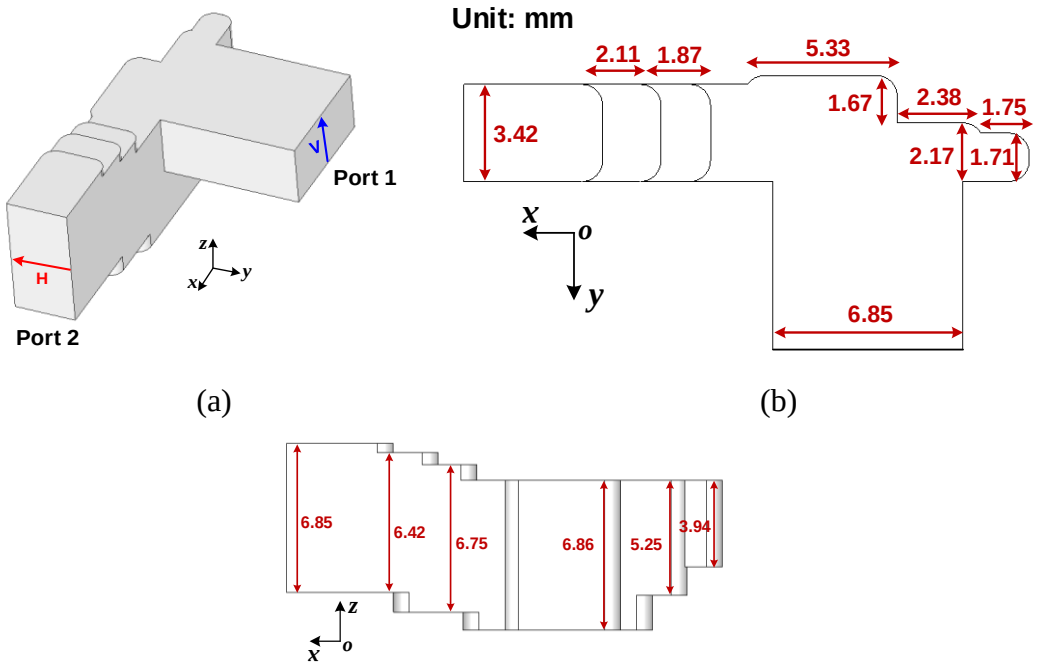

Figure 4.16 The structure of waveguide twist-bend transition. (a) Three-dimensional view. (b) Vertical view. (c) Side view

antenna. It consists of a square waveguide port and a horn port. The square waveguide port connects the horn port through a 29 mm pyramidal waveguide transition. The whole antenna can easily be integrated with the multiport circuit. The simulated radiation patterns at 26 GHz, 28 GHz, and 30 GHz for the dual polarization are presented in Figure 4.15(a) to verify the radiation performance over its operating frequency band. It can be observed that the average gain of the antenna for both polarizations is about 16.62 dBi. Figure 4.15(b) shows the S-parameters of the square horn antenna. As can be seen from Figure 4.15(b), the reflection coefficients for both polarizations are below -15 dB and isolation is better than 45 dB over the frequency band from 26 GHz and 30 GHz.

4.4 Waveguide transitions and device integration

4.4.1 Waveguide twist-bend transition

With respect to the dually polarized multiport network, the OMTs are used to separate the polarization signals. However, the output ports of OMTs are orthogonal, which will increase the difficulty of integration with the multiport circuit. Therefore, a waveguide twist-bend transition is required for the interconnection of those components. In [235], a broadband waveguide twist-bend

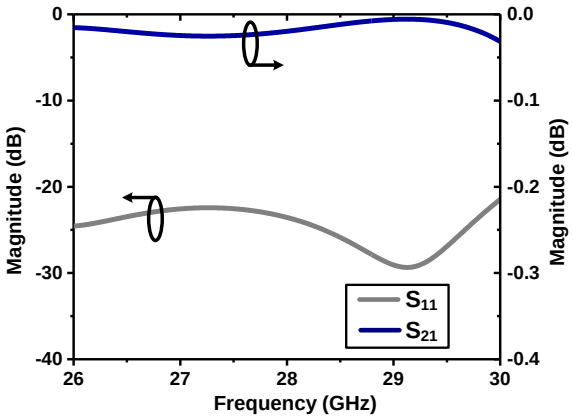

Figure 4.17 Simulated results of the waveguide twist-bend transition

transition has been proposed, combining waveguide bend and twist. It achieves excellent performance over a wide bandwidth. However, the waveguide twist-bend transition lacks compactness and is not suitable for receiver systems. To achieve a compact interconnection, a combined waveguide twist-bend transition [236] is adopted in this work. Figure 4.16 shows the structure of the waveguide twist-bend transition. It is composed of an E-plane waveguide, an H-plane waveguide, and the central waveguide transformer structure. The vertical E-plane waveguide directly combines the horizontal H-plane waveguide with the central waveguide transformer structure for compactness. To extend the bandwidth performance, multi-stage impedance matching circuits are loaded along the E-plane waveguide. Figure 4.17 shows the simulated results of the waveguide twist-bend transition. From Figure 4.17, one can see that over the frequency range from 26-30 GHz, the reflection coefficient is below -21 dB and the insertion loss is better than 0.1 dB. Thus, the proposed waveguide twist-bend transition presents a good performance and is suitable for the proposed receiver system.

4.4.2 SIW-to-E-plane Waveguide transition

To integrate planar circuits, a rectangular waveguide-to- substrate integrated waveguide (SIW) transition is developed and used in the receiver system. Considering easy assembly and loss minimization at the cutting plane, the E-plane waveguide transition is chosen instead of the H-plane waveguide transition. As shown in Figure 4.18, the proposed transition structure consists of three parts, i.e., an E-plane rectangular waveguide, an SIW, and a fin-line structure. The fin-line structure [237] contains two antipodal fins on opposite sides of the substrate, which are placed into

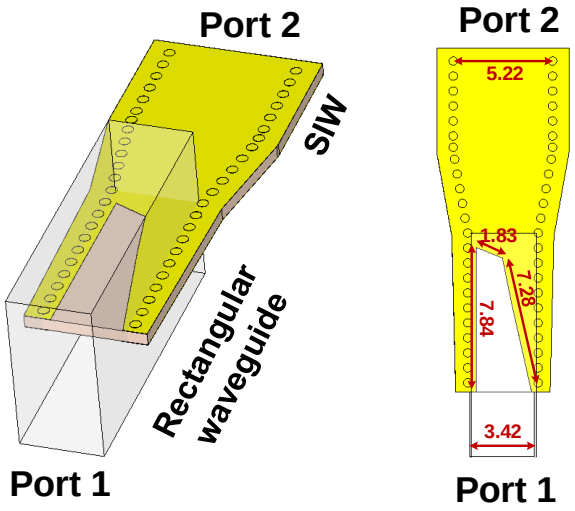

Figure 4.18 Structure of the SIW-to-E-plane waveguide transition

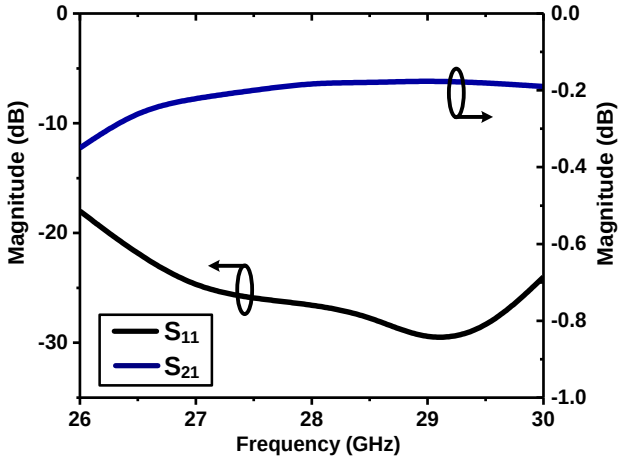

Figure 4.19 Simulated results of the SIW-to-waveguide transition

the center of the rectangular waveguide to obtain maximum coupling. At first, the TE_{10} mode of rectangular waveguide is coupled and transferred into quasi-TEM mode through the tapered aperture. Then, the quasi-TEM mode is transformed into the TE_{10} mode of SIW through a tapered microstrip line structure. By properly adjusting the dimensions of the fin-line structure, the desired impedance-matching performance can be achieved. Figure 4.19 shows the simulated results of the SIW-to-waveguide transition. It can be seen that over the frequency band 26-30 GHz, the reflection coefficient is below -18 dB and the insertion loss is better than 0.4 dB.

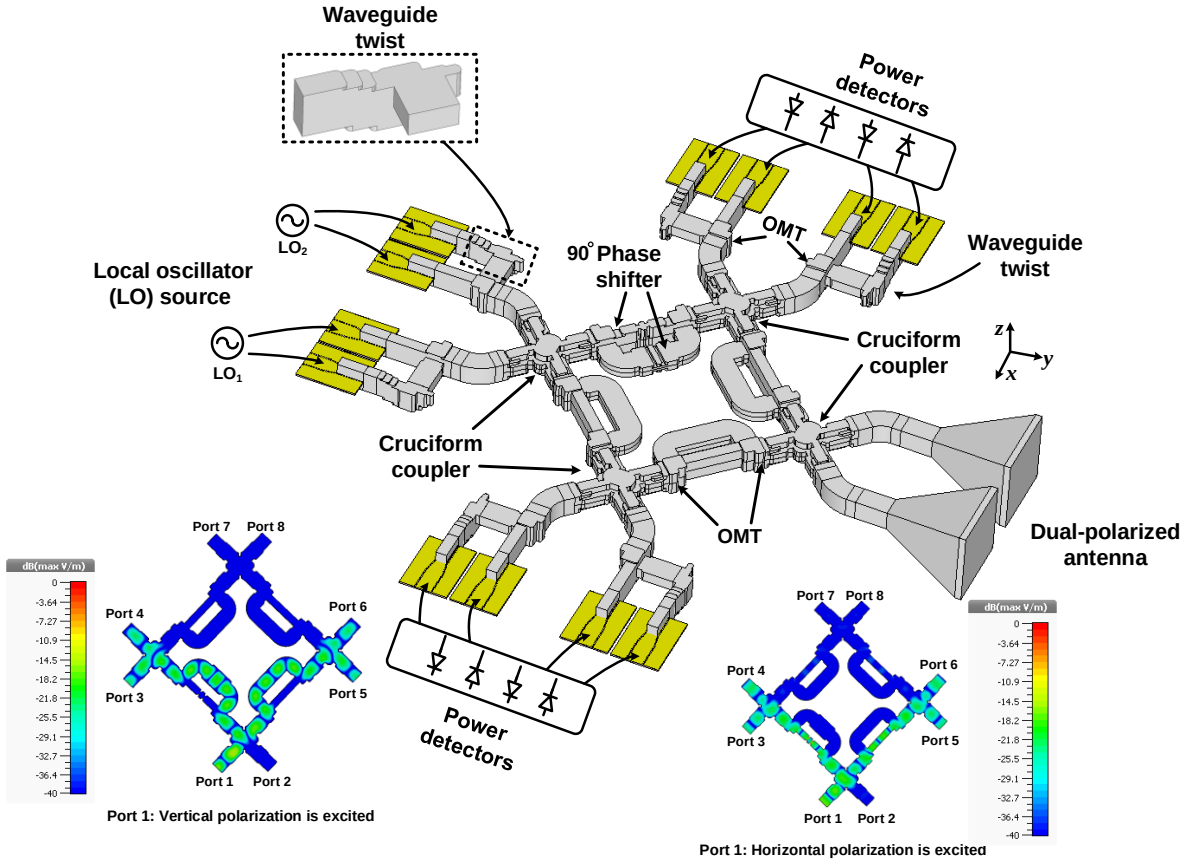

Figure 4.20 The proposed structure assembly of the linear interferometric metallic waveguide receiver that integrates individual component blocks. The input ports connect the two local oscillators and the output ports connect the power detectors. The E-field distributions of the multiport circuit are for the vertical polarization and horizontal polarization, respectively

4.4.3 Device Integration

In this part, the assembly of the proposed metallic waveguide interferometric receiver is presented as shown in Figure 4.20. Four couplers are integrated with the OMTs to equally distribute the amount of power fed by one of the input ports to the output ports, which correspond to -6 dB transmission coefficient between the input port and the output port. A dually polarized phase shifter is loaded to the multiport circuit to provide the additional required 90° phase shift. Figure 4.21 shows the simulated results of the dually-polarized multiport network. It can be seen that over the frequency band from 26 to 28 GHz, the simulated return losses for both polarizations are better than 10 dB and the simulated isolations between ports 1 and 2, for both polarizations, are better

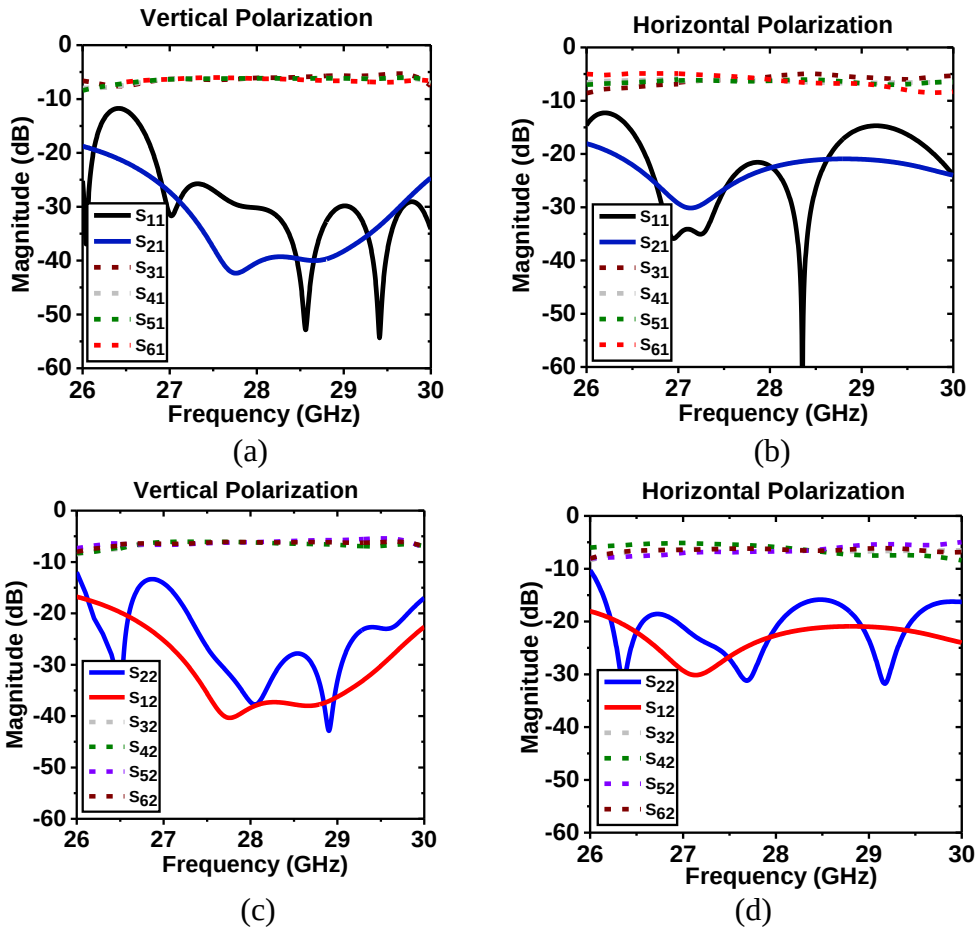

Figure 4.21 Simulated S-parameters of dually-polarized multiport network. (a) Magnitude when exciting vertical polarization from port 1. (b) Magnitude when exciting horizontal polarization from port 1. (c) Magnitude when exciting vertical polarization from port 2. (d) Magnitude when exciting horizontal polarization from port 2

than 15 dB. The insertion losses for both polarizations at port 1 are around −6.6 ± 1.5 dB and the insertion losses for port 2 are around −6.5 ± 1.2 dB. The antennas connect to the multiport circuit for receiving the modulated signals. Considering the physical size and the integration complexity, the H-plane waveguide port of the OMT is transformed into an E-plane waveguide port by the waveguide twist-bend transition to facilitate integration. By this arrangement, the output ports after the OMT preserve the same direction. Then, the SIW-to-E-plane waveguide transition is connected to the output port of the OMT to integrate the planar circuit. The two local oscillators, as the input source, connect to the input ports and the output ports connect to the power detectors. The power detector, as a square-law device, performs the frequency conversion. Therefore, the non-ideal

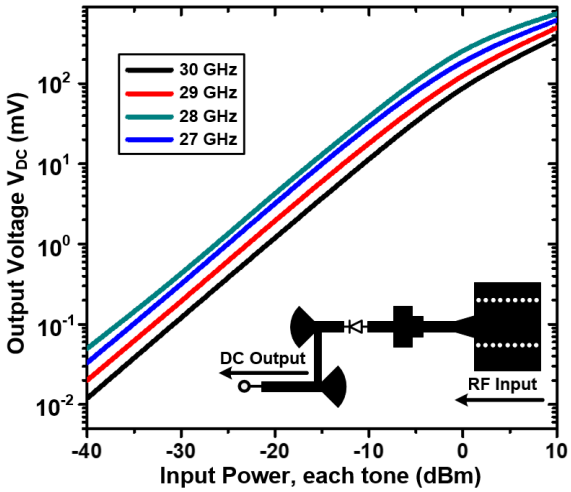

Figure 4.22 Output voltage V_{DC} of the power detector with sweeping input power from -40 to 10 dBm

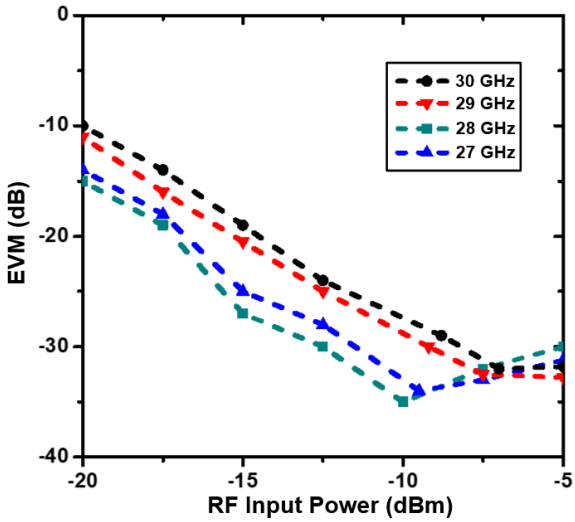

Figure 4.23 The EVM of a 64-QAM signal under different power levels of the power detector as a case study

characteristics of the power detector will directly affect the whole performance of the receiver. Keysight's Advanced Design System (ADS) harmonics balanced (HB) simulator is used to evaluate the power detector performance. Besides, all of the parametric effects such as electrical behaviors and packaging parasitic of the power detector were taken into account. Figure 4.22 shows the simulated output voltage of the detector under different input power levels. It can be seen that the output voltage increase almost linearly with the input power before saturation (about -5 dBm).

The deviation from square-law characteristics will impact the frequency conversion. As a result, the demodulated performance of the receiver will be affected.

A system-level simulation is implemented in ADS to investigate the impact of the non-ideal characteristics of the power detectors on the proposed receiver. As a case study, Figure 4.23 shows the EVM of the demodulated 64-QAM signal under different power levels. It can be observed that the demodulation results are slightly different due to different operating frequencies and input power. For each operating frequency, the EVM improves with increasing of the input power. However, when the power detector saturates near the upper limit of square-law operation, the EVM deteriorates. The receiver can achieve optimal EVM during RF input power of about -10 to -5 dBm. Thus, the receiver performance can be adjusted by controlling the power levels of the power detectors. Besides, it should be mentioned that there are also different techniques of calibration algorithms and IQ regeneration which can be implemented to correct the performance [238], [239].

4.5 Fabrication and measurement results

To validate and evaluate the performance of the proposed interferometric waveguide receiver, an experimental prototype was designed, fabricated, and measured. Figure 4.24 shows a photograph of the fabricated receiver prototype. The receiver is tested with different complex modulated signals using the setup shown in Figure 4.25. Different M-QAM modulated signals are generated using an Arbitrary Waveform Generator (AWG) M8196A at different RF_1 and RF_2 channels, where the operating frequencies (f_{RF1} and f_{RF2}) are 28 and 30 GHz, respectively. Then, the M-QAM modulated signals are sent to the antenna. The gain of the antenna is 20-dBi and the 10 dBm power is transmitted by the transmitter. The communication distance between the transmitter and receiver is set to 1.5 meters. To avoid the interference of the reflected wave, scattering, and diffractions, etc., several absorbing materials are used in the measurement setup. Agilent E8257D PSG Analog Signal Generator and Agilent E8267D PSG Vector Signal Generator, as signal generators, are used to generate the two local oscillator sources. The LO frequencies (f_{LO1} and f_{LO2}) are set to be 28 GHz and 30 GHz and 27 GHz and 29 GHz , respectively, which are applied as the input of the proposed interferometric waveguide receiver. To synchronize the modulated RF and LO signals, a 10-MHz synchronization signal is applied to both the signal generators and analyzers. The demodulated signals after the receiver are captured with a Keysight UXR0702AP Real-Time Oscilloscope (70

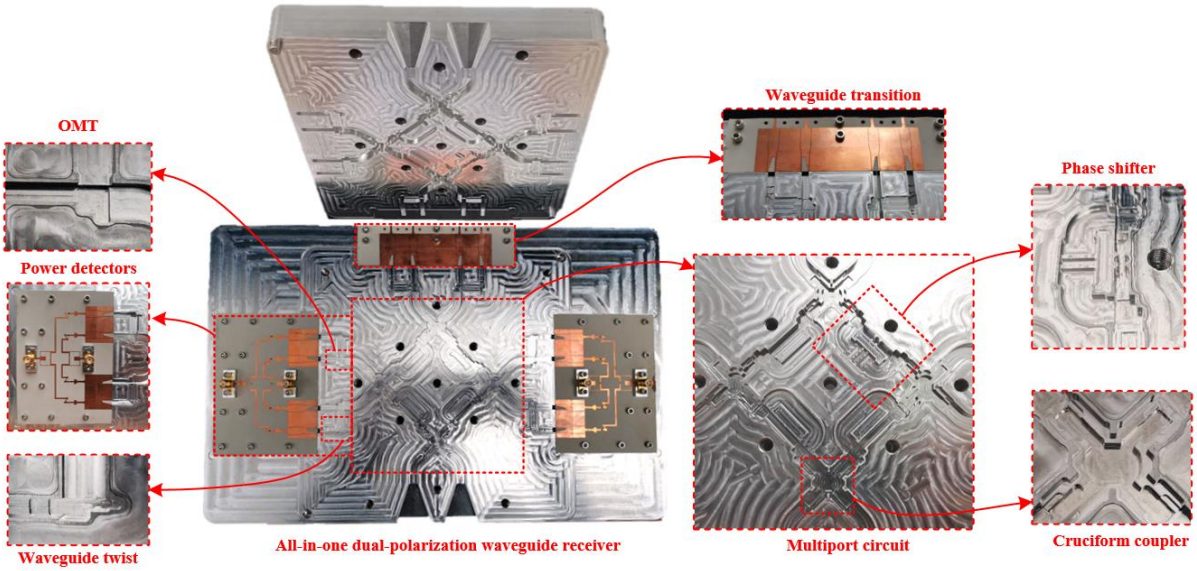

Figure 4.24 Photograph of the fabricated all-in-one interferometric waveguide receiver

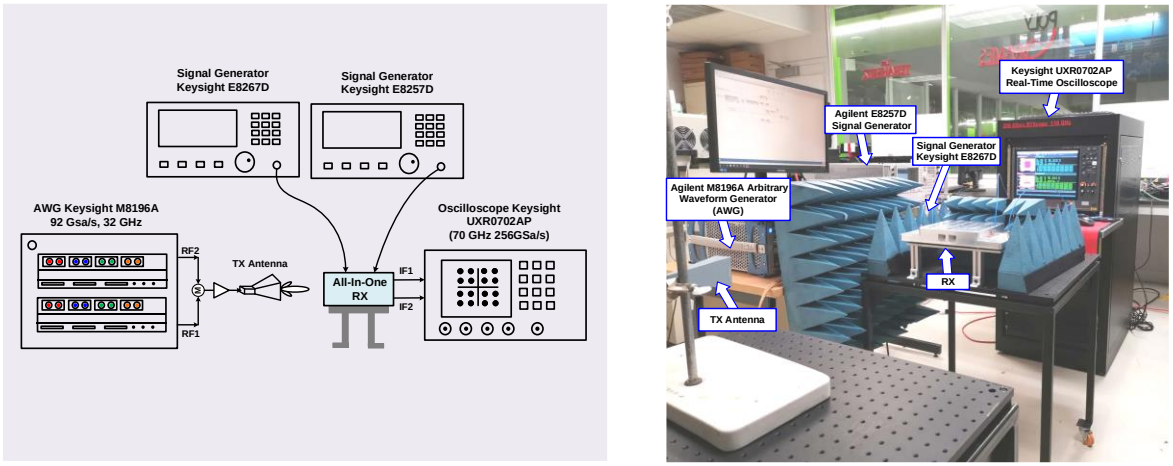

Figure 4.25 Measurement setup for the proposed receiver. (a) The flow chart of test bench. (b) Photograph of measurement setup

GHz, 256Gsa/s, 10-bit). Various modulated signals are visualized with the Keysight Technologies' 89600 VSA software. Tables 4.1 and 4.2 summarize the demodulated signal's constellation and EVM performance for different bit error rates and operating frequencies, where a= 0.35 for the root-raised cosine pulse filter. It can be seen that the proposed receiver can successfully frequency-down-convert with the data rates up to 1.2 Gbps, meanwhile the EVM is better than -27 dB for both polarizations.

Table 4.1 Retrieved constellation diagrams with different orders of modulations (M-QAM) at 28 GHz and 30 GHz

	V-Pol. Constellation	H-Pol. Constellation
RF_1 Channel=28GHz	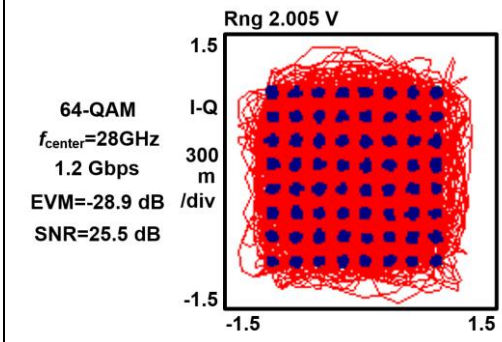	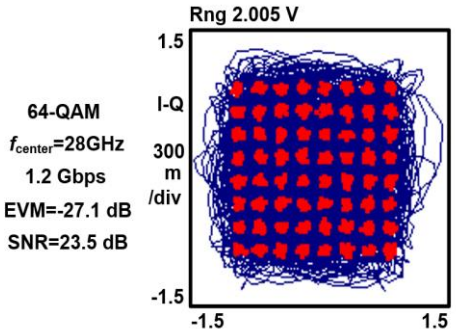
	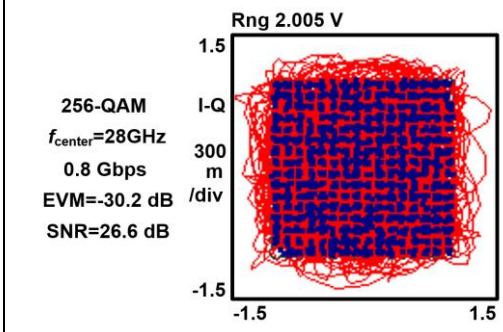	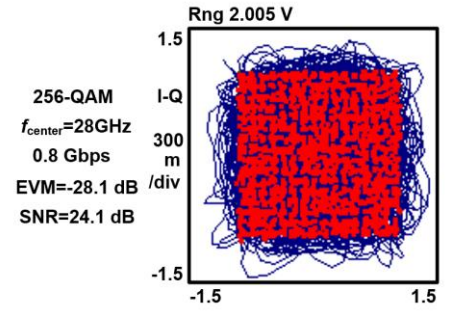
RF_2 Channel=30GHz	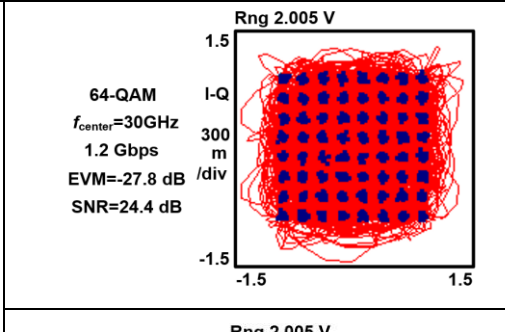	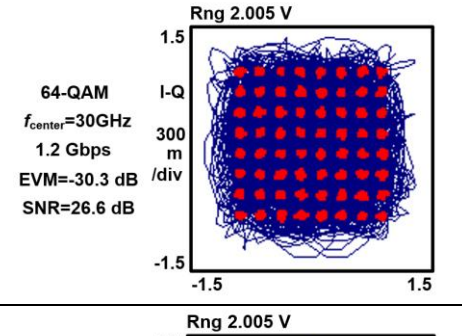
	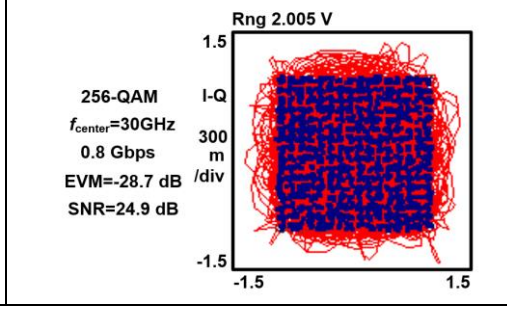	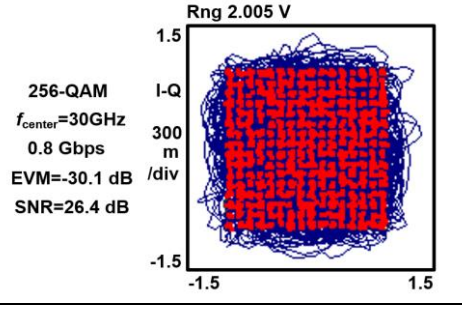

The overall performance of the proposed interferometric waveguide receiver is compared with other state-of-the-art interferometric receivers summarized in Table 4.3. This work based on the square waveguide technology achieves the paralleled-multichannel and dual-polarized operations

Table 4.2 Retrieved constellation diagrams with different orders of modulations (M-QAM) at 27 GHz and 29 GHz

	V-Pol. Constellation	H-Pol. Constellation
RF_1 Channel=27GHz	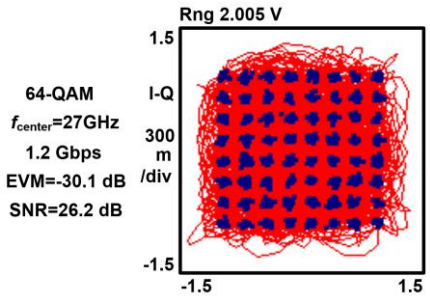	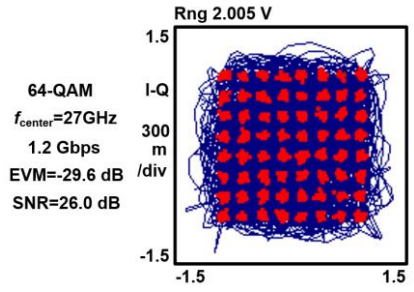
	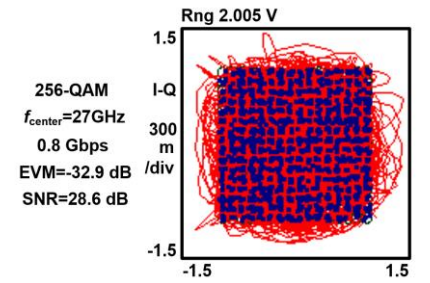	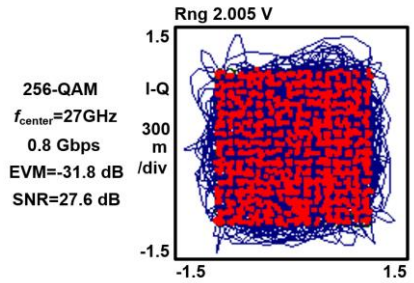
RF_2 Channel=29GHz	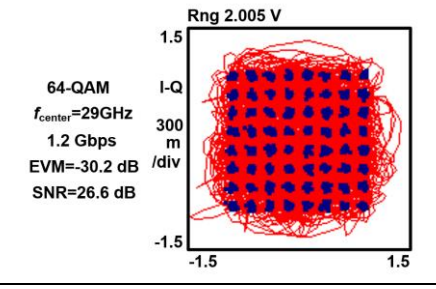	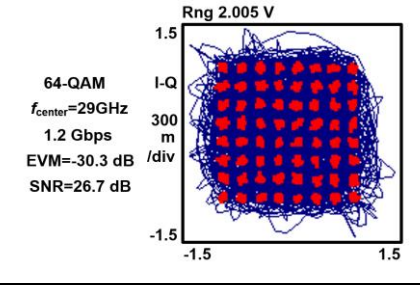
	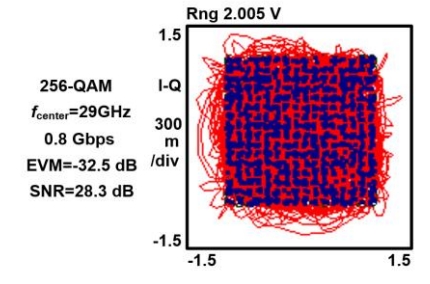	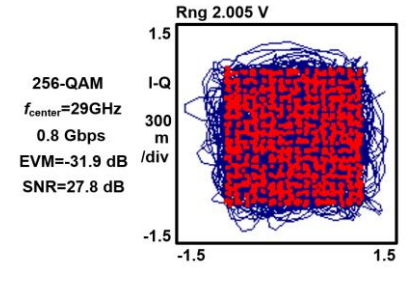

for the first time, which makes it different from previous demonstrations in [74], [76], [79], [95], [124], [191]. Two orthogonal polarizations, namely horizontally polarized wave, and vertically polarized wave, can be excited simultaneously in only a single receiver hardware. Besides, the proposed interferometric receiver achieves a good performance in terms of data rates and EVM free from any post-processing and calibration algorithms as in [76], [124], [191]. Due to the

Table 4.3 Performance summary and comparison with the state-of-the-art interferometric receivers

Ref.	Modulation signal	Frequency (GHz)	Date rate	EVM (dB)	SNR (dB)	Polarization type	Paralleled-Multichannel
[191]	64-QAM	2.6	12 Mbps	-37.72	N.A.	Single-pol.	No
[124]	256-QAM	3.38/3.82	40 Mbps	-33.9	N.A.	Single-pol.	No
[74]	64-QAM	24/28	24 Mbps	-20.0	17.8	Single-pol.	No
[79]	32-QAM	28	5 Mbps	-26.1	20.1	Single-pol.	No
[95]	32-QAM	60	2.5 Gbps	-18.4	N.A	Single-pol.	No
[125]	32-QAM	29	N.A	N.A	N.A	Single-pol.	No
[181]	4-QAM	28	500 Ksps	N.A	N.A	Single-pol	No
[101]	16-QAM	27	40 Mbps	N.A	N.A	Single-pol	No
[104]	4-QAM	27	40 Mbps	N.A	30	Single-pol.	No
This Work	64-QAM	28/30	1.2 Gbps	-28.9v/ -27.8v -27.1h/ -30.3h	25.5v/ 24.4v 23.5h/ 26.6h	Dual-pol.	Yes
	256-QAM	28/30	0.8 Gbps	-30.2v/ -28.7v -28.1h/ -30.1h	26.6v/ 24.9v 24.1h/ 26.4h	Dual-pol.	Yes
	64-QAM	27/29	1.2 Gbps	-30.1v/ -30.2v -29.6h/ -30.3h	26.2v/ 26.6v 26.0h/ 26.7h	Dual-pol.	Yes
	256-QAM	27/29	0.8 Gbps	-32.9v/ -32.5v -31.8h/ -31.9h	28.6v/ 28.3v 27.6v/ 27.8v	Dual-pol.	Yes

metallic waveguide structure, the proposed receiver is more robust than those reported in [74], [76],

[79], [124], [191]. It is worth mentioning that, the structural topology can be further simplified by developing a square waveguide phase shifter. In this case, for example, all OMTs in Figure 4.2(b) would be removed. In addition, by implementing higher-performance dual-polarized waveguide components, the performance of the all-in-one dual-polarization waveguide receiver can be further improved.

4.6 Conclusion

In this paper, an all-in-one waveguide receiver has been proposed, studied, and demonstrated with the square waveguide technique. Due to the capability of handling two orthogonal modes, the proposed receiver increases the supported data rate and enhances the spectral efficiency of the multiport linear interferometric communication systems based on dual polarization. Compared to traditional dually polarized receiver architecture with two separate hardware platforms, the proposed receiver reduces the circuit complexity, size, cost, and power consumption. In addition, thanks to the self-contained dual-input RF channel paths, paralleled-multiband operation can be realized with possible multiband capability, which is suitable for the next generation multifunction wireless applications in a variety of radio propagation environments, such as 5G, 6G, and IoT systems. To evaluate the performance of the proposed receiver, various digitally modulated signals have been successfully demodulated and demonstrated experimentally at different data rates. All demodulated results have confirmed the excellent performance. Thus, the proposed waveguide receiver can be used in multifunction, multi-band, and dual-polarized wireless systems.

CHAPTER 5 ARTICLE 3: WAVEGUIDE RECEIVER ARRAY FOR JOINT COMMUNICATION, SENSING, AND POWER TRANSFER SYSTEMS

Jie Deng, Pascal Burasa, Seyed Ali Keivaan, and Ke Wu

Published in: IEEE Transactions on Microwave Theory and Techniques

Publication date: December 04, 2024

Abstract: This article introduces, for the first time, a waveguide receiver array tailored for joint communication, sensing power, and transfer systems. The receiver utilizes an orthomode transducer (OMT) to achieve polarization diversity, effectively doubling channel capacity and enhancing spectral efficiency without adding circuit complexity or increasing the number of components compared to traditional single-polarization designs. In addition, the receiver integrates a differential rectifier, fabricated using 65-nm bulk CMOS technology, to enable wireless power transfer. This integration allows the system to support both wireless communication and energy harvesting simultaneously. A mathematical model is developed to guide the receiver's design. To validate the concept, a prototype receiver is fabricated and tested. The receiver successfully generates dc power from a 28-GHz wireless power transfer signal, achieving a peak power conversion efficiency (PCE) of up to 18%. Furthermore, it successfully demodulates a range of M-quadrature amplitude modulation (QAM) signals, demonstrating the effectiveness of the proposed design. These results position the multifunctional receiver array as a promising solution for millimeter-wave Internet of Things (IoT) applications.

Index Terms: CMOS rectifier, dual-polarization, energy harvesting, interferometric technology, metallic waveguide, multifunction, receiver arrays, sensing systems, wireless communication systems.

5.1 Introduction

Millimetre wave (mmW) technology has attracted significant attention from both academia and industry due to its broadband spectrum resources and high spatial resolution, among many other outstanding features. It is anticipated that numerous emerging applications, including multimedia

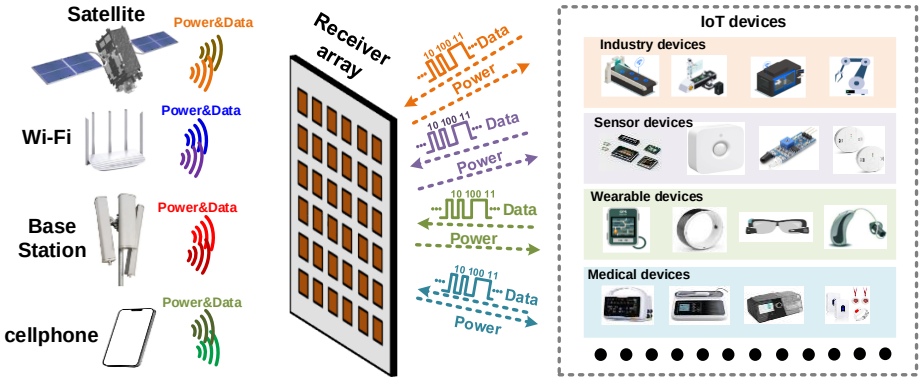

Figure 5.1 Illustration of future mm-Wave waveguide receiver array for IoT-served systems, where all kinds of wireless senor nodes or networks and mmW identification tags are massively deployed in our environment

services, 3D geolocation mapping, virtual reality, and Internet of Things (IoT), will be widely developed and empowered by mmW [18], [20], [46], [168], [170], [213], [240], [241]. To support these versatile services and applications, the next-generation wireless network is required to achieve an agile and reliable connectivity with high-speed data transmission, low latency, high system capacity, and high security. A widely used technique for enhancing the speed and capacity of mmW wireless communication systems is frequency-diversified multi-input and multi-output (MIMO) [32], [182]. This technique has been extensively employed in transmitter and receiver arrays to boost the throughput or enhance frequency diversity of an entire system. In this connection, large-scale antenna arrays are used in the MIMO system to improve channel capacity by creating independent channels in a multipath-rich communication environment. However, these systems are also vulnerable to interference in the analog/RF front-end domain.

With advancements in the development of innovative low-power receiver architectures, future emerging wireless systems will benefit from multiple radio and sensor coexisting operations (multifunction) in an autonomous or semi-autonomous manner such as joint radio-communication (RadCom) or integrated sensing and communication (ISAC) systems, which were proposed, demonstrated and discussed in [22], [26], and [23]. A seamless high-density integration and deployment of such receiver systems will obviously expect the fusion and interplay of energy-reduced, performance-enhanced, and function-diversified features [242], [243]. For example,

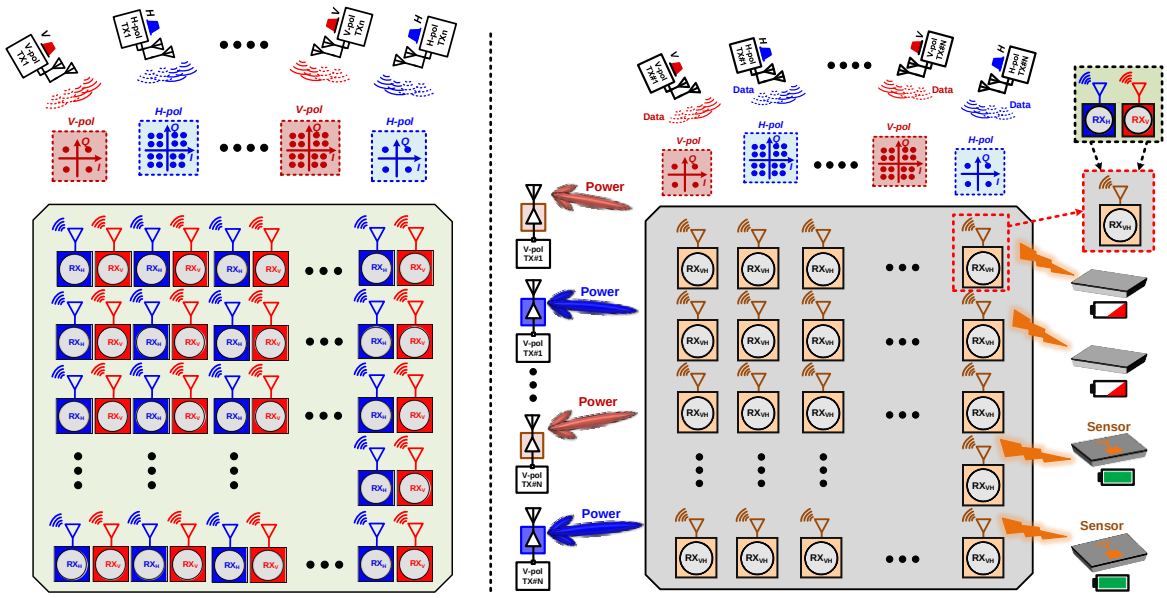

(a) (b)

Figure 5.2 Illustration diagrams of a polarized-diversified receiver system. (a) Conventional dual-polarization receiver array. (b) Proposed multifunctional dual-polarization receiver array enabling wireless communication and power transfer capabilities

Figure 5.1 illustrates a potential mmW multifunctional receiver array for IoT-served systems, where wireless sensor nodes or networks and mmW identification tags are massively deployed [175]. Such a receiver aims to minimize power consumption and activate an autonomous network while autonomously supporting wireless energy harvesting, data reception, storage, processing, and communication.

To further enhance the performance of wireless systems, polarization diversity is introduced into the receiver system, where two orthogonal polarization modes, i.e., the H-polarization (H-pol.) and V-polarization (V-pol.) modes, are enabled. Thus, the receiver can simultaneously support independent data streams at the same carrier frequency, as illustrated in Figure 5.2(a). However, this increase in channel capacity comes at the cost of a higher number of receiving paths as two receiving blocks are typically required to support the orthogonal polarization modes. As the system scale expands, the number of circuit blocks increase significantly. As such, the power consumption, cost, and size of the system are also increased, which will become an obstacle for a wide-spread adoption and/or a large-scale deployment within future wireless communication and sensing systems.

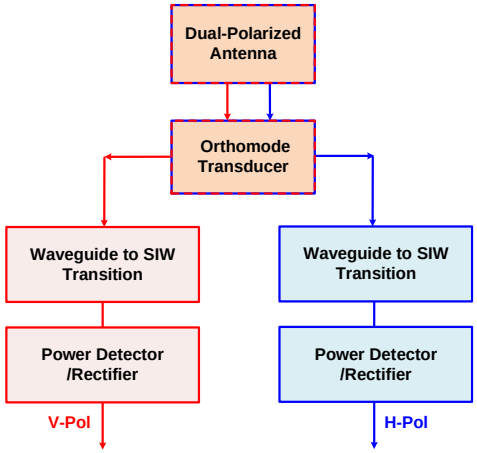

Figure 5.3 Block diagram of the proposed waveguide receiver unit-cell

In this paper, a multifunctional waveguide receiver array for wireless power transfer, communication, and sensing systems, as conceptually illustrated in Figure 5.2(b), is proposed to address the aforementioned issues. It can be seen that the proposed receiver benefits from the use of an orthogonal mode transducer (OMT), which enables dual-polarization features. Both horizontal and vertical polarizations are integrated into a single receiver block, instead of two as discussed before. By doing so, it not only reduces size and complexity but also lowers cost and power consumption. Furthermore, each unit-cell of the receiver array can be dynamically allocated to synthesize channels for data reception, sensing, and energy harvesting. To achieve the function of wireless power transfer, a CMOS differential rectifier can be integrated into the receiver unit. The recovered data and generated dc power from different receiver units can be processed concurrently, resulting in high capacity and efficient power and data management. Interferometric techniques [19], [70], [74], [76], [79], [92], [95], [96], [104], [107], [114], [124], [125], [142], [145], [147], [150], [151], [152], [154], [187], [224], [244], [245], [246], [247] are employed in the proposed receiver array to further reduce the complexity, cost, and power consumption of the system. As a proof of concept, a prototype OMT receiver array is designed, fabricated, and measured. The measured results validate the proposed scheme and demonstrate its excellent performance.

This paper is an extension of [21] and presents more details, analysis, and design insights. Section 5.2 describes the receiver unit's structure, including the dual-polarization antenna, OMT, waveguide transition, power detector, and rectifier. In Section 5.3, an entire receiver array is

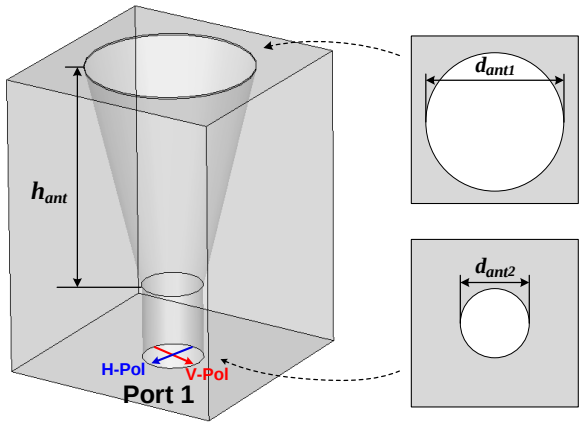

Figure 5.4 Three-dimensional structure of dual-polarization waveguide antenna, where h_{ant}=30 mm, d_{ant1}=11 mm, d_{ant2}=4 mm

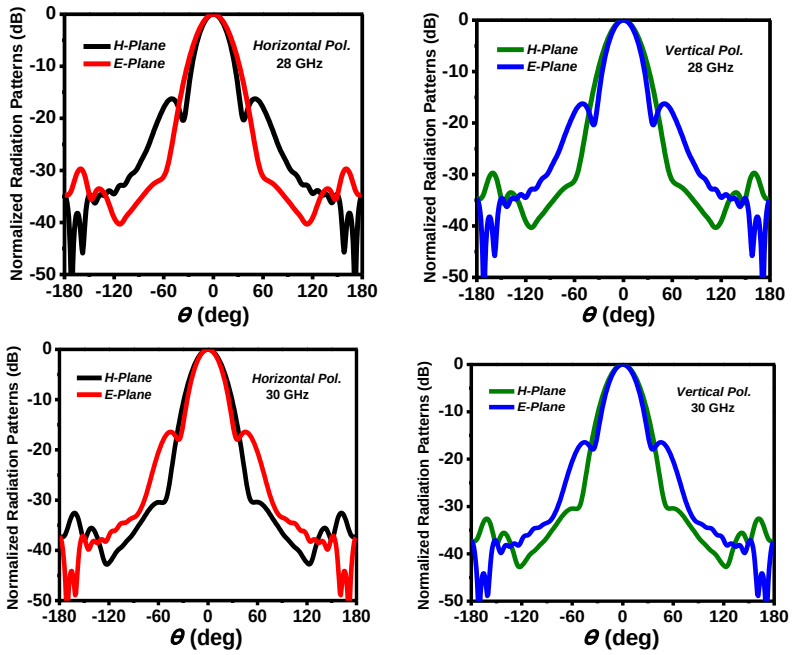

Figure 5.5 Simulated radiation pattern of dual-polarization waveguide antenna

designed based on the previous receiver unit. In Section 5.4, the performance analysis and experimental results are given. Besides, a comparison of performances with previously reported receivers is provided as well. Finally, the conclusion is drawn in Section 5.5.

5.2 Receiver unit: detail structure design

The receiver array is composed of multiple array elements and its unit-cell is shown in Figure 5.3. As depicted in the figure, the dual polarization antenna is used to interconnect the OMT. Then, the

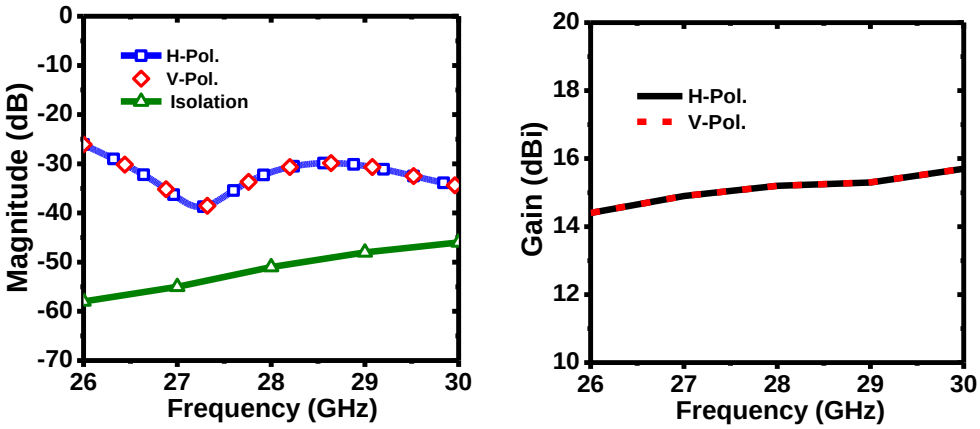

(a) (b)

Figure 5.6 Simulated results of dual-polarization waveguide antenna. (a) Refection coefficient and isolation. (b) Antenna gain

two output ports of the OMT are connected to power detector or rectifier through waveguide-to-SIW transition, respectively. The main design concept is to use the OMT to incorporate the orthogonal polarizations in a single-modular hardware. Additionally, the proposed unit-cell topology features an inline vertical arrangement to enhance structural compactness. The following sections discuss the detailed structure and the design of each individual part.

5.2.1 Dual-polarization antenna

A dual-polarization antenna should be easily integrated with the OMT to separate the two orthogonal polarization signal paths. Therefore, a dual-polarization waveguide horn antenna is adopted in this work. Figure 5.4 shows the configuration of this antenna. It consists of a horn radiation port and a circular waveguide port. The advantages of such an antenna include its simple structure and ease of manufacturing. It should be mentioned that any other dual-polarization antenna type can also be employed. Herein, the horn waveguide antenna is chosen as a compromise for our preliminary verification.

Figure 5.5 shows the simulated radiation patterns for both orthogonal polarizations, which presents the radiation performance over its operating frequency band. Figure 5.6 shows the simulated S-parameters and gains of the dual-polarization antenna. The simulated reflection coefficient is less than -25 dB for both H- and V-polarizations within the 26 to 30 GHz frequency range. The

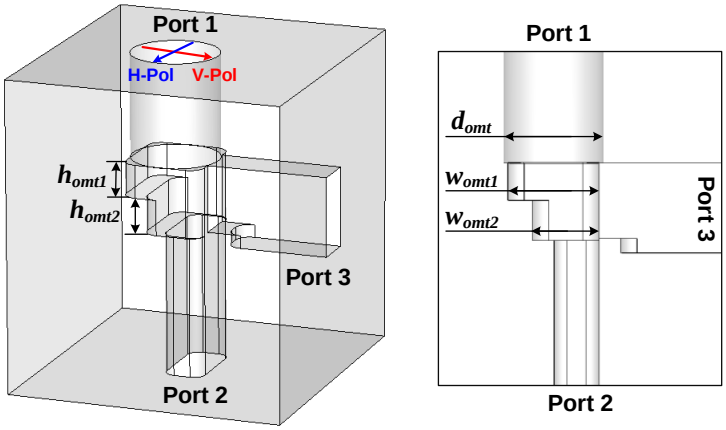

(a) (b)

Figure 5.7 Three-dimensional structure of OMT, where d_{omt}=4 mm. h_{omt1}=2.85 mm. h_{omt2}=3.04 mm. w_{omt1}=6.97 mm. w_{omt2}=5.09 mm

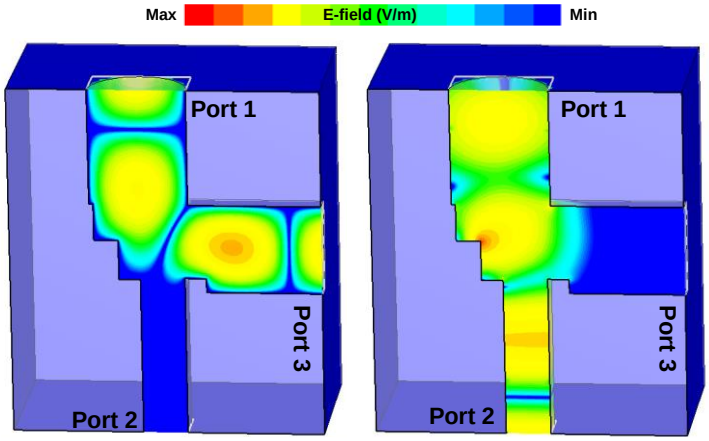

(a) (b)

Figure 5.8 E-field distribution of OMT. (a) H-polarization mode. (b) V-polarization mode

simulated isolation is better than 47 dB. The simulated average gain is around 15.5 dBi for both orthogonal polarizations over the entire operating range.

5.2.2 Orthomode transducer (OMT)

To separate the two orthogonal polarization signals received from the dual-polarization antenna, an OMT is used in this design. There are several possible waveguide OMT geometries, offering different advantages in bandwidth, isolation, cross-polarization, and manufacturability [248], [249], [234]. Taking into account the size, cost, and complexity of the proposed receiver array, an asymmetric OMT geometry is adopted in this work.

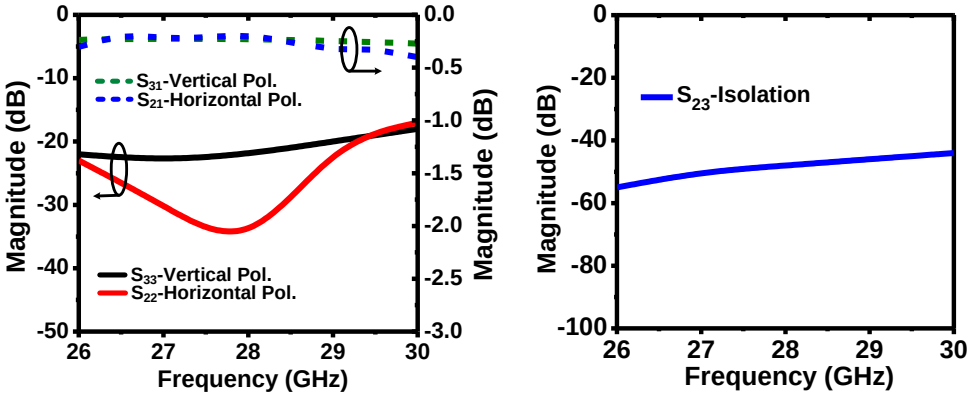

(a) (b)

Figure 5.9 Simulated results of OMT. (a) Refection coefficients and insertion losses. (b) Isolation between ports 2 and 3

In general, the septum and thin iris are utilized in OMT to achieve required polarization separation. However, it is difficult to fabricate these small feature structures in mmW band. Instead, a simple OMT structure [250], as illustrated in Figure 5.7, is used. This OMT is composed of a common circular waveguide port and two rectangular waveguide ports. Two rectangular waveguide ports are orthogonal to each other. The entire structure of OMT forms a branching T-junction shape. However, such a structure introduces the geometrical variation and discontinuities in the central junction region, which can affect the bandwidth and polarization performance. To address these issues, multistage waveguide steps are introduced in the central junction region to realize the required polarization isolation and impedance matching performance.

Figure 5.8 shows the simulated E-field distributions of the OMT for two orthogonal polarization modes. It can be observed that when port 1 excites an H-polarization signal, its signal enters port 3. Conversely, when port 1 excites a V-polarization signal, its signal enters port 3. The simulated performances of the proposed OMT are shown in Figure 5.9. The reflection coefficient for V-polarization is less than -18 dB while the reflection coefficient for H-polarization is lower than -19 dB over the 26 to 30 GHz frequency range. The insertion losses for V-polarization and H-polarization are better than 0.4 dB. The isolation between two orthogonal polarization modes is better than 45 dB. It should be noted that there are small deviation errors in the isolation of the horn antenna and the OMT, which is caused by the numerical error simulation.

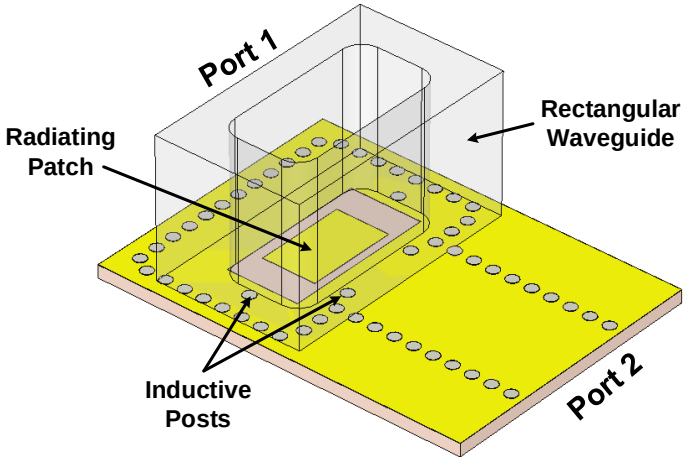

(a)

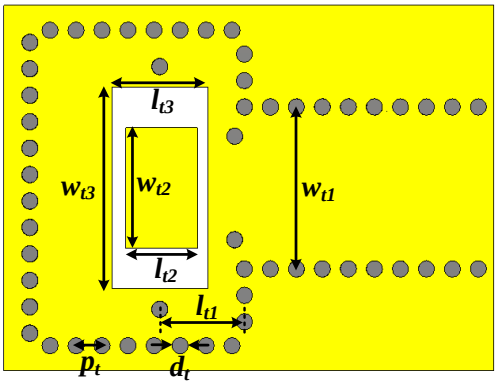

(b)

Figure 5.10 Rectangular waveguide to SIW transition, where p_t=0.8 mm, d_t=0.5 mm, w_{t1}=4.9 mm, l_{t1}=2.6 mm, w_{t2}=3.6 mm, l_{t2}=2.2 mm, w_{t3}=6.1 mm, l_{t3}=2.9 mm. (a) Three-dimensional structure view. (b) Vertical view

5.2.3 Waveguide-to-SIW transition

A waveguide-to-substrate integrated waveguide (SIW) transition is necessary to integrate the planar circuit of the receiver array. Considering the limitations of integration and assembly, single-layer right-angle waveguide-to-SIW transition [251], [252], [253] is adopted instead of in-line transitions. Figure 5.10 shows the geometrical configuration of the proposed transition. It can be seen that the rectangular waveguide port is vertically mounted on the top surface of SIW to form a right-angle transition. To realize a good coupling between the rectangular waveguide and SIW, an aperture-coupled patch antenna structure is utilized, which facilitates the coupling from the TE_{10}

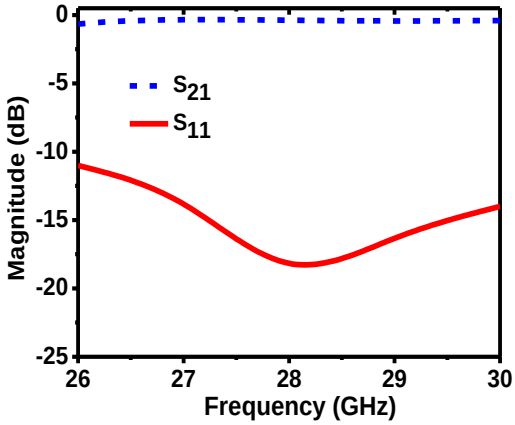

Figure 5.11 Simulated results of rectangular waveguide to SIW transition

mode of the rectangular waveguide to the TE_{10} mode of the SIW. Besides, to expand the bandwidth performance, the inductive posts are symmetrically loaded around the patch antenna structure. By adjusting these inductive posts, the coupling between the SIW port and the rectangular waveguide port can be enhanced.

Figure 5.11 shows the simulated results of the designed right-angle waveguide-to-SIW transition. It can be observed that over the frequency range from 26 to 30 GHz, the reflection coefficient is below -12 dB. The insertion loss of the transition is less than 0.5 dB.

5.2.4 Power detector

The power detector is integrated into the receiver array to perform the frequency conversion. Figure 5.12 shows the geometrical structure of the proposed power detector, which consists of a matching circuit, zero bias Schottky diode, and a low pass filter. The RF signal passes through the OMT and enters the power combiner, while the LO signal is injected through another port of the power combiner. Then, both RF and LO signals are combined and applied to the power detector. The zero bias Schottky diode is adopted in the design, thereby avoiding the basing circuit and related noise, as well as simplifying the circuit complexity. To reduce the reflection caused by the diode and increase the detector efficiency, an input matching circuit is introduced in the power detector. Then, a low pass filter is loaded after the diode to suppress the high-order harmonic signals and extract low-frequency signals.

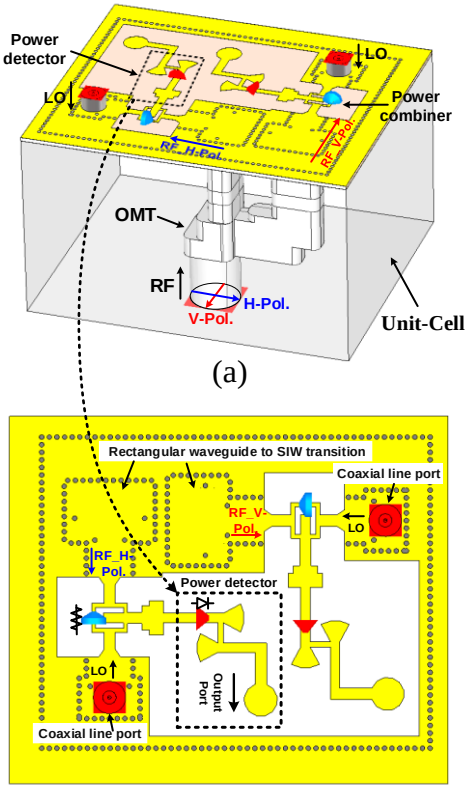

Figure 5.12 Geometry structure of the proposed power detector and its input path of RF and LO signals. (a) Three-dimensional structure view. (b) Vertical view

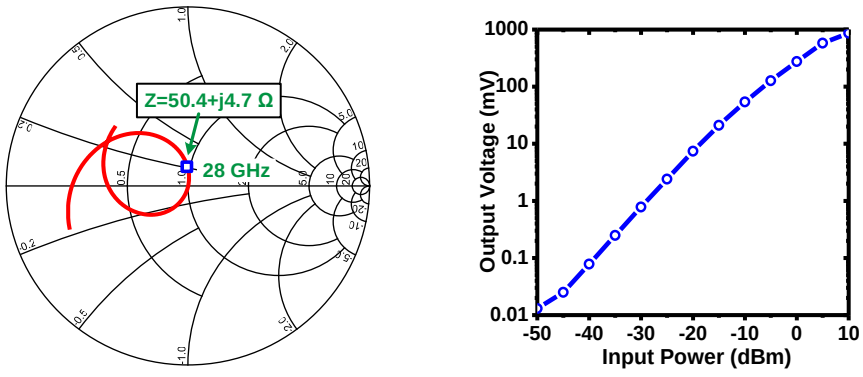

Figure 5.13 (a) Smith chart diagram of the proposed power detector. (b) Output voltage of the proposed power detector with sweeping input power from -50 to 10 dBm

As a square-law device, the nonlinear characteristics of the power detector directly affects the demodulation performance of the receiver array. Therefore, Keysight Advanced Designed System (ADS) harmonic balance (HB) simulator is used to evaluate the detection characteristics. The

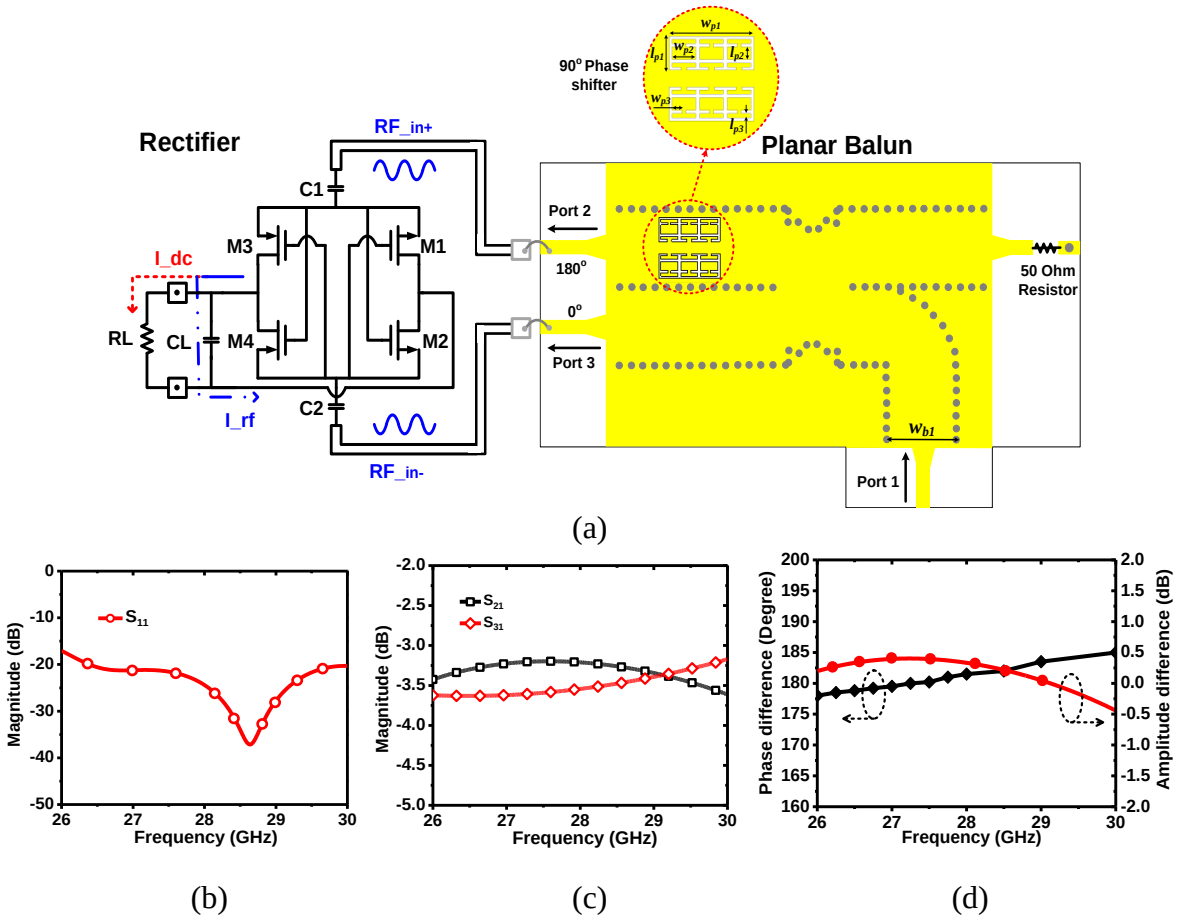

Figure 5.14 Configuration of the proposed CMOS rectifier and planar balun, where w_{p1}=4.62 mm, w_{p2}=1.28 mm, w_{p3}=0.54 mm, l_{p1}=1.73 mm, l_{p2}=0.65 mm, l_{p3}=0.22 mm. (b) Simulated refection coefficient of the balun. (c) Simulated transmission coefficients of the balun. (d) Simulated amplitude difference and phase difference of the balun

simulated Smith chart diagram of the power detector is shown in Figure 5.13(a). The proposed power detector exhibits a good matching performance with the impedance of z_i=50.4+j4.7 Ohm at 28 GHz. Figure 5.13(b) shows the simulated output voltage with different input powers. It can be observed that the output voltage increases almost linearly with increasing input power from -40 to 0 dBm. When the input power is greater than 0 dBm, the output voltage begins to undergo from the square-law region to the linear-law detection response. The best working condition for the square law detection operation is around -5 dBm input power. A deviation from the square-law characteristics of the power detector will affect the demodulation performance of the receiver.

5.2.5 Rectifier

The power detector is integrated into the

To verify the capability of wireless energy harvesting, a rectifier is developed and integrated into the proposed receiver architecture. Figure 5.14(a) shows the structure of the rectifier and the balun, where the balun is used to transform an unbalanced signal to a balanced signal for minimizing the common mode noises. The balun consists of a hybrid coupler and a 90° phase shifter. The phase shifter, based on a complementary split-ring resonator (CSRR) [254], [255], [256] generates slow-wave effect along the transmission line (TL). Therefore, the CSRR changes the propagation constant of the TL and realizes a stable 90° phase shifting with the same physical length. One of the output ports of the coupler is connected with the input of the phase shifter. In such a simple way, when port 1 is excited, two balanced output signals are obtained. Figures 5.14(b)-(d) show the simulated results of the proposed balun. It can be seen that within the frequency range of 26 to 30 GHz, the reflection coefficient at the input port (S_{11}) is around -20 dB and the transmissions (S_{21} and S_{31}) steadily fluctuate around 3.5±0.25 dB. The amplitude difference is around ±5 dB and the phase difference is around 180°±5°. Therefore, the proposed balun achieves a good performance.

The rectifier is driven by a balun with a differential input signal. A standard 65-nm bulk CMOS process is employed to implement the rectifier. Figure 5.14(a) shows the schematic of the rectifier. A cross-coupled bridge topology in [173] is utilized in the design. The transistors M1, M2, M3, and M4 periodically supply DC energy to the output load (RL). The rectifier makes use of a differential charging mechanism to concurrently minimize leakage reverse current while preserving small on-resistance, therefore achieving a high-power conversion efficiency even at mmW frequencies. For example, over the positive cycle of the incoming RF signal, transistors M2 and M3 are in saturation mode and their pulsed currents charge the output capacitor CL. At the same time, leakage current is minimized by forcing the transistors M1 and M4 in off-mode by pulling down and up, respectively, their gate voltages. Similarly, during the negative cycle of the RF signal, CL is charged by M1 and M4 while M2 and M3 are also forced into the off-mode. Thus, a high-efficiency CMOS rectifier for mmW-to-dc energy conversion can be achieved.

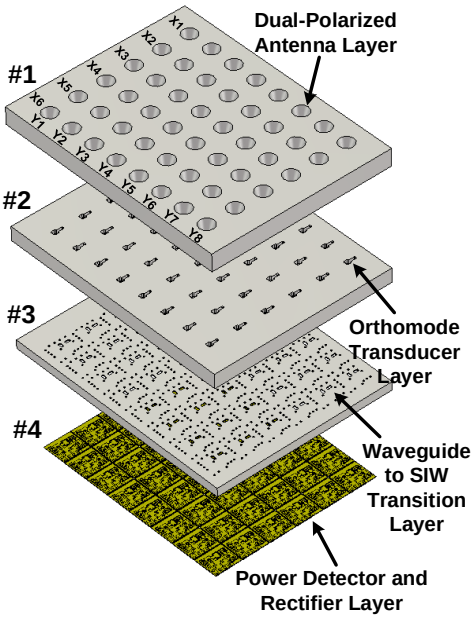

. Figure 5.15 Explosion view of the proposed waveguide receiver array

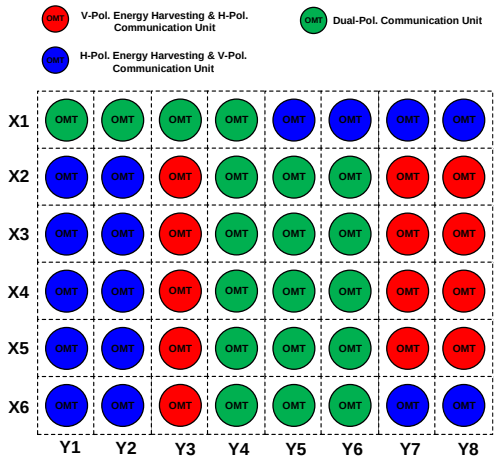

Figure 5.16 Various activated RX units enable wireless communication and energy harvesting

5.3 Receiver arrays

According to the illustrated Figure 5.2, a 6x8 receiver array is implemented to demonstrate the proposed concept. The configuration of the receiver array is shown in Figure 5.15. It can be seen that the receiver array consists of a dual-polarization layer, an OMT layer, a waveguide-to-SIW transition layer, and a power detector/rectifier layer, where each layer has different functionality. The printed circuit board of the bottom layer serves as a carrier for the power detector and the

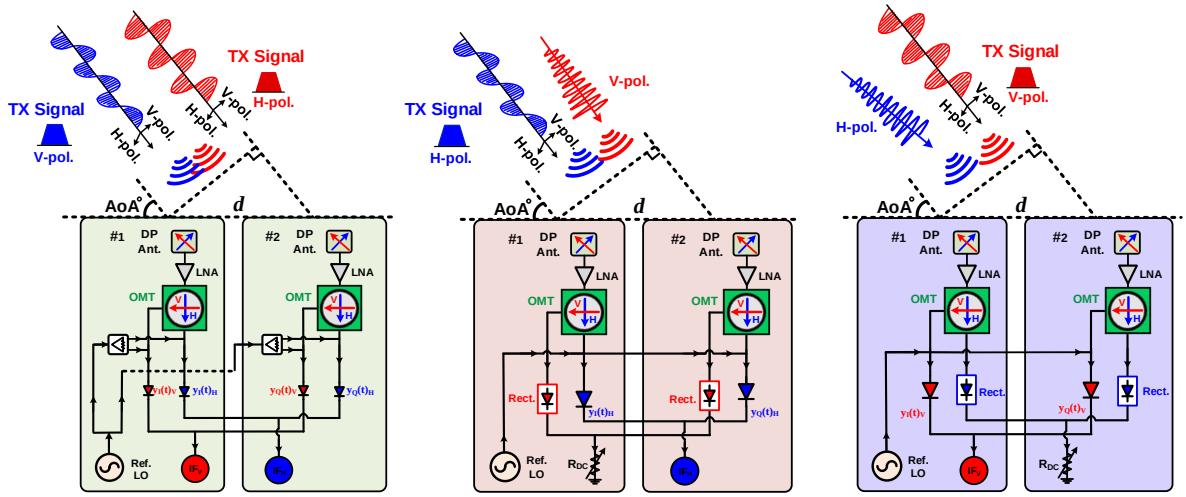

(a) (b) (c)

Figure 5.17 Schematic of the waveguide receiver unit-cell. (a) Dual-polarization demodulation unit-cell. (b) H-pol. demodulation and V-pol energy harvesting unit-cell. (c) V-pol. demodulation and H-pol energy harvesting unit-cell

rectifier, activating the wireless communication and energy harvesting. All layers are vertically stacked up and integrated into a compact structure. Figure 5.16 illustrates the assigned RX units of the waveguide receiver array, designed for energy harvesting and wireless communication. The red unit cell is allocated for V-Pol energy harvesting and H-Pol wireless communication, while the blue unit cell is designated for H-Pol energy harvesting and V-Pol wireless communication. The green unit cell supports both H-Pol and V-Pol wireless communication.

In this work, the interferometric technique is adopted in the receiver array. To enable the demodulation of the signals, two unit-cells are required to be activated simultaneously. Figure 5.17 illustrates three possible combinations of two kinds of receiver unit-cells. For instance, the architecture of Figure 5.17(a) is used to enable dual-polarization demodulation. The architectures of Figures 5.17(b) and (c) are used to achieve single-polarization demodulation and energy harvesting, simultaneously. As illustrated in Figure 5.17(a), the transmitted modulated dual-polarization RF signals can be expressed as:

$$\begin{cases} S_{RF(\mathrm{V})}(t) = a_{RF(\mathrm{V})} \cdot a_{(\mathrm{V})}(t) e^{\mathrm{j}(w_{RF(\mathrm{V})} t + \theta_{(\mathrm{V})}(t))} & (5.1) \\ S_{RF(\mathrm{H})}(t) = a_{RF(\mathrm{H})} \cdot a_{(\mathrm{H})}(t) e^{\mathrm{j}(w_{RF(\mathrm{H})} t + \theta_{(\mathrm{H})}(t))} & (5.2) \end{cases}$$

where $a_{RF(V)}$ is the amplitude of the vertical-polarization signal. $a_{(V)}$ and $\theta_{(V)}(t)$ are the modulated amplitude and phase of the vertical-polarization baseband signal, respectively. $a_{RF(H)}$ is the amplitude of the horizontal-polarization signal. $a_{(H)}$ and $\theta_{(H)}(t)$ are the modulated amplitude and phase of the horizontal-polarization signal, respectively. The injected dual-polarization LO signals can be expressed as:

$$\begin{cases} S_{LO(V)}(t) = a_{LO(V)} \cdot (t) e^{jw_{LO(V)}(t)} & (5.3) \\ S_{LO(H)}(t) = a_{LO(H)} \cdot (t) e^{jw_{LO(H)}(t)} & (5.4) \end{cases}$$

where $a_{LO(V)}$ is the amplitude of the vertical-polarization LO signal. $a_{LO(H)}$ is the amplitude of the horizontal-polarization LO signal. Then, the modulated signal and LO signal are set to enter the power detector. The output voltage of the power detector is proportional to the square magnitude of their input signal. Therefore, the output voltages can be written as:

$$\begin{cases} y_I(t)_V = \kappa (a_{LO(V)})^2 \cdot \left[1 + 2 \frac{a_{RF(V)}}{a_{LO(V)}} a_{(V)}(t) \cos(\Delta\theta_{(V)}(t)) + (\frac{a_{RF(V)}}{a_{LO(V)}})^2 a_{(V)}(t)^2 \right] & (5.5) \\ y_I(t)_H = \kappa (a_{LO(H)})^2 \cdot \left[1 + 2 \frac{a_{RF(H)}}{a_{LO(H)}} a_{(H)}(t) \cos(\Delta\theta_{(H)}(t)) + (\frac{a_{RF(H)}}{a_{LO(H)}})^2 a_{(H)}(t)^2 \right] & (5.6) \end{cases}$$

$$\begin{cases} y_Q(t)_V = \kappa (a_{LO(V)})^2 \cdot \left[1 + 2 \frac{a_{RF(V)}}{a_{LO(V)}} a_{(V)}(t) \cos(\Delta\theta_{(V)}(t) + \Delta\phi) + (\frac{a_{RF(V)}}{a_{LO(V)}})^2 a_{(V)}(t)^2 \right] & (5.7) \\ y_Q(t)_H = \kappa (a_{LO(H)})^2 \cdot \left[1 + 2 \frac{a_{RF(H)}}{a_{LO(H)}} a_{(H)}(t) \cos(\Delta\theta_{(H)}(t) + \Delta\phi) + (\frac{a_{RF(H)}}{a_{LO(H)}})^2 a_{(H)}(t)^2 \right] & (5.8) \end{cases}$$

Where $\Delta\Phi$ is the phase difference of the incoming signals between two unit-cells. By adjusting the incident angle of the incoming signal and increasing the LO signal power, the terms of $(a_{RF(V)}/a_{LO(V)})^2$ and $(a_{RF(H)}/a_{LO(H)})^2$ in (5.5), (5.6), (5.7), and (5.8) can be removed. The output voltages of the power detector [188] can be expressed as:

$$\begin{cases} y_I(t)_V = \kappa (a_{LO(V)})^2 \cdot \left[1 + 2 \frac{a_{RF(V)}}{a_{LO(V)}} a_{(V)}(t) \cos(\Delta\theta_{(V)}(t)) \right] & (5.9) \\ y_I(t)_H = \kappa (a_{LO(H)})^2 \cdot \left[1 + 2 \frac{a_{RF(H)}}{a_{LO(H)}} a_{(H)}(t) \cos(\Delta\theta_{(H)}(t)) \right] & (5.10) \end{cases}$$

$$\begin{cases} y_Q(t)_{\mathrm{V}} = \kappa(a_{\mathrm{LO(V)}})^2 \cdot \left[1 - 2\dfrac{a_{\mathrm{RF(V)}}}{a_{\mathrm{LO(V)}}} a_{(\mathrm{V})}(t)\sin(\Delta\theta_{(\mathrm{V})}(t))\right] & (5.11) \\ y_Q(t)_{\mathrm{H}} = \kappa(a_{\mathrm{LO(H)}})^2 \cdot \left[1 - 2\dfrac{a_{\mathrm{RF(H)}}}{a_{\mathrm{LO(H)}}} a_{(\mathrm{H})}(t)\sin(\Delta\theta_{(\mathrm{H})}(t))\right] & (5.12) \end{cases}$$

where *K* is the voltage responsivity of the power detector. Using these voltages, a complex vector S(t) can be expressed as follows:

$$\begin{cases} S(t)_V = y_I(t)_V + y_Q(t)_V = I(t)_V + jQ(t)_V & (5.13) \\ S(t)_H = y_I(t)_H + y_Q(t)_H = I(t)_H + jQ(t)_H & (5.14) \end{cases}$$

Therefore, the demodulated signals $S(t)_V$ and $S(t)_H$ can be extracted by two unit-cells. The $S(t)_V$ and $S(t)_H$ represent the modulated signals sent by the transmitters. As a result, this architecture can act as a direct conversion receiver. It should be noted that the single-polarization receivers of Figures 5.17(b) and (c) have the same operating principle of the dual-polarization receiver. Besides, the energy harvesting in Figures 5.17(b) and (c) is achieved by capturing the unmodulated polarization signal.

5.4 Experimental results

To validate and evaluate the concept of the proposed multifunctional waveguide receiver array, a 6 X 8 receiver prototype based on the aforementioned structures as shown in Figure 5.18 was designed, fabricated, and measured. The photograph of the fabricated whole prototype is shown in Figure 5.18, where the metallic waveguide parts of the receiver are fabricated from aluminum with a high-speed CNC machine. The power detector and rectifier are fabricated using conventional PCB technology and 65-nm CMOS technology, respectively. The receiver unit cell, which includes the OMT element, was measured to estimate the matching performance, Figure 5.19 shows the measured S-parameters of the unit cell. It can be observed that, over the frequency range from 26 to 29 GHz, the measured reflection coefficient for both polarizations is better than -10 dB, and the isolation is greater than 30 dB.

The prototype receiver was then measured to validate its capabilities for energy harvesting and wireless communication. As a measurement example, the receiver unit cells X4Y4 and X4Y5 were utilized and measured for dual-polarized wireless communication, while unit cells such as X3Y2

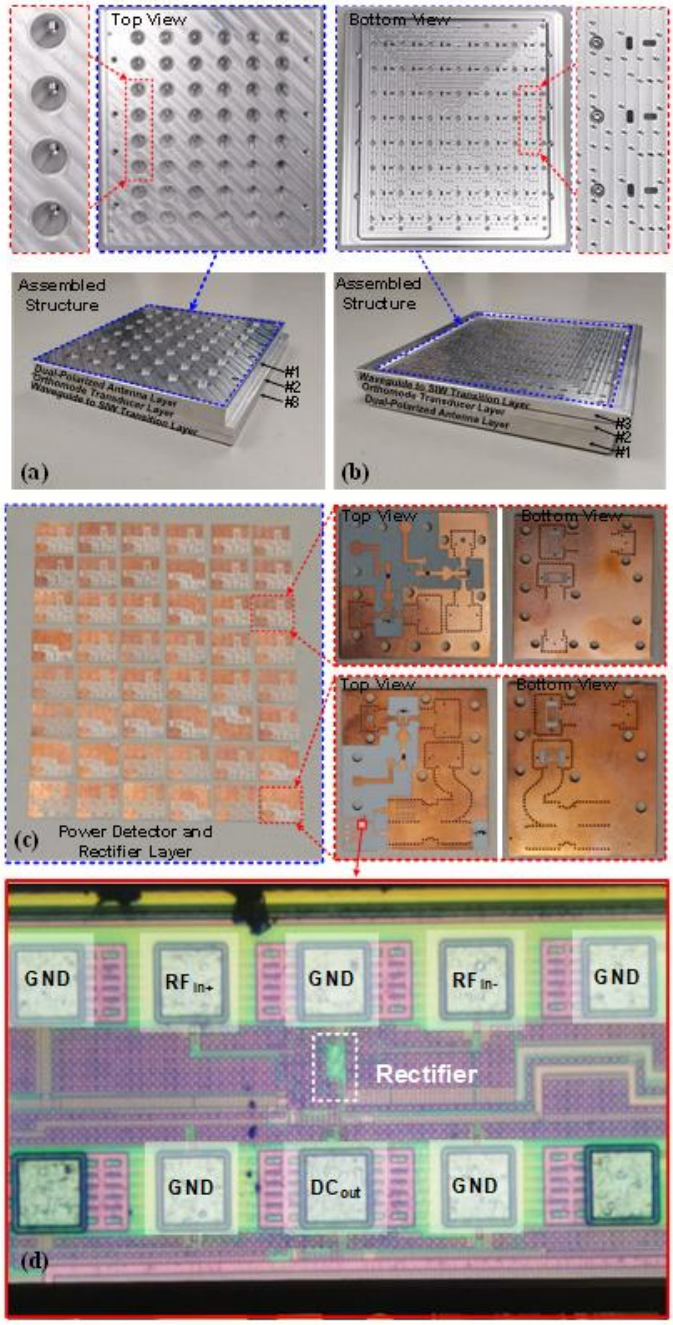

Figure 5.18 Photograph of the fabricated waveguide receiver array. (a) Front view. (b) Bottom view. (c) Power detector and rectifier array. (d) Chip micrograph of the fabricated rectifier

and X3Y4 were tested for energy harvesting (as illustrated in Figure 5.16). Furthermore, other unit cells can be employed to validate the proposed concept. The receiver array was measured with an Agilent E8257D source, an Agilent N1914A power meter, a power amplifier, an attenuator, a voltmeter, a directional coupler, and a high-gain antenna. The generated signal is sent by a high-

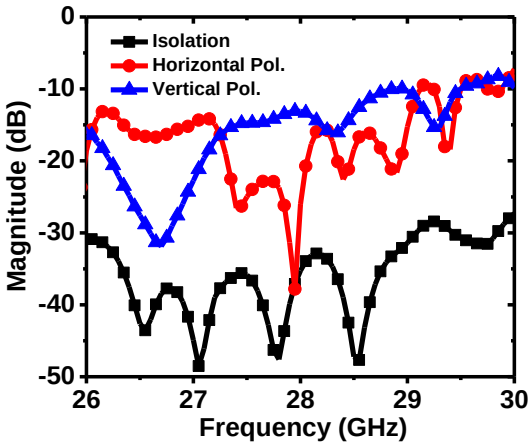

Figure 5.19 The measurement results of the reflection coefficients and isolation of the receiver unit

gain antenna to an array of receivers as illustrated in Figure 5.20. Measurements were performed at three different frequencies: 26, 28, and 30 GHz. Figure 5.21 shows the measured results of the energy harvesting. It can be seen that the rectifier exhibits a maximum power conversion efficiency (PCE) of about 18% for an input power of 9 dBm at 28 GHz and an output DC voltage of about 1.2 V. At 26 and 30 GHz, the measured PCE is around 15% and 13%, respectively and the measured output DC voltages are around 1.1V and 1.0 V, respectively. These measurements demonstrate the feasibility of energy harvesting for IoT applications.

The schematic and measurement setup for evaluating the over-the-air performance of the proposed waveguide receiver array are shown in Figure 5.22. As one of the critical performance indexes, the conversion characteristics of the receiver array are studied by comparing the detected IF output power and the RF input power. Figure 5.23 shows the measured output signal powers of the receiver array as the RF input signal varies from -30 to 5 dBm. It can be observed that with the increase of the RF signal power, the output power also increases. The output power peaks at about -28 dBm, when the RF power reaches 5 dBm. Measurement results indicate that a good linearity of the output power disappears when the input RF power exceeds –5 dBm. To provide a better illustration of the conversion characteristics, the conversion loss of the receiver is shown in Figure 5.24. It can be seen that with increasing the input LO power, the conversion loss gradually decreases.

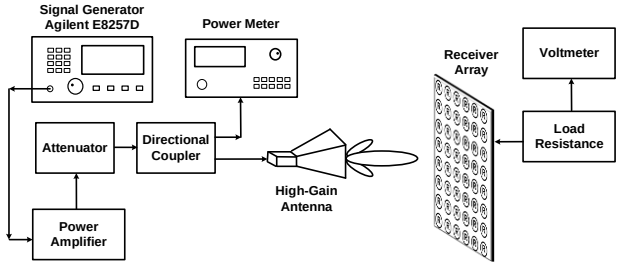

Figure 5.20 Wireless power transfer measurement of the proposed waveguide receiver array

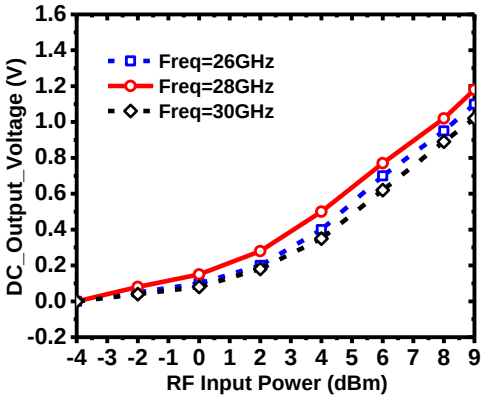

(a)

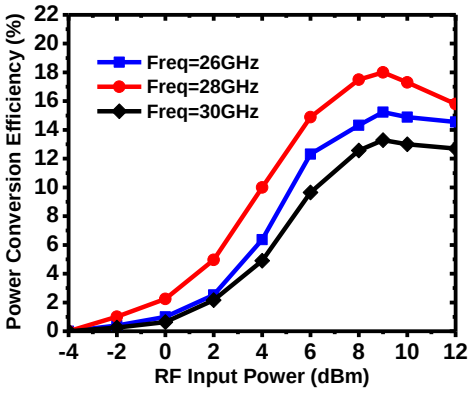

(b)

Figure 5.21 (a) Measured output voltage of the proposed receiver array with sweeping input power from -4 to 9 dBm. (b) Measured power conversion efficiency (PEC) of the proposed receiver array with sweeping input power from -4 to 12 dBm

Various complex modulated signals (M-QAM) at different symbol rates are experimentally studied with the proposed receiver array. The RF signal is generated by an arbitrary waveform generator (AWG) M8196A over the frequency range from 26 GHz to 30 GHz. Then, the M-QAM signals are fed into the antenna. The gain of antenna is around 20 dBi in the operating frequency band. The measurement distance is set to 1.5 m. Agilent E8257D PSG Analog Signal Generator and Agilent

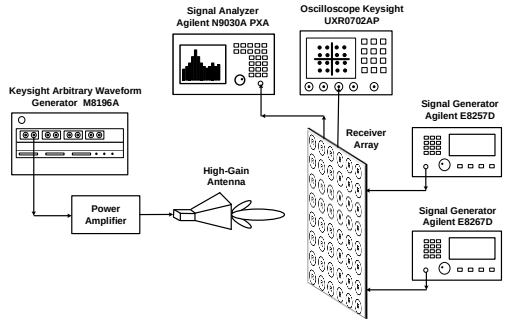

(a)

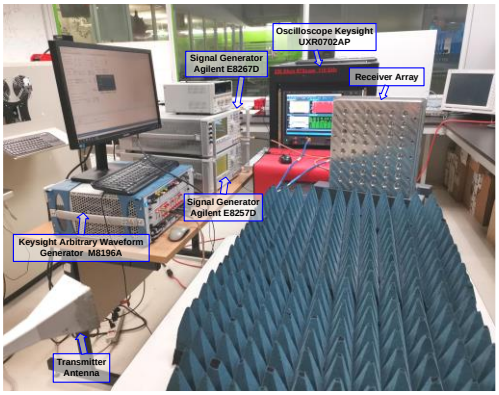

(b)

Figure 5.22 The over-the-air measurement setup of the proposed waveguide receiver array. (a) Simplified block diagram. (b) Photograph of whole setup

E8267D PSG Vector Signal Generator are used to generate the LO signals, which are injected into the receiver array and LO driving signals are set to about -5 dBm. To synchronize the modulated RF and LO signals, a 10-MHz synchronization signal is adopted to the signal generators and AWG. The transmitted bit sequence is created by AWG for all modulation schemes. Keysight UXR0702AP Real-Time Oscilloscope (70 GHz, 256 Gsa/s, 10-bit) is used to capture the demodulated signals. The rms value of the error vector magnitude (EVM) metric is computed by Keysight Technologies' 89600 VSA software. The constellation, output spectrum, and EVM for various modulated input signal are measured, where a = 0.35 for the root-raised cosine pulse filter. Table 5.1 summarizes the measured constellation and EVM for other operating frequencies. It can be seen that an excellent EVM for 4QAM, QAM-16, QAM-32, and QAM-64 at 26, 27, 28, and 29 GHz, respectively, is achieved. The measured EVMs versus the RF input power for a 400-MHz

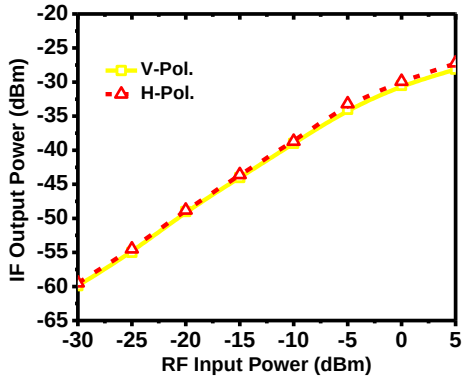

Figure 5.23 Measured output IF signal powers of the receiver with sweep input RF signal power from -30 to 5 dBm

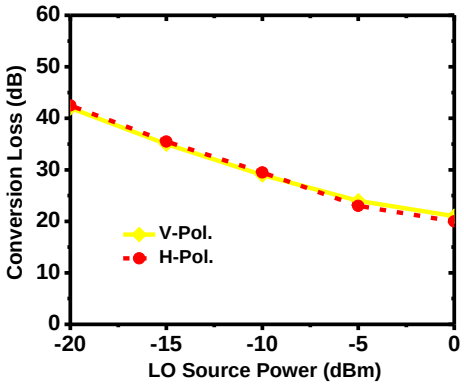

Figure 5.24 Measured conversion losses of the receiver under different input LO driving signal powers

16-QAM signal at different frequencies are shown in Figure 5.25. The EVM value becomes better with a larger input power. However, it will saturate and deteriorate over the upper limit of square-law operation. Figure 5.26 shows the measured EVM versus different symbol rates. It can be observed that low-order modulation has a better EVM value compared with its high-order counterpart. This is due to the increased amplitude and phase requirements associated with higher-order modulation schemes. Besides, with increasing symbol rates, the EVM gradually increases. The EVM measurements demonstrate excellent operation of the proposed receiver array in the 5G frequency bands.

Table 5.2 summarizes the measured results and compares them with other state-of-the-art interferometric receivers. The proposed work is the first interferometric waveguide receiver array

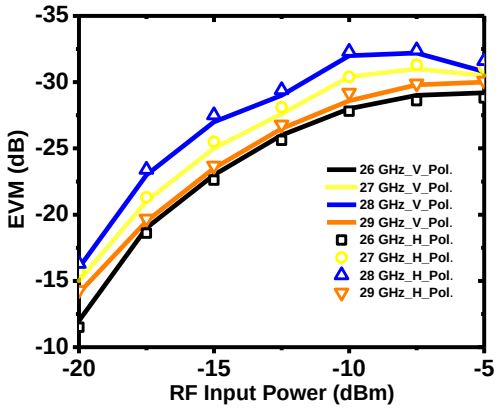

Figure 5.25 Measured EVMs of 16AQM signal under different input RF signal from -20 to -5 dBm

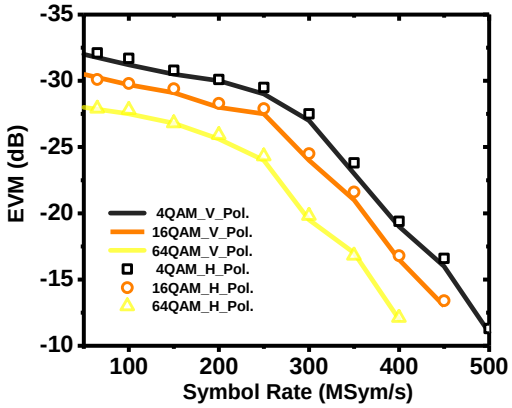

Figure 5.26 Measured EVMs of 4QAM, 16QAM, 64QAM for diffierent symbol rate

with simultaneous communication and energy harvesting capabilities. The receiver array fully leverages the advantages of OMT and realizes dual-polarization operations, i.e., the H-polarized (H-pol.) and V-polarized (V-pol.) modes. Therefore, two orthogonal polarizations can be excited simultaneously in only a single receiver module free from adding the number and complexity of the circuits, compared to conventional receiver counterparts in[74], [95], and [124]. In addition, the proposed receiver array achieves a high-speed performance in terms of data rates, EVM, and BER without any postprocessing [124], while achieving great power efficiency through metallic waveguide technology and interferometric architecture. It is worth mentioning that although the waveguide receiver array is implemented in the mmW band, it can be extended to the terahertz (THz) band.

Table 5.1 Retrieved constellation diagrams with different orders of modulations (M-QAM) and different operating frequencies

f_{RF}	26GHz			
Mod.	4QAM	16QAM	32AQM	64QAM
V-Pol. Cons.	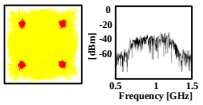	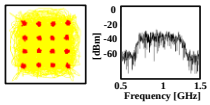	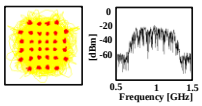	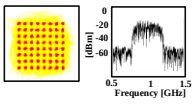
EVM	-24.78 dB	-26.12 dB	-26.67 dB	-29.39 dB
H-Pol. Cons.	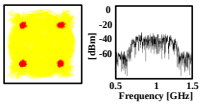	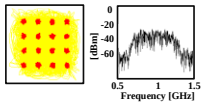	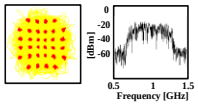	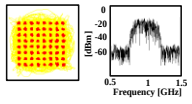
EVM	-24.97 dB	-26.45 dB	-26.23 dB	-29.11 dB
f_{RF}	27GHz			
Mod.	4QAM	16QAM	32AQM	64QAM
V-Pol. Cons.	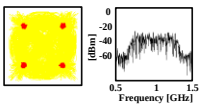	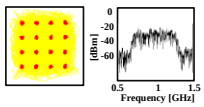	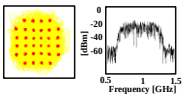	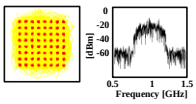
EVM	-27.17 dB	-29.34 dB	-29.25 dB	-32.16 dB
H-Pol. Cons.	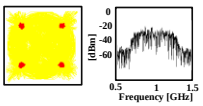	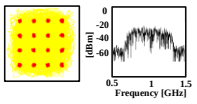	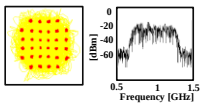	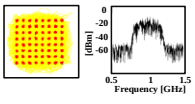
EVM	-27.33 dB	-29.89 dB	-29.62 dB	-31.72 dB
f_{RF}	28 GHz			
Mod.	4QAM	16QAM	32AQM	64QAM
V-Pol. Cons.	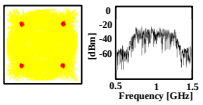	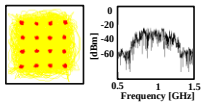	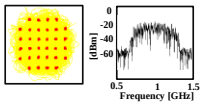	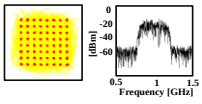
EVM	-30.48 dB	-28.23 dB	-29.12 dB	-31.86 dB
H-Pol. Cons.	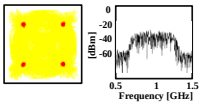	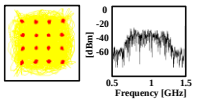	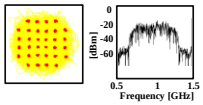	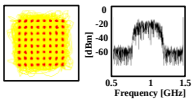
EVM	-30.17 dB	-28.71 dB	-29.62 dB	-31.34 dB
f_{RF}	29 GHz			
Mod.	4QAM	16QAM	32AQM	64QAM
V-Pol. Cons.	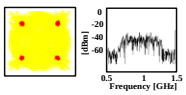	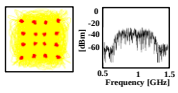	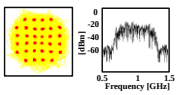	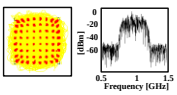
EVM	-27.78 dB	-24.14 dB	-28.91 dB	-28.72 dB
H-Pol. Cons.	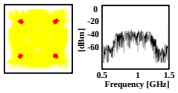	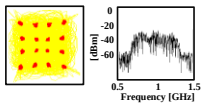	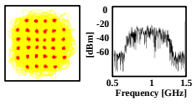	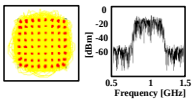
EVM	-27.33 dB	-24.58 dB	-28.46 dB	-29.08 dB

Table 5.2 Performance summary and comparison with the state-of-the-art interferometric receiver systems

Ref.	This work		[145]		[95]		[76]		[124]	
Tech.	Metallic Waveguide +PCB+65nm CMOS		PCB+Metallic Waveguide		PCB		PCB		PCB	
Archi.	Spatially Distributed		Multiport		Multiport		Multiport		Multiport	
Pol. Type	Dual-polarization		Dual-polarization		Single-polarization		Single-polarization		Single-polarization	
Freq.	28 GHz		28 GHz		60 GHz		3 GHz		3.82 GHz	
Mod. Signal	16 QAM	64 QAM	64 QAM	256 QAM	16 QAM	32 QAM	16 QAM	64 QAM	64 QAM	256 QAM
Data Rate	1.6 Gb/s	1.2 Gb/s	1.2 Gb/s	0.8 Gb/s	2.0 Gb/s	2.5 Gb/s	8 Mb/s	12 Mb/s	30 Mb/s	40 Mb/s
EVM (dB)	-21.25 V	-27.46 V	-28.9 V	-30.2 V	-19.2	-18.4	-34.8	-34.4	<-33.9	<-33.9
	-21.38 H	-27.52 H	-27.1 H	-28.1 H						
SNR (dB)	19.21 V	23.43 V	25.5 V	26.6 V	N/A	N/A	N/A	N/A	N/A	N/A
	19.35 H	23.57 H	23.5 H	24.1 H						
BER	$<10^{-5}$	$<10^{-5}$	N/A	N/A	$<10^{-6}$	$<10^{-4}$	$<10^{-4}$	$<10^{-4}$	$<10^{-5}$	$<10^{-5}$
LO Power	-8 dBm	-6 dBm	N/A	N/A	-10 dBm	-10 dBm	N/A	N/A	0 dBm	0 dBm
AC	No		No		No		No		Yes	
EHC	Yes		No		No		No		No	
PCE	18 %		N/A		N/A		N/A		N/A	
Input Power	9 dBm		N/A		N/A		N/A		N/A	
JSC	Yes		No		No		No		No	

Ref.: Reference; Tech.: Technology; Archi.: Architecture; Pol.: Polarization; Freq.: Frequency; Mod.: Modulation; AC: Algorithm Calibratio; EHC: Energy Harvesting capability; PCE: Power conversion efficiency; JSC: Joint Sensing and Communication;

5.5 Conclusion

In this paper, a multifunctional waveguide receiver array based on the interferometric architecture has been proposed, studied, and experimentally validated for joint power transfer, communication,

and sensing systems. The receiver array supports dual-polarization operation without adding circuit complexity. In addition, to enable wireless power transfer, the receiver unit incorporates a 65 nm CMOS differential rectifier. Therefore, based on the proposed approach, RF energy harvesting mode and wireless communication mode can be activated simultaneously to power specific low-power active devices and achieve energy autonomy of the RF receiving system. An experimental prototype was fabricated to validate the proposed concept. Various modulations such as 4-QAM, 16-QAM, 32-QAM, and 64-QAM, as well as energy harvesting, have been successfully measured and demonstrated. The experimental results have confirmed that the proposed receiver is highly suitable for versatile unified communications and IoT sensor applications in future radio environments, including 5G, 6G, and beyond.

CHAPTER 6 ARTICLE 4: JOINT MULTIBAND LINEAR INTERFEROMETRIC RECEIVER FOR INTEGRATED MICROWAVE AND TERAHERTZ SENSING AND COMMUNICATION SYSTEMS

Jie Deng, Pascal Burasa, and Ke Wu

Published in: IEEE Transactions on Microwave Theory and Techniques

Publication date: February 13, 2024

Abstract: Integrating microwave (MW) and terahertz (THz) operations and technologies is a promising solution in support of future multifunction and multistandard wireless systems such as joint sensing and communication platforms. However, the coexistence of MW and THz in a single receiver is a challenge to accommodate such a dual-band scheme of large frequency ratio and to satisfy its stringent performance requirements. To address these issues, a joint dual-band receiver is proposed and demonstrated for simultaneous MW and THz operations in this work. The proposed receiver inherits the advantages of conventional multiport linear interferometric architecture such as simple configuration and low-power consumption. MW and THz signals at individual frequency channels are concurrently received by a single hardware platform, then both signals are translated or converted to the intermediate frequency (IF) bands. The operating mechanism of the proposed receiver is studied and explained in detail. To verify the proposed architecture, an experimental prototype is realized and measured. Various M-quadrature-amplitude modulation (QAM) signals are successfully demodulated in the MW band (5.8 GHz) and THz band (150 GHz), respectively, thus validating the performances of the receiver. To the best of the authors' knowledge, this is the first interferometric receiver that operates in both MW and THz frequencies, simultaneously.

Index Terms: Dual-band, fifth/sixth generation, microwave, millimeter-wave, multiband, multifunction, multiport interferometric receiver, multistandard, terahertz.

6.1 Introduction

Terahertz (THz) technology has recently attracted much attention in the research and development community for 6G and future multifunction wireless systems such as joint sensing and communication techniques due to its broadband spectrum resource, high resolution, frequency reusability, and so forth [53], [56], [59], [61], [257], [258], [259], [260], [261], [262], [263], [264]. It is anticipated that the THz system capacity and speed will be unprecedented against what microwave technology can offer. In fact, the much-publicized 6G systems should operate over a wide range of frequencies from MHz through THz, which present different technical and application features over various frequency bands. In addition, a super-connectivity for all objects with low latency can be enabled, which supports the Internet of Things (IoT)-served wireless sensor nodes. However, caused by severe free-space attenuation and guided-wave loss, current very high-speed communications and/or very high-resolution sensing at THz frequencies are inherently limited to short-range line-of-sight (LOS) applications. In addition, there is a lack of high-power THz sources [49], which makes it more challenging to improve communication and sensing outreach. In contrast, microwave (MW) band can provide reliable wider-range operations and mobility including non-line-of-sight (NLOS) transmissions. Therefore, to realize very high-speed/high-resolution systems and long-haul mobilities, a seamless joint dual THz/MW operation becomes meaningful and attractive. Through such a dual-band integration, the advantages of both THz and MW systems are combined and preserved. The whole system becomes smart thanks to the interplay and fusion of multifunctional ties including multistandard applications [20].

Generally, such a coexisting or co-locating wireless system may be implemented by using two separate MW and THz receiver modules as illustrated in Figure 6.1(a). However, future 5G/6G systems will obviously require a large number of low-power, low-cost, compact, multifunction, and multistandard sensing and communicating devices massively deployed everywhere. Therefore, an all-in-one solution as illustrated in Figure 6.1(b) where both MW and THz receiving blocks are integrated into a single hardware, would alleviate limitations regarding packaging/assembly and empower a class of smartly inter-played wireless sensing and communications with easy information fusion for unprecedented applications.

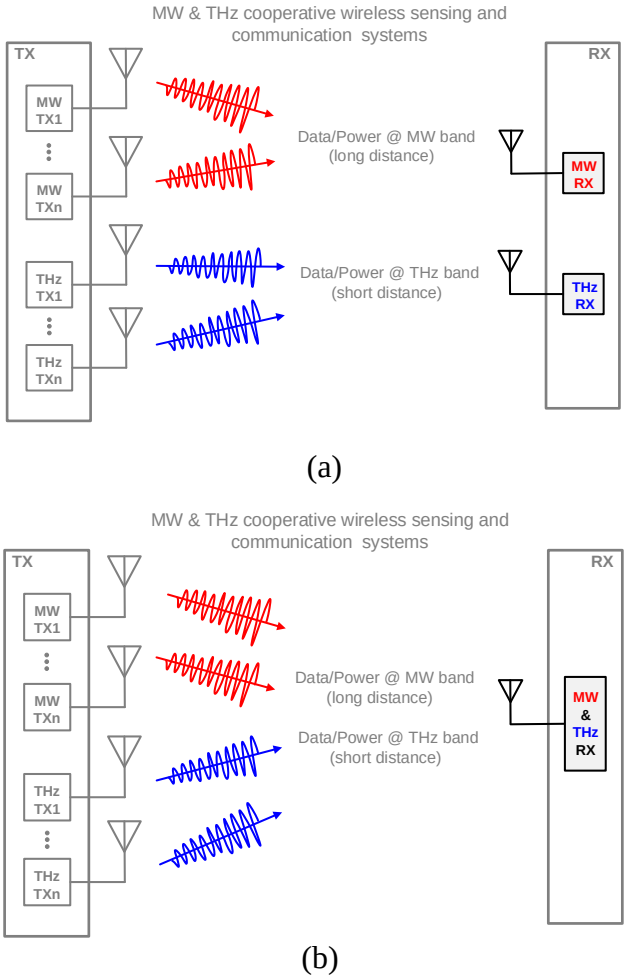

Figure 6.1 Application scenario of microwave and terahertz cooperative wireless sensing and communication systems (involving data transfer, energy harvesting, and sensing operating). (a) Conventional solution with two different RX modules. (b) Proposed solution with only one RX module

Linear interferometric technique [18], [74], [76], [79], [80], [90], [92], [94], [98], [101], [102], [107], [124], [142], [146], [180], [187], [188], [191], [224], [265], [266], [267], as a competitive solution for multistandard, multiband, and multifunction wireless systems, has widely been studied and used in a variety of RF/MW and mmW receivers. Compared to conventional nonlinear mixer-based architecture such as homodyne or super-heterodyne [224], it exhibits attractive advantages of low power consumption, simple configuration, broadband performance, and robustness for power-level variations. Although several dual-band linear interferometric receivers have been proposed [74], [76], [124], [191] none of them has successfully demonstrated joint MW/THz functions into one single receiver due to the architectural restriction.

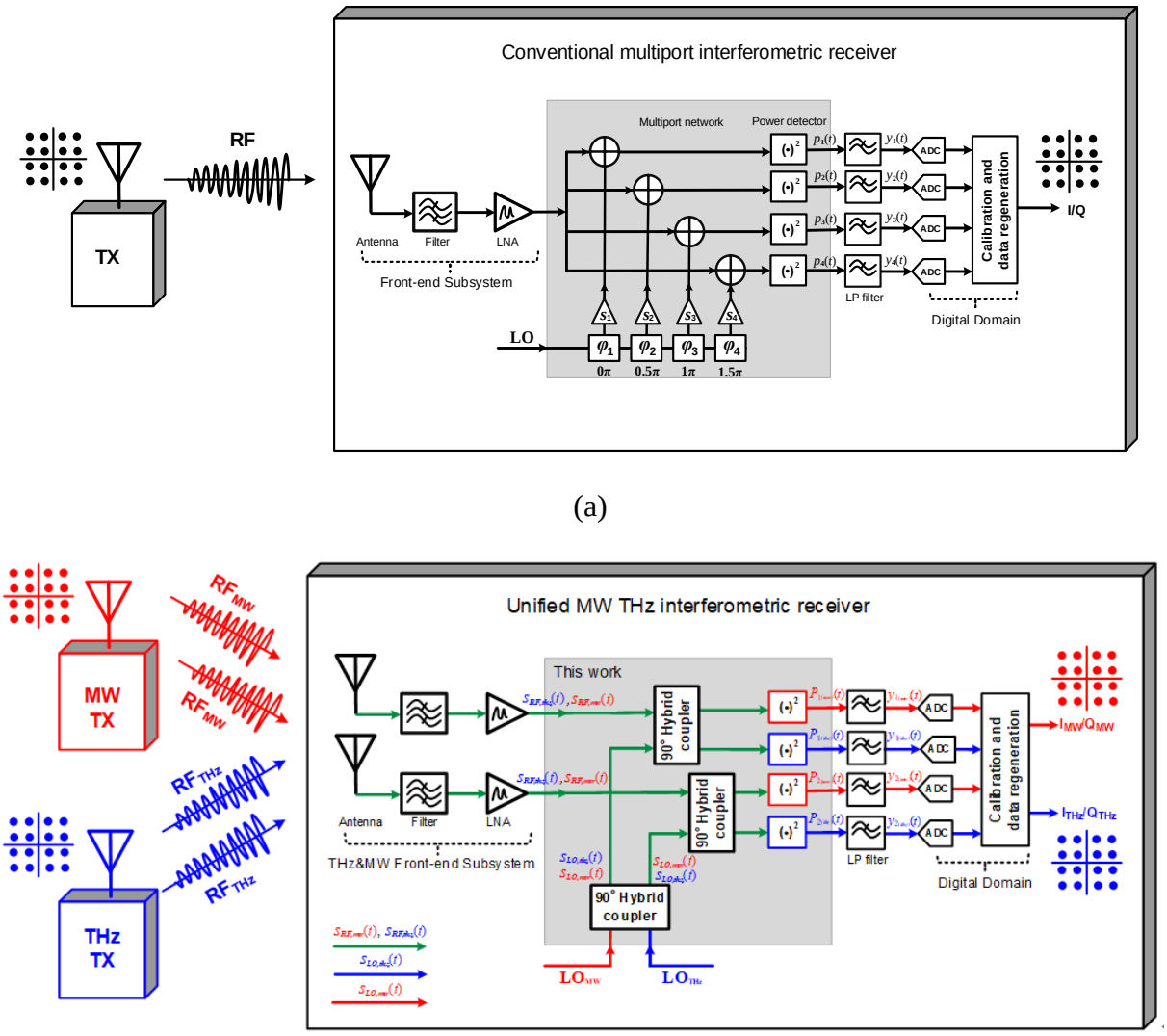

Figure 6.2 Block diagram of multiport interferometric receiver. (a) Conventional multiport interferometric receiver. (b) Proposed unified microwave terahertz interferometric receiver

In this paper, a joint MW/THz interferometric receiver for future multifunction and multistandard wireless sensing and communication is proposed and demonstrated. Detailed analysis and discussions of the proposed receiver architecture are presented. To the best of the authors' knowledge, this type of receiver has never been reported yet. It is worth mentioning that this receiver can also be explored to enable a possible full-scale integration of data-energy-sensing

functions, i.e., joint MW energy harvesting and THz communication and sensing. Therefore, this receiver is a viable platform that can involve data transfer, energy harvesting, sensing operations, etc.

The rest of this paper is organized as follows. In Section 6.2, the system architecture of the state-of-the-art linear interferometric receiver is studied and discussed. Besides, a system model of the proposed interferometric receiver is presented, and its operating principle is explained with a theoretical analysis. In Section 6.3, the detailed design of MW and THz power detectors is given. Section 6.4 presents the system-level simulation and demonstrates the performance of the receiver through an experimental prototype. Various demodulated results for both MW and THz bands are presented. Finally, this work is concluded in Section 6.5.

6.2 Receiver architecture

6.2.1 Conventional multiport interferometric receiver

As opposed to high-nonlinearity-driven mixing techniques, the operating principle of conventional multiport receivers is based on linear interference as shown in Figure 6.2(a). The receiver consists of a passive network comprising of quadrature hybrid couplers, power dividers or phase shifters, and power detectors. The modulated RF and LO signals are superposed to each other under different relative phase conditions such as 0π, 0.5π, 1π, and 1.5π. The modulated RF and LO signals can be expressed as:

$$a_{\_RF} = | a_{\_RF} || I(t)+jQ(t)| e^{jw_{RF}(t)} \tag{6.1}$$

and

$$a_{\_LO} = | a_{\_LO} | e^{j(w_{LO}(t)+\theta_{LO})} \tag{6.2}$$

where $|a_{\_RF}|$ and $|a_{\_LO}|$ are the signal amplitudes and θ_{RF} and Φ_{LO} are the signal phases. The modulation symbols are denoted by I and Q. The power detectors operate in their square-law linear region for signal mixing, resulting in a frequency conversion. The detected power (P_i) at different output of power detectors, can be expressed as:

$$\begin{aligned} p_{\mathrm{i}} &= |\, S_{\mathrm{LOi}} a_{\_\mathrm{LO}} + S_{\mathrm{RFi}} a_{\_\mathrm{RF}} \,|^2 \\ &= |\, S_{\mathrm{LOi}} \,|^2 |\, a_{\_\mathrm{LO}} \,|^2 + |\, S_{\mathrm{RFi}} \,|^2 |\, a_{\_\mathrm{RF}} \,|^2 + \\ &= |\, S_{\mathrm{LOi}} \,||\, S_{\mathrm{RFi}} \,||\, a_{\_\mathrm{LO}} \,||\, a_{\_\mathrm{RF}} \,| e^{j[w_{\mathrm{RF}}(\mathrm{t}) - w_{\mathrm{LO}}(\mathrm{t}) + \theta_{\mathrm{LO}} + (\theta_{\mathrm{RFi}} - \theta_{\mathrm{LOi}})]} \end{aligned} \tag{6.3}$$

The power difference between the outputs of two pairs of detectors after the low-pass filter can be calculated as:

$$\begin{aligned} y_i - y_j = &-2KI\sin\left(\frac{\sigma + 2(w_{\mathrm{RF}} - w_{\mathrm{LO}})}{2}\right)\sin(\frac{\delta}{2}) \\ &+ 2KQ\cos\left(\frac{\sigma + 2(w_{\mathrm{RF}} - w_{\mathrm{LO}})}{2}\right)\sin(\frac{\delta}{2}) \end{aligned} \tag{6.4}$$

where $\sigma=\theta_{\mathrm{RFi}}-\theta_{\mathrm{LOi}}+\theta_{\mathrm{RFj}}-\Phi_{\mathrm{LOj}}+2\theta_{\mathrm{LO}}$, $\delta=\theta_{\mathrm{RFi}}-\theta_{\mathrm{LOi}}-\theta_{\mathrm{RFj}}+\theta_{\mathrm{LOj}}$, and $K=|S_{\mathrm{LOi}}||S_{\mathrm{RFi}}||a\_{\mathrm{LO}}||a\_{\mathrm{RF}}|$. From (6.4), the in-phase I and quadrature Q signals can be extracted. In the case of $w_{\mathrm{LO}}=w_{\mathrm{RF}}$, the outputs are y_1-y_3=-2KI and y_2-y_4=-2KQ. Otherwise, when $w_{\mathrm{LO}}\neq w_{\mathrm{RF}}$, the output signals are further processed to retrieve the data stream. An adequate calibration algorithm could be utilized to improve the performance of the receiver [187].

6.2.2 Joint MW/THz interferometric receiver

Figure 6.2(b) shows the architecture of the proposed joint MW/THz interferometric receiver. The modulated MW and THz signals are combined with both associated MW and THz reference LOs with different relative phases, thanks to the wave-correlator network. The linearly interfered signals are sent to the four power detectors. Unlike the conventional architecture that uses the four identical power detectors to down-convert modulated signals, the proposed architecture employs two distinct MW and THz power detectors to simultaneously demodulate the associated incoming MW and THz signals which is different from other interferometric receivers proposed so far. It is worth mentioning that there are some reflected MW and THz signals caused by the power detectors' matching networks. However, in practice, these reflected signals cannot be reradiated through the antennas due to the nonreciprocal feature of LNAs. Therefore, the reported RX architecture will not lead to undesired radiations.

The input modulated signals, i.e., MW and THz signals, can be expressed as:

$$a_{\_RF(MW)} = | a_{\_RF(MW)} || I_{MW}(t) + jQ_{MW}(t) | e^{jw_{RF(MW)}(t)} \tag{6.5}$$

and

$$a_{\_RF(THz)} = | a_{\_RF(THz)} || I_{THz}(t) + jQ_{THz}(t) | e^{jw_{RF(THz)}(t)} \tag{6.6}$$

where I_{THz} and Q_{THz} represent the in-phase and quadrature components of THz signal, respectively, while I_{MW} and Q_{MW} stand for the in-phase and quadrature components of MW signal, respectively. $a\_{RF(THz)}$ and $a\_{RF(MW)}$ are the signal amplitudes. The corresponding LO signals can be expressed as:

$$a_{\_LO(MW)} = | a_{\_LO(MW)} | e^{j(w_{LO(MW)}(t)+\Phi_{LO(MW)})} \tag{6.7}$$

and

$$a_{\_LO(THz)} = | a_{\_LO(THz)} | e^{j(w_{LO(THz)}(t)+\Phi_{LO(THz)})} \tag{6.8}$$

where $a\_{LO(THz)}$ and $a\_{LO(MW)}$ are the LO signal amplitudes, and $\Phi\_{LO(THZ)}$ and $\Phi\_{LO(MW)}$ the phases. The modulated RF signals can be expressed as:

$$\begin{aligned} a_{\_RF(mix)} = & | a_{\_RF(THz)} | [I_{THz}(t)\cos(w_{RF(THz)}t) - Q_{THz}(t)\sin(w_{RF(THz)}t)] \\ & + | a_{\_RF(THz)} | [I_{THz}(t)\sin(w_{RF(THz)}t) + Q_{THz}(t)\cos(w_{RF(THz)}t)]j \\ & + | a_{\_RF(MW)} | [I_{MW}(t)\cos(w_{RF(MW)}t) - Q_{MW}(t)\sin(w_{RF(MW)}t)] \\ & + | a_{\_RF(MW)} | [I_{MW}(t)\sin(w_{RF(MW)}t) + Q_{MW}(t)\cos(w_{RF(MW)}t)]j \end{aligned} \tag{6.9}$$

The LO signals as:

$$\begin{aligned} a_{\_LO(mix)} = & | a_{\_LO(THz)} | \cos(w_{LO(THz)}t+\Phi_{LO(THz)}) \\ & + | a_{\_LO(THz)} | \sin(w_{LO(THz)}t + \Phi_{LO(THz)})j \\ & + | a_{\_LO(MW)} | \cos(w_{LO(MW)}t + \Phi_{LO(MW)}) \\ & + | a_{\_LO(MW)} | \sin(w_{LO(MW)}t + \Phi_{LO(MW)})j \end{aligned} \tag{6.10}$$

Both MW and THz power detectors operate in their square-law region for frequency conversion. Going through the power detectors, both modulated MW and THz signals are down-converted simultaneously, and the output signal can be expressed as:

$$
\begin{aligned}
&p_{i(\mathrm{THz})}(t) = c_0 + c_1\left(I_{\mathrm{THz}}(t)\cos(2\pi f_{\mathrm{RF(THz)}}t) - Q_{\mathrm{THz}}(t)\sin(2\pi f_{\mathrm{RF(THz)}}t) + K_1\cos(2\pi f_{\mathrm{LO(THz)}}t + \phi_i)\right)\\
&+\frac{c_2}{4}\left(I^2{}_{\mathrm{THz}}(t) + Q^2{}_{\mathrm{THz}}(t) + K_1^2\right)\\
&+\frac{c_2}{2}\begin{pmatrix} I_{\mathrm{THz}}(t)K_1\cos(2\pi(f_{\mathrm{RF(THz)}} - f_{\mathrm{LO(THz)}})t + \phi_i)\\ +Q_{\mathrm{THz}}(t)K_1\sin(2\pi(f_{\mathrm{RF(THz)}} - f_{\mathrm{LO(THz)}})t + \phi_i)\end{pmatrix}\\
&+\frac{c_2}{2}\begin{pmatrix} I_{\mathrm{THz}}(t)K_1\cos(2\pi(f_{\mathrm{RF(THz)}} + f_{\mathrm{LO(THz)}})t + \phi_i)\\ -Q_{\mathrm{THz}}(t)K_1\cos(2\pi(f_{\mathrm{RF(THz)}} + f_{\mathrm{LO(THz)}})t + \phi_i)\end{pmatrix}\\
&+\frac{c_2}{4}\begin{pmatrix} K^2{}_1\cos\left(4\pi f_{\mathrm{RF(THz)}}t + 2\phi_i\right) + \left(I^2{}_{\mathrm{THz}}(t) - Q^2{}_{\mathrm{THz}}(t)\right)\cos\left(4\pi f_{\mathrm{LO(THz)}}t\right)\\ -2I_{\mathrm{THz}}(t)Q_{\mathrm{THz}}(t)\sin\left(4\pi f_{\mathrm{LO(THz)}}t\right)\end{pmatrix}
\end{aligned}
\tag{6.11}
$$

$$
\begin{aligned}
&p_{i(\mathrm{MW})}(t) = \gamma_0 + \gamma_1\left(I_{\mathrm{MW}}(t)\cos(2\pi f_{\mathrm{RF(MW)}}t) - Q_{\mathrm{MW}}(t)\sin(2\pi f_{\mathrm{RF(MW)}}t) + G_1\cos(2\pi f_{\mathrm{LO(MW)}}t + \theta_i)\right)\\
&+\frac{\gamma_2}{4}\left(I^2{}_{\mathrm{MW}}(t) + Q^2{}_{\mathrm{MW}}(t) + G_1^2\right)\\
&+\frac{\gamma_2}{2}\begin{pmatrix} I_{\mathrm{MW}}(t)G_1\cos(2\pi(f_{\mathrm{RF(MW)}} - f_{\mathrm{LO(MW)}})t + \theta_i)\\ +Q_{\mathrm{MW}}(t)G_1\sin(2\pi(f_{\mathrm{RF(MW)}} - f_{\mathrm{LO(MW)}})t + \theta_i)\end{pmatrix}\\
&+\frac{\gamma_2}{2}\begin{pmatrix} I_{\mathrm{MW}}(t)G_1\cos(2\pi(f_{\mathrm{RF(MW)}} + f_{\mathrm{LO(MW)}})t + \theta_i)\\ -Q_{\mathrm{MW}}(t)G_1\cos(2\pi(f_{\mathrm{RF(MW)}} + f_{\mathrm{LO(MW)}})t + \theta_i)\end{pmatrix}\\
&+\frac{\gamma_2}{4}\begin{pmatrix} G^2{}_1\cos\left(4\pi f_{\mathrm{RF(MW)}}t + 2\theta_i\right) + \left(I^2{}_{\mathrm{MW}}(t) - Q^2{}_{\mathrm{MW}}(t)\right)\cos\left(4\pi f_{\mathrm{LO(MW)}}t\right)\\ -2I_{\mathrm{MW}}(t)Q_{\mathrm{MW}}(t)\sin\left(4\pi f_{\mathrm{LO(MW)}}t\right)\end{pmatrix}
\end{aligned}
\tag{6.12}
$$

where higher-order harmonics and intermodulation are not presented for the sake of analysis simplicity. Then, the outputs after low-pass filters are:

$$
\begin{aligned}
y_{i(\mathrm{THz})}(t) &= \mathrm{LP}(p_{i(\mathrm{THz})}(t)) \\
&= \frac{c_2}{4}\left(I^2{}_{\mathrm{THz}}(t) + Q^2{}_{\mathrm{THz}}(t) + K_1^2\right) \\
&+ \frac{c_2}{2} I_{\mathrm{THz}}(t) K_1 \cos(2\pi(f_{\mathrm{RF(THz)}} - f_{\mathrm{LO(THz)}})t + \phi_i) \\
&+ \frac{c_2}{2} Q_{\mathrm{THz}}(t) K_1 \sin(2\pi(f_{\mathrm{RF(THz)}} - f_{\mathrm{LO(THz)}})t + \phi_i)
\end{aligned}
\tag{6.13}
$$

$$
\begin{aligned}
y_{i(\mathrm{MW})}(t) &= \mathrm{LP}(p_{i(\mathrm{MW})}(t)) \\
&= \frac{\gamma_2}{4}\left(I^2{}_{\mathrm{MW}}(t) + Q^2{}_{\mathrm{MW}}(t) + G_1^2\right) \\
&+ \frac{\gamma_2}{2} I_{\mathrm{MW}}(t) G_1 \cos(2\pi(f_{\mathrm{RF(MW)}} - f_{\mathrm{LO(MW)}})t + \theta_i) \\
&+ \frac{\gamma_2}{2} Q_{\mathrm{MW}}(t) G_1 \sin(2\pi(f_{\mathrm{RF(MW)}} - f_{\mathrm{LO(MW)}})t + \theta_i)
\end{aligned}
\tag{6.14}
$$

From (6.13) and (6.14), the desired I and Q components can be retrieved simultaneously, without any restriction on the incoming MW and THz signals for the regeneration of baseband signals whatsoever. Therefore, this confirms that MW and THz signals at individual frequency channels can be received and demodulated concurrently based on only a single hardware platform.

6.3 Microwave and terahertz power detection

6.3.1 MW power detector

The MW signal frequency conversion is performed by the associated MW power detector. Figure 6.3(a) presents the schematic of the developed power detector comprising of an input DC grounding circuit, an input impedance matching network, a zero-bias GaAs Schottky diode (SMS7630-40), and an RF chocking circuit. The SPICE and packaging parasitic parameters of the diode are listed in Table 6.1. Figure 6.3(b) shows the geometric configuration of the power detector, which is designed on a thin Al_2O_3 ceramic substrate (ε_r = 9.9 and h =127 um) with 1 um Au metallization. To accurately model and predict the behavior of the power detector, both the harmonic balance (HB) simulator of Keysight Advanced Designed System (ADS) and the full-

Table 6.1 Spice and packaging parameters of SMS7630-40 diode

C_{j0}(pF)	I_s(A)	R_s(Ω)	M	V_{bi}(V)	C_p(pF)	L_p(nH)	N
0.14	5e-6	20	0.4	0.34	0.16	0.7	1.05

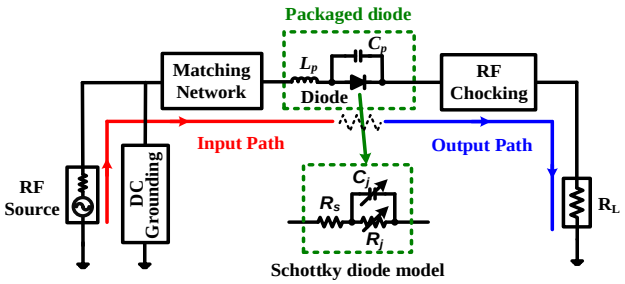

(a)

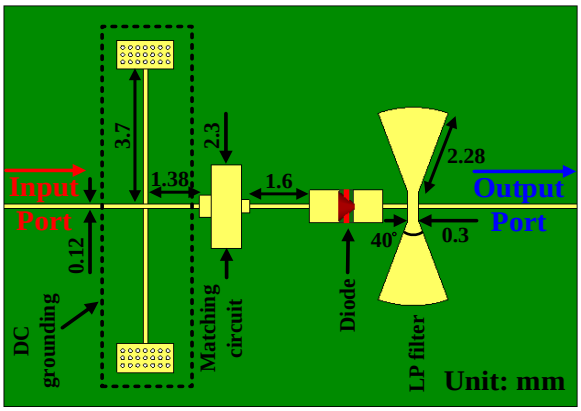

(b)

Figure 6.3 (a) Schematic description of microwave power detector with SMS7630-40 Schottky diode. (b) Geometric configuration of the designed microwave power detector

wave simulator of Computer Simulation Technology (CST) microwave studio were used in this work.

The simulated frequency response with an input power of 0-dBm is shown in Figure 6.4(a). It can be seen that over the frequency range from 5.5 to 8.5 GHz, the output voltage is higher than 100 mV and the maximum output voltage is around 480 mV. Figure 6.4(b) shows the output voltage versus input power. It can be observed that the output voltage increases almost linearly along with

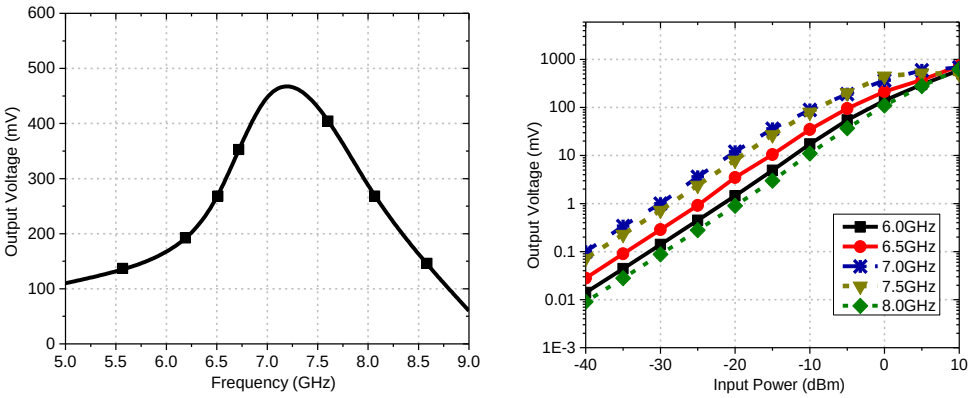

(a) (b)

Figure 6.4 Frequency and power response of the power detector. (a) Response of output voltage with frequency under 0 dBm drive power. (b) Output voltage of power detector with sweeping input power from -40 to 10 dBm

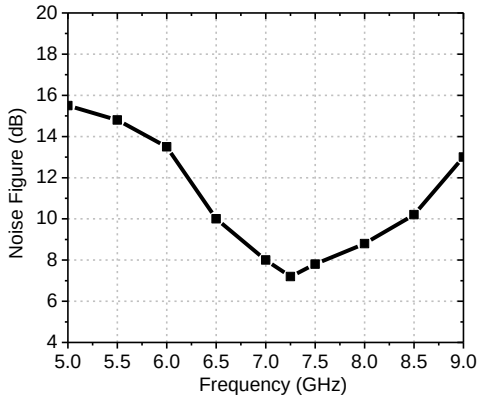

Figure 6.5 Simulated noise figure of the MW power detector

increasing input power from -40 to 0 dBm. Figure 6.5 shows the simulated noise of the MW power detector. It can be seen that the best noise performance is around 7.0 dB.

6.3.2 THz power detector

Unlike the MW power detector, the development of a THz power detector is challenging. Generally, in the MW band, equivalent circuit models are good enough to accurately simulate its electrical performances in such well-characterized frequency bands. However, as the operating frequency moves to the THz bands, parasitic effects and geometric details related to diode packaging have become non-negligible. They can yield a significant impact on circuit performances, leading to unexpected and generally deteriorated experimental or practical results. Since the equivalent circuit

Table 6.2 Spice and packaging parameters of SMS7630-40 diode Extracted nonlinear spice parameters and dimensions of VDI G-band zero bias Schottky diode

Parameters	I_s (uA)	C_{jo} (fF)	R_s (ohm)	N	W (um)	H (um)	L (um)
Value	6.0	5.0	25	1.3	120	60	300

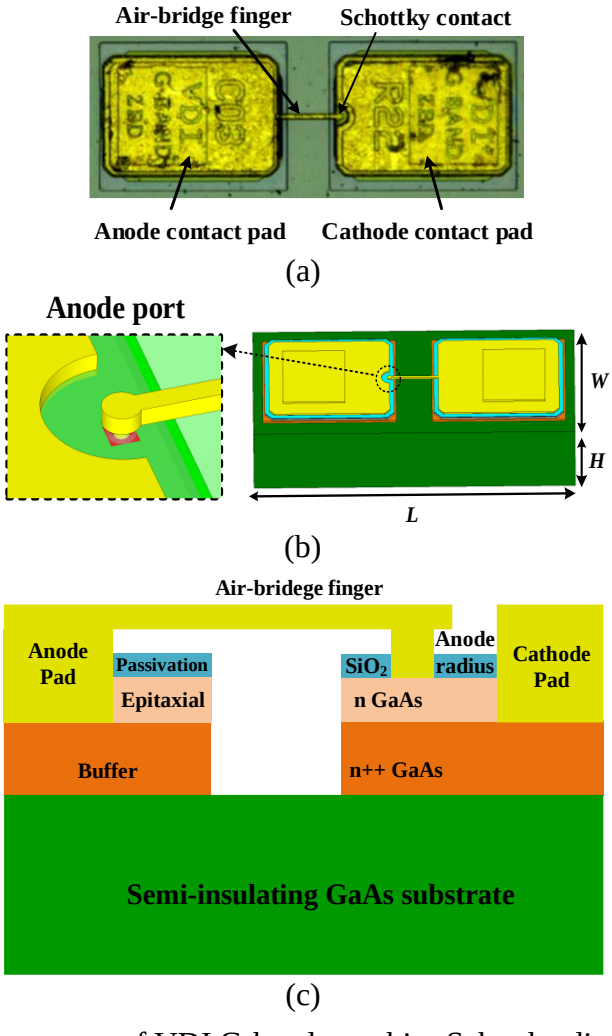

Figure 6.6 (a) Physical structure of VDI G-band zero bias Schottky diode under microscope. (b) Three-dimensional model of the Schottky diode. (c) Cross section view of the Schottky diode

model is difficult to predict parasitic effects, especially over a wide bandwidth, this makes it unsuitable for THz designs and applications. Therefore, three-dimensional electromagnetic (3D-EM) modeling is used to account for all of the parametric effects over THz bands such as electrical behaviors and packaging parasitic.

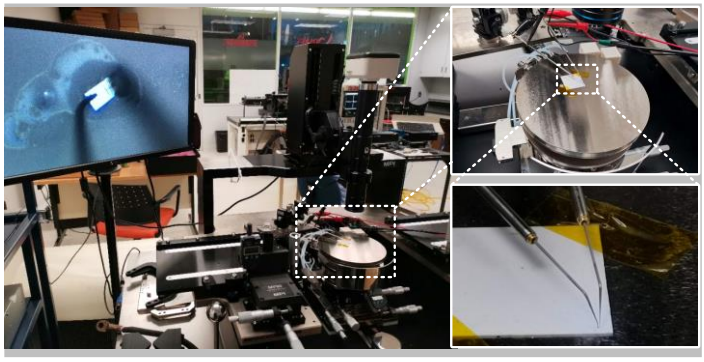

(a)

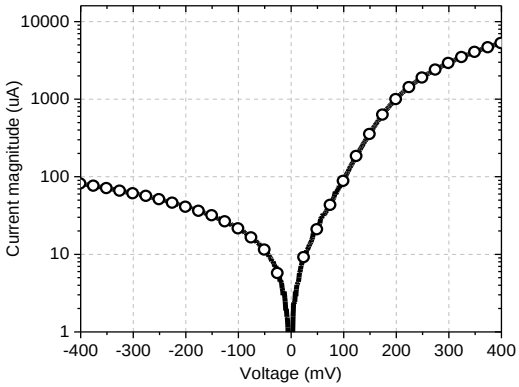

(b)

Figure 6.7 (a) Measurement setup photograph of VDI G-band zero bias Schottky diode characterization for SPICE parameters extraction. (b) Measured current (I)-voltage (V) curve of VDI G-band zero bias Schottky diode

Commercial VDI G-band zero-bias Schottky diode is used to develop the THz power detector in this work. This diode is a good candidate for the development of a high-sensitivity power detector due to its low junction resistance and junction capacitance. However, the manufacturer does not provide its 3D-EM model and key SPICE parameters, which limits its practical applications. Therefore, a 3D-EM model of the VDI G-band zero-bias Schottky diode is constructed first. The physical structure of the diode under a microscope is shown in Figure 6.6(a), from which we can see that it includes an air-bridge finger, a Schottky contact, and two contact pads. As shown in the cross-section view of Figure 6.6(c), one can see underneath the contact pads a silicon dioxide passivation layer (SiO_2), a lightly doped epitaxial layer (n-GaAs), a heavily doped buffer layer (n++GaAs), and a semi-insulating membrane substrate (GaAs). The constructed 3D-EM model is shown in Figure 6.6(b).

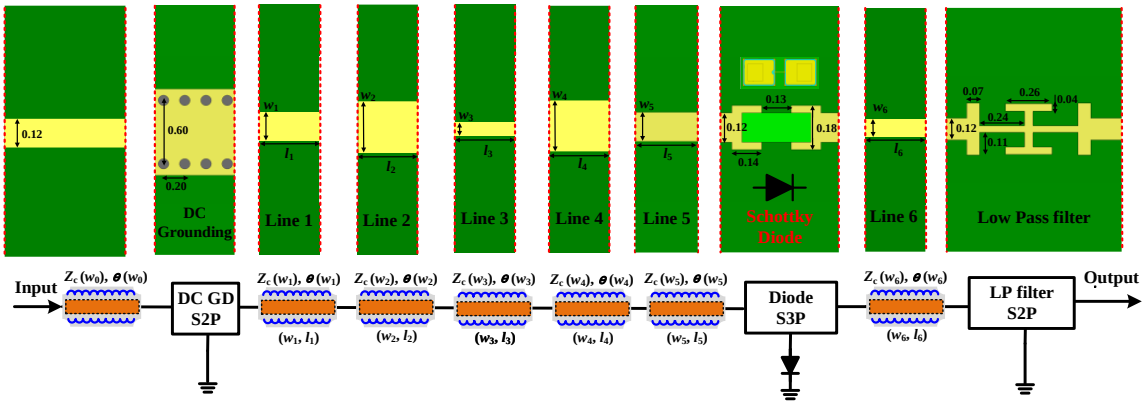

Figure 6.8 Geometric configuration and circuit model of THz power detector

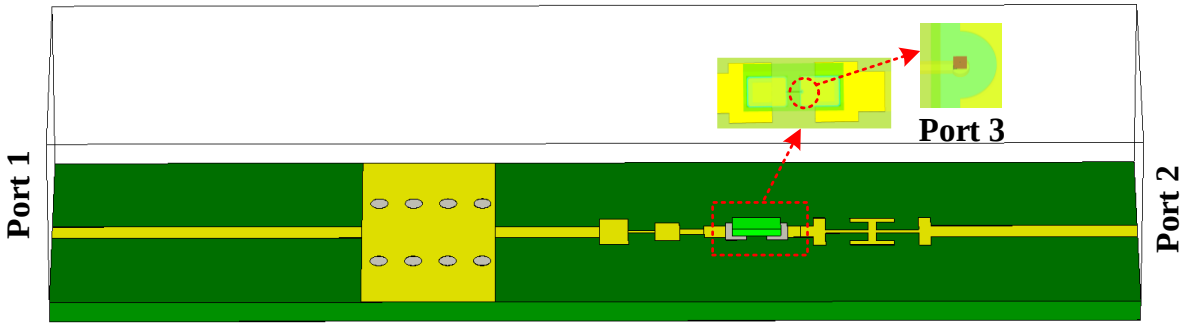

Figure 6.9 The detailed 3-D structure of the THz power detector

In addition to the 3D-EM model, the complete Schottky diode model includes active nonlinear SPICE parameters. The nonlinear SPICE parameters are extracted by Keysight B1500A semiconductor device analyzer. Measurements were carried out on wafer as shown in Figure 7(a), where the diode was attached to a ceramic substrate with conductive resin. The measured current (I)-voltage (V) curve is shown in Figure 7(b). The key parameters such as saturation current (Is), ideality factor (N), series resistance (Rs), breakdown voltage (Bv), and current at the breakdown voltage (Ibv) are obtained. All extracted SPICE parameters are listed in Table 6.2. Based on the constructed 3D-EM model and the extracted nonlinear SPICE parameters, a THz power detector is designed according to the circuit model as shown in Figure 6.8. Figure 6.9 shows the detailed 3-D structure of the THz power detector. To accurately simulate the electromagnetic properties of the diode, a port excitation (anode port) is set on the Schottky junction. Therefore, all the passive parasitic parameters and the active nonlinear parameters of the diode are considered. The analysis of the whole power detector is implemented with the co-simulation of CST and ADS. The estimated

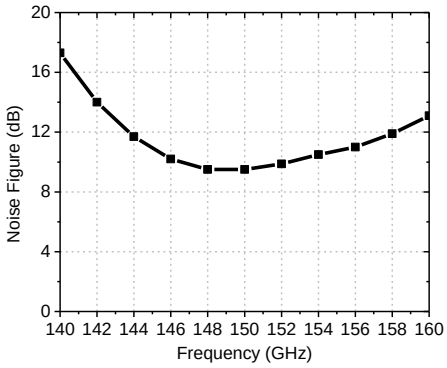

Figure 6.10 Simulated noise figure of the THz power detector

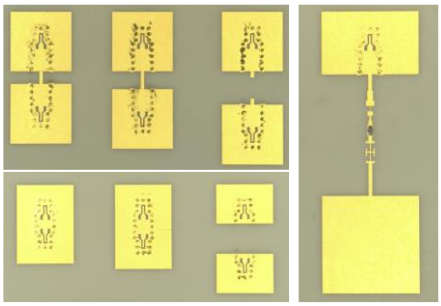

(a)

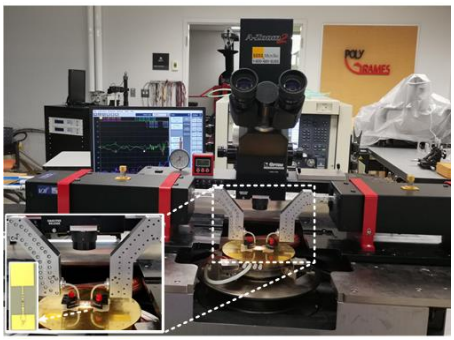

(b)

Figure 6.11 (a) Fabricated prototype THz power detector and its TRL calibration kit pieces. (b) Measurement setup photograph of the prototype THz power detector

attenuation of the diode is around 5.5 dB. The filter and transmission line are around 0.8 dB and 1.2 dB, respectively. The optimal circuit dimensions are w_1=0.18 mm, l_1=0.32 mm, w_2=0.27 mm, l_2=0.16 mm, w_3=0.03 mm, l_3=0.16 mm, w_4=0.18 mm, l_4=0.14 mm, w_5=0.10 mm, l_5=0.15 mm, w_6=0.12 mm, and l_6=0.18 mm. Figure 6.10 shows the simulated noise of the THz power detector.

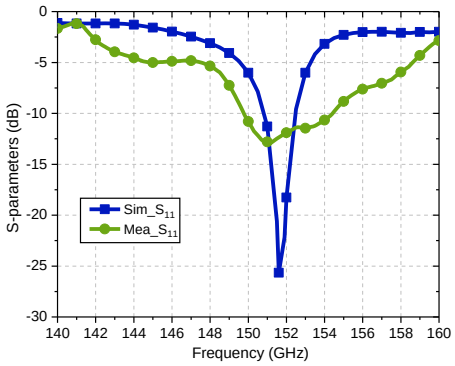

Figure 6.12 Measured and simulated reflection coefficients of the prototype power detector

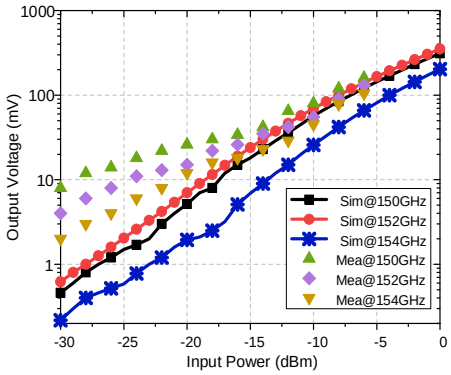

Figure 6.13 Measured and simulated output voltages versus sweeping input power from -30 to 0 dBm

It can be observed that the noise figure is between 17 and 14 dB over the frequency range from 140 to 160 GHz.

Figure 6.11(a) shows the prototype of the power detector, which is fabricated on a thin ceramic substrate (ε_r=9.9, h=127 um), using an MHMIC (Miniature Hybrid Microwave Integrated Circuits) fabrication process in our Poly-Grames Research Center. The power detector consists of a conductor-backed coplanar waveguide part, a substrate-integrated waveguide (SIW)-to-microstrip line transition, a matching network, a Schottky diode, a DC-pass filter, and a load resistor. The conductor-backed coplanar waveguide section at the detector input is used to accommodate GSG on-wafer probes, where the diode is driven through an SIW-to-microstrip line transition. The rectified output voltage (Vout) is measured across a load resistor (R_L).

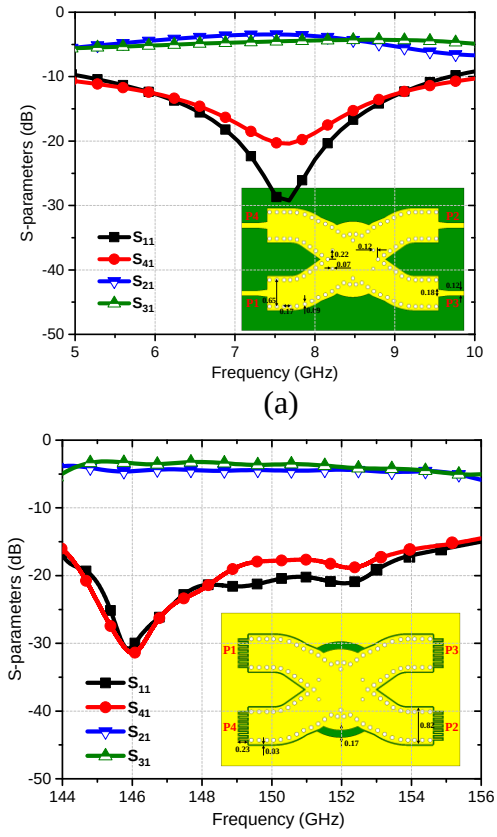

Figure 6.14 Simulated results of the microwave THz coupler. (a) MW band performance. (b) THz band performance

Figure 6.11(b) shows the measurement setup, where the measured and simulated reflection coefficients are shown in Figure 6.12. It can be observed that the best reflection coefficients for both simulated and measured results are around 151 GHz. Small frequency deviations may be related to the diode mounting and circuit fabrication. Figure 6.13 presents the output voltages of the power detector versus input power. The output voltages are about 10 mV and 100 mV for -30 dBm and -5 dBm input power, respectively, at 150 GHz. The measured output voltages of the proposed power detector agree quite well with the simulated counterparts.

6.4 Receiver implementation

A system-level simulation based on the architecture in Figure 6.2(b) is implemented in ADS to evaluate the proposed receiver and its theoretical results. The power detectors and the couplers are extracted together and co-simulated with the ADS Ptolemy simulator. Figure 6.14 shows the

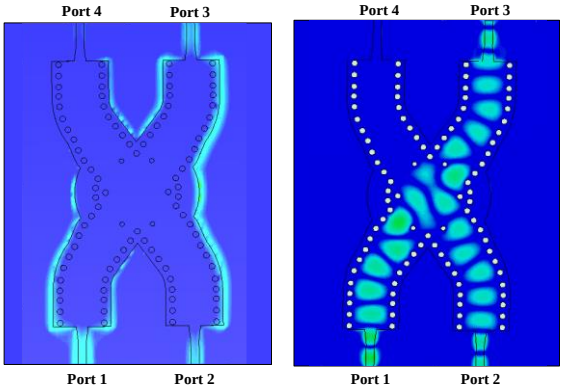

(a) (b)

Figure 6.15 Simulated electric field distributions of the proposed hybrid coupler. (a) Microwave band at 5.8 GHz. (b) Terahertz band at 150 GHz

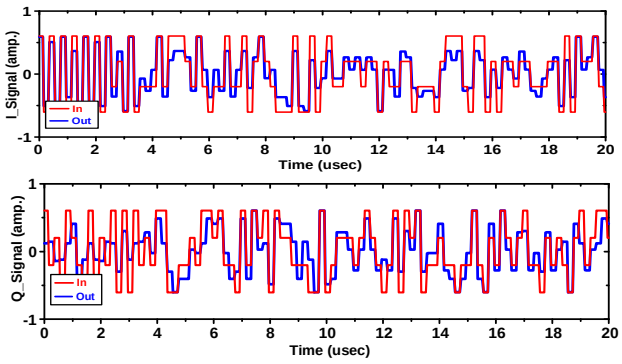

(a)

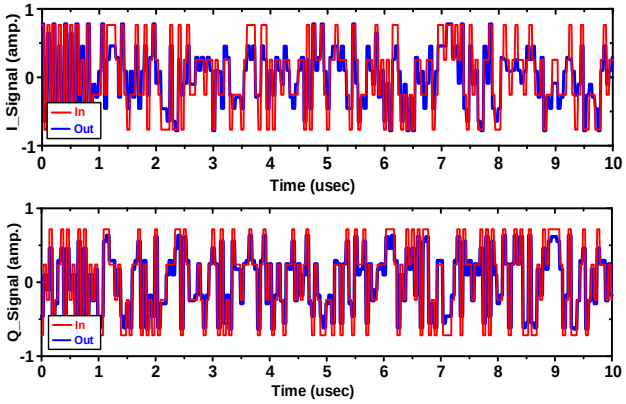

(b)

Figure 6.16 Comparison of modulated and demodulated 16-QAM waveforms of the input and output I and Q signals. (a) MW band at 5.8 GHz. (b) THz band at 150 GHz

structure of the proposed hybrid coupler. The hybrid coupler has a composite waveguide structure, which is constructed with CPW hybrid coupler and SIW hybrid coupler. Therefore, when the MW signal enters the coupler, the coupler operates as a CPW coupler. The MW signal will not enter

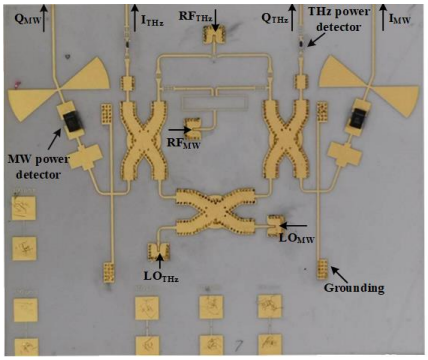

Figure 6.17 Fabricated prototype of the unified MW-THz interferometric receiver. For proof-of-concept, the antennas are replaced by Wilkinson power dividers to facilitate the measurement with probes

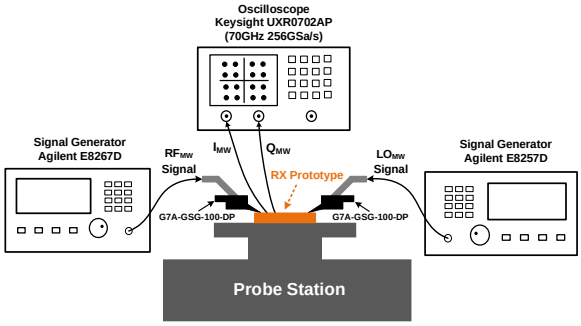

(a)

(b)

Figure 6.18 Measurement setup for the proposed interferometric receiver under MW band. (a) Simplified block diagram. (b) Whole measurement set-up

SIW coupler due to the cut-off frequency of the SIW property. Similarly, when the THz signal enters the coupler, the coupler operates as an SIW coupler. The simulated results of the couplers are also shown in Figure 6.14. It can be seen that from 6 to 9 GHz, the reflection coefficient (S_{11})

Table 6.3 Measured constellation diagrams with different orders of modulations at 5.8 GHz

4QAM	16QAM
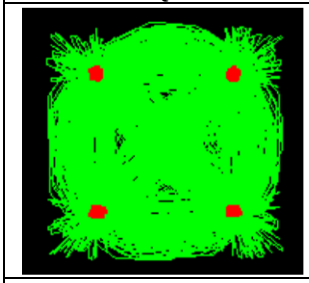	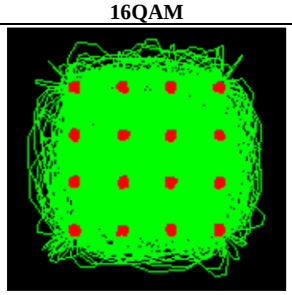
EVM=-30.81dB	EVM=-33.59dB
32QAM	**64QAM**
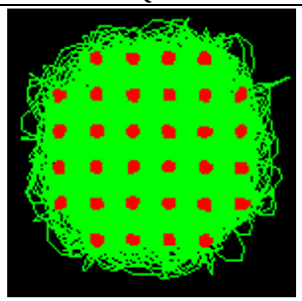	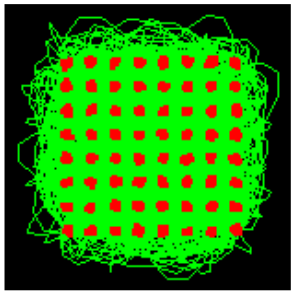
EVM=-35.08dB	EVM=-34.15dB
128QAM	**256QAM**
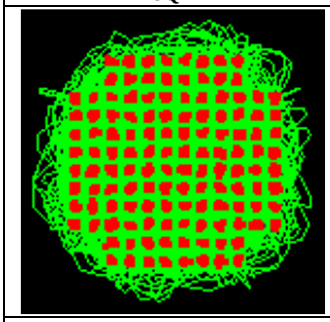	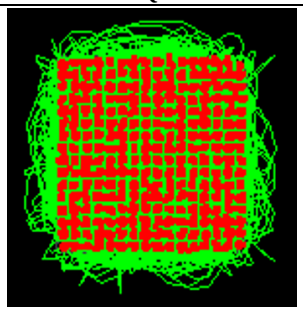
EVM=-35.65dB	EVM=-35.18dB

is better than -15 dB and the isolation (S_{41}) is greater than 15 dB. The transmissions (S_{21} and S_{31}) vary from 3.7 ± 0.8 dB. On the other hand, from 145 to 155 GHz, the reflection coefficient (S_{11}) is better than -15 dB and the isolation (S_{41}) is larger than 15 dB. The transmissions (S_{21} and S_{31}) vary from 3.8 ± 1.5 dB. Figure 6.15 illustrates the simulated electric field distributions of the proposed hybrid coupler. It can be seen that the excited MW signal propagates along the CPW structure without entering SIW structure. The excited THz signal propagates along the SIW structure without entering CPW structure. There is no interference between those MW and THz bands. The simulated results confirm the operating of the proposed hybrid coupler.

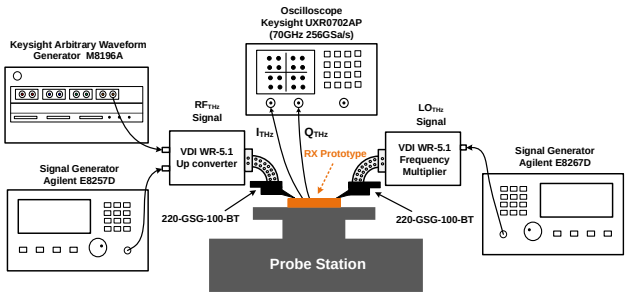

(a)

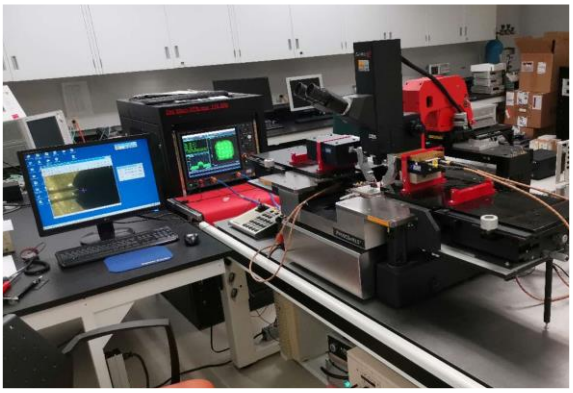

(b)

Figure 6.19 Measurement setup for the proposed interferometric receiver under THz band. (a) Simplified block diagram. (b) Whole measurement set up

The RF channels are selected at 5.8 GHz and 150 GHz. The transmitted signals are modulated by the different quadrature amplitude modulations (QAM). The data flow and envelope simulators are performed to retrieve the I and Q signals in the two bands simultaneously. Figure 6.16 shows the waveforms of the input and output I and Q signals for 16-QAM modulation schemes at both MW and THz bands. It can be observed that the output I and Q signals are in agreement with the input I and Q signals, which verifies the proposed joint MW/THz receiver concept. The sensitivity of the receiver for a 64 QAM signal is about -58 dBm at the MW band and -45 dBm at the THz band. A proof-of-concept experimental prototype is fabricated on a thin ceramic substrate (ε_r=9.9, h=127 um), using our MHMIC fabrication process, as shown in Figure 6.17. The entire circuit is mounted on a metal base and the output of the receiver is connected to the PCB through wire-bonding to facilitate the measurements.

Figure 6.18 shows the MW measurement setup. An Agilent PSG E8267D Vector Signal Generator is used to generate modulated RF signal at 5.8 GHz and a PSG E8257D Analogy Signal Generator

Table 6.4 Measured constellation diagrams with different orders of modulations at 150 GHz

4QAM	16QAM
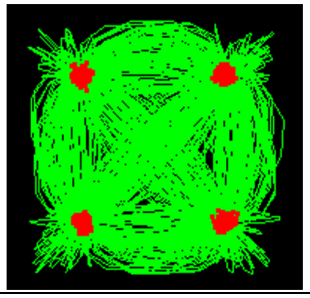	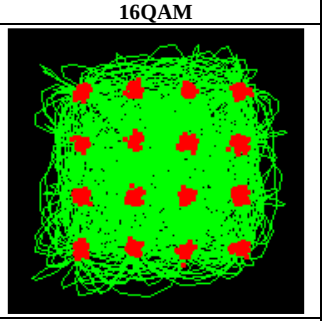
EVM=-24.58dB	EVM=-26.51dB
32QAM	**64QAM**
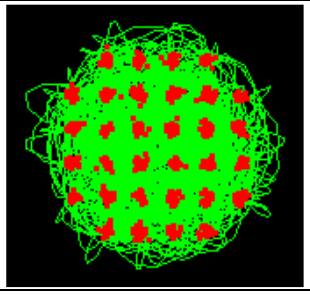	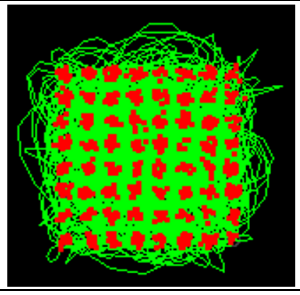
EVM=-27.63dB	EVM=-27.72dB

generates LO signal at 5.7 GHz. A 10-MHz synchronization signal is used to synchronize the RF and LO signals. The output signals of the receiver are sent to the Keysight UXR0702AP Real-Time Oscilloscope, and the demodulated constellations and error vector magnitude (EVM) are extracted. Various modulation schemes, i.e., 4-QAM, 16-QAM, 32-QAM, 64-QAM, 128-QAM, and 256-QAM have been experimentally demonstrated. Table 6.3 summarizes the demodulated signals' constellation and EVM at a symbol rate of 30 MSps, where the symbols are filtered with a raised cosine filter having a 0.3 roll-off factor. It can be seen that the measured average EVM does not exceed -30 dB.

Figure 6.19 shows the THz measurement setup. The Agilent PSG E8257D Analogy Signal Generator and the VDI WR-5.1 frequency multiplier are used to generate the LO signal at 149 GHz. Similarly, the Keysight Arbitrary Waveform Generator (AWG) M8196A and the up-converter are used to generate the RF signal at 150 GHz. The demodulated signals are captured by the Keysight UXR0702AP Real-Time Oscilloscope, extracting the signal constellation and EVM. Table 6.4

Table 6.5 Performance summary and comparison with the state-of-the-art terahertz receivers

Reference	Frequency (GHz)	Modulation signal	Data rate	EVM (dB)	Technology	THz&MW
[263]	125	8-PSK	36 Gbps	N.A.	Mixer-based architecture	No
[264]	140	4-QAM	80 Gbps	-10.80	Mixer-based architecture	No
		16-QAM	120 Gbps	-19.50		
		32-QAM	150 Gbps	-23.60		
[268]	140	16-QAM	4.0 Gbps	-25.00	Mixer-based architecture	No
[270]	120	4-QAM	8.0 Gbps	-17.90	Mixer-based architecture	No
		16-QAM	8.0 Gbps	-17.24		
[272]	145.4	16-QAM	7.2 Gbps	-24.15	Mixer-based architecture	No
		64-QAM	10.8 Gbps	-24.80		
[273]	220	16-QAM	11.2 Gbps	-17.60	Mixer-based architecture	No
		64-QAM	2.4 Gbps	-25.70		
[274]	150	QPSK	12 Gbps	-16.20	Mixer-based architecture	No
		16-QAM	10 Gbps	-19.70		
[275]	135	16-QAM	6.0 Gbps	-20.10	Mixer-based architecture	No
This work	**5.8**	**4-QAM**	**60 Mbps**	**-30.81**	**Multiport linear interferometric architecture**	**Yes**
	150		**1.0 Gbps**	**-24.58**		
	5.8	**16-QAM**	**120 Mbps**	**-33.59**		
	150		**2.0 Gbps**	**-26.51**		
	5.8	**32-QAM**	**150 Mbps**	**-35.08**		
	150		**2.5 Gbps**	**-27.63**		
	5.8	**64-QAM**	**180 Mbps**	**-34.15**		
	150		**3.0 Gbps**	**-27.72**		
	5.8	**128-QAM**	**210 Mbps**	**-35.65**		
	5.8	**256-QAM**	**240 Mbps**	**-35.18**		

summarizes the demodulated 4-QAM, 16-QAM, 32-QAM, and 64-QAM signals with a symbol rate of 500 MSps. The measured average EVM does not exceed -24 dB.

Table 6.5 summarizes and compares previously published state-of-the-art terahertz receivers [268], [269], [270], [271], [272], [273], [274], [275]. The proposed receiver achieves a good performance in both MW and THz bands. In addition, due to the unified MW and THz operating, the proposed receiver is completely different from all previously reported techniques in this regard.

6.5 Conclusion

In this work, a joint MW/THz interferometric receiver suitable for future multifunctional wireless sensing and communication systems is proposed, studied, and demonstrated for the first time. MW and THz signals, at individual frequency channels, are concurrently received and demodulated by a single hardware platform, while it preserves the advantages of conventional multiport interferometric receivers such as simple configuration and low power consumption. An experimental prototype was designed and fabricated with an MHMIC fabrication process. Various modulation schemes were demonstrated for both MW and THz bands. It is worth mentioning that the proposed receiver can be extended to operate in energy harvesting at MW band and data communication at THz band, which will enable energy autonomy and make the receiver totally or partially self-powered.

CHAPTER 7 CONCLUSION

7.1 Conclusion

The rapid advancement of emerging applications has created an urgent need for ultra-high data rates and uncompressed, high-quality communications. These applications demand extremely low latency, high reliability, and precise synchronization, making advanced wireless communication solutions indispensable. Addressing these requirements calls for a fundamental reassessment of traditional wireless principles, driving ongoing research and innovation. As a result, next-generation systems are evolving toward highly integrated, multifunctional, multimode, and multichannel architectures. Among the potential solutions, multiport interferometric architectures stand out as an efficient and competitive approach for front-end design. Compared to conventional heterodyne and homodyne mixers, they offer greater simplicity, wideband operation, lower cost, compatibility at mmW and THz frequencies, and reduced power consumption. This Ph. D. thesis explores and demonstates a series of innovative multiport interferometric receivers for multichannel and multifunction mmW and THz systems and applications.

Chapter 2 summarizes a comprehensive review of the historical development of interferometric receivers, outlining the technological milestones that shaped their design. A detailed comparison between mixer-based front-ends and interferometric front-ends is presented, highlighting their operating principles, performance trade-offs, and cost implications. Various interferometric architectures are then examined, with particular focus on their benefits, including improved sensitivity, wider dynamic range, and lower power consumption. Their applications in wireless communication, radar, and sensing are discussed, providing motivation for the development of innovative designs to address future demands.

In chapter 3, a self-contained dual-input interferometric receiver is proposed and demonstrated for parallel-multichannel systems. This receiver combines dual RF input paths with a single frequency translation unit, reducing the number of required output ports from four to two. This significantly lowers circuit complexity, footprint, cost, and power usage. Unlike conventional solutions that rely on multiple six-port receivers, the proposed design reduces the number of receiver platforms needed in N-path MIMO systems by half, yielding substantial system-level efficiency gains.

In chapter 4, to further enhance system performance, polarization diversity is incorporated. By enabling independent data streams on the same channel, this technique doubles channel capacity and maximizes spectrum efficiency. A compact dual-polarization interferometric receiver based on a square waveguide is proposed and experimentally validated. Prototype measurements confirm the successful demodulation of dual-polarized signals, demonstrating the practicality of the design.

In chapter 5, for IoT environments where wireless sensor nodes and mmW identification tags are pervasive, the need for energy-efficient solutions is paramount. To this end, an interferometric receiver array is developed to enable joint communication, sensing, and wireless power transfer. Using OMTs for polarization diversity and a CMOS-based differential rectifier for energy harvesting, the array supports both wireless communication and power delivery, paving the way for self-sustaining IoT networks.

Finally, chapter 6 introduces the first dual-band interferometric receiver capable of simultaneously handling MW and THz signals on a single hardware platform. This design maintains the simplicity and low power consumption of interferometric architectures while enabling concurrent dual-band operation, with signals converted into distinct IF bands. This innovation overcomes the challenges of integrating widely separated frequency bands and establishes a pathway toward multifunctional, multistandard wireless systems of the future.

7.2 Furture work

This research work offers new horizons for innovative multiport interferometric receiver architectures, with a focus on multichannel and multifunction mmW and THz systems and applications. Multiport interferometric technology stands out due to its low cost, minimal LO power requirements, simple architecture, and wideband capabilities. Extensive research and practical applications have proven the effectiveness of this technology in diverse domains, including next-generation communication systems, high-precision sensing, and high-resolution imaging, highlighting its wide-ranging applicability and value in modern wireless technologies. This thesis primarily addresses the development of receivers, but the transmitter also plays a crucial role in wireless communication systems. Future research could explore the use of multiport interferometric architecture in transmitters. For example, as shown in Figure 7.1, integrating polarization diversity into multiport interferometric transmitter can improve performance by

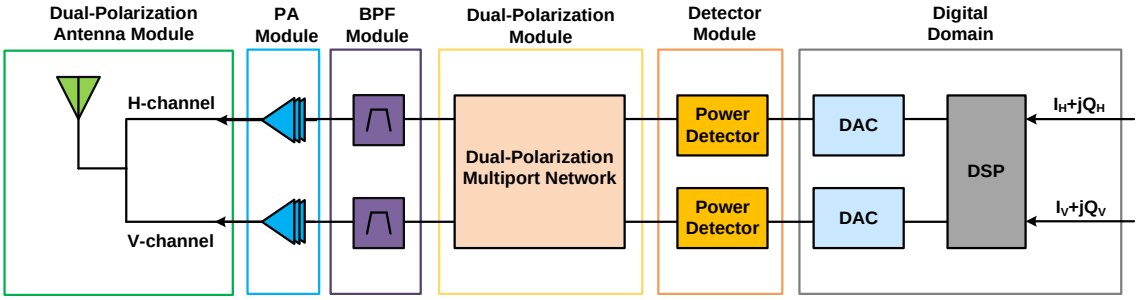

Figure 7.1 Bolck diagram of dual-polarization multiport interferometric transmitter

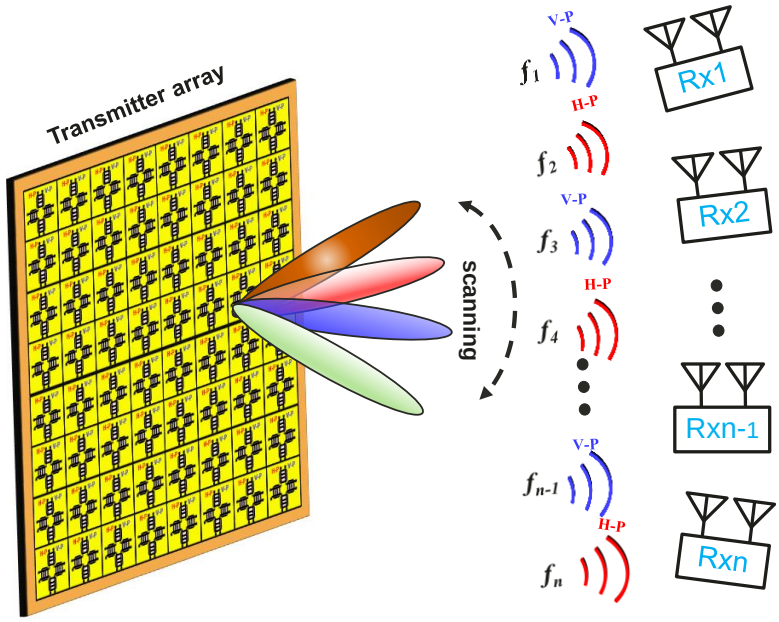

Figure 7.2 Illustration of a multifunctional, multichannel, dual-polarization interferometric transmitter array for future high data-rate, high-capacity, and high-throughput wireless communication systems

supporting independent data streams on the same frequency channel, doubling effective capacity and enhancing spectrum efficiency compared to single-polarized systems. Besides, based on this multiport interferometric transmitter, a multifunctional, multichannel, dual-polarization interferometric transmitter array can be developed as shown in Figure 7.2. This transmitter array can support beam steering capabilities, enabling high-data-rate, high-capacity, and high-throughput communication systems essential for next-generation wireless networks.

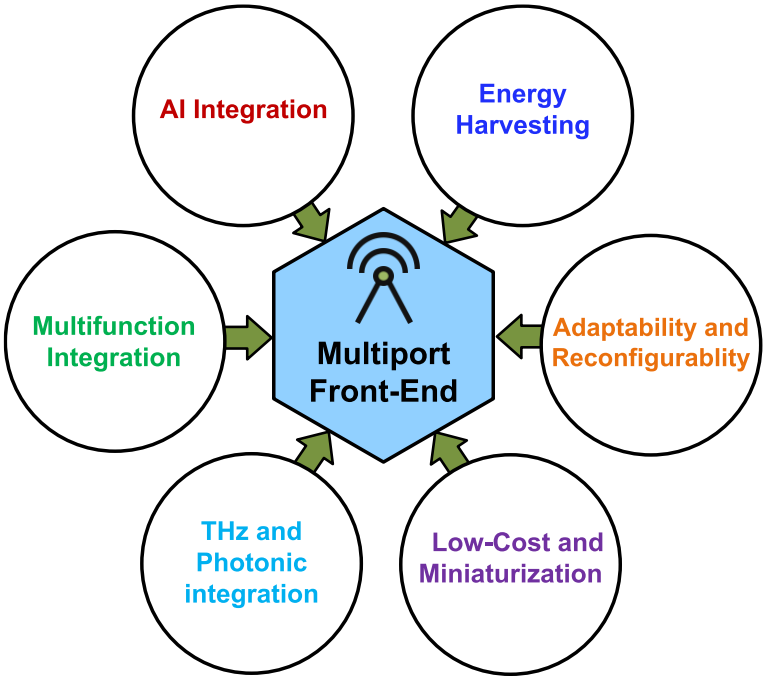

Figure 7.3 Future research perspective for multiport front-end

In addition, to support high-frequency bands, the choice of transmission line becomes crucial. A wide range of transmission line technologies—including microstrip, CPW, SIW, rectangular waveguides, suspended substrate striplines, and composite waveguides—have been employed to realize multiport front-ends. However, microstrip-line implementations remain dominant at lower frequencies due to their ease of fabrication, compact design, and overall simplicity. With the rapid development of THz technology, the demand for low-loss waveguide structures has increased significantly in order to efficiently realize THz circuits and systems. Consequently, future multiport front-ends are expected to adopt SIW and rectangular waveguide structures, which provide lower propagation losses and enhanced performance compared to microstrip lines. Additionally, SIW-based structures and their derivatives are gaining increasing attention in the development of THz multiport front-ends, including those fabricated using CMOS and III-V semiconductor technologies. These advancements will likely drive the integration of multifunctional multiport front-ends, facilitating the development of next-generation THz systems across diverse applications. Future developments in multiport front-end technology will likely emphasize the integration of multiple technological platforms, as illustrated in Figure 7.3. This unified approach is crucial for supporting next-generation intelligent wireless systems, where cross-band

interoperability will enable enhanced performance and flexibility. At the same time, advances in multiport interferometric techniques are expected to drive new innovations in high-resolution THz imaging, offering compact, low-cost, and scalable alternatives to traditional system architectures.

REFERENCES

[1] D. C. Nguyen *et al.*, "6G Internet of Things: A Comprehensive Survey," *IEEE Internet Things J*, vol. 9, no. 1, pp. 359–383, Jan. 2022, doi: 10.1109/JIOT.2021.3103320.

[2] M. Z. Chowdhury, M. Shahjalal, S. Ahmed, and Y. M. Jang, "6G Wireless Communication Systems: Applications, Requirements, Technologies, Challenges, and Research Directions," *IEEE Open Journal of the Communications Society*, vol. 1, pp. 957–975, 2020, doi: 10.1109/OJCOMS.2020.3010270.

[3] T. Maiwald *et al.*, "A Review of Integrated Systems and Components for 6G Wireless Communication in the D-Band," *Proceedings of the IEEE*, vol. 111, no. 3, pp. 220–256, Mar. 2023, doi: 10.1109/JPROC.2023.3240127.

[4] S. Dang, O. Amin, B. Shihada, and M.-S. Alouini, "What should 6G be?," *Nat Electron*, vol. 3, no. 1, pp. 20–29, Jan. 2020, doi: 10.1038/s41928-019-0355-6.

[5] J. Zhang and D. Tao, "Empowering Things with Intelligence: A Survey of the Progress, Challenges, and Opportunities in Artificial Intelligence of Things," May 15, 2021, *Institute of Electrical and Electronics Engineers Inc.* doi: 10.1109/JIOT.2020.3039359.

[6] K. Li *et al.*, "When Internet of Things Meets Metaverse: Convergence of Physical and Cyber Worlds," *IEEE Internet Things J*, vol. 10, no. 5, pp. 4148–4173, Mar. 2023, doi: 10.1109/JIOT.2022.3232845.

[7] A. Nauman, Y. A. Qadri, M. Amjad, Y. Bin Zikria, M. K. Afzal, and S. W. Kim, "Multimedia Internet of Things: A Comprehensive Survey," *IEEE Access*, vol. 8, pp. 8202–8250, 2020, doi: 10.1109/ACCESS.2020.2964280.

[8] W. Jiang, B. Han, M. A. Habibi, and H. D. Schotten, "The Road Towards 6G: A Comprehensive Survey," *IEEE Open Journal of the Communications Society*, vol. 2, pp. 334–366, 2021, doi: 10.1109/OJCOMS.2021.3057679.

[9] W. Saad, M. Bennis, and M. Chen, "A Vision of 6G Wireless Systems: Applications, Trends, Technologies, and Open Research Problems," *IEEE Netw*, vol. 34, no. 3, pp. 134–142, May 2020, doi: 10.1109/MNET.001.1900287.

[10] J. Deng, P. Burasa, and K. Wu, “A 325–500-GHz Waveguide Balun With Polarization Twist Characteristics for THz Integrated Circuits and Systems,” *IEEE Trans Microw Theory Tech*, pp. 1–11, Jul. 2025, doi: 10.1109/TMTT.2025.3591738.

[11] W. Hong *et al.*, “The Role of Millimeter-Wave Technologies in 5G/6G Wireless Communications,” *IEEE Journal of Microwaves*, vol. 1, no. 1, pp. 101–122, Jan. 2021, doi: 10.1109/JMW.2020.3035541.

[12] H. Viswanathan and P. E. Mogensen, “Communications in the 6G Era,” *IEEE Access*, vol. 8, pp. 57063–57074, 2020, doi: 10.1109/ACCESS.2020.2981745.

[13] A. Asit Kumar Majhi and S. Mohanty, “A Comprehensive Review on Internet of Things Applications in Power Systems,” *IEEE Internet Things J*, vol. 11, no. 21, pp. 34896–34923, Nov. 2024, doi: 10.1109/JIOT.2024.3447241.

[14] J. Liu, H. Guo, H. Nishiyama, H. Ujikawa, K. Suzuki, and N. Kato, “New Perspectives on Future Smart FiWi Networks: Scalability, Reliability, and Energy Efficiency,” *IEEE Communications Surveys & Tutorials*, vol. 18, no. 2, pp. 1045–1072, Apr. 2016, doi: 10.1109/COMST.2015.2500960.

[15] Y. A. Qadri, A. Nauman, Y. Bin Zikria, A. V. Vasilakos, and S. W. Kim, “The Future of Healthcare Internet of Things: A Survey of Emerging Technologies,” *IEEE Communications Surveys & Tutorials*, vol. 22, no. 2, pp. 1121–1167, Apr. 2020, doi: 10.1109/COMST.2020.2973314.

[16] S. S. Sefati *et al.*, “A Comprehensive Survey on Resource Management in 6G Network Based on Internet of Things,” *IEEE Access*, vol. 12, pp. 113741–113784, 2024, doi: 10.1109/ACCESS.2024.3444313.

[17] G. Aceto, V. Persico, and A. Pescape, “A Survey on Information and Communication Technologies for Industry 4.0: State-of-the-Art, Taxonomies, Perspectives, and Challenges,” *IEEE Communications Surveys & Tutorials*, vol. 21, no. 4, pp. 3467–3501, Oct. 2019, doi: 10.1109/COMST.2019.2938259.

[18] J. Moghaddasi and K. Wu, “Multifunction, Multiband, and Multimode Wireless Receivers: A Path Toward the Future,” *IEEE Microw Mag*, vol. 21, no. 12, pp. 104–125, Dec. 2020, doi: 10.1109/MMM.2020.3023223.

[19] J. Deng, P. Burasa, and K. Wu, “Multichannel and Multifunction Interferometric Receiver Architectures for Multistandard Millimeter-Wave and Terahertz Applications,” in *2024 IEEE Wireless and Microwave Technology Conference (WAMICON)*, IEEE, Apr. 2024, pp. 1–4. doi: 10.1109/WAMICON60123.2024.10522810.

[20] K. Wu, “MHz-Through-THz (MTT) Challenges and Opportunities [President’s Column],” *IEEE Microw Mag*, vol. 17, no. 2, pp. 8–10, Feb. 2016, doi: 10.1109/MMM.2015.2501159.

[21] J. Deng, P. Burasa, S. A. Keivaan, and K. Wu, “Spatially Distributed Polarization Receiver Array for Communication and Sensing Multifunction Systems,” in *2024 54th European Microwave Conference (EuMC)*, IEEE, Sep. 2024, pp. 148–151. doi: 10.23919/EuMC61614.2024.10732822.

[22] L. Han and K. Wu, “24-GHz joint radar and radio system capable of time-agile wireless sensing and communication,” in *2011 IEEE MTT-S International Microwave Symposium*, IEEE, Jun. 2011, pp. 1–4. doi: 10.1109/MWSYM.2011.5972832.

[23] J. Moghaddasi and K. Wu, “Multifunctional Transceiver for Future Radar Sensing and Radio Communicating Data-Fusion Platform,” *IEEE Access*, vol. 4, pp. 818–838, 2016, doi: 10.1109/ACCESS.2016.2530979.

[24] Z. Feng, Z. Fang, Z. Wei, X. Chen, Z. Quan, and D. Ji, “Joint radar and communication: A survey,” *China Communications*, vol. 17, no. 1, pp. 1–27, Jan. 2020, doi: 10.23919/JCC.2020.01.001.

[25] V. Shatov *et al.*, “Joint Radar and Communications: Architectures, Use Cases, Aspects of Radio Access, Signal Processing, and Hardware,” *IEEE Access*, vol. 12, pp. 47888–47914, 2024, doi: 10.1109/ACCESS.2024.3383771.

[26] L. Han and K. Wu, “Joint wireless communication and radar sensing systems – state of the art and future prospects,” *IET Microwaves, Antennas & Propagation*, vol. 7, no. 11, pp. 876–885, Aug. 2013, doi: 10.1049/iet-map.2012.0450.

[27] A. Liu *et al.*, “A Survey on Fundamental Limits of Integrated Sensing and Communication,” *IEEE Communications Surveys & Tutorials*, vol. 24, no. 2, pp. 994–1034, 2022, doi: 10.1109/COMST.2022.3149272.

[28] X. Cheng, D. Duan, S. Gao, and L. Yang, “Integrated Sensing and Communications (ISAC) for Vehicular Communication Networks (VCN),” *IEEE Internet Things J*, vol. 9, no. 23, pp. 23441–23451, Dec. 2022, doi: 10.1109/JIOT.2022.3191386.

[29] C. Ouyang, Y. Liu, and H. Yang, “Performance of Downlink and Uplink Integrated Sensing and Communications (ISAC) Systems,” *IEEE Wireless Communications Letters*, vol. 11, no. 9, pp. 1850–1854, Sep. 2022, doi: 10.1109/LWC.2022.3184409.

[30] Z. Wei *et al.*, “Integrated Sensing and Communication Signals Toward 5G-A and 6G: A Survey,” *IEEE Internet Things J*, vol. 10, no. 13, pp. 11068–11092, Jul. 2023, doi: 10.1109/JIOT.2023.3235618.

[31] P. Burasa, B. Mnasri, and K. Wu, “A Sourceless Low-Power mmW Receiver Architecture Using Self-Oscillating Mixer Array in 65-nm CMOS,” in *2018 IEEE Wireless Power Transfer Conference (WPTC)*, IEEE, Jun. 2018, pp. 1–3. doi: 10.1109/WPT.2018.8639454.

[32] P. Burasa, B. Mnasri, and K. Wu, “Millimeter-wave CMOS sourceless receiver architecture for 5g-served ultra-low-power sensing and communication systems,” in *IEEE Transactions on Microwave Theory and Techniques*, Institute of Electrical and Electronics Engineers Inc., May 2019, pp. 1688–1696. doi: 10.1109/TMTT.2019.2903051.

[33] F. Chastellain, C. Botteron, and P.-A. Farine, “Looking Inside Modern Receivers,” *IEEE Microw Mag*, vol. 12, no. 2, pp. 87–98, Apr. 2011, doi: 10.1109/MMM.2010.940105.

[34] S. Bronckers, A. Roch, and B. Smolders, “Wireless Receiver Architectures Towards 5G: Where Are We?,” *IEEE Circuits and Systems Magazine*, vol. 17, no. 3, pp. 6–16, Jul. 2017, doi: 10.1109/MCAS.2017.2713306.

[35] C. Andrews and A. C. Molnar, “A passive mixer-first receiver with digitally controlled and widely tunable RF interface,” in *IEEE Journal of Solid-State Circuits*, Dec. 2010, pp. 2696–2708. doi: 10.1109/JSSC.2010.2077151.

[36] S. Zhou and M. C. F. Chang, “A CMOS passive mixer with low flicker noise for low-power direct-conversion receiver,” *IEEE J Solid-State Circuits*, vol. 40, no. 5, pp. 1084–1093, May 2005, doi: 10.1109/JSSC.2005.845981.

[37] P. Song and H. Hashemi, “Mm-Wave Mixer-First Receiver with Selective Passive Wideband Low-Pass Filtering,” *IEEE J Solid-State Circuits*, vol. 56, no. 5, pp. 1454–1463, May 2021, doi: 10.1109/JSSC.2021.3063726.

[38] S. Maas, “Armstrong and the Superheterodyne: A Historical Look at the Mixer,” *IEEE Microw Mag*, vol. 14, no. 6, pp. 34–39, Sep. 2013, doi: 10.1109/MMM.2013.2269858.

[39] S. A. Keivaan, P. Burasa, J. Deng, and K. Wu, “Concurrent Detection of 2-D Angle-of-Arrival and Polarization Enabled by Virtual Transceiver Matrix Architecture,” *IEEE Trans Microw Theory Tech*, 2025, doi: 10.1109/TMTT.2025.3550089.

[40] P. Burasa, T. Djerafi, N. G. Constantin, and K. Wu, “High-Data-Rate Single-Chip Battery-Free Active Millimeter-Wave Identification Tag in 65-nm CMOS Technology,” *IEEE Trans Microw Theory Tech*, vol. 64, no. 7, pp. 2294–2303, Jul. 2016, doi: 10.1109/TMTT.2016.2575826.

[41] M. R. Akdeniz *et al.*, “Millimeter wave channel modeling and cellular capacity evaluation,” *IEEE Journal on Selected Areas in Communications*, vol. 32, no. 6, pp. 1164–1179, 2014, doi: 10.1109/JSAC.2014.2328154.

[42] J. Hasch, E. Topak, R. Schnabel, T. Zwick, R. Weigel, and C. Waldschmidt, “Millimeter-Wave Technology for Automotive Radar Sensors in the 77 GHz Frequency Band,” *IEEE Trans Microw Theory Tech*, vol. 60, no. 3, pp. 845–860, Mar. 2012, doi: 10.1109/TMTT.2011.2178427.

[43] P. Burasa, N. G. Constantin, and K. Wu, “Low-Power Injection-Locked Zero-IF Self-Oscillating Mixer for High Gbit/s Data-Rate Battery-Free Active Tag at Millimeter-Wave Frequencies in 65-nm CMOS,” *IEEE Trans Microw Theory Tech*, vol. 64, no. 4, pp. 1055–1065, Apr. 2016, doi: 10.1109/TMTT.2016.2530717.

[44] P. Burasa, T. Djerafi, N. G. Constantin, and K. Wu, “On-Chip Dual-Band Rectangular Slot Antenna for Single-Chip Millimeter-Wave Identification Tag in Standard CMOS Technology,” *IEEE Trans Antennas Propag*, vol. 65, no. 8, pp. 3858–3868, Aug. 2017, doi: 10.1109/TAP.2017.2710215.

[45] J. Deng and Q. Wang, “A Novel Compact Oversized Rectangular Waveguide Transition Based on Quadruple-Ridged Waveguide for Millimeter Wave Applications,” *J Infrared*

Millim Terahertz Waves, vol. 41, no. 7, pp. 776–784, Jul. 2020, doi: 10.1007/s10762-020-00715-0.

[46] S. Rangan, T. S. Rappaport, and E. Erkip, "Millimeter-wave cellular wireless networks: Potentials and challenges," *Proceedings of the IEEE*, vol. 102, no. 3, pp. 366–385, 2014, doi: 10.1109/JPROC.2014.2299397.

[47] J. Beas, G. Castanon, I. Aldaya, A. Aragon-Zavala, and G. Campuzano, "Millimeter-wave frequency radio over fiber systems: A survey," 2013. doi: 10.1109/SURV.2013.013013.00135.

[48] J. Gao, Y. Qin, B. Deng, H. Wang, and X. Li, "A Novel Method for 3-D Millimeter-Wave Holographic Reconstruction Based on Frequency Interferometry Techniques," *IEEE Trans Microw Theory Tech*, vol. 66, no. 3, pp. 1579–1596, Mar. 2018, doi: 10.1109/TMTT.2017.2772862.

[49] H.-J. Song and N. Lee, "Terahertz Communications: Challenges in the Next Decade," *IEEE Trans Terahertz Sci Technol*, vol. 12, no. 2, pp. 105–117, Mar. 2022, doi: 10.1109/TTHZ.2021.3128677.

[50] J. Deng, P. Burasa, and K. Wu, "Waveguide Coupler With Polarized Rotation Characteristics for Terahertz Applications," *IEEE Trans Microw Theory Tech*, vol. 71, no. 5, pp. 2091–2103, May 2023, doi: 10.1109/TMTT.2022.3223650.

[51] J. Deng, P. Burasa, and K. Wu, "Waveguide Coupler with Self-Contained 90° Polarization Rotation for Integrated THz Waveguide Circuits and Systems," in *2022 IEEE MTT-S International Wireless Symposium (IWS)*, IEEE, Aug. 2022, pp. 1–3. doi: 10.1109/IWS55252.2022.9977877.

[52] J. Deng, P. Burasa, and K. Wu, "Compact 140–220 GHz E/H Waveguide Phase Shifter and Its Application to Terahertz Multiport Circuits," *IEEE Trans Terahertz Sci Technol*, vol. 13, no. 5, pp. 511–525, Sep. 2023, doi: 10.1109/TTHZ.2023.3291456.

[53] J. Deng, P. Burasa, and K. Wu, "Full-Band E- Plane Waveguide Phase Shifters with Self-Compensating Characteristics for THz Circuits and Systems," in *2022 52nd European Microwave Conference (EuMC)*, IEEE, Sep. 2022, pp. 199–202. doi: 10.23919/EuMC54642.2022.9924360.

[54] H.-J. Song and T. Nagatsuma, “Present and Future of Terahertz Communications,” *IEEE Trans Terahertz Sci Technol*, vol. 1, no. 1, pp. 256–263, Sep. 2011, doi: 10.1109/TTHZ.2011.2159552.

[55] P. Hillger, J. Grzyb, R. Jain, and U. R. Pfeiffer, “Terahertz Imaging and Sensing Applications With Silicon-Based Technologies,” *IEEE Trans Terahertz Sci Technol*, vol. 9, no. 1, pp. 1–19, Jan. 2019, doi: 10.1109/TTHZ.2018.2884852.

[56] P. H. Siegel, “Terahertz technology,” *IEEE Trans Microw Theory Tech*, vol. 50, no. 3, pp. 910–928, Mar. 2002, doi: 10.1109/22.989974.

[57] J. Deng, P. Burasa, and K. Wu, “Unified Microwave Terahertz Waveguide Coupler for Multiband Wireless Applications,” *IEEE Trans Compon Packaging Manuf Technol*, vol. 15, no. 5, pp. 1032–1043, 2025, doi: 10.1109/TCPMT.2025.3556594.

[58] J. Hebling, K. Lo Yeh, M. C. Hoffmann, and K. A. Nelson, “High-power THz generation, THz nonlinear optics, and THz nonlinear spectroscopy,” *IEEE Journal on Selected Topics in Quantum Electronics*, vol. 14, no. 2, pp. 345–353, Mar. 2008, doi: 10.1109/JSTQE.2007.914602.

[59] C. Chaccour, M. N. Soorki, W. Saad, M. Bennis, P. Popovski, and M. Debbah, “Seven Defining Features of Terahertz (THz) Wireless Systems: A Fellowship of Communication and Sensing,” *IEEE Communications Surveys and Tutorials*, vol. 24, no. 2, pp. 967–993, 2022, doi: 10.1109/COMST.2022.3143454.

[60] S. Koenig *et al.*, “Wireless sub-THz communication system with high data rate,” *Nat Photonics*, vol. 7, no. 12, pp. 977–981, Dec. 2013, doi: 10.1038/nphoton.2013.275.

[61] P. Hillger, J. Grzyb, R. Jain, and U. R. Pfeiffer, “Terahertz Imaging and Sensing Applications With Silicon-Based Technologies,” *IEEE Trans Terahertz Sci Technol*, vol. 9, no. 1, pp. 1–19, Jan. 2019, doi: 10.1109/TTHZ.2018.2884852.

[62] T. Kawanishi, “THz and photonic seamless communications,” *Journal of Lightwave Technology*, vol. 37, no. 7, pp. 1671–1679, Apr. 2019, doi: 10.1109/JLT.2019.2897042.

[63] R. Halir *et al.*, “Integrated Optical Six-Port Reflectometer in Silicon on Insulator,” *Journal of Lightwave Technology*, vol. 27, no. 23, pp. 5405–5409, Dec. 2009, doi: 10.1109/JLT.2009.2031613.

[64] K. Sengupta, T. Nagatsuma, and D. M. Mittleman, “Terahertz integrated electronic and hybrid electronic–photonic systems,” *Nat Electron*, vol. 1, no. 12, pp. 622–635, Dec. 2018, doi: 10.1038/s41928-018-0173-2.

[65] I. Molina-Fernandez, J. G. Wanguemert-Perez, A. Ortega-Monux, R. G. Bosisio, and K. Wu, “Planar lightwave circuit six-port technique for optical measurements and characterizations,” *Journal of Lightwave Technology*, vol. 23, no. 6, pp. 2148–2157, Jun. 2005, doi: 10.1109/JLT.2005.849944.

[66] G. Vinci, S. Lindner, F. Barbon, R. Weigel, and A. Koelpin, “Promise of a Better Position,” *IEEE Microw Mag*, vol. 13, no. 7, pp. S41–S49, Nov. 2012, doi: 10.1109/MMM.2012.2216710.

[67] V. Adler and K. Hoffmann, “Six-Port Spatial Electromagnetic Wave Measurement,” *IEEE Trans Microw Theory Tech*, vol. 62, no. 12, pp. 3161–3171, Dec. 2014, doi: 10.1109/TMTT.2014.2365024.

[68] B. Laemmle, G. Vinci, L. Maurer, R. Weigel, and A. Koelpin, “A 77-GHz SiGe Integrated Six-Port Receiver Front-End for Angle-of-Arrival Detection,” *IEEE J Solid-State Circuits*, vol. 47, no. 9, pp. 1966–1973, Sep. 2012, doi: 10.1109/JSSC.2012.2201271.

[69] F. Lurz, F. Michler, B. Scheiner, R. Weigel, and A. Koelpin, “Microw(h)att?! Ultralow-Power Six-Port Radar: Realizing Highly Integrated Portable Radar Systems with Good Motion Sensitivity at Relatively Low Cost,” *IEEE Microw Mag*, vol. 19, no. 1, pp. 91–98, Jan. 2018, doi: 10.1109/MMM.2017.2759640.

[70] F. Michler, B. Scheiner, T. Reissland, R. Weigel, and A. Koelpin, “Micrometer Sensing With Microwaves: Precise Radar Systems for Innovative Measurement Applications,” *IEEE Journal of Microwaves*, vol. 1, no. 1, pp. 202–217, Jan. 2021, doi: 10.1109/JMW.2020.3034988.

[71] A. Koelpin, G. Vinci, B. Laemmle, S. Lindner, F. Barbon, and R. Weigel, “Six-Port Technology for Traffic Safety,” *IEEE Microw Mag*, vol. 13, no. 3, pp. 118–127, May 2012, doi: 10.1109/MMM.2012.2185390.

[72] S. Julrat and S. Trabelsi, “Portable Six-Port Reflectometer for Determining Moisture Content of Biomass Material,” *IEEE Sens J*, vol. 17, no. 15, pp. 4814–4819, Aug. 2017, doi: 10.1109/JSEN.2017.2718659.

[73] C. Huan, P. Kontou, S. Ben Smida, and D. E. Anagnostou, “Dual-Band CW Radar System for Vital Signs Detection With Interference Cancellation Method,” *IEEE Trans Microw Theory Tech*, pp. 1–16, 2024, doi: 10.1109/TMTT.2024.3494546.

[74] I. Hussain and K. Wu, “Concurrent Dual-Band Heterodyne Interferometric Receiver for Multistandard and Multifunction Wireless Systems,” *IEEE Trans Microw Theory Tech*, vol. 69, no. 11, pp. 4995–5007, Nov. 2021, doi: 10.1109/TMTT.2021.3099403.

[75] F. R. De Sousa, B. Huyart, and S. Y. Cavalcanti Catunda, “A-to-D converter and lookup table dimensioning for six- or five-port phase discriminators,” *IEEE Trans Instrum Meas*, vol. 54, no. 3, pp. 1254–1259, Jun. 2005, doi: 10.1109/TIM.2005.847193.

[76] A. O. Olopade, A. Hasan, and M. Helaoui, “Concurrent Dual-Band Six-Port Receiver for Multi-Standard and Software Defined Radio Applications,” *IEEE Trans Microw Theory Tech*, vol. 61, no. 12, pp. 4252–4261, Dec. 2013, doi: 10.1109/TMTT.2013.2288690.

[77] P. Feng, B. Huang, Y. Cao, J. Chen, and S. Yan, “A Novel Compact Broadband SIW Six-Port Junction for Angle-of-Arrival Applications,” *IEEE Trans Instrum Meas*, vol. 72, pp. 1–8, 2023, doi: 10.1109/TIM.2023.3280528.

[78] B. Tegowski, M. Wenzel, and A. Koelpin, “Antenna Phase Center Determination Using a Six-Port-Based Direction-of-Arrival Detector,” *IEEE Trans Antennas Propag*, vol. 71, no. 5, pp. 4007–4016, May 2023, doi: 10.1109/TAP.2023.3256485.

[79] S. A. Keivaan, P. Burasa, and K. Wu, “Virtual Receiver Matrix and Combinatory Analog Operations for Future Multifunction Reconfigurable Sensing and Communication Wireless Systems,” *IEEE Trans Microw Theory Tech*, vol. 71, no. 1, pp. 424–433, Jan. 2023, doi: 10.1109/TMTT.2022.3228947.

[80] T. Hentschel, “The six-port as a communications receiver,” *IEEE Trans Microw Theory Tech*, vol. 53, no. 3, pp. 1039–1047, Mar. 2005, doi: 10.1109/TMTT.2005.843507.

[81] G. F. Engen and C. A. Hoer, “Application of an Arbitrary 6-Port Junction to Power-Measurement Problems,” *IEEE Trans Instrum Meas*, vol. 21, no. 4, pp. 470–474, 1972, doi: 10.1109/TIM.1972.4314069.

[82] G. F. Engen, “The Six-Port Reflectometer: An Alternative Network Analyzer,” *IEEE Trans Microw Theory Tech*, vol. 25, no. 12, pp. 1075–1080, Dec. 1977, doi: 10.1109/TMTT.1977.1129277.

[83] G. F. Engen, “An Improved Circuit for Implementing the Six-Port Technique of Microwave Measurements,” *IEEE Trans Microw Theory Tech*, vol. 25, no. 12, pp. 1080–1083, Dec. 1977, doi: 10.1109/TMTT.1977.1129278.

[84] H. M. Cronson and L. Susman, “A Six-Port Automatic Network Analyzer,” *IEEE Trans Microw Theory Tech*, vol. 25, no. 12, pp. 1086–1091, Dec. 1977, doi: 10.1109/TMTT.1977.1129280.

[85] Ji Li, R. G. Bosisio, and K. Wu, “A six-port direct digital millimeter wave receiver,” in *Proceedings of IEEE National Telesystems Conference - NTC ’94*, IEEE, 1994, pp. 79–82. doi: 10.1109/NTC.1994.316688.

[86] Ji Li, R. G. Bosisio, and K. Wu, “Computer and measurement simulation of a new digital receiver operating directly at millimeter-wave frequencies,” *IEEE Trans Microw Theory Tech*, vol. 43, no. 12, pp. 2766–2772, Dec. 1995, doi: 10.1109/22.475633.

[87] J. Deng, P. Burasa, and K. Wu, “Multiport Interferometric Technology: A Versatile Transceiver Solution for Wireless Communication, Sensing, and Imaging Systems,” *Integrated Circuits and Systems*, vol. 2, no. 4, pp. 175-204, Sept.-Oct. 2025, doi: 10.23919/ICS.2025.3618809.

[88] A. J. Venere, J. I. Fernandez Michelli, M. Hurtado, and C. H. Muravchik, “Design of a Multiport Microwave Modulator for Dynamic Polarization Reconfiguration,” *IEEE Trans Microw Theory Tech*, vol. 67, no. 5, pp. 1937–1945, May 2019, doi: 10.1109/TMTT.2019.2899327.

[89] S. O. Tatu and E. Moldovan, “Millimeter Wave Multi-Port Interferometric Radar Sensors: Evolution of Fabrication and Characterization Technologies,” *Sensors*, vol. 20, no. 19, p. 5477, Sep. 2020, doi: 10.3390/s20195477.

[90] K. Haddadi, M. M. Wang, D. Glay, and T. Lasri, “A 60 GHz Six-Port Distance Measurement System With Sub-Millimeter Accuracy,” *IEEE Microwave and Wireless Components Letters*, vol. 19, no. 10, pp. 644–646, Oct. 2009, doi: 10.1109/LMWC.2009.2029744.

[91] K. Haddadi and T. Lasri, “Scanning Microwave Near-Field Microscope Based on the Multiport Technology,” *IEEE Trans Instrum Meas*, vol. 62, no. 12, pp. 3189–3193, Dec. 2013, doi: 10.1109/TIM.2013.2270918.

[92] K. Haddadi, M. M. Wang, K. Nouri, D. Glay, and T. Lasri, “Calibration and Performance of Two New Ultra-Wideband Four-Port-Based Systems,” *IEEE Trans Microw Theory Tech*, vol. 56, no. 12, pp. 3137–3142, Dec. 2008, doi: 10.1109/TMTT.2008.2007138.

[93] L. Chioukh, T. Djerafi, D. Deslandes, and K. Wu, “Concurrent cardiopulmonary detection using 12/24 GHz harmonic multiport interferometer radar architecture,” *IET Microwaves, Antennas & Propagation*, vol. 13, no. 13, pp. 2396–2404, Oct. 2019, doi: 10.1049/iet-map.2018.5665.

[94] E. E. Djoumessi, S. O. Tatu, and Ke Wu, “Frequency-Agile Dual-Band Direct Conversion Receiver for Cognitive Radio Systems,” *IEEE Trans Microw Theory Tech*, vol. 58, no. 1, pp. 87–94, Jan. 2010, doi: 10.1109/TMTT.2009.2035952.

[95] M. D. Ardakani and S. O. Tatu, “V-Band Six-Port Interferometer Receiver: High Data-Rate Wireless Applications, BER and EVM Analysis, and CFO Compensation,” *IEEE Access*, vol. 9, pp. 160847–160854, 2021, doi: 10.1109/ACCESS.2021.3132635.

[96] W. Zhang *et al.*, “Concurrent Dual-Band Low Intermediate Frequency Receiver Based on the Multiport Correlator and Single Local Oscillator,” *IEEE Microwave and Wireless Components Letters*, vol. 28, no. 4, pp. 353–355, Apr. 2018, doi: 10.1109/LMWC.2018.2805459.

[97] J. Osth, Owais, M. Karlsson, A. Serban, S. Gong, and P. Karlsson, “Direct Carrier Six-Port Modulator Using a Technique to Suppress Carrier Leakage,” *IEEE Trans Microw Theory Tech*, vol. 59, no. 3, pp. 741–747, Mar. 2011, doi: 10.1109/TMTT.2011.2104972.

[98] E. Moldovan, S.-O. Tatu, T. Gaman, K. Wu, and R. G. Bosisio, “A new 94-GHz six-port collision-avoidance radar sensor,” *IEEE Trans Microw Theory Tech*, vol. 52, no. 3, pp. 751–759, Mar. 2004, doi: 10.1109/TMTT.2004.823533.

[99] H. Arab, L. Chioukh, M. Dashti Ardakani, S. Dufour, and S. O. Tatu, “Early-Stage Detection of Melanoma Skin Cancer Using Contactless Millimeter-Wave Sensors,” *IEEE Sens J*, vol. 20, no. 13, pp. 7310–7317, Jul. 2020, doi: 10.1109/JSEN.2020.2969414.

[100] J. Osth *et al.*, “Six-Port Gigabit Demodulator,” *IEEE Trans Microw Theory Tech*, vol. 59, no. 1, pp. 125–131, Jan. 2011, doi: 10.1109/TMTT.2010.2091198.

[101] S. O. Tatu, E. Moldovan, K. Wu, and R. G. Bosisio, “A new direct millimeter-wave six-port receiver,” *IEEE Trans Microw Theory Tech*, vol. 49, no. 12, pp. 2517–2522, 2001, doi: 10.1109/22.971644.

[102] S. O. Tatu, E. Moldovan, G. Brehm, K. Wu, and R. G. Bosisio, “Ka-band direct digital receiver,” *IEEE Trans Microw Theory Tech*, vol. 50, no. 11, pp. 2436–2442, Nov. 2002, doi: 10.1109/TMTT.2002.804646.

[103] A. Stelzer, C. G. Diskus, K. Lubke, and H. W. Thim, “A microwave position sensor with submillimeter accuracy,” *IEEE Trans Microw Theory Tech*, vol. 47, no. 12, pp. 2621–2624, 1999, doi: 10.1109/22.809015.

[104] S. O. Tatu, E. Moldovan, K. Wu, R. G. Bosisio, and T. A. Denidni, “Ka-band analog front-end for software-defined direct conversion receiver,” *IEEE Trans Microw Theory Tech*, vol. 53, no. 9, pp. 2768–2776, Sep. 2005, doi: 10.1109/TMTT.2005.854181.

[105] Xinyu Xu, R. G. Bosisio, and K. Wu, “Analysis and implementation of six-port software-defined radio receiver platform,” *IEEE Trans Microw Theory Tech*, vol. 54, no. 7, pp. 2937–2943, Jul. 2006, doi: 10.1109/TMTT.2006.877449.

[106] J. Pérez-Dueñas, J. Wangüemert-Pérez, and I. Molina-Fernández, “Novel modulation scheme and six-port based RAKE receiver for DS-UWB,” *IEEE Trans Wirel Commun*, vol. 8, no. 7, pp. 3628–3633, Jul. 2009, doi: 10.1109/TWC.2009.080576.

[107] P. Cheong and K. Wu, “Full-Range CSRR-Based Angular Displacement Sensing With Multiport Interferometric Platform,” *IEEE Trans Microw Theory Tech*, vol. 69, no. 11, pp. 4813–4821, Nov. 2021, doi: 10.1109/TMTT.2021.3089778.

[108] Y. Zhao, C. Viereck, J. F. Frigon, R. G. Bosisio, and K. Wu, “Direct quadrature phase shift keying modulator using six-port technology,” *Electron Lett*, vol. 41, no. 21, pp. 1180–1181, Oct. 2005, doi: 10.1049/el:20052466.

[109] B. Luo and M. Y. W. Chia, “Direct 16 QAM six-port modulator,” *Electron Lett*, vol. 44, no. 15, pp. 910–911, Jul. 2008, doi: 10.1049/el:20080913.

[110] W. Ciccognani, M. Ferrari, F. Giannini, and E. Limiti, “A novel broadband MMIC vector modulator for V-band applications,” *International Journal of RF and Microwave Computer-Aided Engineering*, vol. 20, no. 1, pp. 103–113, Jan. 2010, doi: 10.1002/mmce.20405.

[111] W. Lee, K. Oh, D. Kim, and J. Yu, “Direct six-port modulator using polyphase networks,” *Microw Opt Technol Lett*, vol. 53, no. 10, pp. 2321–2324, Oct. 2011, doi: 10.1002/mop.26288.

[112] S. Z. Ibrahim, A. M. Abbosh, and M. A. Antoniades, “Direct quadrature phase shift keying modulation using compact wideband six-port networks,” *IET Microwaves, Antennas & Propagation*, vol. 6, no. 8, pp. 854–861, Jun. 2012, doi: 10.1049/iet-map.2012.0010.

[113] J. Osth, M. Karlsson, A. Serban, and S. Gong, “M-QAM Six-Port Modulator Using Only Binary Baseband Data, Electrical or Optical,” *IEEE Trans Microw Theory Tech*, vol. 61, no. 6, pp. 2506–2513, Jun. 2013, doi: 10.1109/TMTT.2013.2259255.

[114] J. Osth, M. Karlsson, A. Serban, and S. Gong, “A Comparative Study of Single-Ended vs. Differential Six-Port Modulators for Wireless Communications,” *IEEE Transactions on Circuits and Systems I: Regular Papers*, vol. 62, no. 2, pp. 564–570, Feb. 2015, doi: 10.1109/TCSI.2014.2362310.

[115] X. Song *et al.*, “Six-Port Direct Modulator With Carrier Suppression Technology for High-Speed High-Frequency Wireless Communications,” *IEEE Microwave and Wireless Components Letters*, vol. 27, no. 8, pp. 745–747, Aug. 2017, doi: 10.1109/LMWC.2017.2723950.

[116] H. Moazzen, A. Mohammadi, and R. Mirzavand, “Multilevel outphasing system using six-port modulators and doherty power amplifiers,” *Analog Integr Circuits Signal Process*, vol. 90, no. 2, pp. 361–372, Feb. 2017, doi: 10.1007/s10470-016-0908-9.

[117] V. Riess, P. Starke, C. Carta, and F. Ellinger, “An Integrated mm-Wave Quadrature Up-Conversion Mixer Based on a Six-Port Modulator,” in *2019 14th European Microwave Integrated Circuits Conference (EuMIC)*, IEEE, Sep. 2019, pp. 176–179. doi: 10.23919/EuMIC.2019.8909459.

[118] M. Tu, P. Cheong, W.-W. Choi, and K. Wu, “Multiport Transmitter Front-End Architecture for Concurrent Dual-Band Digital Predistortion,” *IEEE Transactions on Circuits and Systems II: Express Briefs*, vol. 71, no. 2, pp. 572–576, Feb. 2024, doi: 10.1109/TCSII.2023.3308597.

[119] Z. Peng, L. Ran, and C. Li, “A κ-Band Portable FMCW Radar with Beamforming Array for Short-Range Localization and Vital-Doppler Targets Discrimination,” *IEEE Trans Microw Theory Tech*, vol. 65, no. 9, pp. 3443–3452, Sep. 2017, doi: 10.1109/TMTT.2017.2662680.

[120] S. M. Moon, I. B. Yom, and H. L. Lee, “K-band phase discriminator using multiport downconversion for monopulse tracker,” *IEEE Microwave and Wireless Components Letters*, vol. 27, no. 6, pp. 599–601, Jun. 2017, doi: 10.1109/LMWC.2017.2701331.

[121] M. Voelkel, H. Hirsch, M. Dietz, R. Weigel, A. Hagelauer, and D. Kissinger, “A Low-Power 120-GHz integrated sixport receiver front-end with digital adjustable gain in a 130-nm bicmos technology,” in *2017 IEEE Bipolar/BiCMOS Circuits and Technology Meeting (BCTM)*, IEEE, Oct. 2017, pp. 82–85. doi: 10.1109/BCTM.2017.8112916.

[122] M. Voelkel, R. Weigel, and A. Hagelauer, “A Digital Adjustable 60-GHz Integrated Sixport Receiver Front-End in a 130-nm BiCMOS Technology,” in *2019 IEEE 19th Topical Meeting on Silicon Monolithic Integrated Circuits in RF Systems (SiRF)*, IEEE, Jan. 2019, pp. 1–3. doi: 10.1109/SIRF.2019.8709117.

[123] V. Riess, D. Fritsche, P. Starke, C. Carta, and F. Ellinger, “A mm-Wave Quadrature Down-Conversion Mixer Based on a Six-Port Junction in 130-nm SiGe BiCMOS,” in *2019 IEEE MTT-S International Microwave Symposium (IMS)*, IEEE, Jun. 2019, pp. 232–235. doi: 10.1109/MWSYM.2019.8700739.

[124] P. Cheong and K. Wu, “Compendious Concurrent Dual-Band Receiver Based on Multiport Interferometric Architecture,” *IEEE Trans Microw Theory Tech*, vol. 69, no. 7, pp. 3388–3398, Jul. 2021, doi: 10.1109/TMTT.2021.3061578.

[125] M. Akbari *et al.*, “Highly Efficient Front End Direct Conversion Receiver for 28-GHz Wireless Access Point,” *IEEE Access*, vol. 9, pp. 88879–88893, 2021, doi: 10.1109/ACCESS.2021.3089582.

[126] K. Haddadi, C. Lenoir, M. Sebbache, J. Morán-Meza, and F. Piquemal, “Demonstration of Scanning Near-Field Microwave Microscopy of Sub-fF Vertical MOS Capacitors Using Six-Port Interferometry,” in *2025 IEEE MTT-S Latin America Microwave Conference (LAMC)*, IEEE, Jan. 2025, pp. 128–131. doi: 10.1109/LAMC63321.2025.10880556.

[127] Yanyang Zhao, J.-F. Frigon, K. Wu, and R. G. Bosisio, “Multi(Six)-port impulse radio for ultra-wideband,” *IEEE Trans Microw Theory Tech*, vol. 54, no. 4, pp. 1707–1712, Jun. 2006, doi: 10.1109/TMTT.2006.871988.

[128] Jaber Moghaddasi; Ke Wu, *Unified radar-communication (RadCom) multi-port interferometer transceiver*. Nuremberg: IEEE, 2013. doi: 10.23919/EuMC.2013.6687026.

[129] A. Serban *et al.*, “Six-port transceiver for 6–9 GHz ultrawideband systems,” *Microw Opt Technol Lett*, vol. 52, no. 3, pp. 740–746, Mar. 2010, doi: 10.1002/mop.25021.

[130] J. Osth, O. Owais, M. Karlsson, A. Serban, and Shaofang Gong, “Schottky diode as high-speed variable impedance load in six-port modulators,” in *2011 IEEE International Conference on Ultra-Wideband (ICUWB)*, IEEE, Sep. 2011, pp. 68–71. doi: 10.1109/ICUWB.2011.6058924.

[131] Bin Luo and M. Y.-W. Chia, “Performance Analysis of Serial and Parallel Six-Port Modulators,” *IEEE Trans Microw Theory Tech*, vol. 56, no. 9, pp. 2062–2068, Sep. 2008, doi: 10.1109/TMTT.2008.2001955.

[132] I. Hussain and K. Wu, “Low-Power Receiver Architecture for 5G and IoT-Oriented Wireless Information and Power Transfer Applications,” in *2019 IEEE MTT-S International Microwave Symposium (IMS)*, IEEE, Jun. 2019, pp. 1148–1151. doi: 10.1109/MWSYM.2019.8701030.

[133] K. Haddadi and C. Loyez, “Millimeter-wave six-port IQ demodulator in 65 nm SOI CMOS technology,” in *2016 IEEE International Instrumentation and Measurement Technology Conference Proceedings*, IEEE, May 2016, pp. 1–5. doi: 10.1109/I2MTC.2016.7520391.

[134] J. J. Kucera and U. Lott, “A zero DC-power low-distortion mixer for wireless applications,” *IEEE Microwave and Guided Wave Letters*, vol. 9, no. 4, pp. 157–159, Apr. 1999, doi: 10.1109/75.763246.

[135] M. Mailand, R. Richter, and H.-J. Jentschel, “Nonlinearity analysis of power detectors in direct conversion receivers utilizing six-port technology,” in *International Symposium on Signals, Circuits and Systems, 2005. ISSCS 2005.*, IEEE, pp. 123–126. doi: 10.1109/ISSCS.2005.1509866.

[136] W. Zhang *et al.*, “Homodyne Digitally Assisted and Spurious-Free Mixerless Direct Carrier Modulator With High Carrier Leakage Suppression,” *IEEE Trans Microw Theory Tech*, vol. 66, no. 3, pp. 1475–1488, Mar. 2018, doi: 10.1109/TMTT.2017.2735408.

[137] X. Ma *et al.*, “Analysis of dark current considering trap-assisted tunneling mechanism for InGaAs PIN photodetectors,” *Opt Quantum Electron*, vol. 49, no. 12, p. 407, Dec. 2017, doi: 10.1007/s11082-017-1242-x.

[138] I. Hussain, L.-P. Carignan, and K. Wu, “Balanced Detection in Multiport Direct-Conversion Interferometric Receiver for IoT Systems,” *IEEE Syst J*, vol. 18, no. 1, pp. 612–619, Mar. 2024, doi: 10.1109/JSYST.2023.3337379.

[139] J. Osth *et al.*, “Diode configurations in six-port receivers with simplified interface to amplifier and filter,” in *2010 IEEE International Conference on Ultra-Wideband*, IEEE, Sep. 2010, pp. 1–4. doi: 10.1109/ICUWB.2010.5615597.

[140] T. Liu *et al.*, “Influences of contact electrode shape and incidence direction on p-i-n photodiodes,” *IET Optoelectronics*, vol. 13, no. 4, pp. 151–154, Aug. 2019, doi: 10.1049/iet-opt.2018.5037.

[141] K. Wu, “Multiport interferometer techniques for innovative transceiver applications,” in *2010 IEEE Radio and Wireless Symposium (RWS)*, IEEE, Jan. 2010, pp. 531–534. doi: 10.1109/RWS.2010.5434107.

[142] K. Haddadi, M. M. Wang, C. Loyez, D. Glay, and T. Lasri, “Four-port communication receiver with digital IQ-regeneration,” *IEEE Microwave and Wireless Components Letters*, vol. 20, no. 1, pp. 58–60, Jan. 2010, doi: 10.1109/LMWC.2009.2035969.

[143] C. de la Morena-Alvarez-Palencia, K. Mabrouk, B. Huyart, A. Mbaye, and M. Burgos-Garcia, “Direct Baseband I-Q Regeneration Method for Five-Port Receivers Improving DC-Offset and Second-Order Intermodulation Distortion Rejection,” *IEEE Trans Microw Theory Tech*, vol. 60, no. 8, pp. 2634–2643, Aug. 2012, doi: 10.1109/TMTT.2012.2199512.

[144] M. Hazer-Sahlabadi, A. Abdipour, and A. Mohammadi, “A Seven-Port Receiver for MIMO 2x2 Communication Systems,” in *2019 27th Iranian Conference on Electrical Engineering (ICEE)*, IEEE, Apr. 2019, pp. 1382–1386. doi: 10.1109/IranianCEE.2019.8786755.

[145] J. Deng, P. Burasa, and K. Wu, “All-in-One Dual-Polarization Waveguide Receiver for Multichannel Wireless Systems,” *IEEE Trans Microw Theory Tech*, vol. 72, no. 8, pp. 4998–5013, Aug. 2024, doi: 10.1109/TMTT.2024.3355306.

[146] B. Mnasri, T. Djerafi, S. O. Tatu, and K. Wu, “Spatially Distributed Multi-Input Interferometric Receiver for 5G Wireless Systems and Beyond,” *IEEE Trans Microw Theory Tech*, vol. 67, no. 7, pp. 2904–2915, Jul. 2019, doi: 10.1109/TMTT.2018.2876260.

[147] J. Moghaddasi and K. Wu, “Millimeter-Wave Multifunction Multiport Interferometric Receiver for Future Wireless Systems,” *IEEE Trans Microw Theory Tech*, vol. 66, no. 3, pp. 1452–1466, Mar. 2018, doi: 10.1109/TMTT.2017.2772927.

[148] C.-H. Wang *et al.*, “A 60GHz Low-Power Six-Port Transceiver for Gigabit Software-Defined Transceiver Applications,” in *2007 IEEE International Solid-State Circuits Conference. Digest of Technical Papers*, IEEE, Feb. 2007, pp. 192–596. doi: 10.1109/ISSCC.2007.373359.

[149] H. S. Lim, W. K. Kim, J. W. Yu, H. C. Park, W. J. Byun, and M. S. Song, “Compact six-port transceiver for time-division duplex systems,” *IEEE Microwave and Wireless Components Letters*, vol. 17, no. 5, pp. 394–396, 2007, doi: 10.1109/LMWC.2007.895731.

[150] X. Song *et al.*, “A Six-Port Transceiver for Frequency-Division Duplex Systems,” *IEEE Microwave and Wireless Components Letters*, vol. 28, no. 10, pp. 936–938, Oct. 2018, doi: 10.1109/LMWC.2018.2860781.

[151] J. Deng, P. Burasa, and K. Wu, “Self-Contained Dual-Input Interferometric Receiver for Paralleled-Multichannel Wireless Systems,” *IEEE Transactions on Circuits and Systems I: Regular Papers*, vol. 71, no. 2, pp. 934–947, Feb. 2024, doi: 10.1109/TCSI.2023.3338214.

[152] J. Deng, P. Burasa, and K. Wu, “Joint Multiband Linear Interferometric Receiver for Integrated Microwave and Terahertz Sensing and Communication Systems,” *IEEE Trans Microw Theory Tech*, vol. 72, no. 9, pp. 5550–5562, Sep. 2024, doi: 10.1109/TMTT.2024.3363173.

[153] M. D. Ardakani, R. Karimian, J. Pourahmadazar, S. Tatu, S. Ahmadi, and M. Zaghloul, "Characterization of a Highly Efficient Waveguide Front-End Direct-Conversion Receiver for 60-GHz Wireless Systems," in *2021 IEEE International Symposium on Antennas and Propagation and North American Radio Science Meeting, APS/URSI 2021 - Proceedings*, Institute of Electrical and Electronics Engineers Inc., 2021, pp. 529–530. doi: 10.1109/APS/URSI47566.2021.9703708.

[154] P. Cheong, M. Tu, W.-W. Choi, and K. Wu, "An Ingenious Multiport Interferometric Front-End for Concurrent Dual-Band Transmission," *IEEE Trans Microw Theory Tech*, vol. 70, no. 3, pp. 1725–1731, Mar. 2022, doi: 10.1109/TMTT.2021.3134692.

[155] P. Burasa, J. Deng, and K. Wu, "A 300-GHz Dual-Polarized CMOS Waveguide Receiver for High-Density Terahertz Integrated Multichannel Wireless Systems-on-Chip," *IEEE Trans Microw Theory Tech*, pp. 1–15, 2024, doi: 10.1109/TMTT.2024.3487519.

[156] J. Deng, P. Burasa, S. A. Keivaan, and K. Wu, "Waveguide Receiver Array for Joint Communication, Sensing, and Power Transfer Systems," *IEEE Trans Microw Theory Tech*, pp. 1–14, 2024, doi: 10.1109/TMTT.2024.3505842.

[157] M. Voelkel, M. Dietz, A. Hagelauer, E. M. Hussein, D. Kissinger, and R. Weigel, "A Digital Adjustable Fully Integrated Bistatic Interferometric Radar Transceiver at 60 GHz in a 130 nm BiCMOS Technology," in *2019 14th European Microwave Integrated Circuits Conference (EuMIC)*, IEEE, Sep. 2019, pp. 220–223. doi: 10.23919/EuMIC.2019.8909608.

[158] M. Voelkel, S. Pechmann, E. M. Hussein, D. Kissinger, R. Weigel, and A. Hagelauer, "A Cascadable Integrated Bistatic Six-port Transceiver at 60 GHz in a 130-nm BiCMOS Technology for SIMO-Radar Applications," in *2019 IEEE Asia-Pacific Microwave Conference (APMC)*, IEEE, Dec. 2019, pp. 622–624. doi: 10.1109/APMC46564.2019.9038421.

[159] M. Voelkel, S. Pechmann, H. J. Ng, D. Kissinger, R. Weigel, and A. Hagelauer, "An Integrated Bistatic 4TX/4RX Six-Port MIMO-Transceiver at 60 GHz in a 130-nm SiGe BiCMOS Technology for Radar Applications," in *2020 IEEE/MTT-S International Microwave Symposium (IMS)*, IEEE, Aug. 2020, pp. 1219–1222. doi: 10.1109/IMS30576.2020.9224001.

[160] H.-C. Yen, L.-Y. Ou Yang, and Z.-M. Tsai, “3-D Indoor Localization and Identification Through RSSI-Based Angle of Arrival Estimation With Real Wi-Fi Signals,” *IEEE Trans Microw Theory Tech*, vol. 70, no. 10, pp. 4511–4527, Oct. 2022, doi: 10.1109/TMTT.2022.3194563.

[161] S. Julrat and S. Trabelsi, “Free-Space Transmission Dielectric Properties Measurement Based on Six-Port Technology,” *IEEE Trans Instrum Meas*, vol. 70, pp. 1–7, 2021, doi: 10.1109/TIM.2021.3084292.

[162] J. Moghaddasi, T. Djerafi, and K. Wu, “Multiport Interferometer-Enabled 2-D Angle of Arrival (AOA) Estimation System,” *IEEE Trans Microw Theory Tech*, vol. 65, no. 5, pp. 1767–1779, May 2017, doi: 10.1109/TMTT.2017.2690869.

[163] S. Mann *et al.*, “High-Precision Interferometric Radar for Sheet Thickness Monitoring,” *IEEE Trans Microw Theory Tech*, vol. 66, no. 6, pp. 3153–3166, Jun. 2018, doi: 10.1109/TMTT.2018.2825328.

[164] H. Hirayama, T. Yakabe, and Y. Kami, “An imaging system for EM emitting sources using a 6-port correlator,” in *2001 IEEE EMC International Symposium. Symposium Record. International Symposium on Electromagnetic Compatibility (Cat. No.01CH37161)*, IEEE, pp. 374–377. doi: 10.1109/ISEMC.2001.950667.

[165] K. Haddadi and T. Lasri, “Six-port technology for millimeter-wave radar and imaging applications,” in *2014 IEEE Topical Conference on Wireless Sensors and Sensor Networks (WiSNet)*, IEEE, Jan. 2014, pp. 1–3. doi: 10.1109/WiSNet.2014.6825508.

[166] Hsin-Chia Lu and Tah-Hsiung Chu, “Microwave diversity imaging using six-port reflectometer,” *IEEE Trans Microw Theory Tech*, vol. 47, no. 1, pp. 84–87, 1999, doi: 10.1109/22.740082.

[167] K. Haddadi and T. Lasri, “Six-port-based compact and low-cost near-field 35GHz microscopy platform for non-destructive evaluation,” *NDT & E International*, vol. 55, pp. 102–108, Apr. 2013, doi: 10.1016/j.ndteint.2013.01.018.

[168] S. Ladan, A. B. Guntupalli, and K. Wu, “A high-efficiency 24 GHz rectenna development towards millimeter-wave energy harvesting and wireless power transmission,” *IEEE*

Transactions on Circuits and Systems I: Regular Papers, vol. 61, no. 12, pp. 3358–3366, 2014, doi: 10.1109/TCSI.2014.2338616.

[169] J. Hu and K. Ma, "Analysis and Design of a Broadband Receiver Front End for 0.1-to-40-GHz Application," *IEEE Transactions on Circuits and Systems I: Regular Papers*, vol. 68, no. 6, pp. 2393–2403, Jun. 2021, doi: 10.1109/TCSI.2021.3064262.

[170] L. Han and K. Wu, "24-GHz integrated radio and radar system capable of time-agile wireless communication and sensing," *IEEE Trans Microw Theory Tech*, vol. 60, no. 3 PART 1, pp. 619–631, Mar. 2012, doi: 10.1109/TMTT.2011.2179552.

[171] T. Chi, J. S. Park, S. Li, and H. Wang, "A millimeter-wave polarization-division-duplex transceiver front-end with an on-chip multifeed self-interference-canceling antenna and an all-passive reconfigurable canceller," *IEEE J Solid-State Circuits*, vol. 53, no. 12, pp. 3628–3639, Dec. 2018, doi: 10.1109/JSSC.2018.2878823.

[172] J. Hu, K. Ma, S. Mou, and F. Meng, "A Seven-Octave Broadband LNA MMIC Using Bandwidth Extension Techniques and Improved Active Load," *IEEE Transactions on Circuits and Systems I: Regular Papers*, vol. 65, no. 10, pp. 3150–3161, Oct. 2018, doi: 10.1109/TCSI.2018.2803299.

[173] P. Burasa, N. G. Constantin, and K. Wu, "High-Efficiency Wideband Rectifier for Single-Chip Batteryless Active Millimeter-Wave Identification (MMID) Tag in 65-nm Bulk CMOS Technology," *IEEE Trans Microw Theory Tech*, vol. 62, no. 4, pp. 1005–1011, Apr. 2014, doi: 10.1109/TMTT.2014.2305136.

[174] Z. Cao *et al.*, "Advanced integration techniques on broadband millimeter-wave beam steering for 5G wireless networks and beyond," Jan. 01, 2016, *Institute of Electrical and Electronics Engineers Inc.* doi: 10.1109/JQE.2015.2509256.

[175] P. Burasa, T. Djerafi, and K. Wu, "A 28 GHz and 60 GHz Dual-Band On-Chip Antenna for 5G-Compatible IoT-Served Sensors in Standard CMOS Process," *IEEE Trans Antennas Propag*, vol. 69, no. 5, pp. 2940–2945, May 2021, doi: 10.1109/TAP.2020.3025236.

[176] T. S. Rappaport *et al.*, "Millimeter wave mobile communications for 5G cellular: It will work!," *IEEE Access*, vol. 1, pp. 335–349, 2013, doi: 10.1109/ACCESS.2013.2260813.

[177] S. Jain, Y. Wang, and A. Natarajan, “A 10GHz CMOS RX frontend with spatial cancellation of co-channel interferers for MIMO/digital beamforming arrays,” in *2016 IEEE Radio Frequency Integrated Circuits Symposium (RFIC)*, IEEE, May 2016, pp. 99–102. doi: 10.1109/RFIC.2016.7508260.

[178] E. G. Larsson, O. Edfors, F. Tufvesson, and T. L. Marzetta, “Massive MIMO for next generation wireless systems,” *IEEE Communications Magazine*, vol. 52, no. 2, pp. 186–195, Feb. 2014, doi: 10.1109/MCOM.2014.6736761.

[179] S. Jain, A. Agrawal, R. Garg, and A. Natarajan, “Recent Developments in Integrated Interferer-Tolerant Receivers for Reconfigurable Radios,” *IEEE Journal of Microwaves*, vol. 1, no. 3, pp. 723–737, Jul. 2021, doi: 10.1109/JMW.2021.3070470.

[180] Ji Li, R. G. Bosisio, and K. Wu, “Dual-tone calibration of six-port junction and its application to the six-port direct digital millimetric receiver,” *IEEE Trans Microw Theory Tech*, vol. 44, no. 1, pp. 93–99, Jan. 1996, doi: 10.1109/22.481390.

[181] S. A. Keivaan, P. Burasa, and K. Wu, “Interferometric Receiver Architecture for Multifunction Wireless Systems,” in *2022 52nd European Microwave Conference (EuMC)*, IEEE, Sep. 2022, pp. 16–19. doi: 10.23919/EuMC54642.2022.9924460.

[182] T. Jiang et al., “Six-port technology for millimeter wave MIMO systems,” in *2013 European Microwave Conference*, Germany: IEEE, Dec. 2013, pp. 1591–1594.

[183] S. M. Moon and H. L. Lee, “Dual-Band Direct Conversion Receiver with Additive Mixing Architecture,” *IEEE Access*, vol. 10, pp. 15436–15442, 2022, doi: 10.1109/ACCESS.2022.3149346.

[184] S. M. Moon, J. W. Yu, and M. Q. Lee, “CMOS four-port direct conversion receiver for BPSK demodulation,” *IEEE Microwave and Wireless Components Letters*, vol. 19, no. 9, pp. 581–583, Sep. 2009, doi: 10.1109/LMWC.2009.2027091.

[185] I.-D. Choi, K. Lee, J. Kim, S. Choi, U. Yoon, and J. Y. Lee, “A six-port modulator based RF transmission system: Application in an OFDM environment,” in *2017 IEEE International Conference on Communications (ICC)*, IEEE, May 2017, pp. 1–6. doi: 10.1109/ICC.2017.7997351.

[186] Mingquan Bao, Jingjing Chen, and L. Aspemyr, “A single-chip 15 to 30 GHz six-port demodulator for multi-Gb/s communication,” in *2012 IEEE/MTT-S International Microwave Symposium Digest*, IEEE, Jun. 2012, pp. 1–3. doi: 10.1109/MWSYM.2012.6258412.

[187] K. Haddadi, M. M. Wang, D. Glay, and T. Lasri, “Performance of a compact dual six-port millimeter-wave network analyzer,” *IEEE Trans Instrum Meas*, vol. 60, no. 9, pp. 3207–3213, Sep. 2011, doi: 10.1109/TIM.2011.2124690.

[188] M. Mailand, “System Analysis of Six-Port-Based RF-Receivers,” *IEEE Transactions on Circuits and Systems I: Regular Papers*, vol. 65, no. 1, pp. 319–330, Jan. 2018, doi: 10.1109/TCSI.2017.2734922.

[189] Y. Xu and R. G. Bosisio, “Four-port digital millimetric receiver (FP/DMR),” *Microw Opt Technol Lett*, vol. 22, no. 5, pp. 350–355, Sep. 1999, doi: 10.1002/(SICI)1098-2760(19990905)22:5<350::AID-MOP17>3.0.CO;2-X.

[190] K. Haddadi, M. M. Wang, D. Glay, and T. Lasri, “A New Range Finder Based on a Four-Port Junction,” *IEEE Sens J*, vol. 9, no. 6, pp. 697–698, 2009, doi: 10.1109/JSEN.2009.2021189.

[191] W. Zhang *et al.*, “Concurrent Dual-Band Receiver Based on the Multi-Port Correlator for Wireless Applications,” *IEEE Transactions on Circuits and Systems II: Express Briefs*, vol. 65, no. 6, pp. 759–763, Jun. 2018, doi: 10.1109/TCSII.2017.2777993.

[192] G. Neveux, B. Huyart, and G. J. Rodriguez-Guisantes, “Wide-band RF receiver using the ‘five-port’ technology,” *IEEE Trans Veh Technol*, vol. 53, no. 5, pp. 1441–1451, Sep. 2004, doi: 10.1109/TVT.2004.832392.

[193] K. Mabrouk, B. Huyart, and G. Neveux, “3-D aspect in the five-port technique for zero-IF receivers and a new blind calibration method,” *IEEE Trans Microw Theory Tech*, vol. 56, no. 6, pp. 1389–1396, Jun. 2008, doi: 10.1109/TMTT.2008.923347.

[194] A. Hasan and M. Helaoui, “Performance Driven Six-Port Receiver and Its Advantages over Low-IF Receiver Architecture,” *Journal of Electrical and Computer Engineering*, vol. 2014, pp. 1–8, 2014, doi: 10.1155/2014/198120.

[195] J. L. R. Quirarte and J. P. Starski, “Novel Schiffman phase shifters,” *IEEE Trans Microw Theory Tech*, vol. 41, no. 1, pp. 9–14, 1993, doi: 10.1109/22.210223.

[196] Y. J. Cheng, W. Hong, and K. Wu, “Broadband self-compensating phase shifter combining delay line and equal-length unequal-width phaser,” *IEEE Trans Microw Theory Tech*, vol. 58, no. 1, pp. 203–210, 2010, doi: 10.1109/TMTT.2009.2035942.

[197] I. Boudreau, K. Wu, and D. Deslandes, “Broadband phase shifter using air holes in Substrate Integrated Waveguide,” in *2011 IEEE MTT-S International Microwave Symposium*, IEEE, Jun. 2011, pp. 1–4. doi: 10.1109/MWSYM.2011.5972871.

[198] H. Schmiedel and F. Arndt, “Field Theory Design of Rectangular Waveguide Multiple-Slot Narrow-Wall Couplers,” *IEEE Trans Microw Theory Tech*, vol. 34, no. 7, pp. 791–798, Jul. 1986, doi: 10.1109/TMTT.1986.1133442.

[199] S. E. Miller, “Coupled Wave Theory and Waveguide Applications,” *Bell System Technical Journal*, vol. 33, no. 3, pp. 661–719, May 1954, doi: 10.1002/j.1538-7305.1954.tb02359.x.

[200] R. D. M. Pozar, *Microwave Engineering*, 4th ed. Hoboken, NJ, USA: Wiley, 2012.

[201] T. Djerafi, D. Hammou, K. Wu, and S. O. Tatu, “Ring-Shaped Substrate Integrated Waveguide Wilkinson Power Dividers/Combiners,” *IEEE Trans Compon Packaging Manuf Technol*, vol. 4, no. 9, pp. 1461–1469, Sep. 2014, doi: 10.1109/TCPMT.2014.2342156.

[202] S. Horst, R. Bairavasubramanian, M. M. Tentzeris, and J. Papapolymerou, “Modified wilkinson power dividers for millimeter-wave integrated circuits,” *IEEE Trans Microw Theory Tech*, vol. 55, no. 11, pp. 2439–2445, Nov. 2007, doi: 10.1109/TMTT.2007.908672.

[203] A. Moulay and T. Djerafi, “Wilkinson Power Divider with Fixed Width Substrate-Integrated Waveguide Line and a Distributed Isolation Resistance,” *IEEE Microwave and Wireless Components Letters*, vol. 28, no. 2, pp. 114–116, Feb. 2018, doi: 10.1109/LMWC.2018.2790706.

[204] D. Hammou, E. Moldovan, and S. O. Tatu, “Novel MHMIC millimeter wave power divider/combiner,” in *2011 24th Canadian Conference on Electrical and Computer Engineering(CCECE)*, IEEE, May 2011, pp. 000280–000283. doi: 10.1109/CCECE.2011.6030454.

[205] P. Antognetti, G. Massobrio, and and G. Massobrio, *Semiconductor Device Modeling With SPICE*. New York, NY, : USA: McGraw-Hill, 1998.

[206] L. Guo, X. Li, P. Chu, and K. Wu, "Accurately Modeling Zero-Bias Diode-Based RF Power Harvesters with Wide Adaptability to Frequency and Power," *IEEE Transactions on Circuits and Systems I: Regular Papers*, vol. 68, no. 12, pp. 5194–5205, Dec. 2021, doi: 10.1109/TCSI.2021.3112672.

[207] A. Li and K. M. Luk, "Single-Layer Wideband End-Fire Dual-Polarized Antenna Array for Device-to-Device Communication in 5G Wireless Systems," *IEEE Trans Veh Technol*, vol. 69, no. 5, pp. 5142–5150, May 2020, doi: 10.1109/TVT.2020.2979636.

[208] X. Zou, C. M. Tong, J. S. Bao, and W. J. Pang, "SIW-fed yagi antenna and its application on monopulse antenna," *IEEE Antennas Wirel Propag Lett*, vol. 13, pp. 1035–1038, 2014, doi: 10.1109/LAWP.2014.2327161.

[209] M. Esquius-Morote, B. Fuchs, J. F. Zurcher, and J. R. Mosig, "Novel thin and compact H-plane SIW horn antenna," *IEEE Trans Antennas Propag*, vol. 61, no. 6, pp. 2911–2920, 2013, doi: 10.1109/TAP.2013.2254449.

[210] A. Hasan and M. Helaoui, "Novel modeling and calibration approach for multiport receivers mitigating system imperfections and hardware impairments," *IEEE Trans Microw Theory Tech*, vol. 60, no. 8, pp. 2644–2653, 2012, doi: 10.1109/TMTT.2012.2201742.

[211] F. Boccardi *et al.*, "Spectrum Pooling in MmWave Networks: Opportunities, Challenges, and Enablers," *IEEE Communications Magazine*, vol. 54, no. 11, pp. 33–39, Nov. 2016, doi: 10.1109/MCOM.2016.1600191CM.

[212] M. Agiwal, A. Roy, and N. Saxena, "Next Generation 5G Wireless Networks: A Comprehensive Survey," *IEEE Communications Surveys & Tutorials*, vol. 18, no. 3, pp. 1617–1655, Jul. 2016, doi: 10.1109/COMST.2016.2532458.

[213] M. N. Tehrani, M. Uysal, and H. Yanikomeroglu, "Device-to-device communication in 5G cellular networks: challenges, solutions, and future directions," *IEEE Communications Magazine*, vol. 52, no. 5, pp. 86–92, May 2014, doi: 10.1109/MCOM.2014.6815897.

[214] R. G. Vaughan, "Polarization diversity in mobile communications," *IEEE Trans Veh Technol*, vol. 39, no. 3, pp. 177–186, 1990, doi: 10.1109/25.130998.

[215] W. C. Jakes, *Microwave Mobile Communications*. Piscataway, NJ, USA: IEEE Press, 1994.

[216] L. Chettri and R. Bera, "A Comprehensive Survey on Internet of Things (IoT) Toward 5G Wireless Systems," *IEEE Internet Things J*, vol. 7, no. 1, pp. 16–32, Jan. 2020, doi: 10.1109/JIOT.2019.2948888.

[217] L. Dong, H. Choo, R. W. Heath, and H. Ling, "Simulation of MIMO channel capacity with antenna polarization diversity," *IEEE Trans Wirel Commun*, vol. 4, no. 4, pp. 1869–1872, Jul. 2005, doi: 10.1109/TWC.2005.850318.

[218] J. Song, J. Choi, S. G. Larew, D. J. Love, T. A. Thomas, and A. A. Ghosh, "Adaptive Millimeter Wave Beam Alignment for Dual-Polarized MIMO Systems," *IEEE Trans Wirel Commun*, vol. 14, no. 11, pp. 6283–6296, Nov. 2015, doi: 10.1109/TWC.2015.2452263.

[219] S. Liao *et al.*, "Passive millimeter-wave dual-polarization imagers," *IEEE Trans Instrum Meas*, vol. 61, no. 7, pp. 2042–2050, 2012, doi: 10.1109/TIM.2012.2183032.

[220] K. Dasgupta *et al.*, "A 60-GHz transceiver and baseband with polarization MIMO in 28-nm CMOS," *IEEE J Solid-State Circuits*, vol. 53, no. 12, pp. 3613–3627, Dec. 2018, doi: 10.1109/JSSC.2018.2876473.

[221] C. M. Cooke *et al.*, "A 220-GHz InP HEMT Direct Detection Polarimeter," *IEEE Trans Microw Theory Tech*, vol. 67, no. 12, pp. 5191–5201, Dec. 2019, doi: 10.1109/TMTT.2019.2944908.

[222] C. M. Cooke *et al.*, "A 220 GHz Dual Channel LNA Front-End for a Direct Detection Polarimetric Receiver," in *2019 IEEE MTT-S International Microwave Symposium (IMS)*, IEEE, Jun. 2019, pp. 508–511. doi: 10.1109/MWSYM.2019.8701101.

[223] H. Bakli, K. Haddadi, and T. Lasri, "Interferometric technique for scanning near-field microwave microscopy applications," *IEEE Trans Instrum Meas*, vol. 63, no. 5, pp. 1281–1286, 2014, doi: 10.1109/TIM.2013.2296416.

[224] S. O. Tatu, A. Serban, M. Helaoui, and A. Koelpin, "Multiport Technology: The New Rise of an Old Concept," *IEEE Microw Mag*, vol. 15, no. 7, pp. S34–S44, Nov. 2014, doi: 10.1109/MMM.2014.2356149.

[225] A. Koelpin, G. Vinci, B. Laemmle, D. Kissinger, and R. Weigel, “The Six-Port in Modern Society,” *IEEE Microw Mag*, vol. 11, no. 7, pp. 35–43, Dec. 2010, doi: 10.1109/MMM.2010.938584.

[226] W. Zhang, A. Hasan, F. M. Ghannouchi, M. Helaoui, Y. Wu, and Y. Liu, “Concurrent dual-band receiver based on novel six-port correlator for wireless applications,” *IEEE Access*, vol. 5, pp. 25826–25834, Oct. 2017, doi: 10.1109/ACCESS.2017.2768364.

[227] A. A. Sakr, W. M. Dyab, and K. Wu, “A dually polarized six-port junction based on polarization-selective coupling for polarization-inclusive remote sensing,” *IEEE Trans Microw Theory Tech*, vol. 66, no. 8, pp. 3817–3827, Aug. 2018, doi: 10.1109/TMTT.2018.2834513.

[228] W. M. Dyab, A. A. Sakr, and K. Wu, “Dually-Polarized Butler Matrix for Base Stations With Polarization Diversity,” in *IEEE Transactions on Microwave Theory and Techniques*, Institute of Electrical and Electronics Engineers Inc., Dec. 2018, pp. 5543–5553. doi: 10.1109/TMTT.2018.2880786.

[229] F. Alessandri and R. Ravanelli, “A new class of dual-mode directional couplers for compact dual-polarization beam-forming networks,” *IEEE Microwave and Guided Wave Letters*, vol. 7, no. 9, pp. 300–301, 1997, doi: 10.1109/75.622548.

[230] M. Kishihara, K. Yamane, and I. Ohta, “Design of Cruciform Directional Couplers in E-Plane Rectangular Waveguide,” in *2006 IEEE MTT-S International Microwave Symposium Digest*, IEEE, 2006, pp. 1722–1725. doi: 10.1109/MWSYM.2006.249712.

[231] M. Kishihara, I. Ohta, T. Kawai, K. Okubo, and J. Yamakita, “Design of H-plane waveguide cruciform hybrid using dielectric posts,” in *2008 Asia-Pacific Microwave Conference*, IEEE, Dec. 2008, pp. 1–4. doi: 10.1109/APMC.2008.4958206.

[232] T. J. Reck and G. Chattopadhyay, “A 600 GHz asymmetrical orthogonal mode transducer,” *IEEE Microwave and Wireless Components Letters*, vol. 23, no. 11, pp. 569–571, 2013, doi: 10.1109/LMWC.2013.2280642.

[233] D. W. Porterfield, “Broadband Millimeter-Wave Hybrid Circulators,” *IEEE Trans Microw Theory Tech*, vol. 71, no. 8, pp. 3501–3507, Aug. 2023, doi: 10.1109/TMTT.2023.3239886.

[234] C. A. Leal-Sevillano, Y. Tian, M. J. Lancaster, J. A. Ruiz-Cruz, J. R. Montejo-Garai, and J. M. Rebollar, "A micromachined dual-band orthomode transducer," *IEEE Trans Microw Theory Tech*, vol. 62, no. 1, pp. 55–63, 2014, doi: 10.1109/TMTT.2013.2292611.

[235] J. A. Ruiz-Cruz, J. R. Montejo-Garai, and J. M. Rebollar, "Multi-section bow-tie steps for full-band waveguide polarization rotation," *IEEE Microwave and Wireless Components Letters*, vol. 20, no. 7, pp. 375–377, 2010, doi: 10.1109/LMWC.2010.2049428.

[236] U. Rosenberg and R. Beyer, "Combined twist-bend for very compact interconnections in integrated waveguide subsystems," in *in Proc. 42nd Eur. Microw. Conf.*, Amsterdam, The Netherlands, Oct. 2012, pp. 1154–1157.

[237] Z. C. Hao, W. Q. Ding, and W. Hong, "Developing Low-Cost W-Band SIW Bandpass Filters Using the Commercially Available Printed-Circuit-Board Technology," *IEEE Trans Microw Theory Tech*, vol. 64, no. 6, pp. 1775–1786, Jun. 2016, doi: 10.1109/TMTT.2016.2553029.

[238] S. Linz, F. Lurz, R. Weigel, and A. Koelpin, "Squircle-Based Calibration Algorithm for Six-Port Radar," *IEEE Trans Microw Theory Tech*, vol. 67, no. 10, pp. 4023–4030, Oct. 2019, doi: 10.1109/TMTT.2019.2931968.

[239] S. Krause, F. Michler, A. Kolpin, M. Rudolph, and W. Heinrich, "A Digital Correction Method for Increased Dynamic Range in Interferometric Six-Port Radars," *IEEE Microwave and Wireless Components Letters*, vol. 31, no. 8, pp. 997–1000, Aug. 2021, doi: 10.1109/LMWC.2021.3084338.

[240] M. Xiao *et al.*, "Millimeter Wave Communications for Future Mobile Networks," Sep. 01, 2017, *Institute of Electrical and Electronics Engineers Inc.* doi: 10.1109/JSAC.2017.2719924.

[241] K. Sarabandi, A. Jam, M. Vahidpour, and J. East, "A Novel Frequency Beam-Steering Antenna Array for Submillimeter-Wave Applications," *IEEE Trans Terahertz Sci Technol*, vol. 8, no. 6, pp. 654–665, Nov. 2018, doi: 10.1109/TTHZ.2018.2866019.

[242]L. Han and K. Wu, "Multifunctional transceiver for future intelligent transportation systems," *IEEE Trans Microw Theory Tech*, vol. 59, no. 7, pp. 1879–1892, Jul. 2011, doi: 10.1109/TMTT.2011.2138156.

[243] L. Han and K. Wu, “Emerging advances in transceiver technology fusion of wireless communication and radar sensing systems,” in *in Proc. Asia–Pacific Microw. Conf.,* , Melbourne, VIC, Australia, Dec. 2011, pp. 951–954.

[244] C. Hannachi and K. Wu, “Dual-Mode RF Mixer for Low-Power Direct-Conversion Receiver,” *IEEE Microwave and Wireless Components Letters*, vol. 32, no. 6, pp. 583–586, Jun. 2022, doi: 10.1109/LMWC.2022.3147432.

[245] K. Haddadi and T. Lasri, “Formulation for complete and accurate calibration of six-port reflectometer,” *IEEE Trans Microw Theory Tech*, vol. 60, no. 3 PART 1, pp. 574–581, Mar. 2012, doi: 10.1109/TMTT.2011.2181861.

[246] S. A. Keivaan, P. Burasa, and K. Wu, “Virtual Receiver Matrix for Multifunction Communication and Sensing Wireless Systems Using Simultaneous Incident Waves at the Same Carrier Frequency,” in *2023 IEEE/MTT-S International Microwave Symposium - IMS 2023*, IEEE, Jun. 2023, pp. 1176–1179. doi: 10.1109/IMS37964.2023.10188201.

[247] S. A. Keivaan, P. Burasa, and K. Wu, “Virtual Receiver Matrix for Future Multifunction Wireless Systems,” in *IEEE MTT-S International Microwave Symposium Digest*, Institute of Electrical and Electronics Engineers Inc., 2022, pp. 386–389. doi: 10.1109/IMS37962.2022.9865247.

[248] A. Navarrini and R. L. Plambeck, “A turnstile junction waveguide orthomode transducer,” in *IEEE Transactions on Microwave Theory and Techniques*, Jan. 2006, pp. 272–277. doi: 10.1109/TMTT.2005.860505.

[249] N. J. G. Fonseca, “Two-Probe Waveguide Orthomode Transducer with Twofold Rotational Symmetry,” *IEEE Trans Microw Theory Tech*, vol. 69, no. 7, pp. 3228–3235, Jul. 2021, doi: 10.1109/TMTT.2021.3075957.

[250] L. Gerhardt, F. C. C. De Castro, C. Müller, and M. C. F. De Castro, “Compact Symmetric Opposed Port Orthomode Transducer,” *IEEE Microwave and Wireless Components Letters*, vol. 29, no. 7, pp. 471–473, Jul. 2019, doi: 10.1109/LMWC.2019.2917770.

[251] I. Mohamed and A. R. Sebak, “Broadband Transition of Substrate-Integrated Waveguide-to-Air-Filled Rectangular Waveguide,” *IEEE Microwave and Wireless Components Letters*, vol. 28, no. 11, pp. 966–968, Nov. 2018, doi: 10.1109/LMWC.2018.2871330.

[252] B. Yuan, P. Wu, Z. Yu, and C. Hao, “Wideband End-Wall Transition From Microstrip to Waveguide With via-Less Choke Structure for Terahertz Application,” *IEEE Trans Terahertz Sci Technol*, vol. 12, no. 3, pp. 317–320, May 2022, doi: 10.1109/TTHZ.2022.3163356.

[253] G. A. Kumar and D. R. Poddar, “Broadband Rectangular Waveguide to Suspended Stripline Transition Using Dendritic Structure,” *IEEE Microwave and Wireless Components Letters*, vol. 26, no. 11, pp. 900–902, Nov. 2016, doi: 10.1109/LMWC.2016.2615009.

[254] S. Liu and F. Xu, “Novel Substrate-Integrated Waveguide Phase Shifter and its Application to Six-Port Junction,” *IEEE Trans Microw Theory Tech*, vol. 67, no. 10, pp. 4167–4174, Oct. 2019, doi: 10.1109/TMTT.2019.2934435.

[255] Y. D. Dong, T. Yang, and T. Itoh, “Substrate integrated waveguide loaded by complementary split-ring resonators and its applications to miniaturized waveguide filters,” in *IEEE Transactions on Microwave Theory and Techniques*, Jan. 2009, pp. 2211–2223. doi: 10.1109/TMTT.2009.2027156.

[256] Y. Dong and T. Itoh, “Substrate integrated waveguide loaded by complementary split-ring resonators for miniaturized diplexer design,” *IEEE Microwave and Wireless Components Letters*, vol. 21, no. 1, pp. 10–12, Jan. 2011, doi: 10.1109/LMWC.2010.2091263.

[257] S. Shi, C. Li, J. Hu, X. Zhang, and G. Fang, “A High Frequency Vibration Compensation Approach for Terahertz SAR Based on Sinusoidal Frequency Modulation Fourier Transform,” *IEEE Sens J*, vol. 21, no. 9, pp. 10796–10803, May 2021, doi: 10.1109/JSEN.2021.3056519.

[258] R. Han *et al.*, “Filling the Gap: Silicon Terahertz Integrated Circuits Offer Our Best Bet,” *IEEE Microw Mag*, vol. 20, no. 4, pp. 80–93, Apr. 2019, doi: 10.1109/MMM.2019.2891379.

[259] D. Kissinger, M. Kaynak, and A. Mai, “Integrated Millimeter-Wave and Terahertz Analyzers for Biomedical Applications,” *IEEE Trans Microw Theory Tech*, vol. 70, no. 11, pp. 5141–5158, Nov. 2022, doi: 10.1109/TMTT.2022.3185053.

[260] T. S. Rappaport *et al.*, “Wireless communications and applications above 100 GHz: Opportunities and challenges for 6g and beyond,” *IEEE Access*, vol. 7, pp. 78729–78757, 2019, doi: 10.1109/ACCESS.2019.2921522.

[261] J. W. Holloway, G. C. Dogiamis, and R. Han, “Innovations in Terahertz Interconnects: High-Speed Data Transport over Fully Electrical Terahertz Waveguide Links,” *IEEE Microw Mag*, vol. 21, no. 1, pp. 35–50, Jan. 2020, doi: 10.1109/MMM.2019.2945139.

[262] D. Simic, K. Guo, and P. Reynaert, “A 420-GHz Sub-5-µm Range Resolution TX-RX Phase Imaging System in 40-nm CMOS Technology,” *IEEE J Solid-State Circuits*, vol. 56, no. 12, pp. 3827–3839, Dec. 2021, doi: 10.1109/JSSC.2021.3111152.

[263] H. Mohammadnezhad, H. Wang, A. Cathelin, and P. Heydari, “A 115-135-GHz 8PSK Receiver Using Multi-Phase RF-Correlation-Based Direct-Demodulation Method,” *IEEE J Solid-State Circuits*, vol. 54, no. 9, pp. 2435–2448, Sep. 2019, doi: 10.1109/JSSC.2019.2920117.

[264] A. Karakuzulu, W. A. Ahmad, D. Kissinger, and A. Malignaggi, “A Four-Channel Bidirectional D-Band Phased-Array Transceiver for 200 Gb/s 6G Wireless Communications in a 130-nm BiCMOS Technology,” *IEEE J Solid-State Circuits*, vol. 58, no. 5, pp. 1310–1322, May 2023, doi: 10.1109/JSSC.2022.3232948.

[265] K. Haddadi and T. Lasri, “60-GHz near-field six-port microscope using a scanning slit probe for subsurface sensing,” *IEEE Sens J*, vol. 12, no. 8, pp. 2575–2576, 2012, doi: 10.1109/JSEN.2012.2197197.

[266] M. Hofmann, G. Fischer, R. Weigel, and D. Kissinger, “Microwave-based noninvasive concentration measurements for biomedical applications,” *IEEE Trans Microw Theory Tech*, vol. 61, no. 5, pp. 2195–2204, 2013, doi: 10.1109/TMTT.2013.2250516.

[267] R. G. Bosisio *et al.*, “New-Wave Radio,” *IEEE Microw Mag*, vol. 9, no. 1, pp. 89–100, Feb. 2008, doi: 10.1109/MMM.2007.910923.

[268] A. Agrawal *et al.*, “A 128-Gb/s D-Band Receiver with Integrated PLL and ADC Achieving 1.95-pJ/b Efficiency in 22-nm FinFET,” *IEEE J Solid-State Circuits*, vol. 58, no. 12, pp. 3364–3379, Dec. 2023, doi: 10.1109/JSSC.2023.3315692.

[269] J.-B. Dore *et al.*, “Technology Roadmap for Beyond 5G Wireless Connectivity in D-band,” in *2020 2nd 6G Wireless Summit (6G SUMMIT)*, IEEE, Mar. 2020, pp. 1–5. doi: 10.1109/6GSUMMIT49458.2020.9083890.

[270] T. H. Jang *et al.*, “120-GHz Wideband I/Q Receiver Based on Baseband Equalizing Technique,” *IEEE J Solid-State Circuits*, vol. 56, no. 6, pp. 1697–1710, Jun. 2021, doi: 10.1109/JSSC.2020.3032022.

[271] P. Heydari, “Transceivers for 6G Wireless Communications: Challenges and Design Solutions,” in *2021 IEEE Custom Integrated Circuits Conference (CICC)*, IEEE, Apr. 2021, pp. 1–8. doi: 10.1109/CICC51472.2021.9431450.

[272] A. Hamani *et al.*, “A 108-Gb/s 64-QAM CMOS D-Band Rx with Integrated LO Generation,” *IEEE Solid State Circuits Lett*, vol. 3, pp. 202–205, 2020, doi: 10.1109/LSSC.2020.3011529.

[273] Z. Li *et al.*, “A 220-GHz Sliding-IF Quadrature Transmitter and Receiver Chipset for High Data Rate Communication in 0.13-μm SiGe BiCMOS,” *IEEE J Solid-State Circuits*, vol. 58, no. 7, pp. 1913–1927, Jul. 2023, doi: 10.1109/JSSC.2023.3236621.

[274] W. Deng *et al.*, “A D-Band Joint Radar-Communication CMOS Transceiver,” *IEEE J Solid-State Circuits*, vol. 58, no. 2, pp. 411–427, Feb. 2023, doi: 10.1109/JSSC.2022.3185160.

[275] C. D’heer and P. Reynaert, “A 135 GHz 24 Gb/s Direct-Digital Demodulation 16-QAM Receiver in 28 nm CMOS,” in *ESSCIRC 2022- IEEE 48th European Solid State Circuits Conference (ESSCIRC)*, IEEE, Sep. 2022, pp. 485–488. doi: 10.1109/ESSCIRC55480.2022.9911340.

[276] K. Haddadi and T. Lasri, “Six-port technology for millimeter-wave radar and imaging applications,” in *2014 IEEE Topical Conference on Wireless Sensors and Sensor Networks (WiSNet)*, IEEE, Jan. 2014, pp. 1–3. doi: 10.1109/WiSNet.2014.6825508.

APPENDIX A LIST OF PUBLICATIONS

1. Journal papers:

[1] **J. Deng**, P. Burasa and K. Wu, "Multiport Interferometric Technology: A Versatile Transceiver Solution for Wireless Communication, Sensing, and Imaging Systems," *Integrated Circuits and Systems*, vol. 2, no. 4, pp. 175-204, Sept.-Oct. 2025.

[2] **J. Deng**, P. Burasa, S. Ali Keivaan and K. Wu, "Waveguide Receiver Array for Joint Communication, Sensing, and Power Transfer Systems," *IEEE Trans. Microw. Theory Tech.*, vol. 73, no. 7, pp. 4204-4217, July 2025.

[3] **J. Deng**, P. Burasa and K. Wu, "Joint Multiband Linear Interferometric Receiver for Integrated Microwave and Terahertz Sensing and Communication Systems," *IEEE Trans. Microw. Theory Tech.*, vol. 72, no. 9, pp. 5550-5562, Sept. 2024.

[4] **J. Deng**, P. Burasa and K. Wu, "All-in-One Dual-Polarization Waveguide Receiver for Multichannel Wireless Systems," *IEEE Trans. Microw. Theory Tech.*, vol. 72, no. 8, pp. 4998-5013, Aug. 2024.

[5] **J. Deng**, P. Burasa, and K. Wu, "Self-contained dual-input interferometric receiver for paralleled-multichannel wireless systems," *IEEE Trans. Circuits Syst. I, Reg. Papers*, vol. 71, no. 2, pp. 934–947, Feb. 2024.

[6] **J. Deng**, P. Burasa and K. Wu, "Unified Microwave Terahertz Waveguide Coupler for Multiband Wireless Applications," *IEEE Trans. Compon., Packag., Manuf. Technol.*, vol. 15, no. 5, pp. 1032-1043, May 2025.

[7] **J. Deng**, P. Burasa, and K. Wu, "A 325–500-GHz Waveguide Balun With Polarization Twist Characteristics for THz Integrated Circuits and Systems," *IEEE Trans. Microw. Theory Tech.*, early access, pp. 1–11, Jul. 2025.

[8] **J. Deng**, P. Burasa, and K. Wu, "Compact 140–220 GHz E/H waveguide phase shifter and its application to terahertz multiport circuits," *IEEE Trans. Terahertz Sci. Technol.*, vol. 13, no. 5, pp. 511–525, Sep. 2023.

[9] **J. Deng**, P. Burasa, and K. Wu, "Waveguide coupler with polarized rotation characteristics for terahertz applications," *IEEE Trans. Microw. Theory Tech.*, vol. 71, no. 5, pp. 2091–2103, May 2023.

[10] P. Burasa, **J. Deng** and K. Wu, "A 300-GHz Dual-Polarized CMOS Waveguide Receiver for High-Density Terahertz Integrated Multichannel Wireless Systems-on-Chip," *IEEE Trans. Microw. Theory Tech*., vol. 73, no. 5, pp. 3044-3058, May 2025.

[11] S. Ali Keivaan, P. Burasa, **J. Deng** and K. Wu, "Concurrent Detection of 2-D Angle-of-Arrival and Polarization Enabled by Virtual Transceiver Matrix Architecture," *IEEE Trans. Microw. Theory Techn.*, vol. 73, no. 9, pp. 6863-6878, Sept. 2025.

2. Conference papers:

[1] **J. Deng**, P. Burasa, S. A. Keivaan and K. Wu, "Spatially Distributed Polarization Receiver Array for Communication and Sensing Multifunction Systems," *2024 54th European Microwave Conference (EuMC)*, Paris, France, 2024, pp. 148-151.

[2] **J. Deng**, P. Burasa and K. Wu, "Multichannel and Multifunction Interferometric Receiver Architectures for Multistandard Millimeter-Wave and Terahertz Applications," *2024 IEEE Wireless and Microwave Technology Conference (WAMICON)*, Clearwater, FL, USA, 2024, pp. 1-4.

[3] **J. Deng**, P. Burasa and K. Wu, "Waveguide Coupler with Self-Contained 90° Polarization Rotation for Integrated THz Waveguide Circuits and Systems," *2022 IEEE MTT-S International Wireless Symposium (IWS)*, Harbin, China, 2022, pp. 1-3.

[4] **J. Deng**, P. Burasa and K. Wu, "Full-Band E- Plane Waveguide Phase Shifters with Self-Compensating Characteristics for THz Circuits and Systems," *2022 52nd European Microwave Conference (EuMC)*, Milan, Italy, 2022, pp. 199-202.